Università degli Studi di Palermo

AREA QUALITÀ, PROGRAMMAZIONE E SUPPORTO STRATEGICO
SETTORE STRATEGIA PER LA RICERCA
U. O. DOTTORATI

Dottorato di Ricerca in Scienze Fisiche e Chimiche
Dipartimento di Fisica e Chimica - Emilio Segrè
Settore Scientifico Disciplinare FIS-01

FLUORESCENT NANOCARBONS AS BUILDING BLOCKS FOR OPTICAL HYBRID STRUCTURES

DOTTORE
MARCO REALE

COORDINATORE
PROF. MARCO CANNAS

TUTOR
PROF. FABRIZIO MESSINA

CO TUTOR
DR. ALICE SCIORTINO

CICLO XXXVI
ANNO CONSEGUIMENTO TITOLO 2023

Table of Contents

Abstract

Carbon nanomaterials play a central role in the field of nanoscience. In particular, luminescent zero-dimensional nanocarbons (0DNCs) such as Carbon Dots (CDs) and nanographenes (NGs) are garnering significant attention for their efficient light harvesting properties and tunable optical properties. CDs are a relatively recent class of nearly-spherical nanoparticles, typically smaller than 10 nm, consisting of a carbonaceous core and a surface shell that can be decorated by a variety of chemical functional groups. On the other hand, NGs are nanosized graphenic fragments with precisely defined structures, synthesized through precise organic chemistry methods that provide tight control over their atomic structure. These 0DNCs can be considered as the carbon-based counterparts of semiconductor quantum dots, which have been just recognized with the Nobel Prize in Chemistry 2023, possessing the advantage of absence of toxic chemical elements with respect to their inorganic analogues. 0DNCs display exceptional optical properties, such as bright optical transition in the visible range and photoinduced charge or energy transfer behaviours. In addition, 0DNCs exhibit an exceptional structural flexibility, which arises from the unique chemistry of carbon, allowing for the design and functionalization of their structures as desired. Because of all these qualities, 0DNCs represent ideal building blocks for creating innovative hybrid structures. By combining them with other opportunely chosen materials, the properties of the different components can be synergistically exploited, enhancing or modulating existing properties or introducing entirely new functionalities absent in the original components. This capability has led to the creation of a diverse range of multifunctional nanohybrids, which are currently a subject of very large scientific interest due to their countless potential applications.

Within this context, the aim of this Thesis is to perform a fundamental photophysical study of specific 0DNC-based hybrid materials, based on the use of either NGs or CDs as fundamental building blocks. Firstly, a comprehensive photophysical characterization of a palette of various atomically-precise NGs is performed to investigate the impact of structural variations or slightly different edge functionalization on their optical properties. After the study of their standalone properties, specific NGs are selected to build all-carbon hybrids by coupling them to fullerenes or polystyrene microparticles. In the first case, the supramolecular interactions between a properly functionalized nanographene and fullerenes are exploited to promote photoinduced charge-transfers. In the second case, polystyrene microparticles serve as microresonators to modulate the emission features of the NGs they are doped with to obtain fluorescent microtags with unique spectroscopic characteristics. Moving to the second category of hybrid nanomaterials, various carbon/plasmonic nanohybrid structures are designed through the coupling of a specific type of CDs with silver and gold nanoparticles. Depending on their mutual separation, metallic nanopar-

ticles can act as a charge reservoir to produce charge pair separation or help to modulate the optical properties of CDs *via* plasmonic interactions. The results provide substantial new insight on several aspects of the fundamental photophysics of 0DNCs, and demonstrate their versatility to a wide range of applications in the ever-evolving landscape of nanotechnology.

Chapter 1

Introduction

"If the elaboration of carbon were not a common daily occurrence, on the scale of billions of tons a week, wherever the green of a leaf appears, it would by full right deserve to be called a miracle."

P. Levi, *Periodic Table*

An element more than others emerges as the enigmatic thread weaving the intricate design of life. Carbon, with its unique characteristics, not only provides the foundation for terrestrial existence but also stands as a cornerstone in the field of nanoscience. While conventional *bulk* manifestations of carbon are predominantly limited to graphite and diamond, the world at the nanoscale reveals a wide array of carbon-based nanosystems. The crucial role played by carbon can be attributed to its extraordinary ability to assume diverse allotropic structures, made possible by its unique chemistry, which allows it to engage in various hybridization schemes.

This Chapter aims to provide a brief introduction to the current state of the art in carbon nanostructures, with a particular focus on luminescent carbon-based nanosystems and hybrid structures containing them as basic building block. The first part of the Chapter will rapidly present the richness of intricate carbon-based nanostructures that have been extensively studied in the last few decades, encompassing fullerenes, nanotubes and graphene. More recently, several luminescent nanocarbon systems have attracted significant scientific interest as they challenge the paradigm of carbon as "black" material unable to emit light. Among them, two main categories can be recognized, namely Carbon Dots and Nanographenes, to which consistent part of this Chapter is dedicated. In particular, the central role that these luminescent nanocarbons have started to play in the design of more complex hybrid structures, through their coupling with other materials, will be highlighted. Finally, the main goals of the present Thesis will presented in the conclusive section of this Chapter.

1.1 The small huge world of Carbon

In the realm of natural materials, the two main encountered forms of carbon are graphite and diamond [1]. Graphite consists of layers of sp^2 hybridized carbon atoms, forming hexagonal net-

works stacked on top of each other through weak van der Waals interactions. In contrast, diamond is composed of carbon atoms with a tetrahedral covalent bond structure and sp^3 hybridization. Graphite and diamond appear emblematically representative of how, despite having the same chemical composition, materials can exhibit entirely dissimilar physical properties due to their different structures. Indeed, diamond is exceptionally hard and transparent, while graphite is soft and opaque. Electrically and thermally, diamond is an insulator, while graphite, particularly along its basal planes, behaves as a semiconductor with almost zero band gap, enabling conduction even at room temperature [1].

In contrast, the world of carbon-based nanomaterials is infinitely more diverse and intricate. This is not surprising, given that nanomaterials are defined as substances where at least one dimension falls within the nanometer scale. Indeed, beyond the specific structures formed by carbon atoms, the confinement of the dimensions of these materials within the nanoscale, strongly influences their characteristics and properties, which become also highly dependent on their morphology, a factor that is irrelevant at the macroscopic scale [2]. In addition, the high surface-to-volume ratio of nanomaterials means that even minor surface modifications can lead to substantial changes in their overall physical and chemical properties.

1.1.1 Fullerenes

Chronologically speaking, in the domain of carbon nanomaterials, the discovery of C_{60} fullerene in 1985 [3] played a pioneering role in the chemistry of that time. This discovery, awarded with the Nobel Prize of Chemistry in 1996, shed light on how the simple rearrangement of carbon atoms to form nanostructures could give rise to a class of new carbon nanomaterials. Fullerenes with a closed mesh topology are denoted by the empirical formula C_n, where n represents the number of carbon atoms. In fullerenes, the latter are arranged to form always twelve pentagons and varying number of hexagons depending on n, giving rise to ball-shaped structures with diameters which can range from 0.7 to 1.6 nm. The structures of two of the most representative fullerenes, namely C_{60} and C_{70}, are reported in Figure 1.1. Despite their limited employment due to a quite low chemical activity, fullerenes are known to be remarkably good electron acceptors: for example, a C_{60} molecule in solution can reversibly accept up to six electrons [4].

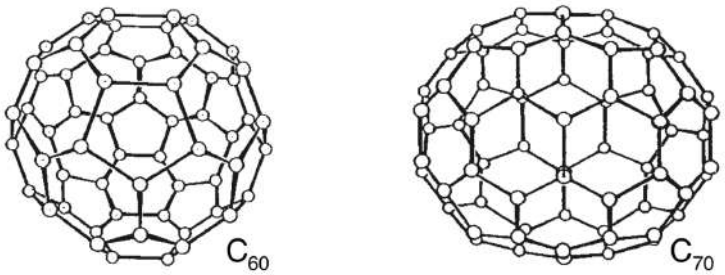

Figure 1.1: Chemical structures of C_{60} and C_{70} fullerenes [Adapted from [5]].

1.1.2 Carbon Nanotubes

In 1990s, the spotlight of nanoscience shifted towards carbon nanotubes (CNTs), rolled hexagonal networks of sp^2 carbon atoms forming tubular nanostructures with internal empty space and notably high aspect ratio, making them as a perfect archetypal of 1D material. The simplest forms of CNTs consist of a single wall structures, known as Single-Walled Carbon Nanotubes (SWCNTs) with diameters ranging from approximately 0.4 to 2 nanometers and lengths extending even for several micrometers. CNTs can also exist as double-walled (DWCNTs) or multi-walled (MWCNTs) structures, depending on the number of rolled layers in their cylindrical structure. Figure 1.2(a) and Figure 1.2(b) show HRTEM images of a SWCNT and a DWCNT, respectively. Notably, the aspect ratio, *i.e.* the length-to-diameter ratio, often exceeds 10^4, making CNTs one of the most anisotropic materials known. In addition to diameter and length, chirality, which refers to the angle between the hexagonal arrangement and the axis of the nanotube is a crucial characteristic of CNTs. Depending on it, the sequence of C-C bonds that spans the circumference perpendicular to the tube axis can be arranged in various ways, with zigzag, armchair and chiral patterns which profoundly determine the physical properties of the CNTs [1, 6]. For instance, the electronic characteristics of SWCNTs can range from conductive to semiconductive depending on the specific chirality [6]. These nanotubes typically exhibit outstanding mechanical properties, extraordinary electrical and thermal conductivity, and, in general, versatile chemical reactivity [1].

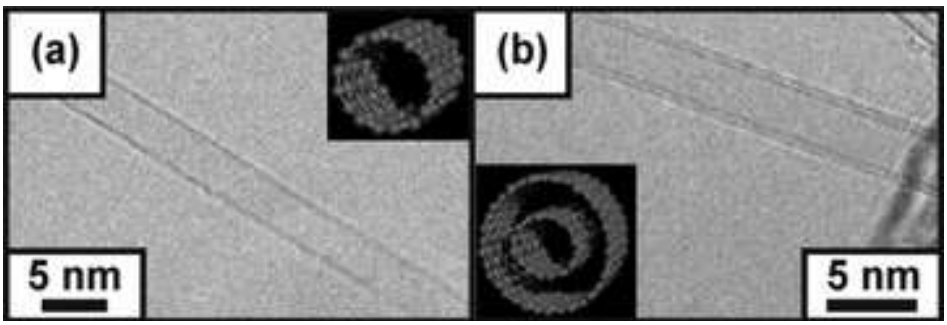

Figure 1.2: HRTEM images of (a) SWCNTs. (b) DWCNTs. [Adapted from [1]].

1.1.3 Graphene

Although it had been used before, the term 'graphene' was clearly defined by Hans Peter Boehm in 1986 [7] to describe a single sheet of graphite. Consequently, as also recognized by IUPAC in 1997, graphene is the two-dimensional allotropic form of carbon, consisting on a carbon sheet constituted by a hexagonal lattice of sp^2 hybridized carbon atoms, which makes it as the most representative 2D material. Effective isolation of graphene was achieved in 2004 by Geim and Novoselov [8], which were awarded the Nobel Prize in Physics in 2010. They accomplished graphene isolation by exfoliation from highly oriented pyrolytic graphite using an extremely cheap and straightforward method known as *scotch taping*. Remarkably, this technique turned out to be

highly efficient, yielding high-quality graphene without the need for more complex and expensive equipment. TEM imaging allows to visualize graphene monolayers as translucent films atop the underlying substrate, as shown in Figure 1.3(a). HRTEM images, such as the one presented in Figure 1.3(b), can clearly reveal the presence of the iconic honeycomb lattice, which is currently considered one of the mechanically strongest structures. The non-hybridized p orbitals of carbon atoms are positioned perpendicularly to the flat structure of the graphene sheet. These orbitals, highly interacting with each others, create the semi-filled π band which imparts graphene its aromatic character. Graphene is characterized by a linear energy-momentum dispersion relation, aspect which implies that the charge carriers behave as massless Dirac fermions, determining an extremely high electron mobility [9]. Extensive experimental studies confirmed the remarkable properties predicted by earlier theoretical research, making graphene as a highly promising material for applications in fields like electronics, microelectronics, sensing, catalysis, and more [10].

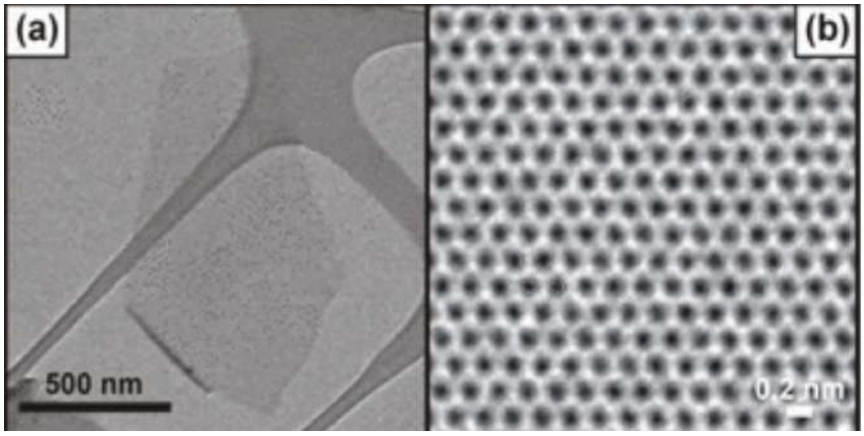

Figure 1.3: (a) TEM image of a single graphene monolayer. (b)HRTEM image of a single graphene monolayer. [Adapted from [1]].

However, despite graphene's marked physical properties, it is not considered interesting from a photophysical perspective due to the lack of an optical bandgap. Indeed, in a perfect single layer of graphene, the highest occupied molecular orbital (HOMO) touches the lowest unoccopied molecular orbital (LUMO) at a single Dirac point [10]. In fact, more generally, the association of carbon nanostructures with photon emission properties has been long missing. Nevertheless, in recent time, luminescent zero-dimensional nanocarbons (0DNC) have emerged as significant players in the realm of nanomaterials, in particular Carbon Dots and Nanographenes to which the following two sections are dedicated.

1.2 Carbon Dots

Carbon Dots (CDs) are carbonaceous surface-functionalized nanoparticles, typically less than 10 nm in size, renowned for their remarkable optical properties, such as an intense and tunable fluorescence. The accidental discovery of CDs in 2004/2006, while purifying SWCNTs [11, 12],

triggered a huge scientific interest, resulting in thousands of annual studies, owing to their extraordinary emission properties in the visible range. These, combined with their inexpensive and straightforward synthesis [13, 14], strong sensitivity to the external environment [15, 16], tendency to display charge transfer processes [17–19], low-toxicity and water solubility both promoting biocompatibility [15, 20], has led to the widespread use of CDs across a broad spectrum of applications, ranging from opto-electronics to sensing [21].

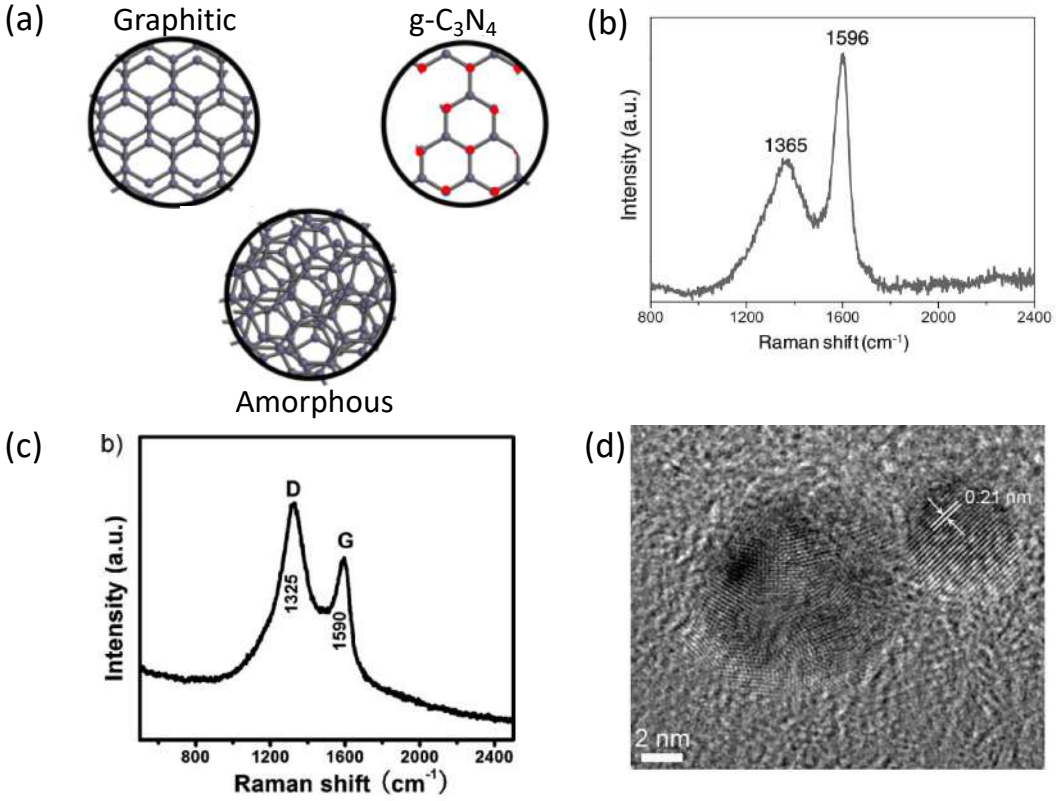

Figure 1.4: (a) Schematic representation of commonly reported CD structures. [Adapted from [21]]. (b) Raman Spectrum of highly graphitic CDs [Adapted from [22]]. (c) Raman Spectrum of lowly graphitic CDs [Adapted from [23]]. (c) HRTEM image of graphitic CDs [Adapted from [24]].

CDs, generally featuring an almost spherical shape, can be characterized by distinct core structures. Although not universally accepted, a common classification of the most significant types of CDs is reported in Figure 1.4(a). CDs may be graphitic as most commonly observed [12, 25–27], characterized by a C_3N_4 crystalline core [28], or amorphous [29, 30], *i.e.* containing a mixture of sp^2 and sp^3 hybridized carbons within their core structure. Similar to other carbon materials, many CDs typically exhibit distinct G and D bands in their Raman spectra. The relative intensity of these two bands, represented as I_D/I_G, often serves as an indicator of the proportion of sp^3 carbons within the core structure. For instance, based on this criterion, the inverted I_D/I_G ratio observed in the Raman spectra presented in Figure 1.4(b) and Figure 1.4(c) suggests that the corresponding CDs possess a more graphitic and amorphous nature, respectively.

As an example, Figure 1.4 shows a HRTEM image of a CD with graphitic structure. In particular, as highlighted, the average latting spacing in this case if 0.21 nm, in agreement with the (100) interplanar distance of graphite.

In general, the surface shell of CDs contains various functional groups and chemical moieties, which are bound to the carbon core and form a disordered external layer that is said to passivate the surface. This passivation layer plays a central role in shaping their properties, across a wide spectrum, encompassing structural, chemical and photo-physical aspects. Indeed, oxygen-containing functional groups, such as carboxyl, carbonyl, and hydroxyl, typically decorate the surface of CDs, favoring their high solubility in polar solvents like water, which represents one of their most appealing advantages compared to inorganic QDs. Furthermore, an opportune functionalization allows tailoring the surface charge of CDs, and more in general modifying their capability to interact with the external environment [17].

Notably, as initially reported in the earliest studies on CDs [12], as referenced in Figure 1.5, these nanocarbon materials only exhibit luminescent properties after surface passivation, making it a fundamental element of CD structure. From Figure 1.5(b)-(c) it is also possible to appreciate another distinctive characteristic of CDs: their typical tunability of emission upon excitation wavelength. This, together with a detailed description of their emission properties, will be discussed after a presentation of the main synthetic routes through which CDs are usually prepared.

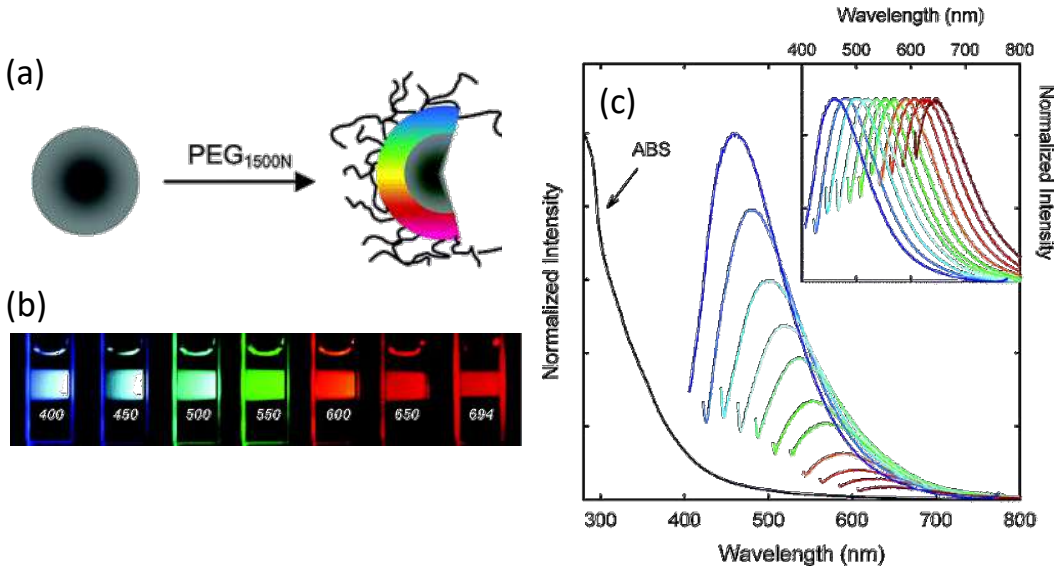

Figure 1.5: (a) Surface passivation of CDs with PEG1500. (b) Photographs of aqueous solution of PEG-attached CDs excited at the indicated wavelengths. (c) Absorption and emission spectra of aqueous solution of PPEI-EI CDs for increasing excitation wavelengths from 400 nm with 20 nm increment. [Adapted from [12]].

1.2.1 Synthetic Methods

Several synthetic routes of CDs have been established in the recent years, resulting in continuous improvements in the control of the final structure of the products and the simplicity of the synthetic processes involved. As common for the synthesis of many nanomaterials, the various methods that are used to synthesize CDs can be categorized into two main approaches: *top-down* and *bottom-up* methods. The former primarily involve breaking down larger *bulkier* carbon architectures, such as carbon soot [31], graphite or CNTs [32], into nanosized dots. In contrast, bottom-up methods revolve around the assembly of CDs through the carbonization of small carbon-containing molecular precursors [21].

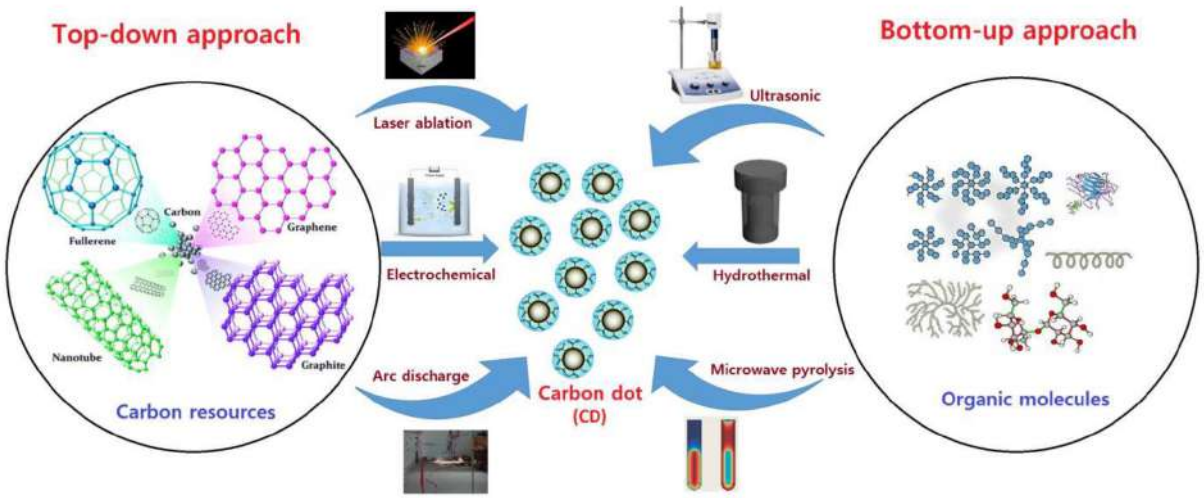

Figure 1.6: Schematic representations of different synthetic approaches for CD. [Adapted from [33]].

Top-down approaches

Many top-down methods follow a two-steps process. In the initial step, the starting carbon source is broken down to create the core structures of CDs while, in the second step, the critical passivation of the CD's surface is achieved. In fact, as mentioned, surface passivation's importance in relation to the photoluminescence properties of CDs has been evident since the earliest studies [12]. Although also non-passivated carbon nanoparticles have been reported to exhibit fluorescence, their emission quantum yield are often quite low [31, 32]. Moreover, a well-considered choice of organic or polymeric molecules for surface functionalization can dramatically enhance CD solubility [34, 35].

Historically, many of the initial synthetic pathways primarily utilized top-down methods, as iconically demonstrated by the arc discharge techinque employed during the first unplanned synthesis of CDs [11]. Initially designed for SWCNT production, this method frequently yielded impure soot, containing not just SWCNTs but various other by-products. Notably, when HNO_3

was employed to oxidize the soot generated via arc discharge, and NaOH was used for neutralisation, a fluorescent fraction was discovered alongside the nanotubes. This fraction, isolated after separation via gel electrophoresis, was found to consist of spherical nanoparticles. These nanoparticles likely had their carbon core formed during the arc discharge stage, with oxidative treatment in HNO_3 possibly contributing to surface passivation.

The first method used to synthesize CDs in a controlled manner was laser ablation [12]. In this technique, a graphite substrate was ablated under an argon flow, initially producing non-fluorescent carbon nanoparticles. However, these were transformed into effective CDs with strong luminescent properties after undergoing an acidic treatment, leading to surface passivation through organic moieties functionalization. Building on this pioneering work, numerous laser ablation methods have been explored to understand the role played by specific parameters like wavelength [36] or pulse duration [36, 37] of the laser in influencing the final CD products.

Another frequently employed top-down method involves electrochemical routes, which encompass a redox reaction of a specific precursor within an electrochemical cell under the influence of an electric current applied between two solid electrodes separated by a liquid electrolyte [38]. The first electrochemical route utilized MWCNTs as an electrode and produced graphitics CDs characterized by strong blue emission [32]. Subsequent improvements were achieved upon the discovery that alkaline environment can play a pivotal role facilitating effective oxidation of CD surface due to the high concentration of OH^- groups, thereby enhancing their luminescence [39].

Bottom-up approaches

Compared to top-down approach, bottom-up methods offer the enormous advantage of generally exploiting one-pot routes, making them quite straightforward and rapid. These methods enable the production of CDs characterized by strong emission right after the synthesis, eliminating the need for subsequent surface passivation procedures. Indeed, in bottom-up methods, both the core formation and surface passivation occur simultaneously. However, while top-down methods often produce CDs that reflect the structure of the starting precursors, bottom-up approaches generally yield products that are much less structurally controlled and leading, in some cases, to the production of small fluorescent molecules as side products of the synthetic routes. Thermal and microwave decompositions are widely employed bottom-up methods for synthesizing CDs. In these methods, carbon-containing molecular precursors are subjected to high-temperature decomposition, either through thermal heating or microwave radiation. These processes promote chemical reactions with other reagents, leading to the spontaneous assembly of carbons into nano-sized dots [30, 40]. These methods are frequently referred to as solvothermal routes, particularly when the synthesis is conducted in a liquid phase, or hydrothermal methods when water is used as the solvent [21]. Both thermal and microwave decompositions have become popular approaches for the controlled and efficient production of CDs with various properties and tunable fluorescence characteristics.

The first reported thermal decomposition for CD production led to the synthesis of two distinct amorphous CDs, differing in their hydrophilic or organophilic nature, based on the choice of precursors [30]. Conversely, the pioneering microwave pyrolysis involved the production of CDs

through the carbonization of an aqueous solution containing various amounts of polyethylene glycol (PEG-200) and saccharides like glucose and fructose [40]. It was observed that these CDs exhibited luminescence only when PEG-200 was included during the synthesis, highlighting the critical role of PEG-200 in passivating the surfaces of the nanoparticles.

Following these initial works, numerous studies have adopted these approaches for CD synthesis due to their distinct advantages over top-down approaches. Notably, these methods are cost-effective, with some researchers utilizing unconventional raw materials such as orange juice, grass, etc [41]. Additionally, the synthesis is rapid, often taking just a few minutes, and eliminates the need for further passivation, a requirement in most top-down routes. Moreover, these bottom-up synthesis provides an avenue for facile introduction of external atoms which serve as doping agents, hereby altering the structural and optical properties of the resulting CDs [21]. Common doping agents include sulfur [42, 43], boron [44, 45], phosphorous [46, 47] and nitrogen atoms [28, 48]. The latter, in particular, appears to markedly enhance the emission efficiency: even a small nitrogen content has been hypothesized to create a new electron-trapping surface state, promoting a high yield of radiative recombination [49]. In addition to surface-bound organic moieties like amides and amines, some studies have suggested that nitrogen can influence the electronic properties by integrating into the core structure [50]. Consequently, high levels of nitrogen doping can lead to the formation of unique structures such as carbon nitride nanocrystals [48], which are challenging or even impossible to obtain using top-down methodologies [21].

It should be clear that the enormous variety of synthetic methods can result in CDs with very distinct structures. In certain cases, good control over their structure has been achieved by opportunely manipulating the synthesis parameters. This manipulation can allow for tailoring the core structure, ranging from amorphous to crystalline, based on the specific synthesis techniques employed.

Purification

CD synthesis often results in highly heterogeneous samples. This heterogeneity can manifest as variations in size, surface structure, and optical properties from one CD to another [51]. Furthermore, as said, many side-products, typically including small fluorescent molecules, are obtained during synthesis alongside CDs. This pervasive issue of sample heterogeneity in CDs has led to the exploration of purification and separation methods as a means to effectively isolate CDs and gaining better control over the size dispersion and surface structure of the synthesized nanosystems. In some instances, separation methods have been employed to isolate the most fluorescent portion of a CD sample from an otherwise heterogeneous distribution of fluorescence quantum yields. This approach has resulted in the attainment of some of the highest reported fluorescence quantum yields in the literature [52, 53].

Among the most common purification techniques are dialysis, utilized for the removal of small impurities [54], and centrifugation, predominantly used to eliminate aggregates [55]. Size exclusion chromatography (SEC) permits to separate CDs based on their size [27, 53, 56]. For instance in [56], two fractions of CDs with different optical properties are separated by taking advantage of their different morphology, while in [53] SEC is used to obtain highly-monodisperse

green emitting CDs. High performance liquid chromatography (HPLC) can give similar results allowing for a size separation [57] or can separate CDs depending other structural characteristics such as the surface charge, as done with anion-exchange HPLC [58]. However, the overall yield of these purification technique result to be typically low.

For instance, Figure 1.7 shows the results of the separation *via* silica column chromatography of the CDs obtained in [59] through the hydrothermal route pictured at the top of the Figure. As evident from the photographs in Figure 1.7(b) and the emission spectra shown in Figure 1.7(c), the fractionated CDs exhibit distinct emission colors. The authors ascribed the differences in fluorescence characteristics among these CDs to their varied surface chemistries. As the chromatographic separation exploited the different surface polarity, it was possible relate a reduction of bandgap to the degree of surface oxidation, thus resulting in a redshift of the emission spectrum.

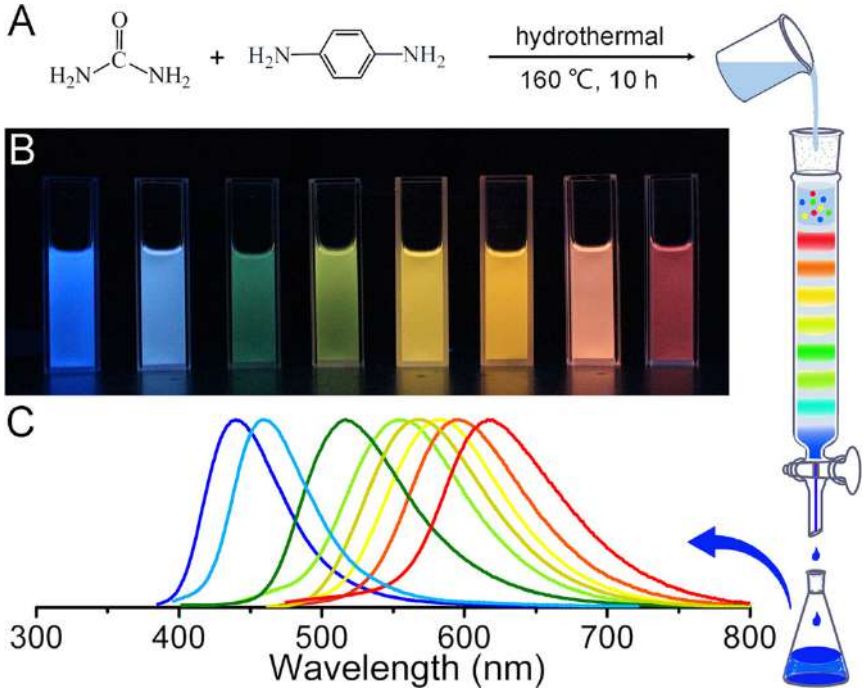

Figure 1.7: (a) One pot synthesis and purification route of CDs with distinct emission characteristics. (b) Eight CD samples under 365 nm UV light. (c) Corresponding emission spectra of the eight samples. [Adapted from [59]].

It is worth to note that, beyond practical considerations, obtaining CDs with simple and well-defined optical features is essential for establishing meaningful connections between emission mechanisms and specific structural attributes, ultimately advancing our knowledge of these versatile nanomaterials.

1.2.2 Optical properties

The distinctive light absorption and emitting properties, characterized by broad emission shapes, large Stokes-Shift, and nanosecond emission-lifetimes, usually tunable and depending on the

excitation wavelength, are defining characteristics of CDs, which have attracted significant interdisciplinary interest [14, 21]. Nevertheless, due to the inherent structural diversity among CDs, it is not appropriate to directly compare their characteristics across different research studies with the aim of establishing a comprehensive and unified theory. While reviewing the existing literature can certainly help to trace the recurrent aspects of their photophysical properties, it is essential to be aware of the challenges involved in making comparisons among systems that may be completely different from each other. CDs are usually characterized by broad and structureless electronic absorption spectra mainly ranging in the UV-blue spectral region, slowly decreasing to longer wavelengths. In some cases, sharper peaks are superimoposed to the broad absorption lineshape, which are ascribed to electronic transitions related to surface groups, like the $n \rightarrow \pi^*$ transitions due to non-bonding orbitals of carboxylic moieties [21]. Moreover, in some nitrogen doped CDs, additional broad absorption bands are observed in the 400-500 nm region, and associated with intraband transitions [26, 60]. Photopopulation of CD excited states is followed by a ground state recovery occurring also through radiative recombination, determining the emission of photons. Indeed, as mentioned, one of the most appealing characteristic of CDs is represented by their strong emission characteristics in the visible part of the spectrum, as many CDs can sustain blue [32], green [12] and orange-red [61, 62] emissions. In some cases, some works have reported how CDs of different emission colors can be synthesized by just changing a specific precursor in the synthetic route [63, 64], or a specific synthesis parameter such as the pressure [65]. From a spectral point of view, such emissions are characterized by quite broad unstructured PL bands, lacking of fine-structures. Interestingly, these emission properties may be either independent of the excitation wavelength [53, 61, 66], or more often "tunable", with the emission bands continuously redshifting by moving the excitation to longer wavelength [12, 67, 68], as seen in Figure 1.5.

Emission mechanism and electronic properties

Historically, the initial studies aimed to unravel the emission mechanisms of CDs assumed that they shared similarities with semiconductor Quantum Dots (QDs), which received the Nobel Prize in Chemistry in 2023 for their significant impact across various fields. The emission mechanism of QDs originates from radiative transitions within semiconductor bandgaps, and their optical properties are strongly influenced by the size of the nanoparticles [69, 70]. Indeed, the term "quantum" in QDs refers to the quantum confinement effect experienced by excitons, where larger particles have lower energy bandgaps, resulting in a red-shifted emission due to the inverse proportionality between energy level positions and the square of their size [71].

A similar interpretation was initially proposed also for CDs, suggesting that the nanosized sp^2-domains within, or constituting, the CD core were the emissive chromophores. Some studies supported this idea, as experiments involving size separation indicated that smaller CDs emitted shorter wavelengths [39], and in some cases, a quite regular dependence on size was found. However, this hypothesis was strongly disputed by later works. Some researchers observed effects contrary to what quantum confinement would predict [56], leading to doubts regarding its applicability, at least for specific CDs [72]. Additionally, the size distribution of CDs did not align

with the observed broadening of emission spectra, further questioning the role of quantum confinement [73]. More in general, it is worth noting that quantum confinement, usually associated with crystalline structures, cannot be straightforwardly attributed to the emission properties of CDs, as they mainly exhibit amorphous structures.

Furthermore, it is well accepted that optical properties of CDs are primarily influenced by surface-related factors. As mentioned, early studies on CDs synthesis suggested that fluorescence only occurs after surface passivation, underscoring its crucial role. Additionally, environmental factors significantly impact CDs' optical properties, primarily relating to exciton localisation at the level of the surface rather than in the core. For instance, CD absorption and fluorescence may be affected by factors like pH [74, 75] and solvents [76, 77], as shown in Figure 1.8. Moreover,

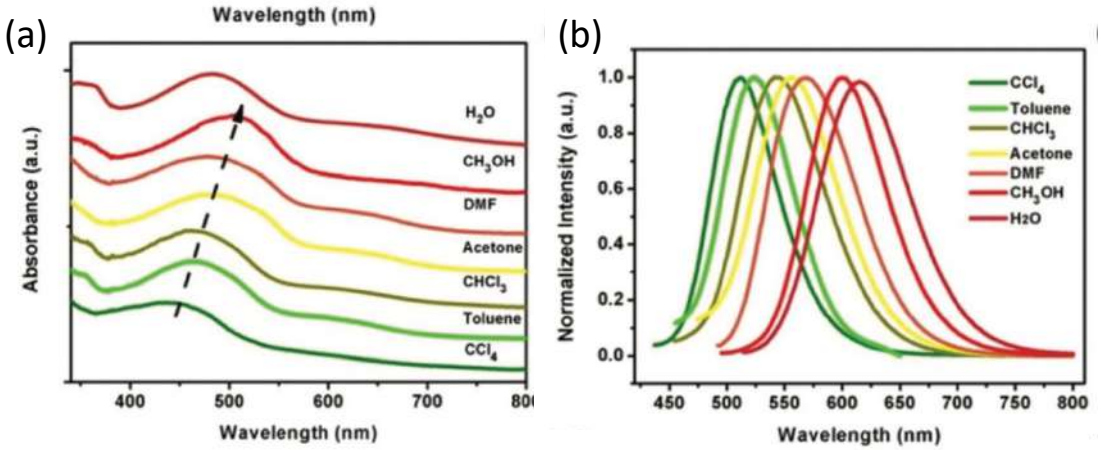

Figure 1.8: (a) UV-Vis absorption and (b) emission spectra ($\lambda_{exc} = 420$ nm) of CDs in different solvents. [Adapted from [78]].

surface characteristics, including oxidation levels, significantly impact the emission quantum yield [59, 79]. Therefore, surface defects, surface charge traps, and surface molecular-like states are recognized to play a significant role in the photophysics of CDs, while emission stemming from states delocalized in the core, affected by quantum-size effects appears to be very rare, and the specific core crystalline structure of the dots may be, in many cases, hardly relevant. However, the contribution of both intrinsic and extrinsic states to the optical behaviour of CDs is not mutually exclusive. Depending on structural characteristics of the specific CD, various potential interactions between core and surface states have been reported. A widely accepted model involves the migration of excitation from the core to the surface. In this model, the core is responsible for initial photon absorption, followed by spontaneous charge separation with electrons and holes trapped on surface states. The subsequent fluorescence arises from the radiative recombination of these charges released from the surface traps [12, 80–84]. A recent contrasting model proposed in the literature suggests an optical charge transfer transition, wherein a surface-localized exciton forms directly upon photon absorption [77]. This model, supported by solvatochromic, time-resolved, and single-molecule fluorescence studies, suggests that electron transfer from core states to surface traps occurs during photoexcitation, and fluorescence results from the inverse

recombination transition [21]. Spectroscopic features consistent with this mechanism include a well-defined charge transfer band in the electronic absorption spectra and a single-exponential fluorescence decay [77], in contrast with the typical broad, unstructured optical absorption and multi-exponential decays observed in most CDs [21].

In this intricate scenario, a recent debate has emerged in the literature with regard to the emission of CDs produced through specific bottom-up methods, particularly those with blue emission [21]. Some researchers have proposed that the emission in this case is primarily associated with small fluorescent organic molecules linked to CD surfaces or the $\pi-$conjugated core, rather than originating from the CD itself [85, 86]. Alternatively, other studies attribute the dual-emitting behaviour of CD to aggregates of multiple molecular chromophores, and some even suggest the involvement of free molecules in solution [87]. Notably, as mentioned, certain bottom-up CD syntheses yield small fluorescent molecular derivatives alongside CD carbonization. For instance, CDs produced from citric acid and a nitrogen-containing precursors can form 2-pyridone derivatives like citrazinic acid [86]. Evidence supporting these ideas includes the similarity between the blue emission of citrazinic acid and that of many CDs derived from citric acid [55, 88], theoretical simulations [86], and the lack of tunability in the emission band of these CDs, in contrast with the marked tunability characterizing the emission of CDs when excited at higher wavelengths [89]. In this perspective, discriminating between the emission from molecular chromophores and the CD itself is very challenging. Researchers have suggested that tunable emission is associated with the CD's core, while non-tunable emission is related to the presence of small molecules in solution, possibly existing in two forms: free or attached to CD surfaces [89]. Some studies have explored bi-exponential kinetics and proposed the presence of two forms of the same chromophore, one attached to the CD and the other free in solution [55]. Some investigations into UV-photobleaching suggest that the chromophore is a molecule of citrazinic acid attached to the CD's surface [86].

In this context, another method for tailoring the emission of CDs involves the incorporation of fluorescent molecules within amorphous carbonaceous particles of nanometric size. This enables the selective selection of specific chromophore that emit light in a desired spectral region, allowing for the integration of a similar optical response within the carbon matrix [90, 91]. However, even when the emission results from localized chromophores, whether attached to or embedded within the core of a CD, it significantly influences its properties, making them no longer strictly molecular. From this perspective, a representative theoretical study [92] demonstrated that the distinctive optical properties of CDs can be explained by the linear optical response of partially sp^2-hybridized carbon domains on the CD's sp^3-hybridized amorphous cores. In these domains, electrons are found to be partially delocalized, maintaining a strong coupling to the amorphous host matrix

As demonstrated, despite numerous studies on the emission mechanisms of CDs have been reported, no singular model has emerged to comprehensively explain their origin. The ongoing debate is further complicated by the substantial variability of CDs, observed not only among those produced through different synthesis methods but also within individual CD samples, where heterogeneity is prevalent.

Beyond the specific origin behind their emission properties, one of the most remarkable properties of CDs, is represented by their ability to undergo charge and energy transfer processes

under photoexcitation. Electron donor/acceptor features in CDs are well-documented and go beyond their interactions with metal ions. Charge transfer dynamics have been observed between CDs and organic molecules [18], or various types of metal complexes [93], or when CDs adhere to semiconductor surfaces [39], allowing them to serve as photosensitizers. When CDs come into contact with other electron donors (stronger than CDs), they can take the role of electron acceptor [18]. Among the several energy transfer mechanisms that can occur in CDs, Förster Resonance Energy Transfer is one of the more common [94]. Notably, these charge or electron transfer processes unfold extremely rapidly, often within picoseconds or even less, making them impossible to detect directly using standard spectroscopic methods. Instead, direct identification of these processes is only achievable through ultrafast spectroscopies, like femtosecond Transient Absorption [17, 93, 95].

Emission tunability

The emission tunability in CDs has attracted significant attention due to its apparent deviation from the Kasha-Vavilov rule, which states that the same emission transition should occur regardless of the specific excitation wavelength [96]. The origin behind this quite unique feature has been very debated among researchers. Nowadays, many attribute the tunability of CD emission to an intrinsic sample heterogeneity, composed of CDs with varying properties, including a wide size distribution of structures, and a variety of functional groups on the surface shell. This diversity within a sample, leads to different subsets of CDs being photoexcited with varying efficiencies when the excitation wavelength changes, resulting in a overall tunability of emission at an enseble level. In a complementary way, CDs featuring emission characteristics independent of the excitation wavelength reflect a high homogeneity, suggesting a "molecular" emission mechanism in which the fluorescence stems from a specific and well-defined molecular fragment embedded in the carbonaceous structure [53, 66, 97]. Spectroscopic evidence of substantial heterogeneity in many CDs is supported by broad, unstructured absorption and emission bands, non-exponential decay of emission, and discrepancies between ensemble and single-molecule behaviours [53] .

To investigate whether tunability persists at the individual dot level, single particle experiments have been conducted [51, 67, 77, 98]. In some cases [51], single dots exhibit narrower emission spectra compared to ensemble measurements (see Figure 1.9(a)) and the absence of multi-exponential decay of emission (Figure 1.9(b)). These observations suggest the ensemble tunability result from dot-to-dot variability which contribute to the inhomogenous width of ensemble emission bands, resulting from the superposition of almost overlapping emission of different dots, and complex excited-state dynamics. Moreover, as shown in Figure 1.9(c), the tunability was absent at the single particle level, pointing out that each single CD behaves as individual quantum emitter with its specific optical energy gap [51]. However, in striking contrast, other works reported that tunability is maintained even at the single particle level [67, 98], suggesting the possibility that distinct emission sites may exist within a single CD.

On the other hand, as mentioned, fractionation experiments allow to separate CDs based on specific structural, morphological, or optical characteristics. These approaches have enabled the isolation of particular subsets of monodisperse CDs to elucidate some structure-properties

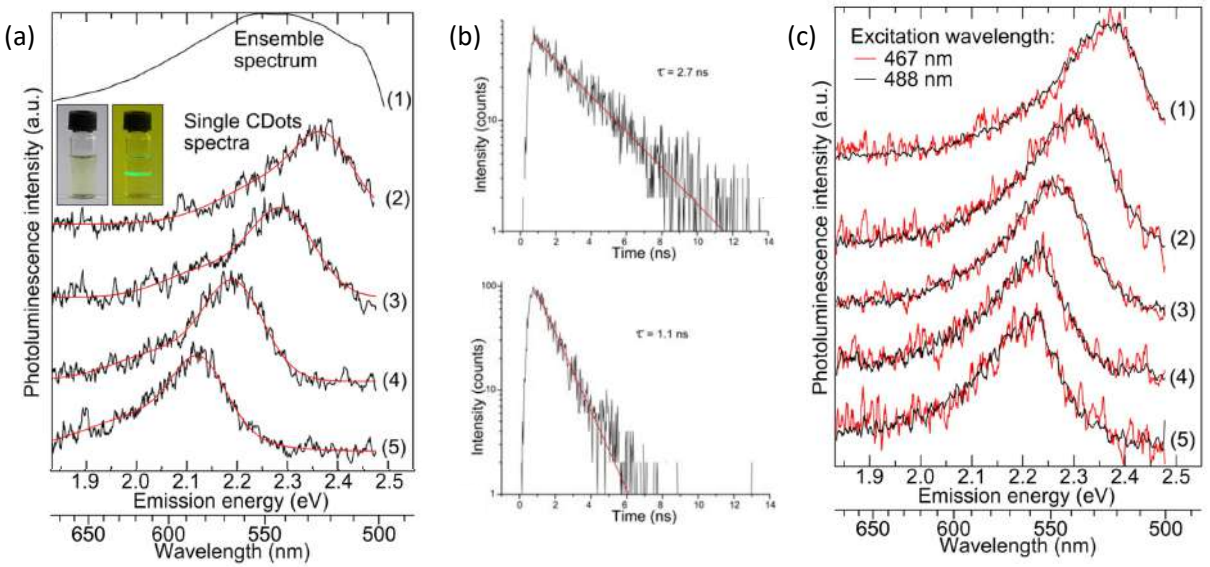

Figure 1.9: (a) Bulk emission spectrum of CDs in water (spectrum 1) and exemplary PL spectra of single CDs dispersed on the surface on a glass slide (spectra 2-5). (b) PL decay of single CDs. (c) Normalized PL spectra of single CDs dispersed on a glass slide with 467 nm (red curve) and 488 nm (black curve) excitation. [Adapted from [51]].

relationships. Generally, fractioned CDs exhibit clear and distinct optical characteristics, but the reported results are quite variable and closely related to the specific samples investigated. For example, in [39], CDs were separated by SEC, and fractions containing CDs of different sizes showed different emission characteristics, and the absence of tunability within CDs belonging to the same fraction. This led to propose that tunability stems from size polydispersity. Similarly, in [58], CDs separated through HPLC displayed distinct emission bands, and the individual fractions lacked tunability. Consequently, the authors associated the origin of tunability with an initial non-uniformity in CDs' size and/or charge. However, when the same separation technique was applied to CDs reported in [57], it effectively separated them into fractions with varying optical properties while still maintaining emission tunability. For this reason, the authors linked the retained tunability to the presence of sp^2 domains with different sized and shapes within each GQD. Also several works on truly fluorescent excitation-dependent CDs have been reported [67]. For instance, CDs synthesized in [67] display remarkably similar emission intensities across the entire visible spectrum when the excitation wavelength is varied. The demonstrated tunability of emission even at the single particle level was attributed to the existence of multiple emitting sites.

Therefore, despite these notably contrasting outcomes, the majority of reported findings concur on explaining emission tunability as an outcome of disorder, while the statistically distributed characteristics that sometimes maintain the tunable optical properties, even at the single particle level, are still not fully understood due to the great variability of CD structures.

1.3 Nanographenes

A completely distinct category of luminescent 0DNCs can be obtained by reducing the lateral size of 2D graphenic systems to nanoscale, giving rise to the so-called nanographenes. In contrast to extended graphene, these nanographenes can exhibit non-zero optical bandgap, spectrally ranging from IR up to UV depending on the specific structures, associated with strong emission properties [99, 100]. In particular, as elucidated in the following, significant interest has emerged in literature on the study of molecular nanographenes, viewed as model systems for investigating luminescent nanocarbon materials.

1.3.1 Classification of Nanographenes

The most widespread definition of nanographenes was established in 2012 [100], and a schematic representation can be found in Figure 1.10.

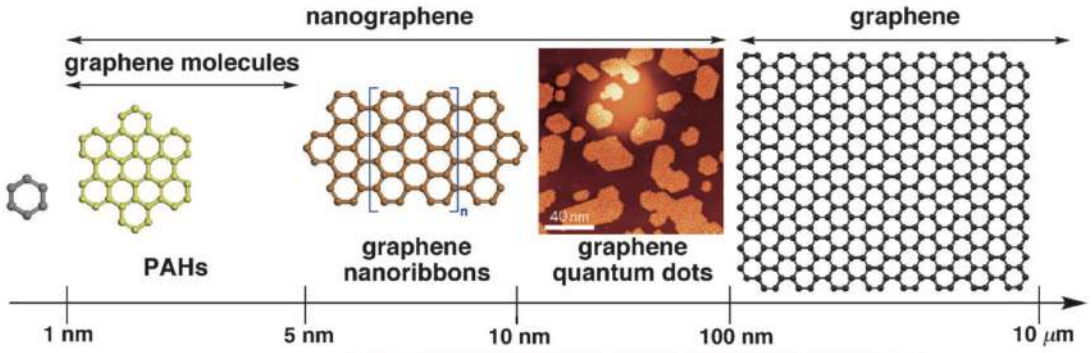

Figure 1.10: Schematic illustration of nanographene terminology based on their size scale. [Adapted from [100]].

From Polycyclic Aromatic Hydrocarbons to Nanographenes Starting from the bottom, polycyclic aromatic hydrocarbons (PAHs) consist of fused conjugated aromatic rings without any heteroatoms or substituents [101]. According to IUPAC rules, the PAH family encompassess 35 distinct molecular structures [100]. These structures vary in size, ranging from naphthalene, which is the smallest and simplest one consisting of a fused pair of benzene rings, to larger compounds that reach nanoscale lateral dimensions and, therefore, can be named as nanographenes. Among them, hexa-*peri*-hexabenzocoronene (HBC), with chemical formula $C_{42}H_{18}$ and chemical structure shown in Figure 1.10 (in yellow), owing to its 13 aromatic rings and 1.1 nm diameter, is often considered as the smallest nanographene [102]. For this reason, it results one of the most representative and studied PAHs [103–106], serving as model system for the investigation of NGs and related materials [107]. As presented below, PAH derivatives are largely used as molecular breaks in synthesizing molecular nanographenes featuring the most disparate structures, such as for example those collected in Figure 1.11.

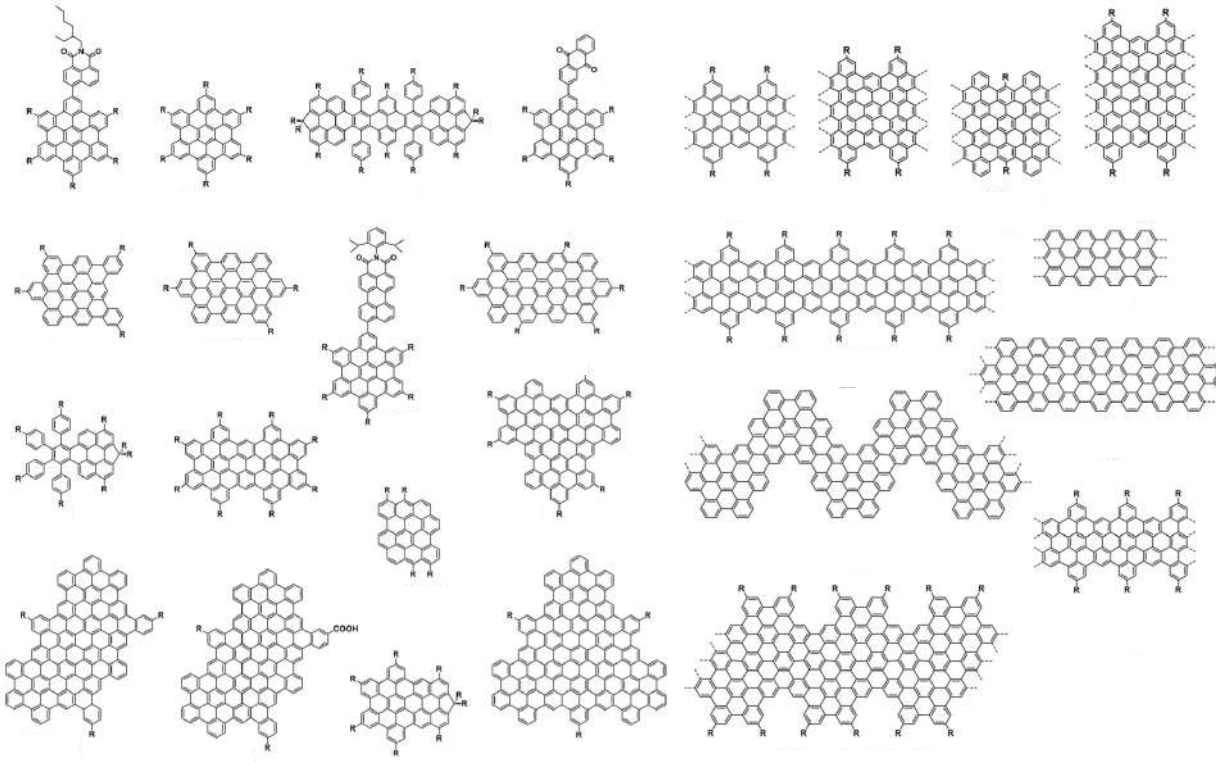

Figure 1.11: Chemical Structures of molecular nanographenes collected in [108]. [Adapted from [108]].

Graphene Nanoribbons (GNRs) A particular subclass of NGs extending into almost one-dimensional structures is represetned by graphene nanoribbons (GNRs). GNRs are essentially nanographene strips with a width less than 10 nm and a large length/width aspect ratio, typically exceeding 10 [100, 109], as in the case shown in Figure 1.12. GNRs can be seen as the planar analogues of CNTs, with optical bandgap depending on their width and edge structure [110]. Not by chance, one top-down method used to obtain GNRs involves the unzipping of CNTs along the longitudinal direction [111–113].

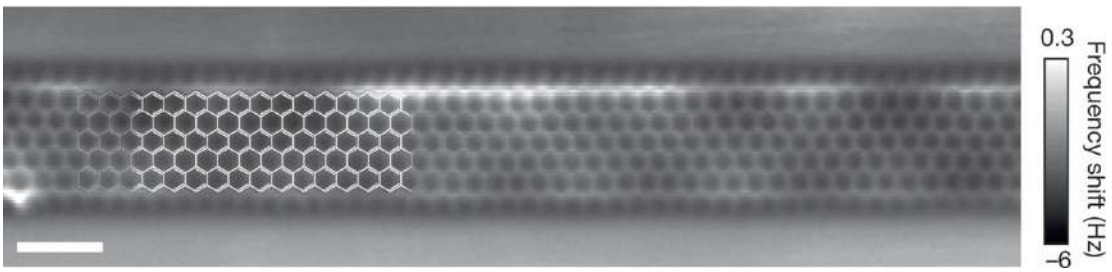

Figure 1.12: Non-contact Atomic Force Microscopy frequency shift image of a GNR. Scale bar is 1 nm. [Adapted from [114]].

Graphene Quantum Dots (GQDs) Graphene Quantum Dots (GQDs) are graphene-like fragments with lateral dimensions ranging from a few to 100 nm. Strictly speaking, GQDs should have a single-layer of sp^2 carbons [115]. However, it is common to include under this term also few-layered (<10) graphene fragments, which may host several oxygen-containing functional groups in their structure [116–120]. As a result, depending on their specific structure, GQDs can be viewed as a particular subset of CDs, but in strict terminology, only single-layered GQDs can be categorized as NGs.

1.3.2 Synthesis of NGs

Research of synthetic strategies that allow for precise control over NG structures has become essential. Similar to what described for CDs, also synthesis routes of NGs can also be classified into top-down and bottom-up approaches.

Top-down approaches

For an extended period, most NGs were obtained using top-down approaches utilizing graphene [23], graphene oxide [121, 122], or carbon black [123], as initial carbon structures, which were subsequently broken down to yield nanosized graphenic fragments. These methods mainly involve lithographic cutting [110, 124], solvo-hydrothermal [23, 125], chemical etching [126, 127], microwave assisted exfoliation [128], oxidative cleavage [129, 130] and chemical oxidation [123] methods. In general, these strategies, often do not yield highly monodisperse final structures, leading to suspensions of graphenic fragments with various and not-controlled sizes, shapes and edge chemistry. Additionally, obtaining effective single-layer NGs with these methods can be challenging, as they typically result in side graphenic products composed of few layers and some purification procedures are needed. This leads to a debate about whether the GQDs typically obtained through these methods can truly be considered part of the NG family or are essentially CDs with a high concentration of sp^2 domains within their structure.

Bottom-up approaches

Bottom-up approaches, such as pyrolysis and solvothermal methods [64, 119, 131] have also been developed to synthesize NGs. They can exploit small molecular precursors, such as HBC [119] or pyrene [64], to yield very monodisperse compounds. For instance, a specific methodology to obtain a collection of NGs from ruthenium-catalyside cage-opening of C_{60} has been reported [132]. At high temperature the fullerene embedded onto the metal fragmented, resulting in carbon clusters that after diffusion and aggregation give rise to geometrically controlled GQDs, whose specific shapes can be customized by optimizing the annealing and the concentration of the starting fullerene molecules.

Although some of these methods can produce highly monodisperse samples of well-defined structures, they do not yet provide an ultimate structural control at the atomic level. Indeed, there is a growing interest in advancing beyond non-stoichiometric forms of NGs. This would

enable the study of model graphene-related systems, facilitating a comprehensive understanding of opto-electronic properties in systems that occupy a middle ground between organic molecules and graphene.

In this regard, bottom-up organic synthesis methods pioneered by Müllen and co-workers and further developed in the recent decades [99, 103], offer meticulous control over atomic structures of what can be termed as molecular NGs, enabling fine-tuning of their structural and electronic characteristics. These organic synthesis exploit well-established protocols, typically involving the oxidative intramolecular cyclodehydrogenation of precursor molecules, like oligophenylene and polyphenylene [103]. For instance, the synthesis of HBCs is generally executed by cyclo-dehydrogenation (CDH) of hexaphenylbenzene (HPB) through optimized Scholl reactions (Scheme (a) in Figure 1.13) [133]. In turn, sixfold symmetric HBCs can be obtained through [2+2+2] cyclotrimerization reaction of substituted diphenylacetylenes (DPA) followed by oxidative CDH (Scheme (b) in Figure 1.13). In the case of lower symmetric HBCs, it is possible to exploit Diels-Alder cycloaddition between appropriate tetraphenylcyclopentadienone (TPCPD) derivatives and substituted DPA, followed by oxidative CDH (Scheme (c) in Figure 1.13).

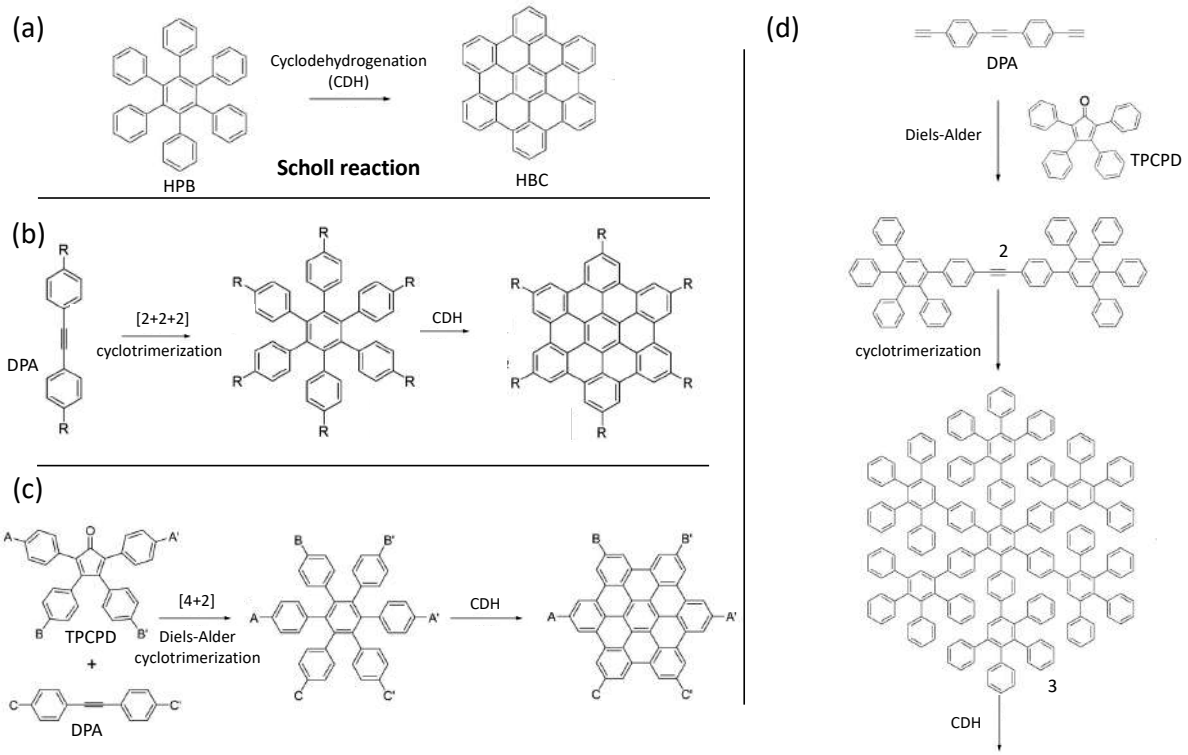

Figure 1.13: Schematic of (a) synthesis of HBC; (b) general synthetic route to sixfold symmetric HBCs; (c) general synthetic route to lower symmetric HBCs; (d) synthetic route followed in [134] for the synthesis of C_{222} NG.

These routes represent general protocols that can be used to construct a variety of atomically-controlled $\pi-$extended systems, thereby expanding the family of molecular NGs to larger and more complex structures, which can be synthesized through a well-planned sequence of Diels-

Alder, cyclotrimerization and Scholl reactions. [99, 109, 134]. For example, synthesis of C_{222} NG was achieved using the scheme detailed in Figure 1.13(d) [134]. This involves a combination of Diels-Alder reaction of DPA with two TPCPD molecules to get 2, followed by cyclotremerisation to produce the large oligophenylene 3. Subsequently, oxidative CDH is employed to obtain the final NG.

Through similar approaches, a plethora of different atomically-precise NGs can be synthesized, each with distinct sizes [135, 136], edge structures [137, 138], and nonplanar configurations [139], all deliberately predefined by the careful selection and design of custom precursor molecules. Furthermore, this approach allows for the deliberate introduction of side chains and other functional groups at peripheral position [136, 140–142], further enhancing the tunability of NGs' electronic properties and solubility, making them more easily processable in various organic solvents [99]. In this evolving scenario, driven by the growing interest in the literature regarding the investigation of model systems, the term 'nanographene' is now primarily used to refer to stoichiometrically defined graphenic nanostructures obtained through synthetic routes that allow precise atomic-level control over their structure. These NGs can be regarded as model systems for the comprehensive study of graphene-related materials.

Innovative NGs

Recent years have witnessed a significant expansion in the variety of NG-bases structures. Notably, progress has been achieved in the fabrication of NGs with intricate geometries, alongside the successful synthesis of non-planar structures including distorted, twisted or helical NGs. In particular, as mentioned, recent forms of NGs deviate from the archetypal of perfect hexagonal network topology, as long as it predominantly consists of a regular arrangement of sp^2 hybridized carbon atoms.

Currently, several research groups are dedicated to synthesizing PAHs and NGs featuring non-planar networks [143–146]. One common approach to introduce deviations from planarity in NGs involves the incorporation of non-hexagonal rings in their structure. Particularly, the addition of pentagon-rings leads to structures characterized by positive curvature. More recently, a multitude of NGs featuring networks with negative curvature have been reported. These are typically synthesized through the introduction of seven- or eight-membered rings into the sp^2 carbon framework [143, 144], as in the case depicted in Figure 1.14(a), where the shown NG possesses a peripheral heptagon ring in its structure.

An alternative method for creating non-planar NGs involves the inclusion of helicenes [149]. These moieties are polycyclic aromatic compounds with nonplanar skeletons constituted by ortho-fused benzene or other aromatic rings, resulting in the formation screw-shaped, helical motifs. In these, intramolecular steric repulsion cause an intrinsic twisting of the network, which is in turn extended to the overall structure of the carbon systems where they are included, as in the case reported in Figure 1.14(b). The introduction of helicity, which determines a third dimension expansion, and the subsequent introduction of chirality, is expected to lead to markedly different optical properties compared to their planar counterparts. Moreover, the structural

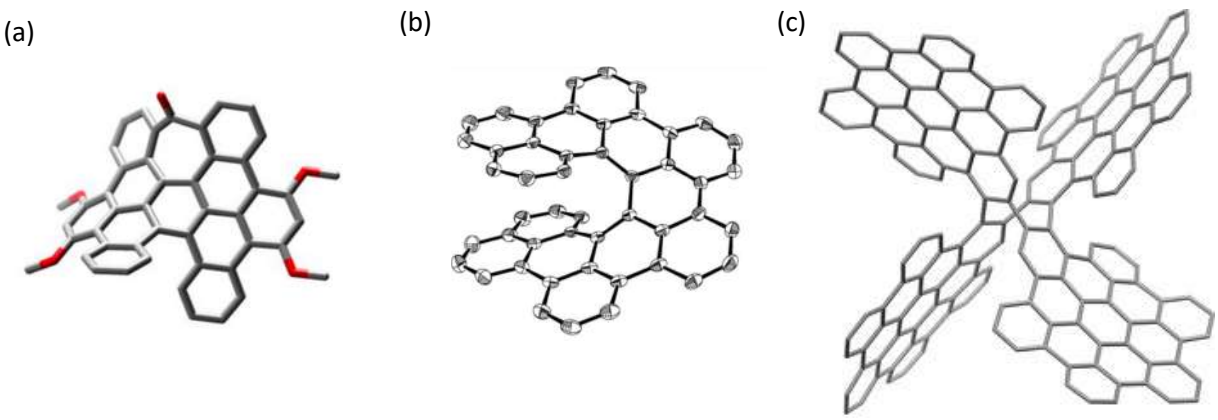

Figure 1.14: Crystal structures of contorted NGs. (a) Distorted heptagon-containing NG [Adapted from [143]]. (b) Helical twisted NG embedding a helicene moiety in the structure [Adapted from [147]]. (c) 3D NG constituted by four HBC-armed structure [Adapted [148]].

twisting significantly enhances their solubility, making them more practical for research and applications [147, 150–152].

Exploration of 3D extended architectures is also achieved by the fusion of smaller NGs subunits [148, 153]. For instance in [148] a four HBC-armed NG is obtained, whose chemical structure is reported in Figure 1.14(c).

The research on the synthesis and engineering of NGs' structures into contorted and intricate geometries is not an end in itself. As will be clarified later, in certain circumstances, this becomes a necessity to enhance morphological complementarity with the surfaces of other systems to which the NGs have to be coupled.

Thanks to the high atomic control guaranteed by the organic synthetic routes, these molecular NGs are usually unambiguously structurally analysed by a combination of mass and NMR spectroscopies, and single-ray X-Ray diffraction, which provide an atomically precise reconstruction of their structures in a complementary way [109, 143, 154]. In addition, in many cases, the validation of their effective structural conformation is assisted by theoretical simulations [139, 155, 156].

1.3.3 Optical properties

As extensively explained, NGs are primarily characterized by a hexagonal network of carbon atoms extending over the nanoscale. However, due to their nanosized lateral dimensions, which put them under the category of 0DNCs, NGs exhibit markedly different photophysical properties compared to graphene. NGs are typically characterized by high molar extinction coefficient. In principle, as reported in Figure 1.15, the optical bandgap of graphenic nanostructures can be tuned from the 0 eV of an ideal graphene sheet to that of benzene by altering their size or, conversely, the number of their constituent conjugated rings [157]. Furthermore, even minor structural modifications, such as substituting heteroatoms or introducing edge functional groups,

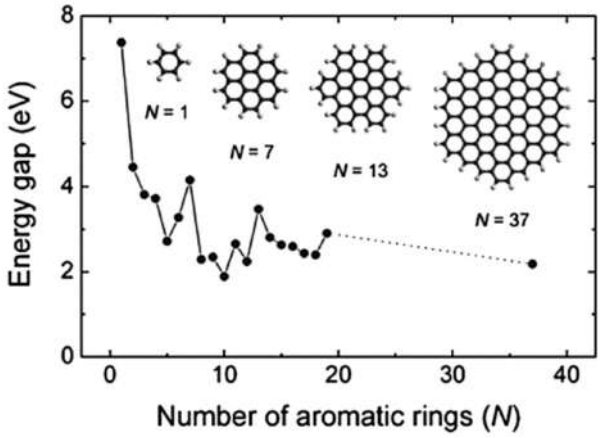

Figure 1.15: Energy gap of $\pi - \pi^*$ transitions calculated by DFT as a function of fused aromatic rings (N). [Adapted from [157]].

can significantly impact their opto-electronic characteristics due to their reduced dimensionality. Consequently, a plethora of both theoretical [158, 159] and experimental studies [136, 160–163] have investigated how the specific structures of NGs influence their properties. In particular, photogenerated electrons and holes within NG result into the formation of excitons, closely bound electron-hole pairs. These excitons can recombine through radiative deactivation, leading to the emission of photons. Indeed, one of the most appealing characteristics of NGs is their strong emission properties, which can be tuned over a wide spectral range, from UV to NIR, by opportunely engineering their structures [164, 165]. In general, it is widely accepted that the emission properties of top-down synthesized NGs are mainly governed by highly localized states, making it extremely hard to establish precise properties-structure relationships [166].

For this reason the focus is on NGs of atomically-precise structure. As anticipated, HBC-derivatives are now considered as particularly representative forms of NGs, given that they can be viewed as the smallest and simplest NG structures. However, despite being among the most extensively studied systems, investigations on their photophysical properties remain limited to a few reports. HBC shares with other PAHs similar optical characteristics. According to Clar's categorization, in PAHs electronic transitions are grouped into three (or four) types, similar to the naming convention for benzene: β and (β') correspond to the most energetic absorption at 360 nm (or 340 nm), while p and α transitions are associated with less energetic absorptions at 390 nm and 450 nm, respectively [167]. In HBC, only β transitions are allowed due to its symmetry, making them the dominant absorption features. Conversely, p and α transitions are symmetry-forbidden and less intense. The introduction of functional groups, especially if in an asymmetric way, can disrupt HBC's symmetry, enhancing α-bands. This effect may occur not only through symmetrical changes but also by shifting electron density when using electron-withdrawing substituents [107, 142]. This aspect is examined for instance in [107], aiming to assess the photophysical impact on HBCs resulting from different edge functional substituents, revealing a progressive charge-transfer character as a function of the strength of the electron-withdrawing effect of the substituent. As can be appreciated from Figure 1.16, as the strength

of the electron-withdrawing unit is increased, the electronic structure of HBC core is highly perturbated [107].

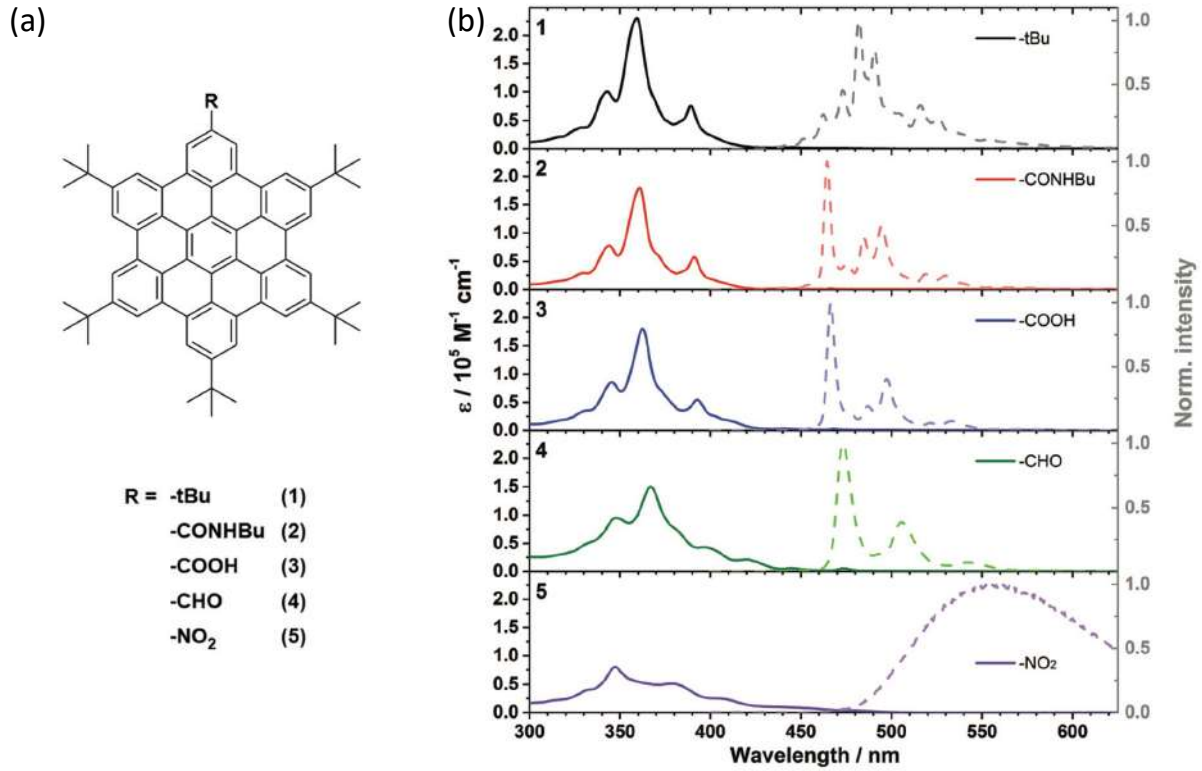

Figure 1.16: (a) Molecular structure of diffent functionalized HBC-derivative. (b) The absorption and emission spectra of the different NGs [Adapted from [107]].

Apart for probing specific effects, edge functionalization of NGs is often necessary to prevent aggregation [168]. For instance, HBC itself has a strong tendency to form columnar-shaped stacks through $\pi - \pi$ interactions [169]. Unsubstituted or HBC functionalized with short linear alkyl chains tends to promote strong aggregation. This issue can be avoided by functionalizing the edge structure with branched and longer alkyl chains, typically ter-butyl moieties, which enhances solubility in most common organic solvents [103]. Conversely, some studies have examined the optical properties of NGs that were not functionalized with solubilizing groups, in order to maintain the maximum similarity with nanostructures of pure graphene, [168], or to deliberately induce aggregation for supramolecular assembly [170].

Controlling the size of π-conjugation represents another effective way for tailoring the optical characteristics of NGs. Several studies have explored this aspect, aiming to make homogeneous comparisons among NG structures with specific size modifications [162, 168]. The different emission colors often encounterd for NGs with various sizes proves that the excited states of NGs are often highly delocalized across the sp^2 network.

Some researchers have proposed specific correlations between the size of various NGs and their absorption α bands [171]. In particular, it has been shown that increasing the one-dimensional

conjugation extension is a more effective method for shifting the emission wavelength towards the IR range compared to extending the conjugation in two dimensions [172]. Moreover, in GNRs, apart from the ribbon width, the electronic and the electrical characteristics are significantly influenced by their edge morphology. Armchair GNRs have garnered extensive research attention due to their excellent stability and their ability to tune bandgaps across a broad spectrum from the IR to the UV-visible range. Zig-zag GNRs, known for their localized edge states, have shown promise in the field of spintronics. However, their practical application is currently hindered by challenges related to limited chemical stability [99].

Some studies have demonstrated that NGs can maintain their emission properties even in the solid-state [99, 162], in contrast to the typical behaviour observed in CDs, where strong emission quenching occurs in the solid state. This represent a significant advantage as it opens up a widener range of potential applications. For example, the authors of [165] build distributed feedback lasers based on NGs as active media embedded in polystyrene matrices.

Usually, it is reasonable to expect that smaller NGs typically exhibit photophysical properties resembling those of simple organic compounds, reflecting their essentially molecular nature [108, 156]. An ongoing question in literature is to determine whether a size limit exists beyond which photophysical properties start to deviate from a molecular paradigm, and this Thesis partially aims to address this debate. Indeed, the investigation of the photophysical properties of extended nanographenes is particularly challenging. While the photophysics of HBC derivatives is relatively well-known, advanced optical characterization of molecular NGs with structures containing more than ∼100 carbon atoms has been rarely reported [162]. The intrinsic higher complexity due to the larger extension is seen as a crucial aspect that may introduce new peculiar physico-chemical characteristics, distinct from those of typical small aromatic molecules. For now, as long as studied samples consisting of NGs with well-defined geometries, even NGs containing up 132 sp^2 carbons [162] appear to exhibit molecular-like photophysical characteristics. From a spectral standpoint, increasing the NG size is often associated with just a broadening of absorption and emission spectra, resulting in featureless profiles [171, 173], in contrast to the usually finely-structured shapes generally observed for smaller NGs. In a complementary way, the synthesis of NGs with intricate geometries [174] partially addresses this need, aiming to investigate weather distorted geometries could introduce new peculiar photophysical features. In this perspective, one of the goals of this Thesis is to address this aspect by performing a fundamental photophysical study of several molecular NGs characterized by non-planar structures. More in general, other objectives of this work include the comprehensive reconstruction of the optical photocycle of these atomically-precise NGs, down to the femtosecond scale to fully reconstruct also the faster processes occurring after photoexcitation, with femtosecond time resolution. Indeed, ultrafast spectroscopic technique such as Transient Absorption have started to be employed for the study of the photophysical characteristics of many CDs to have a direct evidence of a plethora of physical process occurring in the relaxation cascades after photoexcitation on picosecond or sub-picosecond timescale, including internal conversion, solvation, fast radiative and non-radiative decays, intersystem-crossing, charge and energy transfer dynamics, [17, 72, 175]. However, the use of these techniques for the photocharacterization of atomically-precise NGs is still limited to very sparse reports [107, 148, 176]. Also for this reason, one of the primary objectives of this

work is to extensively use ultrafast transient absorption spectoscopy to investigate the photocycle of all the molecular NGs under study.

1.4 0DNC-based hybrid structures

From a certain point of view, part of the recent surge of scientific interest in luminescent 0DNCs like CDs and NGs is motivated by the fact that they can be viewed as carbon-based analogues of semiconductor QDs. While the presence of toxic heavy metals in the latter represents a limiting factor for everyday applications due to their costs and severe environmental and human health impact, one noticeable advantage of 0DNCs over their inorganic counterparts is their cheapness and low toxicity. In addition, while NGs are hardly soluble in water, most of CDs are water soluble and are widely recognized as perfectly biocompatible [26, 177].

Furthermore, these 0DNCs offer unique advantages given by the peculiar chemistry of Carbon, which, among many benefits, makes them easy to functionalize for potential coupling with other suitable systems. Combination of semiconductor QD with other systems has proven to be a successful strategy to design hybrid materials with customizable multifunctional or entirely novel properties [178, 179]. Similarly, researchers have begun exploring hybrid materials that exploit the synergistic combination of the tunable optoelectronics properties of luminescent 0DNCs with the specific characteristics of other carefully chosen systems, thus broadening the range of potential applicative fields for these materials.

Apart from the exploitation of emission properties of 0DNC to build luminescent hybrid systems, also their charge and energy transfer properties have emerged as highly attractive features in the conception of functional hybrid materials with potential application in photocatalysis, solar energy harvesting, optoelectronic, and sensing [180–182]. Thanks to remarkable attributes, both CDs and NGs have found widespread use in creating functional hybrid systems, where they can serve as light harvesting components. The versatility of these hybrid materials stems from the strategic manipulation of the optical properties inherent in CDs and NGs, which can be judiciously fine-tuned, along with the specific interactions that can occur when they interface with other elements within more complex architectures. Indeed, the direct coupling of 0DNCs with other materials can yield a diverse array of multi-functional hybrid systems, holding great promise for a wide range of applications, extending beyond pure scientific interest. The synergistic effects arising from the combinations of different components constituting the hybrid system, can enhance some specific properties of one or more constituting parts, or even introduce completely new features totally absent in the precursors.

1.4.1 Examples of CD-based hybrids

For several years, CD-based hybrids have been at the center of growing scientific interest, as evident by the increasing number of reports on a wide range of systems.

As mentioned, passivation of CDs' surface can be opportunely tailored with specific chemical functional groups depending on the specific need. By means of these groups, CDs can be anchored to the surface of several inorganic, organic, polymeric, or biological systems, by exploiting

electrostatic interactions, covalent or hydrogen bonds [183]. For instance, in [184] pH-induced protonation or deprotonation of the amino groups on the surface of CDs is employed to modify surface charge of the CDs to facilitate their complexation with polyoxometalates possessing an opposite surface charge. In particular, efficient electron-transfer processes occurring within the complexes confirm the strong electronic coupling, paving the way for the use of similar CD-based hybrid materials for photocatalytic applications.

Also coupling of CDs with noble metal nanoparticles (MNPs) like silver, gold, and platinum, or transition metals such as iron, copper, zinc, can lead to enhanced catalytic characteristics [180, 185–188]. However, the interaction of a fluorophore with a nearby metallic nanoparticle can be subjected to specific plasmonic interactions, which generally involve either a local enhancement of excitation field, either the increase of radiative decay rate through a a Purcell-like effect, or the increase of non-radiative decay due to plasmon induced energy transfer. Several studies explored these possible interactions between fluorophores like molecular dye or semiconductor QDs. However, the study of CD/MNPs plasmonic interactions is limited to sparse reports [189–192] and the fundamental interaction mechanism has not been completely unraveled, representing an open question to which this work will try to address. Authors of [180] showed that the plasmonic interactions between CDs and MNPs can depend on several parameters including the type of binding, the specific architecture formed by CD-MNP complexes, such as their size of relative ratio of CD/MNP, and the overlapping degree between the plasmonic band of gold nanoparticles (AuNP) with the absorption and emission spectra of CDs. In particular, in covalently bonded CD/MNPs complexes a larger emission enhancement was achieved compared to analogue complexes obtained through Coulomb-assisted dynamic interactions. More in general, a physical spacer is necessary to prevent emission quenching of CDs due to photoinduced electron or excitation energy transfer toward MNPs [193]. Since such processes occur when CDs and MNPs are in close contact, a common strategy followed to avoid them, passes through the creation of a physical spacer between the interacting systems. One of the most employed way contemplates the capping of MNPs with a dielectric layer, usually SiO_2 [189, 192], but also molecular [190] and polymeric [194] like polyethyleneimine have been used. For instance, this is documented in [194] where the authors found a strong enhancement in the emission properties of CD/plasmonic nanohybirds, upon the presence of PEI spacer, as reported in Figure 1.17. Apart from the modulation of optical properties, coupling of CDs with MNPs can serve also for the constitution of functional hybrid materials acting as ratiometric sensors for the detection of specific molecules [41, 195].

As another representative case, CDs-silica hybrids allow to combine together the physicochemical features of both materials in a single smart functional system [196–198]. Mesoporous materials like silica can host several molecules, allowing for their use for gas sensing. For example, in [181] CDs were impregnated into hollow mesoporous silica microspheres (HMSMS) and mesoporous silica microspheres (MSMs). The dependence of emission intensity of the CDs incorporated into the silica structures was evaluated as a function of oxygen concentration, proving a strong emission quenching in presence of oxygen. Interestingly, the hybrid structures showed a recovery of emission intensity upon nitrogen-oxygen exchange, revealing a short response and recovery time, extremely appealing for oxygen sensor devices. Similarly, CDs doped silica structures can be candidates for ratiometric sensing of metallic analytes [199, 200]. The one-pot

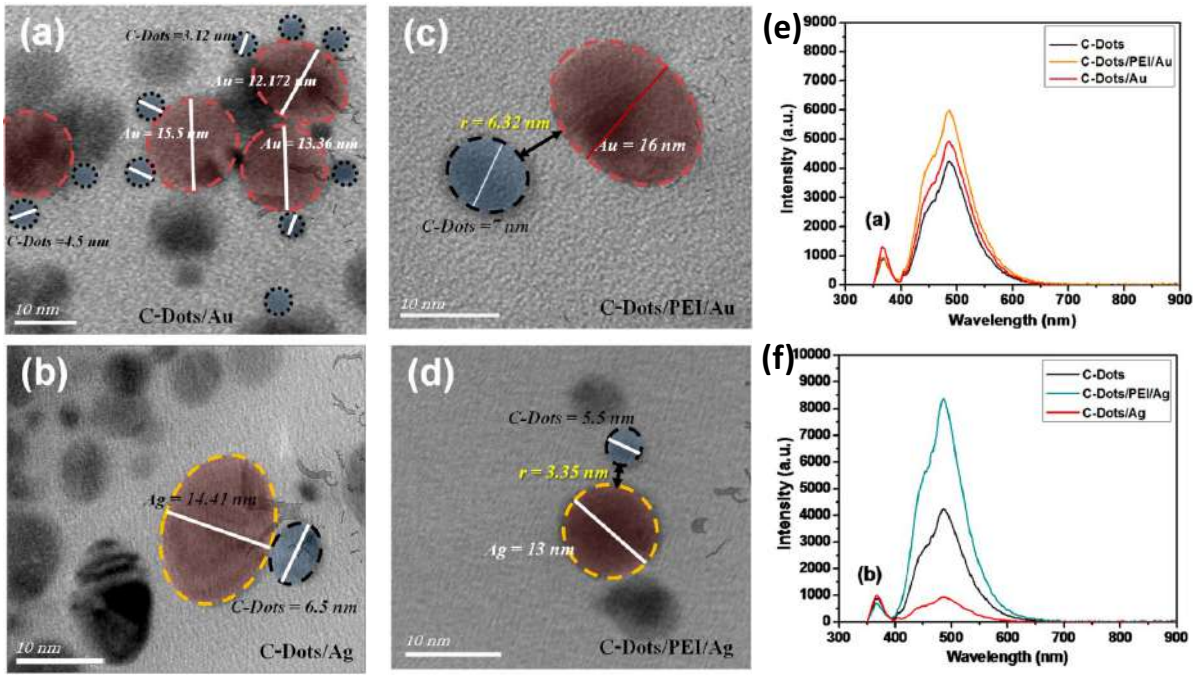

Figure 1.17: TEM micrographs of (a) CD/AuNP; (b) CD/AgNP; (c) CD/PEI/AuNP; (d)CD/PEI/AgNP. Effect of plasmonic (e) gold and (e) silver nanoparticles on emission spectra of CD in presence and in absence of dielectric spacer (PEI). [Adapted from [194]].

synthesized CD/silica nanoparticles reported in [201] are characterized by a marked sensitivity in the detection of cupric ions Cu^{2+}, which is 100 times higher that of free-stated CDs. Instead, as additional example, the combination of CDs with magnetic NPs can be harnessed to create multifunctional imaging platforms, encompassing optical and magnetic resonance techniques. In this sense, ternary conjugates consisting of fluorescent CDs, near-infrared (NIR) responsive NPs such as gold nanorods, and magnetic NPs have been reported to offer significant utility in the context of multi-modal imaging-guided approaches and for the enhancement of chemo-phototherapy with NIR responsiveness [202].

CDs have been also used as panchromatic light-harvesters for Carbon Nanotubes [203–205]. In [203], electrostatic interactions were exploited to decorate two different types of SWCNTs wrapped by a positively charged polymer with negatively charged CDs of uniform size. The reported results revealed the occurrence of charge transfer in the ground and excited states between the interacting CDs and the CNTs, behaving as electron donors and acceptor, respectively. The charge separated lifetime was shown to be dependent of the specific nature of CNT. In [205] similar interactions between CD/SWCNT hybrids (TEM image reported in Figure 1.18(a)) were found to be triggered only by photoexcitation, determining that electron transfer from CD and CNT occurs in less than 100 fs. The subsequent charge recombination was found to be due to a back-electron transfer from CNT to CD, whose temporal dynamics depend on the specific electronic nature of carbon nanotubes, as shown in the schematic depicted in the right part of Figure 1.18. Moreover, thanks to the marked charge separated nature of the excited state, the

constituted CD/CNT hybrids appear to be able to photocatalyze the synthesis of small silver nanoparticles.

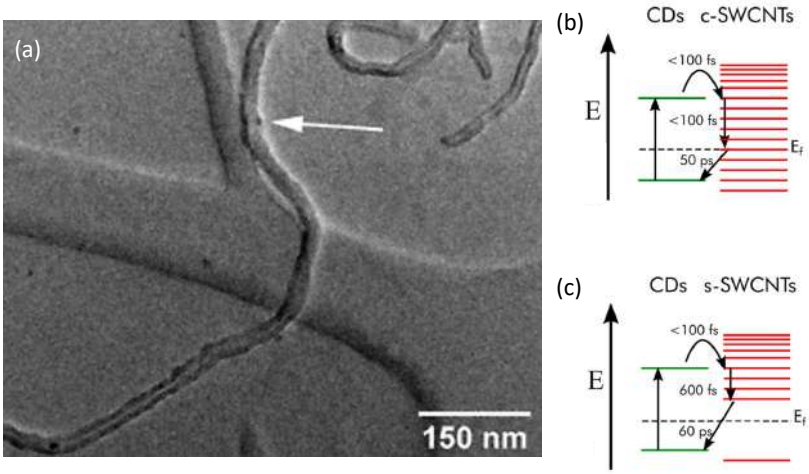

Figure 1.18: (a) HRTEM image of a complex formed by CDs and MWCNT. The white arrow indicates a single CD binding to the wall of nanotube. Right: Schemes of forward- and bak-electron transfer from CDs to SWCNTs and back and relateed characteristic timescale for (b) conductive SWCNT and (c) semiconductive SWCNTs. [Adapted from [205]].

More recently, CDs have started to be used also as auxiliary components for the building of perovskite-based optoelectronic devices [182]. Indeed, CDs can have a notable impact on the extraction and transport of charge carriers [206], facilitate the formation of perovskite crystals, [207], enable effective passivation [208], hinder ion migration [207], and improve the overall environmental stability of perovskite materials [209–212]. In particular, in the context of photovoltaic applications, CDs can absorb the harmful for perovskite UV/blue portion of the spectral light, which is a beneficial aspect for perovskites stability [210]. Additionally, the emission of CD in the visible range can in turn be absorbed by perovskites, thus increasing the number of photo-generated carriers. In CD/perovskite hybrid materials, the perovskite component can also be excited through non-radiative energy transfer from CDs, if they are sufficiently close and there is a sufficient overlap with the perovskite's absorption spectrum [209]. Finally, the emission of CD and perovskite has been also complementary combined and tailored in order to obtain white-light LEDs [213].

1.4.2 Examples of NG-based hybrids

Also molecular NGs have been largely exploited to build more complex hybrid architectures, on one hand by exploiting their optical properties, and on the other hand, by exploiting their structural ease in binding. In some reports photoactive porphyrin molecules were covalently functionalized to NGs. In [214], porphyrin-linked NGs were studied by comparing the effect for two NGs with sp^2 network of different sizes, a HBC-derivative and its ribbon-shaped π-extended version. The photophysics of the two porphyrin-conjugated NGs was found to be different,

emphasizing the influence of NG size. For the smaller NG, photoinduced energy transfer occurred exclusively from the first singlet excited state of NG to the porphyrin. In contrast, for the ribbon-shaped NG, energy transfer occurred from both the first and second singlet excited states of the porphyrin to the NG.

Notably, NGs, apart from specific deliberate edge functionalization, consisting primarily of π-conjugated domains, can easily engage in π-π interactions, making them excellent candidates for designing hybrid materials by self-assembling. In this context, exploring practical methods to precisely control van der Waals interactions in NG assembly is essential for adjusting the interfacial charge-carrier dynamics in various applications. One strategy to achieve this, is tuning the size and composition of NG, such as the relative ratio of hydrogen and carbon atoms, in order to regulate van der Waals interaction and, consequently, the strength of coupling [99]. A theoretical study demonstrated that van der Waals interactions in carbon-based nanomaterials obey to distinct scaling laws, where larger size corresponds to stronger interactions and increased layer number results in reduced interactions [215], as schematically represented in Figure 1.19. According to this, connecting NGs with materials possessing large lateral size and atomically thin thickness would facilitate the creation of highly coupled NG-based assemblies.

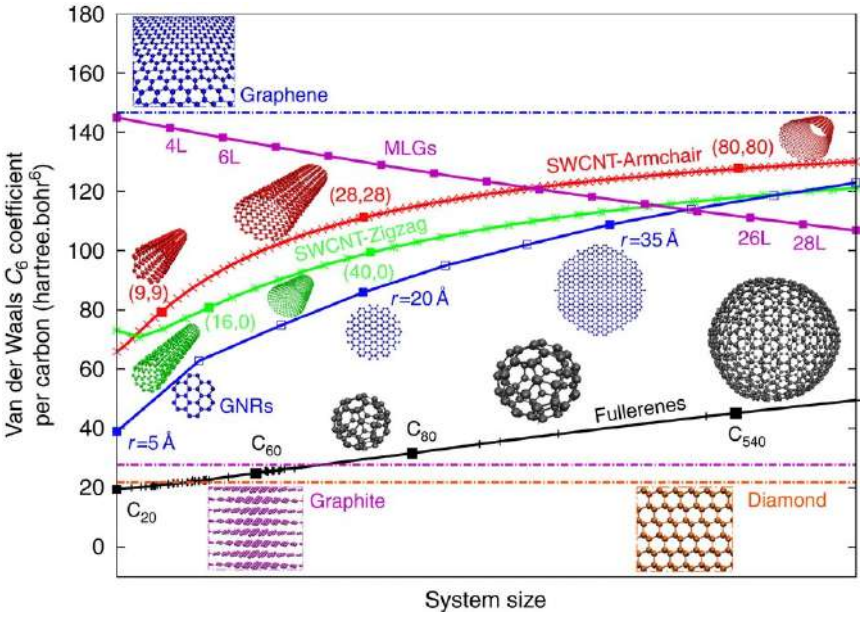

Figure 1.19: Scaling laws for van der Waal interactions per carbon atom for nanostructures of different dimensionality. [Adapted from [215]].

The coupling of NGs with graphene is a highly effective strategy for creating self-assembled hybrid systems taking advantage of $\pi - \pi$ interactions. Particularly, the combination of two nanosystems, each featuring extended sp^2 networks, could give rise to hybrid systems with exceptional charge transport capabilities. This feature, combined with the excitonic properties of NGs, could also allow for the design of high-performance optoelectronic devices, as reported for instance in [216]. Here, $\pi - \pi$ interactions guide the physisorption of NG molecules onto graphene, resulting in van der Waals heterostructures with strong interlayer coupling. By proof of concept

tests, the authors showed that the obtained NG/graphene hybrids can be employed in photodector devices with ultrahigh responsivity and specific detectivity. The remarkable attributes of these devices, demonstrated by ultrafast spectroscopy, is attributed to ultralong charge separation, exceeding 1 ns, at the interfaces between graphene and NG, which occurs after an highly efficient photoinduced transfer of holes from NGs to graphene.

Notably, the efficiency of charge-transfer processes in structurally highly defined systems such as NGs can be correlated with specific structural parameters, like the size of sp^2 domains. For instance, in [217], researchers systematically varied the size of NGs to modulate the interfacial charge transfer with graphene. They found that by increasing the size of NGs from 42 to 96 carbon atoms, charge-transfer efficiency increased by on order of magnitude, driven by the enhanced van der Waals interactions that are expected to occur with increased size [99].

Another example of non-covalent coupling of NGs is provided in [218], where $\pi - \pi$ stacking interactions are exploited to constitute supramolecular hybrids with pyrene-derivatized cobalt and zinc phthalocyanines and porphyrins. The enhancement of the fluorescence of two latter at the expenses of NGs is described in terms of a Förster resonance energy transfer from NGs to the respective macrocyclic complexes.

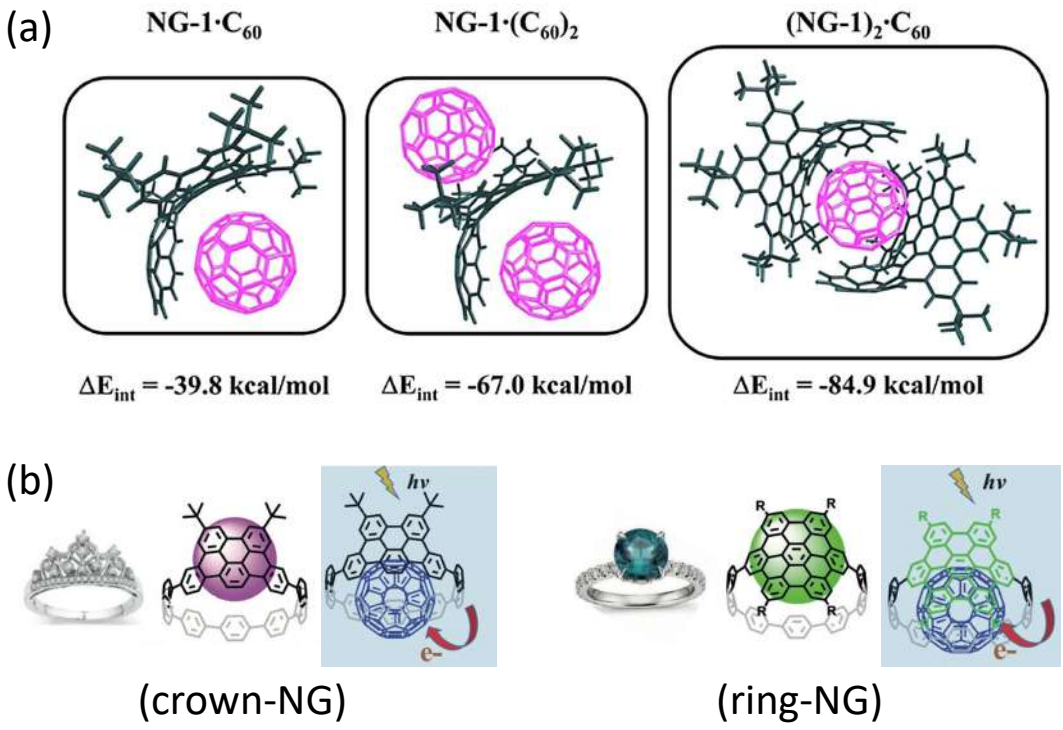

Figure 1.20: (a) Optimized structures and interaction energies of the most stable confomers NG/C_{60} complexes [Adapted from [219]]. (b) Design of π-extended molecular crown and ring shaped NGs for supramolecular interactions with fullerene and subsequent photocurrent generation under light irradiation. [Adapted from [188]].

The tight control over the chemical structure achievable in many NGs, enables the customization of their structures to induce highly specific interactions favoured by a structural complementarity with other systems, facilitating complexation, and leading to the formation of hybrid systems. This ability to finely tune structural characteristics at an atomic level represents a unique feature of atomically-precise NGs. In this context, an especially innovative frontier of research involves engineering molecular NGs by introducing specific structural motifs crucial for establishing interactions with nanomaterials possessing highly curved surfaces, such as fullerenes. This aspect will be further elucidated also in the present work through a photophysical investigation focusing on the specific interactions established within these types of nanosystems. For instance, in [219] the presence of both positive and negative curvature in the sp^2 domain of the studied NG facilitates concave-convex interactions with C_{60}. The two nanosystems were found to easily undergo complexation, forming complexes with 1:1, 1:2, and 2:1 stoichiometries (see Figure 1.20(a)), paving the way to the use of NGs of contorted shapes to establish NG-fullerene hybrid structures. In [188], the authors reported an alternative complexation architecture. They achieved this by creating a spontaneous belt-like hosting of C_{60} using crown-shaped and ring-shaped NGs obtained through the incorporation of a circular motif like cycloparaphenylene, with HBC- and pentaphene-derivatives, respectively. The binding associations between the two pairs of nanocarbons were demonstrated to be significantly strong, and films of these complexes revealed remarkable photocurrents under light irradiation, favoured by a demonstrated electron-transfer from curved NGs and fullerene.

1.5 Aim of the Thesis

Given the significant interest in luminescent 0DNCs, partially driven by the reasons previously described, the present work aims to conduct a comprehensive photophysical study of specific CDs and molecular NGs with a particular focus directed toward the potential possibility of using them as building blocks for constructing optical hybrid systems. As shown, several challenges persist within the current literature, animating an intense debate. In particular, with regards to atomically-precise NGs, one of the most important open issues is represented by the fundamental understanding of their optical properties through an accurate analysis of representative model systems. In particular, by taking advantage of the ultimate atomic precision intrinsically inherent to molecular NGs, the establishment of well-defined structure-properties relationships is particularly appealing, and it can be achieved only by performing direct comparisons among similar systems differing only in slight, specific structural modifications. Moreover, a crucial question pertains to tailoring the structures of these NGs to the extent that their optical response starts to deviate significantly from purely molecular behaviour. Exploring, studying, and optimizing the use of NGs as building blocks of more complex architectures stands as an additional focal point. In this perspective, a relevant part of this study is devoted to designing and characterizing from a photophysical perspective various 0DNC-based optical hybrid systems, obtained through straightforward self-assembly routes, which are considered particularly representative in addressing some of the aforementioned open questions within the literature.

After the present **Chapter 1**, which has been dedicated to a general overview of the state

of the art in the current research on CDs and NGs, exploring also their potential for designing hybrid optical systems, the rest of the Thesis is structured as follows.

- **Chapter 2** provides a description of the synthetic routes followed for the synthesis and preparation of all the samples studied and employed in this work, along with the experimental setups and data analysis procedures used throughout the performed studies.

The presentation of the experimental results is divided into two distinct parts: *Results: Part I* and *Results: Part II*, each dedicated to specific typologies of luminescent 0DNCs. *Results: Part I* focuses on the photophysical study of atomically-precise NGs and their related hybrid systems. In particular:

- **Chapter 3** presents the fundamental photophysical characterization of a palette of atomically-precise NGs using a battery of spectroscopic techniques. The goal is to thoroughly understand their optical characteristics down to the femtosecond scale, establish precise structure-properties relationships, and assess the impact of controlled structural changes.
- **Chapter 4** describes the effective loading of one of the NGs studied in Chapter 3 onto the surface of polystyrene beads, acting as spherical microresonators. This allows to strongly modulate the emission properties of the NGs through the whispering gallery modes due to the sperical microcavity, and the chapter discusses not only the detailed optical study but also a proof-of-concept application of similar systems as photonic tags for anticounterfeiting purposes.
- **Chapter 5** provides a second model example: a binary all-carbon nanohybrid formed by the complexation of fullerenes with one of the studied NGs, opportunely engineered to increase the mutual morphological complementarity, ultimately favouring supramolecular interactions between the two interacting nanosystems. These showed significant photoinducible charge-transfer behaviours, paving the way to a wide range of light-driven applications.

Results: Part II is instead dedicated to hybrid nanosystems obtained through the coupling of a specific type of CD with several types of metallic nanoparticles. Specifically,

- **Chapter 6** mainly investigates the optical response of carbon/plasmonic nanohybrids obtained by direclty combining CDs with silver nanoparticles. A comprehensive photophysical investigation down to the femtosecond scale assesses the strong electron-transfer features characterizing the obtained nanohybrids, leading to emergent photocatalytic activity.
- **Chapter 7** highlights the impact of introducing a polymeric spacer in the CDs when coupled with plasmonic nanostructures. Unlike the previous case, the physical separation between the two interacting systems hinders electron-transfer processes, resulting in significant plasmonic interactions that, in some cases, enhance the emission properties of the CDs.

At the end of each chapter, a brief conclusion summarizes the reported results, while at the end of the Thesis a conclusive chapter will provide a general summary aiming to reviewing the main results achieved in the present work. Most of the results included in this Thesis have been already published as papers on scientific journals.

Chapter 2

Materials and Methods

This chapter is dedicated to an overview of the synthesis procedures, detailed sample preparation methods, the experimental setups utilized, and a thorough explanation of the analysis techniques applied to interpret the results reported in the following chapters.

2.1 Synthetic routes

The samples examined in this Thesis were either synthesized in-house, obtained through collaborations, or purchased commercially. The following section provides a brief description of the samples synthesized in our laboratories and those synthesized by other research groups.

Synthesis of NGs

All the nanographene samples studied in this Thesis (see chemical structures reported in Figure 3.1) were synthesized by the group of Prof. A. Campaña, based at University of Granada. The heptagon-containing HBCs were synthesized according to previously reported routes, following a cobalt-catalyzed alkyne cyclotrimerization reaction between functionalized benzophenone-dialkyne derivatives and diphenylacetylenes, and a subsequent Scholl reaction [139]. As shown in the top part of scheme reported in Figure 2.1, for the synthesis of c-NG1, *tert*-butyl functionalized 2,2'-*bis*(phenylacetylene)-benzophenone (1) and diphenylacetylene (2a) were used, while the exocyclic double bond of m-NG was introduced by reaction of c-NG with Tebbe's reagent [220]. c-Br-NG was prepared using 1,2-*bis*(4-bromophenyl)acetylene during cobalt-catalyzed reaction [152].

The synthetic procedure for the preparation of compound c-NG2 was previously reported in [222]. In this case, as reported in Figure 2.1, the cobalt-catalyzed alkyne cyclotrimerization reaction between benzophenone-dialkyne derivative is performed with iododiphenylacetylene (2b), allowing for a further extension of the aromatic surface after formation of the *hept*-HBC 4. Starting from it, Sonogashira coupling with *p*-*tert*-butylphenylacetylene allowed to obtain 5.

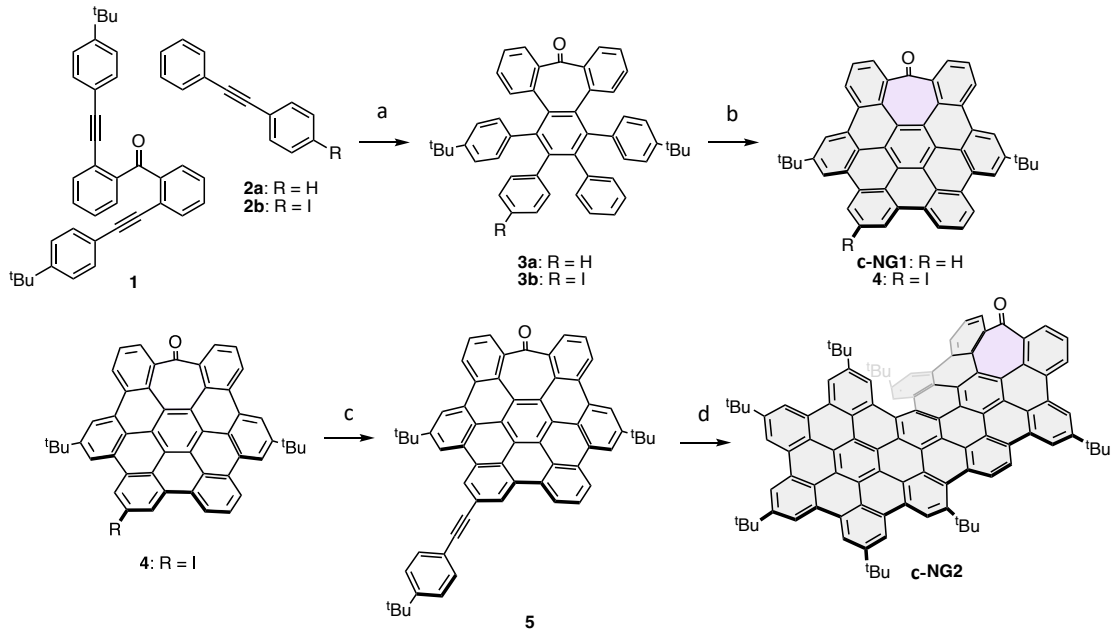

Figure 2.1: Scheme of synthesis of NG1s and NG2. [Adapted from [221]].

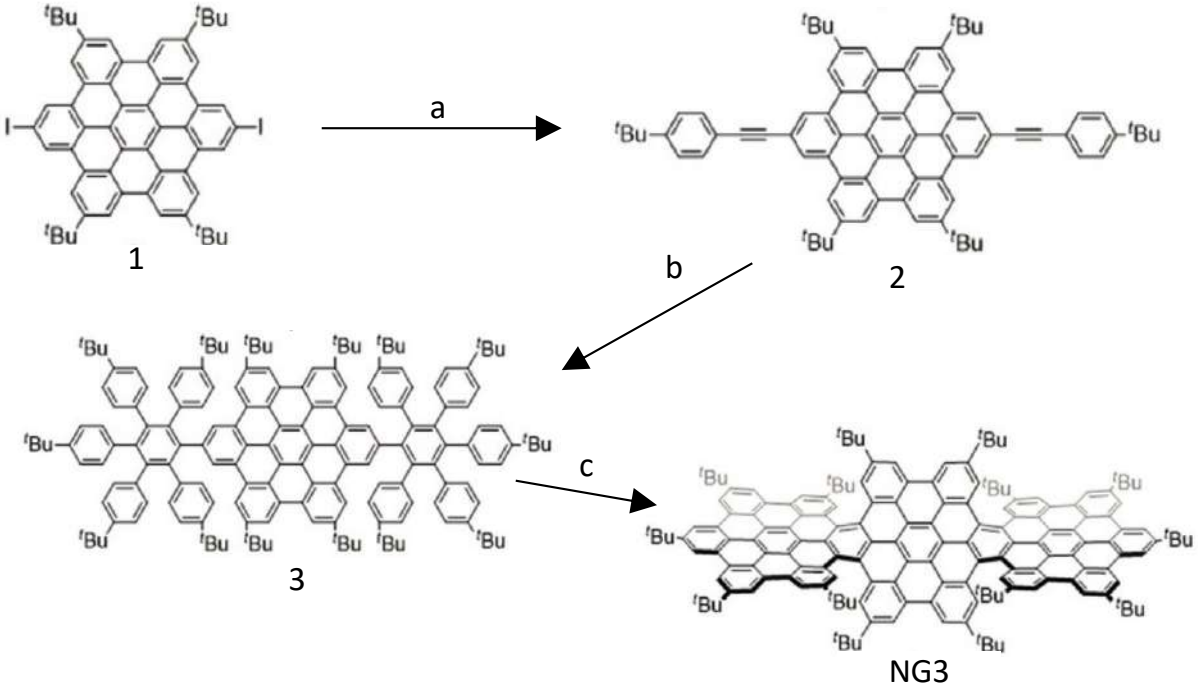

Figure 2.2: Scheme of synthesis of NG3. [Adapted from [155]].

Then, Diels-Alder reaction using the corresponding cyclopentadienone allowed to obtain a direct precursor towards c-NG2, which is finally obtained by Scholl reaction.

Synthesis of NG3 was achieved through an already reported procedure [155], schematically depicted in Figure 2.2. Starting from the difunctionalized HBC 1, a double Sonogashira coupling reaction was performed with 4-tert-butylphenylacetylene to get compound 2. Then, the aromatic surface was extended using a two-fold Diels-Alder reaction with 2,3,4,5-tetrakis-(p-tert-butyl-phenyl)-cyclopentadienone giving precursor 3, which, after cyclodehydrogenation resulted in compound NG3.

Synthesis of CDs

The particular type of CDs used in this work for the constitution of CD-based nanohybrids was obtained in previous studies and synthesized *via* a bottom-up carbonization method outlined in details in [53], summarized here briefly. 3 g of citric acid monohydrate (Sigma Aldrich) and 3 g of urea (Sigma Aldrich) are dissolved in 10 mL of ultra pure water (Chem. Lab.). The resulting aqueous solution is heated on a hotplate and boiled up until a complete evaporation of the water is observed, yielding a strongly hygroscopic black material from which a fine black powder consisting of aggregates of CDs is obtained. This resulting powder is dissolved in water to undergo a separation/purification procedure. Size exclusion chromatography (SEC) is conducted using a glass column (2.5 cm diameter). The column's stationary phase consists of three resins with increasing cutoff values: sephadex G25 (15 g), G15 (15 g) and G10 (15 g) purchased from GE Healthcare. In the SEC procedure, 5 mL of CDs obtained after synthesis and concentrated at ∼3 g/L are added on the top of the column using water as eluant. From the multiple fractions of eluates (each approximately 4 ml), the fraction containing the CDs with the highest quantum yield is selected, according to [53].

PEGylation of CDs

The CDs obtained through the previously described methodology underwent a surface passivation utilizing polyethylene glycol (PEG) molecules with molecular weights of either 400 or 3000 daltons (purchased from Sigma Aldrich), to obtain two typologies of CDs with different surface shell thicknesses. The PEGylation process follows a hydrothermal route conducted within an autoclave. Initially, 1 mL of a ∼ 2 µM aqueous solution of purified CDs is mixed with 1 mL of PEG400. This resulting mixture is then subjected to a 24 h reaction in the autoclave at 120°C. After cooling, SEC separation is employed to purify the obtained sample, with the aim to isolate the fraction mainly composed of PEGylated CDs from unreacted CDs and free PEG molecules. The SEC purification is performed using a glass column with a 2.5 cm diameter and involves 2 mL of the sample obtained after hydrothermal reaction as the eluant, while the stationary phase comprises three resins purchased from GE Healthcare − sephadex G25 (15 g), G15 (15 g) and G10 (15 g) − each with increasing cutoff values for optimal separation.

Synthesis of AgNPs

Silver nanoparticles of ∼50 nm were synthesized using a route inspired by the well-known Turkevich method [223]. A 50 mL volume of 5 mM aqueous citric acid (Sigma Aldrich) solution is adjusted to pH 7 by adding approximately 20 mL of NaOH solution, and then heated on a hotplate under vigorous stirring. Upon reaching the boiling point, 1 mL of 25 mM $AgNO_3$ (Eastman Kodak Company) aqueous solution is quickly introduced into the initially colourless solution. After about 10 minutes, the solution starts showing a yellowish hue. The heating process is stopped after 30 minutes, when the solution has turned into a brownish-yellow color and becomes quite turbid. The obtained solution is naturally cooled at room temperature. To eliminate any residual reagents, the mixture is subjected to two cycles of centrifugation (8000 rpm for 15 minutes) followed by the subsequent re-suspension of the sediment in ultrapure water (Chem. Lab.) post removal of the supernatant.

Silver nanoparticles of ∼30 nm were synthesized by refining the preceding route. A volume of 50 mL of 5 mM aqueous solution of sodium citrate (Sigma Aldrich) is heated on a hotplate under vigorous stirring and continuous refluxing, while covered to prevent water evaporation. Around 2 min after boiling starts, 1 mL of 25 mM $AgNO_3$ (Eastman Kodak Company) solution is quickly introduced. Within approximately ten minutes, the solution begins to transition in color from transparent to yellowish. The solution is maintened at the boiling point for about 40 min, until the color stops changing, indicating the complete formation of silver nanoparticles. To remove any residual reagents, the solution undergoes two cycles of centrifugation (8000 rpm for 15 minutes). The sediment is re-suspended in ultrapure water (Chem. Lab.) after separating it from supernatant. According to [224], after size estimation of AgNPs by morphological measurements, the molar concentration of both the AgNPs was estimated by the knowledge of the maximum extinction observed in the UV-Vis spectra, having simulated the corresponding molar extinction coefficient by MiePlot Software.

Synthesis of AuNPs

Gold nanoparticles having ∼15 nm diameter were synthesized using a seeded growth approach inspired by previous studies [225]. An aqueous solution (75 mL) of 2 mM sodium citrate (Sigma Aldrich) is heated on a hotplate under vigorous stirring and continuous refluxing, while covered to prevent water evaporation. When the solution reaches the boiling point, 1 mL of 12.5 mM of $HAuCl_4$ (Sigma Aldrich) solution is swiftly injected. Within less than ten minutes, the solution's colors from transparent becomes quickly bluish gray and then dark brownish-red, indicating the formation of gold nanoparticles seeds. After the gold seed formation, the solution is cooled down to 90 °C. Then, 0.5 mL of sodium citrate (60 mM) is added, followed by the addition of 1 mL of $HAuCl_4$ (12.5 mM) after 2 min. The reaction is kept for 10 min. The sequential process of adding 0.5 mL of 60 mm sodium citrate and 1 mL of 12.5 mM $HAuCl_4$ is repeated up to five times to obtain the 5th generation of gold nanoparticles. To eliminate any residual reagents, the solution undergoes two rounds of centrifugation (8000 rpm for 15 minutes). The sediment is re-suspended in ultrapure water (Chem. Lab.) following the removal of supernatant. After size estimation of AuNPs by morphological measurements, their molar concentration was estimated

by the knowledge of the maximum extinction observed in the UV-Vis spectra, having simulated the corresponding molar extinction coefficient by MiePlot Software.

Ligand-exchange procedure for MNPs

The metallic nanoparticles obtained according to the previously reported routes, when dispersed in water are characterized by a negative surface charge due to the presence of citrate ions on the surface. In order to obtain their positively charged counterparts, a ligand exchange procedure inspired to previously reported works was followed [226, 227].

For the AgNPs having ∼50 nm diameter, 2 mL of the final purified dispersion of AgNPs was added dropwise into 2 mL of 2 mM cetyltrimethylammonium bromide (CTAB) purchased from Sigma Aldrich solution and the mixture was gently stirred for 24 hours. For AgNPs of ∼30nm diameter, 1 mL of the final purified dispersion of AgNPs was added dropwise into 1 mL of 5 mM CTAB solution and the mixture was gently stirred for 24 hours. Analogously for AuNPs, 1 mL of the final purified dispersion of AuNPs was added dropwise into 1 mL of 5 mM CTAB solution and the mixture was gently stirred for 24 hours. In each case, centrifugation (8000 rpm for 20 min) was used for the removal of free unreacted CTAB molecules.

Loading of NGs onto polystyrene beads

The self-assembly procedure followed to incorporate NGs onto the surface of polystyrene microparticles was inspired by previous works reported in literature that involved doping polystyrene microbeads with quantum dots or fluorescent dyes [228, 229]. For NGs, a similar methodology was employed, taking advantage of the inherent $\pi - \pi$ interactions between the phenyl group of polystyrene and the extended π-conjugated network of NGs. The integration occurred by simply mixing NGs and polystyrene microparticles through an infusion in a chlorobenzene-isopropanol mixture. The procedure starts with the addition of 50 µL (approximately 10^8 particles) of an aqueous dispersion of 3 µm polystyrene microparticles (Polysciences, Inc., polydispersity 5%) to 5 mL of ethanol. Centrifugation at 6000 rpm for 2 minutes separates the particles, followed by removal of the supernatant. The sedimented beads are then re-suspended in 3 mL of isopropanol. Subsequently, 450 µL of this dispersion are combined with 50 µL of a ∼50 µM chlorobenzene solution of a specific NG and gently stirred for 5 hours at room temperature. After this procedure, the beads are isolated from excess NGs through centrifugation at 6000 rpm for 2 minutes, then re-suspended in isopropanol.

2.2 Optical characterization

Steady-State Absorption

Absorption spectra in the UV-Vis range were acquired using an optical fiber spectrophotometer (Avantes, AvaSpec-ULS2048CLEVO) coupled to a dual halogen-xenon lamp as light source. The

light from the source is guided to the sample holder chamber *via* an optical fiber, and the transmitted radiation is collected through a second optical fiber and sent to the detector unit. In the detector unit, the light is dispersed into its spectral components and detected by a CMOS sensor. The instrument outputs the optical density, obtained as follows:

$$A(\lambda) = \log_{10}\left(\frac{I_0(\lambda) - I_b(\lambda)}{I_t(\lambda) - I_b(\lambda)}\right) \tag{2.1}$$

where I_b, I_0 and I_t represent the background intensity (acquired when the light source is off), the reference intensity spectrum of the source and the spectrum of the light transmitted after passing through the sample, respectively.

Steady-State Photoluminescence

Steady-state photoluminescence (PL) measurements were conducted using a JASCO FP-6500 spectrofluorometer, equipped with a 150 W Xenon discharge lamp operating in the 220-750 nm range as excitation source. A monochromator, provided with an 1800 grooves/mm grating, disperses the excitation light. A user-defined bandwidth allows for the selection of a monochromatic excitation beam which, after being focused though a lens, is used to excite the sample. Its emission is collected by a lens in a 90° geometry and directed to an additional monochromator with the same characteristics as the excitation monochromator. Finally, the dispersed emission light is detected by a photomultiplier. The instrument allows for the acquisition of PL spectra with a fixed excitation wavelength by scanning the emission wavelength, or a photoluminescence excitation (PLE) spectra with a fixed emission wavelength by scanning the excitation wavelength. The resolution of both the excitation and emission spectra can be adjusted using slits positioned at the exit of the excitation monochromator and at the entrance of the emission monochromator, as the width of each slit is adjustable from the user.

Data correction When necessary, the photoluminescence data underwent a standard correction procedure to account for the non-flatness of the excitation source spectrum and to calibrate the detector's instrumental response, which may vary in sensitivity at different wavelengths. For the first purpose, the emission spectrum of the light-source was acquired using a concentrated, highly absorbing, ethanol solution of Rhodamine B as a reference. The nearly unitary emission quantum yield of Rhodamine B across a wide spectral range allows to convert each absorbed photon (at different excitation wavelengths) into an emitted photon (at approximately 640 nm, corresponding to the emission peak). Consequently, the PLE spectrum of the this sample corresponds to the emission spectrum of the excitation light source. All the PLE spectra were corrected by point-wise division with the reference PLE spectrum from the reference sample, thus accounting for the intensity modulation of the spectrum caused by the lamp's emission. To determine the spectral instrumental response of the detector, a synchronous spectrum was acquired using a scattering medium in the sample chamber, with data collected at the same wavelength as the excitation ($\lambda_{exc} = \lambda_{em}$). After correction for the source emission spectrum, the resulting spectrum represents the spectral instrumental response of the detector.

Micro-photoluminescence

Single-particle photoluminescence spectra were acquired by using a home-assembled Microphotoluminescence (µPL) setup. This modular setup consists of three primary components: an excitation laser source, an optical microscope and a spectrophotometer as detector. The sample, deposited through drop-casting onto a microscope slide, is photoexcited by a focused laser diode beam (Thorlabs 405 or 532 nm), in a reflection-wide field geometry. A 40X objective mounted in the microscope (Motic BA300) allows for the direct visualization of microparticles and the selection of a specific area within the photoexcited sample. The emission can be selectively collected from microsized regions of the sample, using a 1 mm optical fiber, which is connected on one end to an exit eyepiece of the microscope and on the other end to a spectrophotometer. The coupling of the fiber with the used objective allowed to selectively collect the emission coming from a region of 1 mm/40 = 25 µm. This latter comprises a monochromator (Acton, SpectraPro 2300i) and a CCD camera (Princeton Instruments, Pixis 400). The emission spectra were collected by configuring the acquisition parameters to achieve a ∼2 nm resolution. Fluorescence microscopy images were captured using a smartphone camera attached to one of the microscope's eyepieces, with a test pattern used for scale calibration.

Absolute Quantum Yield measurements

The absolute quantum yield measurements were obtained using an integrating sphere (Labsphere 3P-GPS-053-SL) internally covered by Spectralon, and 405 nm laser diode (Thorlabs) as excitation source. A Star Line ULS2048CLEVO single-beam optical fiber spectrophotometer (Avantes, AvaSpec-ULS2048CLEVO) was used as detector, enabling the acquisition of the spectral distribution of emission intensity.

Relative Quantum Yield measurements

The relative quantum yield measurements were conducted by comparing the PL intensity of the sample under study with the PL intensity of a reference dye with a known quantum yield (QY_{ref}). The choice of the reference dye depended on the spectral emission range of the sample, and commonly used dyes included coumarine, fluorescein and rhodamine B. The QY of the sample was calculated using the following formula:

$$QY = QY_{ref} \frac{I}{I_{ref}} \frac{1 - 10^{-OD_{ref}}}{1 - 10^{-OD}} \frac{n^2}{n_{ref}^2} \tag{2.2}$$

where I and I_{ref} are the spectrally integrated intensity, OD and OD_{ref} the absorbance values at the excitation wavelength, n and n_{ref} the refractive index of the solutions, respectively for the sample under study and the reference.

Time-resolved Photoluminescence

The setup used for acquiring time resolved photoluminescence data comprises three main units: (i) the excitation, (ii) the dispersion and (iii) the detection system (see Figure 2.3).

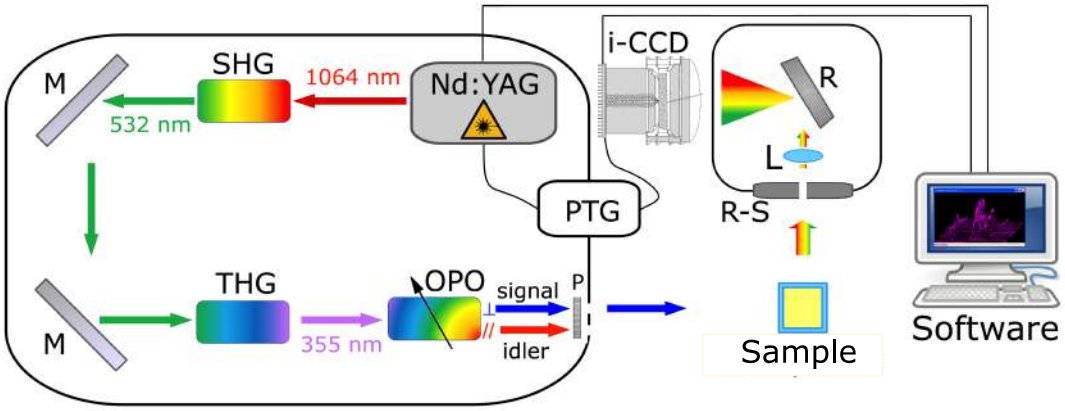

Figure 2.3: Schematic representation of time-resolved photoluminescence setup. SHG: second-harmonic generator crystal; THG: third-armonic generator crystal; OPO: optical parametric oscillator; P: polarizing filter; L: lens; R: grating; i-CCD: intensified CCD.

The excitation unit is represented by a Vibrant OPOTEK tunable laser, which consists of an optical parametric oscillator (OPO) pumped by a Q-switched Nd:YAG laser (QUANTEL). The Nd:YAG laser generates 5 ns duration pulses at 1064 nm, with a maximum repetition rate of 10 Hz. A high-power Xenon lamp is employed to pump the laser's active medium, and a Pockels cell within the laser cavity triggers the Q-switch. The 1064 nm beam undergoes wavelength conversion, first to the second harmonic at 532 nm and then to the third harmonic at 355 nm. This 355 nm beam serves as the pump beam for the birefringent nonlinear crystal inside the OPO unit, generating a signal and an idler beams, perpendicularly polarized in accordance with the conservation of energy and momentum. A polarizer allows the selection of either the signal (410-710 nm) or the idler (710-2400 nm). Additionally, by inserting specific UV-modules into the beam path, it is possible to duplicate the signal or idler beams, extending the tunability range of the excitation beam to the 210-410 nm spectral window.

The chosen output beam is used to excite the sample, and the emitted light is collected by a lens and directed to a monochromator, passing through a slit of adjustable width. The monochromator disperses the emitted light into its spectral components, offering a choice of three different gratings with varying blaze wavelength (λ_b) and groove density:

- λ_b = 300 nm and 1200 gr/mm $\rightarrow$ spectral resolution of 3 nm/mm
- λ_b = 300 nm and 150 gr/mm $\rightarrow$ spectral resolution of 20 nm/mm
- λ_b = 500 nm and 300 gr/mm $\rightarrow$ spectral resolution of 11 nm/mm

The selection of a specific grating and slit aperture, both affecting the spectral resolution, is based on the specific spectral characteristics of the sample's emission spectrum. Typical spectral resolutions during measurements range from 3 nm down to 0.1 nm, particularly for spectra rich in fine-structures. The detection system relies on an intensified CCD camera (PI-Max Princeton Instruments) synchronized with the excitation pulse through a programmable timing generator

(PTG) triggered by the laser. After the monochromator, the spectrally dispersed light is directed to the photocathode of a microchannel plate (MCP), which consists of a semiconductive glass plate punctured by 10-25 µm channels. The photoelectric effect causes photons striking the photocathode to stimulate the emission of electrons, which are subsequently multiplied through a cascade process as they continuously collide with the channel walls, characterized by a high secondary emission coefficient. The multiplied electrons are then accelerated to hit a phosphor screen, resulting in the emission of photons detected by the CCD camera. For the described processes, this CCD camera is referred to as 'intensified' because it detects a greater number of photons compared to the initial photons exiting the monochromator, with the level of intensification depending on the voltage applied to the MCP's photocathode. When activated by a voltage square pulse of very short duration, it allows for the detection of a very small number of photons emitted within a narrow temporal window, enabling the acquisition of ns-resolved PL data.

Time-resolved measurements involve gating the emission of the sample under study over a certain temporal window at different programmable delays from photoexcitation. This allows to reconstruct the kinetics of the entire decaying emission band. The standard analysis of time-resolved emission data typically includes a least-squares fit of the obtained kinetics to exponential functions, convoluted with a gaussian instrumental function accounting for the laser pulse's temporal duration.

Ultrafast Transient Absorption

Transient absorption (TA) is a spectroscopic technique where the changes in absorbance spectrum occurring in a sample after its photoexcitation are probed. In a typical TA experiment, photoexcitation occurs *via* an ultrashort pulse lasting a few femtoseconds, known as the "pump". The variations in the absorbance spectrum are detected by using a second ultrafast pulse, called "probe", spectrally broad to probe the variations over a wide spectral region. The comparison between the signal of the probe transmitted through the sample before and after photoexcitation permits to individuate variations in the sample absorbance spectrum as a function of time, by controlling the relative delay between pump and probe.

Femtosecond transient absorption measurements reported in this Thesis, were carried out using a home-built pump-probe setup, whose scheme is reported in Figure 2.4. The output from a 5 kHz Ti:Sapphire femtosecond amplifier (Spectra Physics, Solstice), consisting of 50 fs pulses centered at 800 nm (FWHM=45 nm), is split into two branches using an 80%/20% beam splitter to create the pump and probe pulses, respectively. In the pump arm, the 800 nm beam passes through a telescope, consisting of a pair of positive and negative lens, with the aim of reducing its size and increasing the power density, to optimize second harmonic generation efficiency. Due to the group velocity dispersion introduced by the telescope [230], the pulse duration increases from 50 to 75 fs. For 400 nm excitation, the pump is generated by frequency-doubling the 800 nm beam using a β-BBO crystal (250 µm). A BG40 Schott filter is used to isolate the 400 nm beam from the fundamental. In cases where the pump has to fall in the visible spectrum, a home-built non-collinear optical parametric amplifier (NOPA) is employed, providing tunable wavelengths between 490 and 570 nm with a bandwidth of 10-20 nm. To produce the probe, the second branch

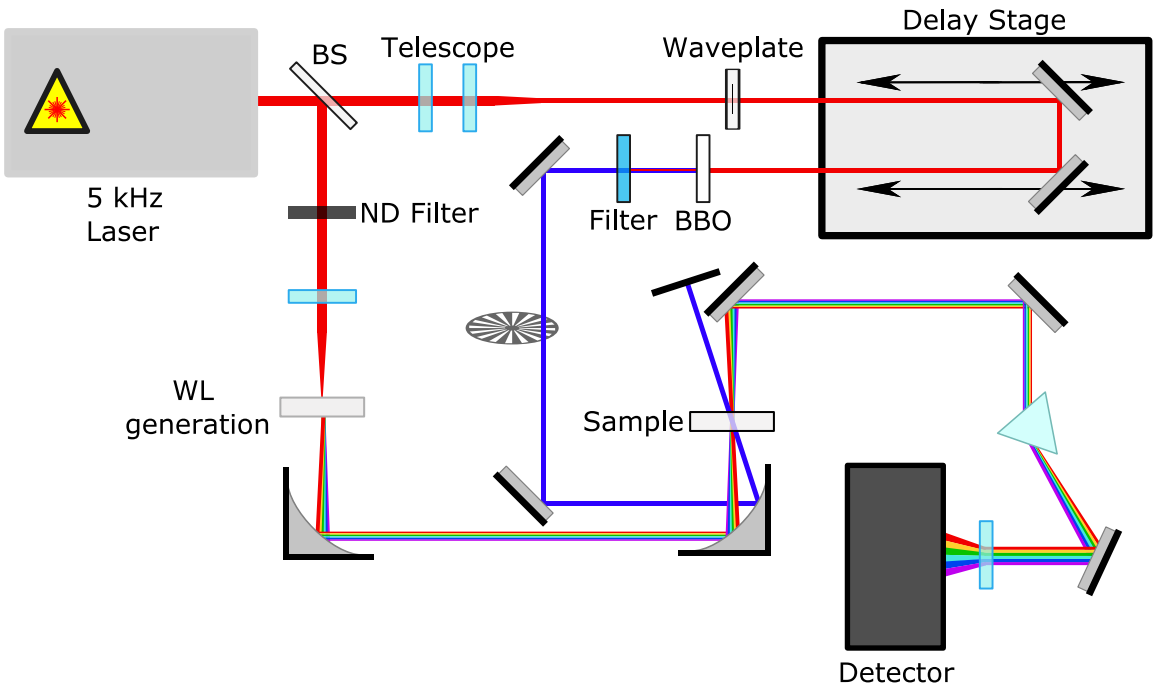

Figure 2.4: Scheme of the pump-probe setup used for ultrafast transient absorption measurements.

of the initial 800 nm beam is focused on a 1 mm quartz cuvette containing D_2O, resulting in supercontinuum pulses with and energy of ∼5 nJ/pulse and a spectrum spanning from 400-700 nm range. Alternatively, whenever it becomes necessary to extend the probe pulse in the UV part, instead of D_2O, a CaF_2 crystal maintained in continous movement is used, allowing for a white light spectrum ranging from 330 to 650 nm. Both the pump and the probe are then focused and spatially overlapped using a parabolic mirror (f=150 mm) onto the sample, which is continuously flowing through a 0.2 mm flowcell driven by a peristaltic pump. The delay between the pump and probe is precisely controlled using a motorized delay stage, and a chopper modulates the pump pulse train at 2.5 kHz, allowing for the alternating recording of 5000 pumped and 5000 unpumped spectra for each pump-probe delay. Finally, the probe transmitted through the sample is dispersed by a Brewster-angle silica prism and then focused onto a single-shot detector (Glaz, LineScan I), carefully synchronized with the experiment. Under optimal conditions, this configuration provides a spectral resolution of 3 nm and a temporal resolution of approximately 90 fs for 400 nm and ∼70 fs in the case of pump obtained through the NOPA.

Data acquisition was always carried out in the linear regime, with the pump energy per pulse typically kept below 50 nJ. The TA data were usually obtained by collecting multiple scans over the pump-probe delay (usually 10-20 times, depending on the signal to noise ratio). To ensure accurate measurements, the magic angle condition was maintained by controlling the polarization of the pump using a waveplate.

The TA data underwent standard correction procedures to eliminate the effects of group

velocity dispersion and cross-phase modulation [230]. Subsequently, singular value decomposition (SVD) analysis was performed on the TA matrix $\mathrm{TA}(\lambda,t)_{M,N}$ constituted by M lines and N columns referring to the wavelengths λ and delays t, respectively. The original TA matrix is thus decomposed as [230]:

$$TA(\lambda,t)_{M,N} = U(\lambda)_{M,M} \times S_{M,N} \times V(t)^{t}_{N,N} \tag{2.3}$$

where matrices $U(\lambda)_{M,M}$, $S_{M,N}$ and $V(t)_{N,N}$ are referred to as eigenspectra, eigenvalues and eigentraces matrices, respectively. Based on eq. (2.3), the TA signal is expressed as a linear combination of three components where the spectral informations are contained in $U(\lambda)_{M,M}$, the kinetic informations in $V(t)_{N,N}$, and the diagonal $S_{M,N}$ matrix contains the weights associated to the corresponding eigenspectra and eigentraces. Specifically, only the eigentraces associated with a few eigenvalues, starting from the largest one, are kept for successive analysis, while all the others are discarded. This allows to filter out the noise from the spectral evolution of the system, simplifying the identification of the most relevant signals and thus reducing the number of spectral and kinetic components for fitting purposes.

Indeed, following SVD of the TA matrix, a global fitting procedure allows the simultaneous fitting of the entire matrix, to obtain the decay associated spectra (DAS). This is achieved by fitting the SVD eigentraces using multiexponential functions convoluted ($*$) with a Gaussian envelope accounting for the instrumental response function IRF:

$$f_j(t) = \sum_i a_{ij} e^{-t/\tau_i} H_0(t) * IRF(\sigma,t) = \sum_i a_{i,j} \left(e^{-t/\tau_i}_{t>0} \mid_{IRF} \right) \tag{2.4}$$

where indexes j and i represent each of the eigentraces and each of the multi-exponential decays, respectively. In the simultaneous fit of eigentraces performed using eq. (2.4), the timescale associated to each decay τ_i and the width σ of the $IRF(\sigma,t)$ are considered as global shared parameters, while the pre-exponential amplitudes a_{ij} are treated as local coefficients. From the result of this fit, it is possible to construct the DAS according to [231]:

$$DAS_i(\lambda) = \sum_j U_j(\lambda) s_{jj} a_{ij} \tag{2.5}$$

where U_j are the eigenspectra, s_{jj} the eigenvalues and a_{ij} the pre-exponential amplitudes obtained from the fit. The spectral contribution of each timescale characterizing the TA signal can be thus ascribed to each single DAS, allowing to write the TA signal in terms of:

$$TA(\lambda,t) = \sum_i DAS_i(\lambda) * \left(e^{-t/\tau_i}_{t>0} \mid_{IRF} \right) \tag{2.6}$$

After identifying the DAS_i and their respective timescales (τ_i), it becomes crucial to attribute a distinct significance to each of these processes from both a spectral and temporal perspective. This attribution ultimately culminates in a comprehensive model detailing the sequence of relaxation events triggered by photo-excitation.

Interpretation of TA data Transient absorption signal is generally calculated as

$$TA(\lambda) = \frac{1}{2.303} \frac{I_u - I_p}{I_u} \tag{2.7}$$

where I_u and I_p refer to the probe light intensities transmitted through the un-excited and photo-excited sample, respectively.

In general, a TA(λ) signal consists in the superposition of three contributions: ground-state bleaching (GSB), stimulated emission (SE) and excited-state absorption (ESA). Their origin is schematically depicted in Figure 2.5 for a three level molecular system. GSB contribution arises

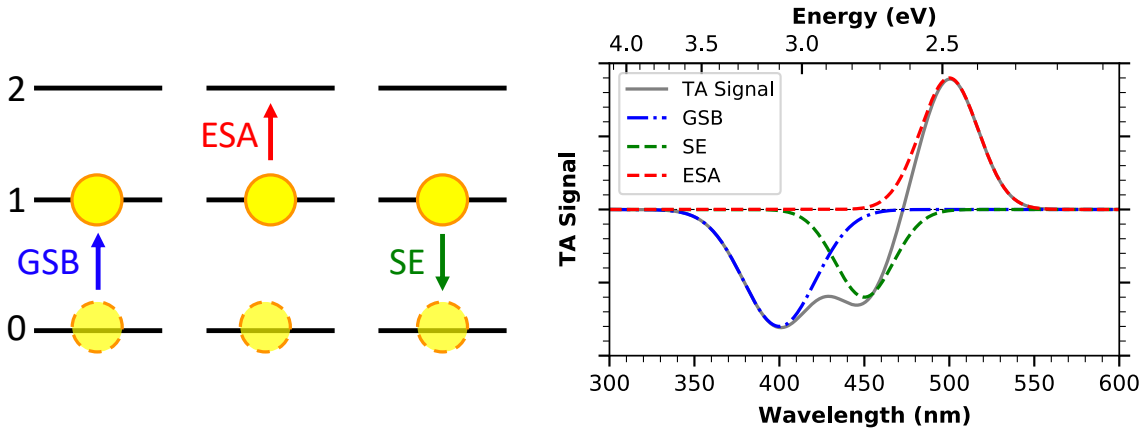

Figure 2.5: Left: diagram of the processes involved in a TA experiment: ground-state bleaching (GSB), excited-state absorption (ESA) and stimulated emission (SE). Right: Exemplary TA signal composed of the three components.

from the partial depopulation of the ground state due to pumping. Photoexcited systems no longer contribute to ground state absorption. This leads to reduced absorption of probe light in the spectral region corresponding to the $0 \rightarrow 1$ transition. Consequently, this results in a negative feature in the TA spectrum, which can resemble one or more of the steady-state absorption bands. In contrast, ESA is the only positive contribution in a TA signal. It is associated with the new electronic transition that can occur from the photoexcited state $1 \rightarrow 2$. As a result, the probe light is partially absorbed in correspondence of this new transition, contributing positively to the TA signal. Finally, SE is another negative component that can emerge when the probe pulse interacts with excited molecules, prompting the stimulated emission of a photon through the $2 \rightarrow 1$ transition. The spectral shape of the SE signal generally closely resembles that of steady-state photoluminescence, except for its negative sign. A slight difference arises from the fact that the SE signal's intensity is directly proportional to the emission frequency, whereas the intensity of stationary emission is proportional to the cube of the emission frequency. Additionally, it is worth noting that in an ideal two-level system, GSB and SE would be indistinguishable, but in a typical molecular system, they are separated by a Stokes-Shift The above description exploited a three-level system for sake of simplicity. However, similar considerations can be generalized and applied also to systems featuring more complex electronic structures.

2.3 Morphological and Structural characterization

Whenever necessary, some of the samples studied in this Thesis were also analysed in terms of their morphological and structural characteristics. In particular, Atomic Force Microscopy and Dynamic Light Scattering were used to extract statistically significant size estimations of the specific samples under study, while Transmission and Scanning Electron Microscopy were employed to achieve direct visualizations of nanoparticles and microparticles, respectively. Zeta potential measurements allowed for considerations regarding the charged nature of the surfaces of the investigated samples.

Dynamic Light Scattering

Dynamic Light Scattering (DLS) measurements were conducted at the University of Palermo's DLS Lab of Prof. A. Emanuele. The measurements were performed using a Brookhaven BI-200SM goniometer with a fixed 90° scattering angle, equipped with a PerkinElmer Optoelectronics APD (SPCM-AQR-14) and a Flex-01 1088 channel multitau correlator. A 671 nm laser line was used as the light source. The samples were properly diluted before the measurements to work under optimal scattering condition. These measurements allowed to determine the diffusion coefficient of particles in solution and calculate the particle radius by analysing the intensity autocorrelation functions.

Atomic Force Microscopy

Atomic Force Microscopy (AFM) images were acquired using a Bruker FAST-SCAN microscope, equipped with a closed-loop piezo-scanner offering a maximum x-y range of approximately 35 µm and a maximum z range of ∼3 µm. For monitoring cantilever deflection a four-segment photodetector is coupled to the instrument. Measurements were conducted in tapping mode in air, employing a FastScan A probe, with a nominal tip radius of 5 nm. The scan area and tip velocity were adjusted to achieve a pixel resolution similar to the tip radius. Samples were prepared by applying a drop-casting technique on a mica substrate, followed by drying under vacuum conditions. The size of the studied nanoparticles was estimated by analysing their height profiles. In cases where a statistical analysis was needed, to obtain a reliable size distribution, multiple images of the same samples were taken from various points on the mica substrate.

Transmission Electron Microscopy

High Resolution Transmission Electron Microscopy (HR-TEM) measurements were performed through the collaboration with Dr. S. Chandra, University of Aalto. HR-TEM images were acquired using a JEM-2200FS Double Cs-corrected transmission electron microscope operating at an acceleration voltage of 200 kV with field-emission guns. To prepare specimens for HR-TEM analysis, the sample was prepared by drop-casting from liquid dispersion onto ultrathin carbon-coated copper grids (less than 10 nm thickness). Subsequently, the sample was deposited

onto a copper TEM grid with a carbon film (CF200-Cu-UL, Electron Microscopy Sciences) and incubated for 5 minutes. Any excess material was carefully rinsed with water and the specimens were left to air-dry.

Scanning Electron Microscopy

Scanning Electron Microscopy images were obtained though the collaboration with Prof. A. Campaña, University of Granada. A Field Emission High Resolution Scanning Electron Microscope AURIGA from Carl Zeiss SMT was used. The images were acquired operating at 3 kV, and setting the acquisition parameters in order to achieve a resolution of $\sim$15 nm.

Zeta Potential

Zeta-potential measurements were performed through the collaboration with Prof. N. Mauro, University of Palermo. Measurements were acquired in 1 mL of aqueous samples, using a Malvern Zetasizer NanoZS instrument equipped with a 532 nm laser with a fixed scattering angle of 173° and Dispersion Technology Software 7.02 software (Malvern Panalytical Ltd, Almelo, The Netherlands). The zeta-potential values (mV) were calculated from the electrophoretic mobility using the Smoluchowski equation. All measurements were performed in triplicate.

Results: Part I

Chapter 3

Photophysics of Atomically Precise Nanographenes

In this chapter, the optical properties of a palette of atomically precise NGs will be thoroughly investigated. The study of such nanosystems of well-defined structures holds a dual significance within the general objectives of this thesis. Firstly, they represent perfect benchmarks for luminescent nanocarbon systems, allowing for the unequivocal correlation of photophysical characteristics with their underlying molecular structures. This investigation will shed light on how even single, controlled structural modifications impact their optical photocycle, as will be thoroughly discussed in the present chapter. Secondly, the attainment of a comprehensive understanding of their optical response is essential when considering the potential integration of these NGs into NG-based composites, where they are envisaged to serve as optically-active components. This latter aspect will be the focus of the following two chapters.

The chemical structures of the five NGs under investigation are presented in Figure 3.1. These structures are named according to the number of HBC-type scaffolds they contain and, for NGs sharing the same core size, a prefix indicating the variation in edge chemical groups is used to differentiate them. Notably, apart from the largest NG3, all other NGs exhibit some degree of structural distortion. This distortion arises from the deliberate inclusion of a heptagon ring within their otherwise purely hexagon networks, which are thus forced out from planarity. The proposed comparison aims to systematically analyse the roles of size, functional groups, and distortions, emphasizing their specific influences to the greatest extent possible. The first part of this chapter is dedicated to a side-by-side comparison of the optical characteristics of the three smallest NGs belonging to the NG1 family, namely c-NG1, m-NG1 and c-Br-NG1. These NGs can be seen as distorted hexabenzocoronene (HBC) derivatives, each featuring a seven-membered ring at the periphery of their carbon network and differing from each other for the functional groups at the periphery of the carbon backbone. Thus, the discussion will move to the larger, distorted c-NG2, which can be approximately considered twofold larger than c-NG1. It also contains a tropone moiety as a heptagon ring and, additionally, the presence of a helicene moiety imparts a deeper distortion away from planarity, making the overall structure more complex. This NG exhibits a series of non-trivial photophysical properties that will be thoroughly discussed and explored.

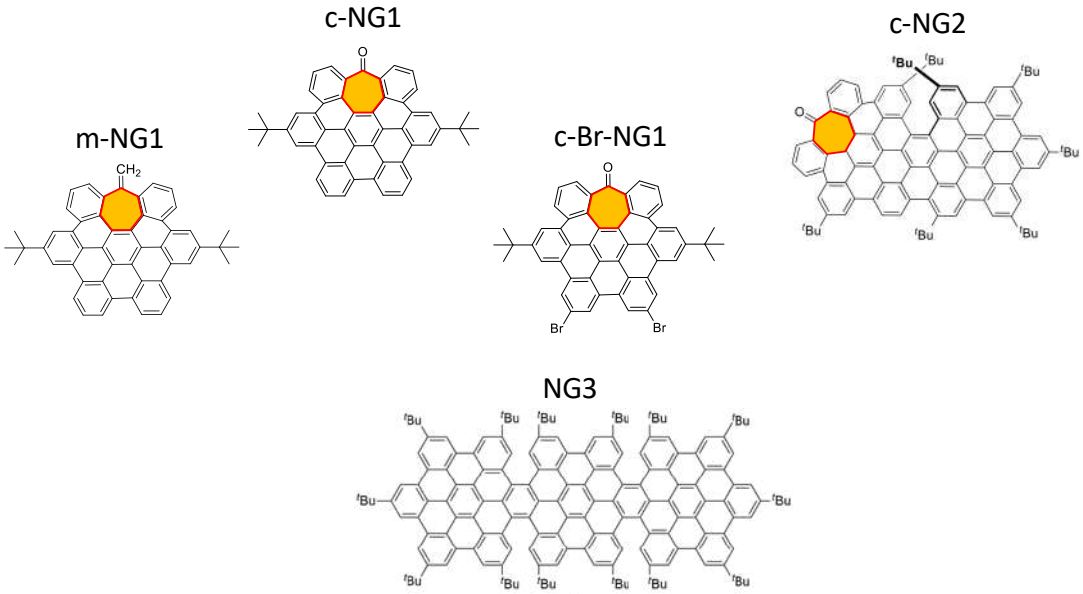

Figure 3.1: Chemical structure of the NGs under investigation. The different NGs are named according to the number of HBC-type units contained in the structure. The NGs belonging to NG1 family are distinguished by a prefix denoting the different edge chemical groups present, namely carbonyl (c), methylene (m) or bromine atoms (Br). In yellow is highlighted the presence of seven-membered rings in their structures.

Finally, the last part is dedicated to presenting and discussing the results related to the largest NG3, the only one characterized by a purely hexagonal core network. It can be viewed as the result of the fusion of three HBC units, forming an aromatic ribbon-shaped backbone.

All five NGs were subjected to a comprehensive optical characterization, combining several steady-state and time-resolved spectroscopic techniques, with the aim of fully reconstructing their photophysical behaviour. Most of the results herein illustrated have been reported in two published papers [221, 232]

3.1 NG1s with different edge functionalization

The NGs within the NG1 family, although sharing substantially the same core structure, differ from one another in terms of distinct chemical attributes. More specifically, when comparing it to c-NG1 as a reference, m-NG1 features a substitution where the oxygen in the peripheral carbonyl group of the tropone moiety is replaced by a methylene group. On the other hand, c-Br-NG1 maintains the same structure as c-NG1 but substitutes two of its edge hydrogen atoms with two bromine atoms. Therefore, these slightly different structures allows for performing a direct comparison of their spectroscopic features, and precisely disentangling the role played by specific and controlled edge chemistry modifications. All the optical measurements reported in the following were performed on chlorobenzene solutions with micromolar nanographenes concentration, unless otherwise specified.

Steady-State Properties

Figure 3.2 displays the main steady-state optical characteristics of the three HBC derivatives c-NG1, m-NG1 and c-Br-NG1, in green, blue and red, respectively. Both the absorption (solid lines) and emission (dashed lines) spectra exhibit well-defined fine structures. The three UV-Vis spectra share a similar structured bandshape reminiscent of HBC [105] featuring appreciable subpeaks at $\lambda \sim 355$, 338 and 380 nm respectively associable to β', β and $p-$bands, according to Clar's rule for PAHs [167].

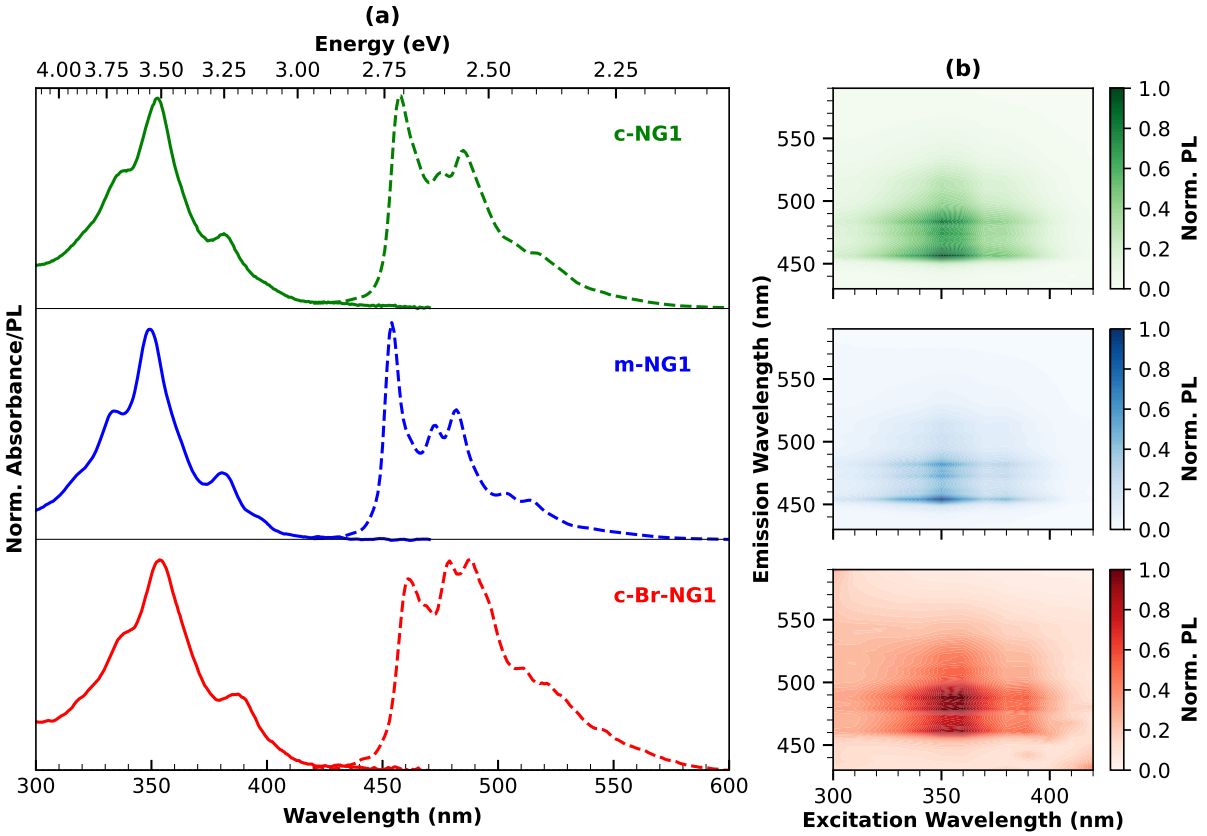

Figure 3.2: (a) Normalized absorption (solid lines) and photoluminescence (dashed lines, $\lambda_{exc} = 350$ nm) spectra of c-NG1 (in green), m-NG1 (blue) and c-Br-NG1 (red) in dichloromethane solutions ($\sim 10^{-6}$ M concentration). (b) Corresponding excitation-emission maps of c-NG1 (green), m-NG1 (blue) and c-Br-NG1 (red). [Adapted from [232]].

All three NGs feature a blue PL whose spectral shape exhibits vibrationally-resolved subpeaks, even at room temperature. For each NG, the emission bandshape turns out to be independent of the excitation wavelength, as highlighted by the corresponding excitation-emission maps reported in Figure 3.2(b). Interestingly, while the absorption bands are similar, the emission bands differ significantly among the three NGs. This suggests that the different functional groups primarily impact the low-energy emissive states, leaving the upper electronic states relatively unaffected.

In addition, beside the high homogeneity of the samples, the finely structured shapes of both

absorption and emission bands, coupled with the excitation independence of emission, suggest that, for each of them, the emission can be associated with a single transition and occurs from the lowest excited state, in compliance with Kasha's rule.

Using c-NG1 as a reference, a qualitative analysis of its emission band allows to identify a zero-phonon line at 457 nm and a dominant vibronic progression (457, 485 and 517 nm) with a spacing of approximately 1300 cm^{-1}, compatible with $C-C$ stretching modes. However, the presence of other maxima indicates the involvement of at least one more vibrational mode coupled to the emissive transition. A similar vibronic progression with a spacing of about 1300 cm^{-1} is also observed in the emission spectra of m-NG1 and c-Br-NG1, with zero phonon lines at 455 and 461 nm, respectively.

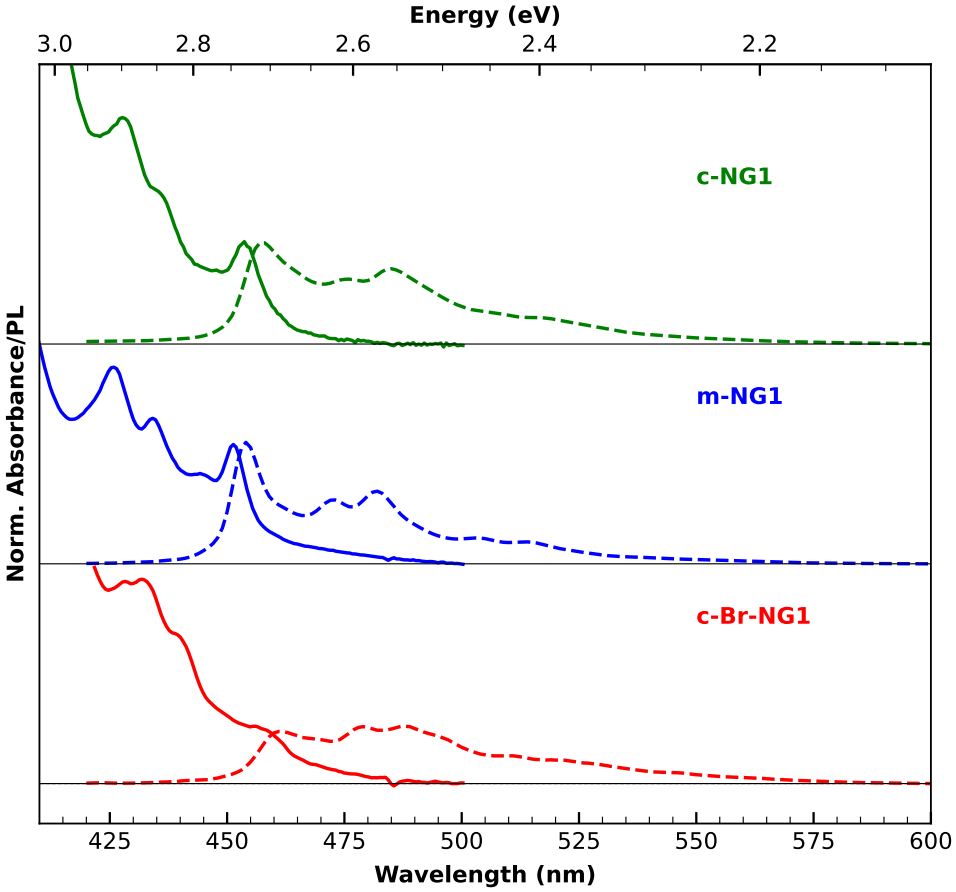

Figure 3.3: Comparison of α absorption bands (solid lines) and fluorescence spectra excited at 350 nm (dashed lines) for c-NG (in green), m-NG (blue) and c-Br-NG (red). [Adapted from [232]].

In addition to the three primary peaks that characterize the absorption spectrum of the NGs, as previously mentioned, there is an additional, very weak absorption in the 430-460 nm range. This absorption contribution becomes more discernible in more concentrated solutions ($\sim 10^{-5}$ M), as illustrated in Figure 3.3. For all the three distorted HBC-based NGs, this absorption

feature is attributed to the so-called α-band, which exhibits a low oscillator strength owing to the partially forbidden nature of such a lowest energy transition, similar to what is expected for similar aromatic molecules [167].

The different edge chemistry exerts a profound influence not only on the shape of the emission band but also on the emission quantum yield. The QY values are $= 2.1 \pm 0.2\%$, $5.2 \pm 0.4\%$ and $0.012 \pm 0.002\%$ for c-NG1, m-NG1 and c-Br-NG1, respectively. When considering c-NG1 as a reference, the substitution of oxygen with a CH_2 group in m-NG1, results in more than a two-fold increase in QY. Conversely, the presence of two bromine atoms in c-Br-NG1 results in a dramatic reduction of the QY by an order of magnitude. Thus, the tunability of both the shape and quantum yield of the emission is a clear indication that controlled edge functionalization of the distorted HBC-derivative core affects the emissive electronic state and relaxation pathways. In essence, while different edge chemistries do not have a significant impact on the main absorption band, they induce substantial modifications in the emission. This observation aligns with findings in the existing literature regarding the effect of various functionalizations on HBC with standard planar lattice [107, 176, 233, 234]. From this perspective, the presence of a heptagon ring appears not to significantly alter the steady-state optical response compared to planar analogues, as it still perfectly adheres to a Kasha-obeying behaviour. As will be illustrated in the following, Kasha-deviating behaviours can instead characterize NGs featuring a higher degree of structural distortion.

Time-resolved Emission

The significant changes of QY resulting from different edge chemistry imply that the relaxation pathways of the three NGs after photoexcitation are highly sensitive to the various functional groups. As expected, this is supported by the time-resolved emission measurements summarized in Figure 3.4. For each nanographene, the PL decay ($\lambda_{exc} = 350$ nm and monitored at the respective emission maximum) is shown at the top of the Figure 3.4, with panel (a) corresponding to c-NG1, (c) to m-NG1 and (e) to c-Br-NG1.

In the case of c-NG1 and m-NG1, the emission is characterized by a purely single exponential decay, with a lifetime τ of 3.5 and 16.7 ns, respectively. Since the change in lifetime is greater than that observed for the corresponding quantum yields, one might infer that the substitution of the oxygen atom with the CH_2 group not only reduces the non-radiative decay rate (k_{nr}), but also alters the radiative one (k_r). More quantitatively, based on the knowledge of QY and τ, under the assumption of negligible sub-nanosecond population losses it is possible to calculate $k_r = QY/\tau = 6 \times 10^6$ s^{-1} and $k_{nr} = (1 - QY)/\tau = 3 \times 10^8$ s^{-1} for c-NG1, while $k_r = 3 \times 10^6$ s^{-1} and $k_{nr} = 6 \times 10^7$ s^{-1} for m-NG1. The low values found for the radiative decay rates confirm the weakly allowed nature of the emissive transition. In addition, in the case of c-NG1, the polar nature of the $C = O$ bond is expected to favour a stronger structural relaxation in the excited state, resulting in a larger non-radiative decay rate [235, 236]. Unlike the PL decay of c-NG1 and m-NG1, the kinetic trace at 460 nm for c-Br-NG1 (Figure 3.4(e)) is substantially pulse-limited in the early stage, *i.e.*, the initial PL decay occurs on a timescale faster or comparable to the temporal resolution provided by the instrument response function (dashed black line).

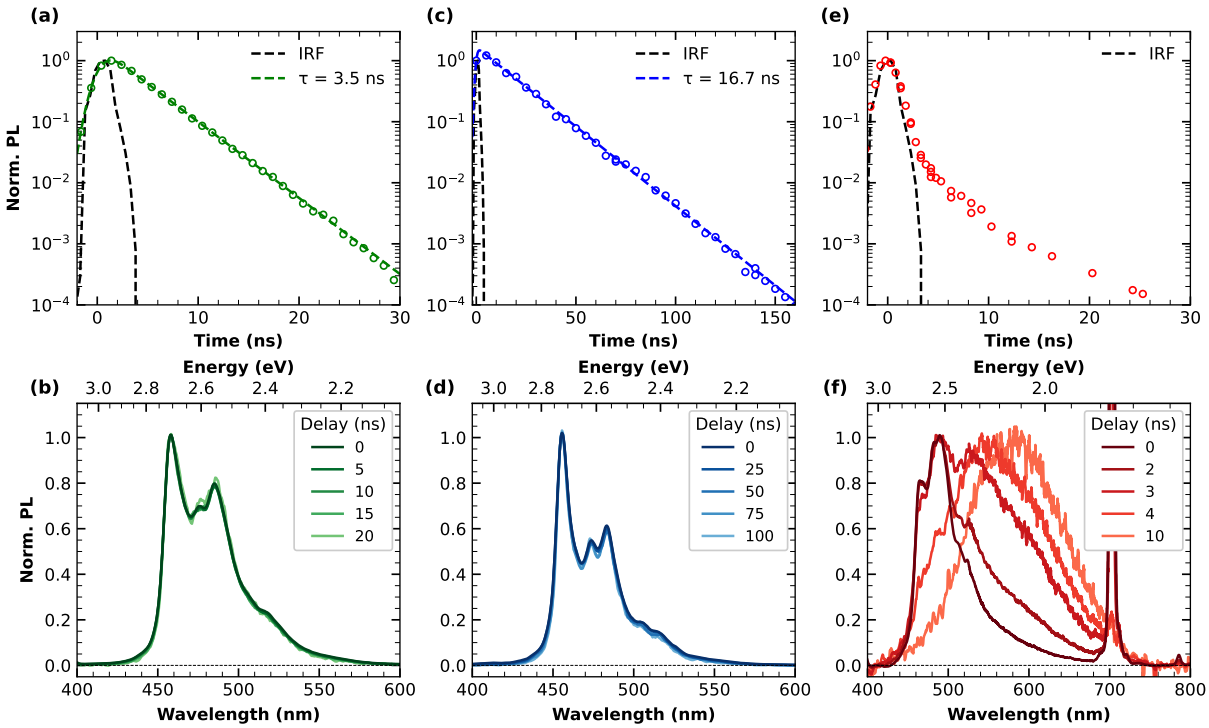

Figure 3.4: Top panels: normalized PL decay (acquired at $\lambda_{exc} = 350$ nm and $\lambda_{em} = 460$ nm) and respective least-squares fitting curves (dashed coloured lines) of (a) c-NG1, (c) m-NG1 and (e) c-Br-NG1 in dichloromethane. The dashed black lines refer to the Instrumental Response Function. In correspondence, in the bottom panels: normalized PL spectra of (b) c-NG1, (d) m-NG1 and (f) c-Br-NG1, acquired at different delays from photoexcitation. [Adapted from [232]].

In correspondence with each PL decay trace shown in the top panels, the bottom part of Figure 3.4 displays the normalized PL spectra acquired at different delays after photoexcitation with panels (b), (d) and (f), referring to c-NG1, m-NG1 and c-Br-NG1, respectively. As evident from panels (b) and (d), no spectral evolution with time is observed for c-NG1 and m-NG1. This confirms the synchronous mono-exponential decay of the entire emission band, indicating emission arises from a single electronic state. In contrast, panel (f) highlights the less trivial relaxation dynamics of c-Br-NG1. Initially, its emission spectrum at zero time delay resembles the steady-state PL (dashed red curve in Figure 3.2). However, over a few ns, a complete conversion of the emission to a broader, red-shifted and unstructured band peaking at ∼590 nm is observed. Since any sample inhomogeneity has been ruled out based on the steady-state characterization mentioned earlier, this dynamics can be modelled in terms of an efficient excited-state interconversion between emissive states, occurring on a timescale comparable to the temporal duration of the excitation pulse used in the setup. A direct comparison of the structures of c-NG1 and c-Br-NG1 suggests that this different behaviour may be attributed to the introduction of two bromine atoms, which likely promote a heavy atom effect [237, 238]. This results in an enhancement of the spin-orbit coupling, leading to an increased intersystem crossing rate from singlet state S_1 to triplet state T_1. Therefore, according to this interpretation, the PL should undergo a complete

conversion to a phosphorescence emission, characterized by a very low emission efficiency.

Ultrafast relaxation dynamics

Ultrafast pump-probe TA measurements help shedding light and fully reconstruct the optical photocycle of the three HBC derivative NGs. The results of these measurements are summarized in Figure 3.5, with the top panels showing the broadband spectral evolution, and the corresponding kinetic traces displayed in the bottom panels.

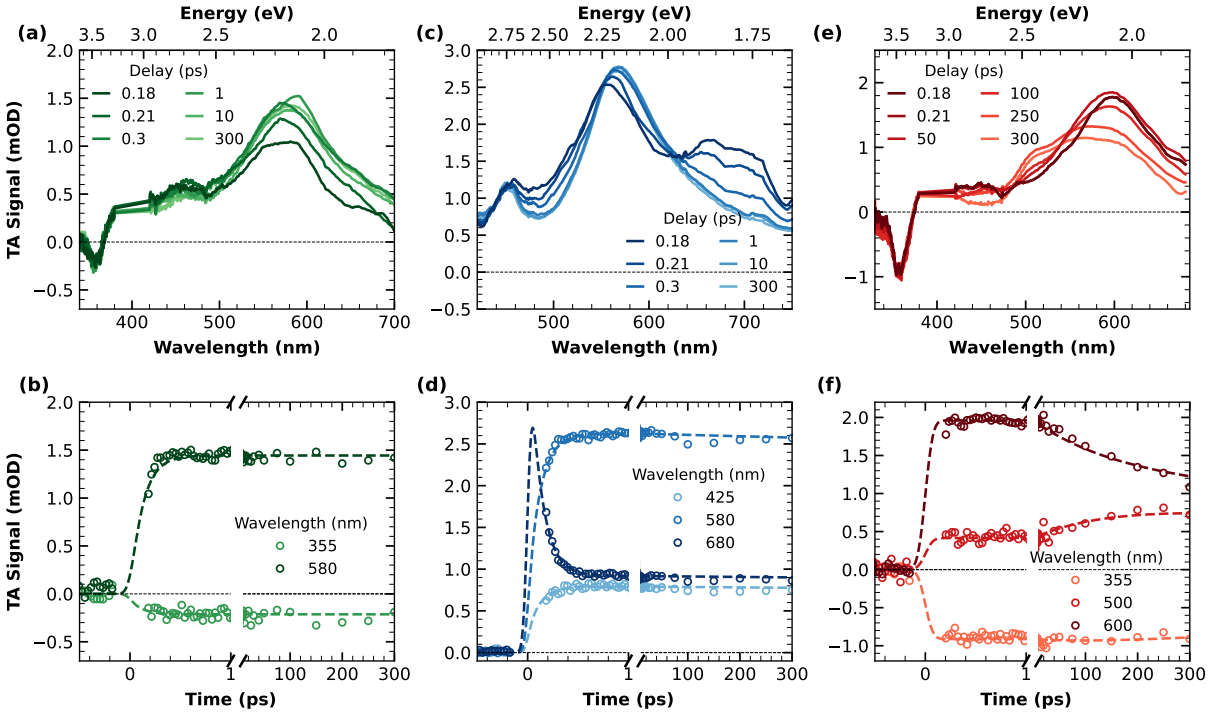

Figure 3.5: Top panels: TA spectra in dichloromethane solution of (a) c-NG1, (c) m-NG1 and (e) c-Br-NG1, acquired at different time delays from photoexcitation (λ_{exc} = 400 nm). Data around 400 nm have been removed because of pump scattering. Bottom panels: Corresponding TA kinetic traces and relative fitting curves cut at different probe wavelengths of (b) c-NG1, (d) m-NG1 and (f) c-Br-NG1. [Adapted from [232]].

The TA signal of c-NG1 (Figure 3.5(a)) consists of an extended ESA that dominates the entire spectral range, featuring a well-defined, unstructured band peaking at approximately 580 nm. Additionally, a negative component is clearly superimposed on the ESA in the region around 360 nm. Based on the steady-state absorption position, this negative contribution can be identified as a GSB. In comparison to the TA signal of planar HBC, the shape of the c-NG1 TA signal is not significantly dissimilar [107], albeit somewhat broader and less structured. The temporal evolution of the spectral shape of the TA signal is characterized by a very fast rise of the ESA, which is fully completed within the first 200 fs after photoexcitation. No additional dynamics are detected, as can also be appreciated from the kinetic traces reported in Figure 3.5(b). Also

from a temporal perspective, the results closely aligns with those documented for standard planar HBC [107], aspect which further corroborates the finding that the presence of a heptagon ring, despite causing distortion, does not significantly alter its molecular-like optical photocycle.

The broadband TA signal of m-NG1 is presented in Figure 3.5(c). Similar to c-NG1, the positive contribution between 400-750 nm arises from a broad ESA, mainly composed of a band in the 550-570 nm range and an additional structured band around 680 nm. The temporal evolution of the signal reveals an isosbestic point between the two ESA bands at ∼630 nm, indicating a transformation between the two ESA bands, compatible with an internal conversion relaxation. This transformation accounts for the decrease in the signal around 680 nm and the concurrent rise and redshift of the main ESA peak to 570 nm. As with c-NG1, apart from clear initial dynamics around the isosbetic point completed in less than 1 ps, no further temporal evolution is observed, as can be better seen in Figure 3.5(d).

Finally, the TA data of c-Br-NG1 are presented in the right part of Figure 3.5. From a spectral point of view, the TA signal closely resembles that found for c-NG1 (Figure 3.5.(a)), featuring a GSB peak at 360 nm and an initially broad ESA peaking at 600 nm. However, as expected, the TA signal undergoes different dynamic evolution. Specifically, a spectral change in the signal is recognizable around an isosbestic point at 550 nm, indicating a simultaneous decrease in the band at 600 nm and the emergence of an ESA contribution around 520 nm. The relatively long timescale (hundreds of ps) characterizing this dynamic, rules out the possibility of associating it with an internal conversion process as seen in c-NG1 and m-NG1, as well as any vibrational relaxation or solvation process, which typically occur on at least two order of magnitude smaller timescale [239, 240]. In addition, the kinetic trace cut a 355 nm and reported in Figure 3.5(f), reveals no GSB evolution, confirming that the described dynamics is not associated with a ground state recovery. Based on these observations, the ESA component at 520 nm may be interpreted as a triplet-triplet absorption $T_1 \rightarrow T_n$, which prgressively rises due to the concurrent population of T_1 from S_1 via an inter-system crossing channel. This assignation aligns with the existence of a triplet-triplet absorption band peaking around 500 nm, as previously reported for standard planar HBC [107]. Moreover, it is worth noting that this interpretation supports the assignment of the temporal evolution of PL previously described (Figure 3.4(e)-(f)) as a conversion of the emission to a phosphorescence.

A global wavelength-time multiexponential fit performed on the TA data after SVD (see Materials and Methods Chapter) allows to describe the entire spectral evolution of TA signals of the three HBC derivative NGs. The TA dynamics of c-NG1 can be modelled in terms of two DAS with respective time constants of $\tau_1 = 120 \pm 15$ fs and $\tau_2 > 1$ ns (shown in Figure 3.6(a)). The first DAS is associated with the fast rise of the ESA, most likely indicative of an internal conversion process, as the pump pulse at $\lambda = 400$ nm photoexcites an electronic state with higher energy than S_1. Such fast excited-state relaxations are commonly observed in photoexcited aromatic molecules, often characterized by the ultrafast population of S_1 state from higher-energy photoexcited states [241, 242]. DAS_2 is instead related to the decay of the overall signal, occurring on the ns-scale, which is consistent with the previously found fluorescence lifetime. For m-NG1, the TA data can be deconstructed into two DAS, reported in Figure 3.6(b), whose corresponding time constants of $\tau_1 = 120 \pm 10$ fs and $\tau_2 > 1$ ns, are identical to those found for c-NG1, suggesting

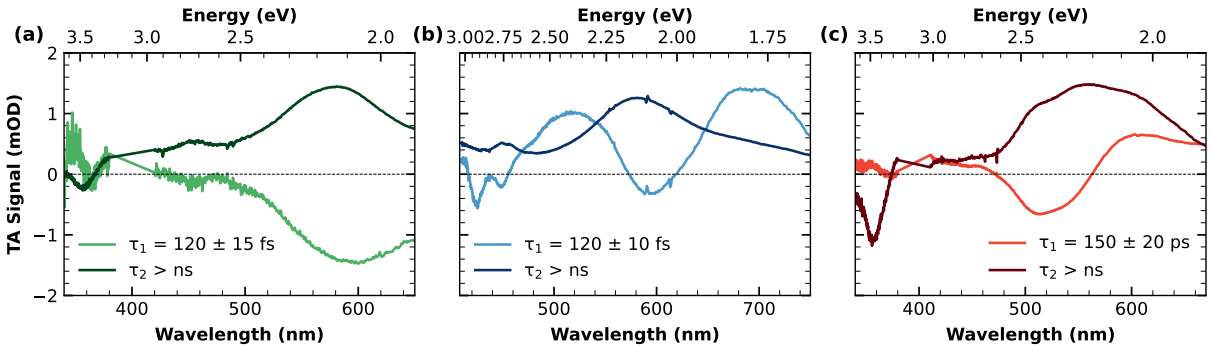

Figure 3.6: Decay associated spectra of (a) c-NG1, (b) m-NG1 and (c) c-Br-NG1. [Adapted from [232]].

a similar interpretation for both. The spectral-temporal decomposition of the TA data of c-Br-NG1 leads to two DAS with lifetimes of $\tau_1 = 150 \pm 20$ ps and $\tau_2 > 1$ ns (Figure 3.6(c)). Again, DAS_2 corresponds to the ns-ground state recovery, while DAS_1 is associated with the rise of a $T_1 \rightarrow T_n$ transition, pointing out the early stage of $S_1 \rightarrow T_1$ inter-system crossing.

Jablonski Diagram

A representation of the Jablonski diagram of the three HBC derivative NGs, drafted based on of the comprehensive optical characterization results presented earlier, is depicted in Figure 3.7. This diagram provide a schematic overview of the relaxation pathways following photoexcitation. As described previously, both c-NG1 and m-NG1 follow nearly identical Kasha-compliant deactivation pathways, involving internal conversion to the first singlet excited state S_1, which occurs within approximately 120 fs, followed by a ground state recovery in 3.5 and 16.7 ns for

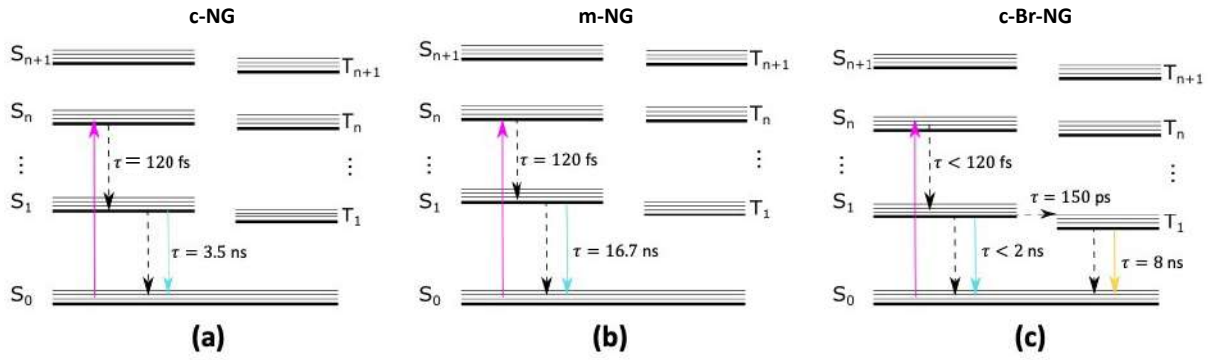

Figure 3.7: Schematic illustration of the excited-state electronic deactivation pathways and associated timescales of (a) c-NG1, (b) m-NG1 and (c) c-Br-NG1. [Adapted from [232]].

c-NG1 and m-NG1, respectively. The two distinct ns-timescales account for the different impacts

of oxygen and methylene group on radiative and non-radiative decay rates. In contrast, the introduction of two peripheral bromine atoms in c-Br-NG1 results in more significant alterations in relaxation dynamics. Notably, this alteration is primarily characterized by an inter-system crossing occurring on the hundred ps scale. This process rapidly depopulates the S_1 state and leads to a substantial reduction in the singlet emission QY. Thus, Bromine atoms produce a critical change in the relaxation dynamics compared to c-NG1 and m-NG1.

3.2 c-NG2

c-NG2 possesses a graphenic backbone approximately 2 nm in length and 1 nm in width, characterized by edge defects. In addition to a saddle-shaped ketone unit, these edge defects include a [5]carbohelicene moiety, which induces more pronounced distortion in its otherwise planar lattice. Probably due to this increased structural complexity, c-NG2 exhibits highly unusual features that notably diverge from the archetypal behaviour observed, for instance, in the photophysics of the three distorted HBC-derivative NGs belonging to the NG1 family, which have been thoroughly investigated in the previous section.

Standard Optical Characteristics

Also in the case of the distorted c-NG2, the absorption spectrum (solid curve in Figure 3.8(a)) exhibits a structured shape, resulting from a progression of several main subpeaks at 375, 395, 443, 474 and 492 nm. This richness of substructures arises from the overlap of various electronic transition and the strong coupling between electronic and vibrational transitions. The lowest

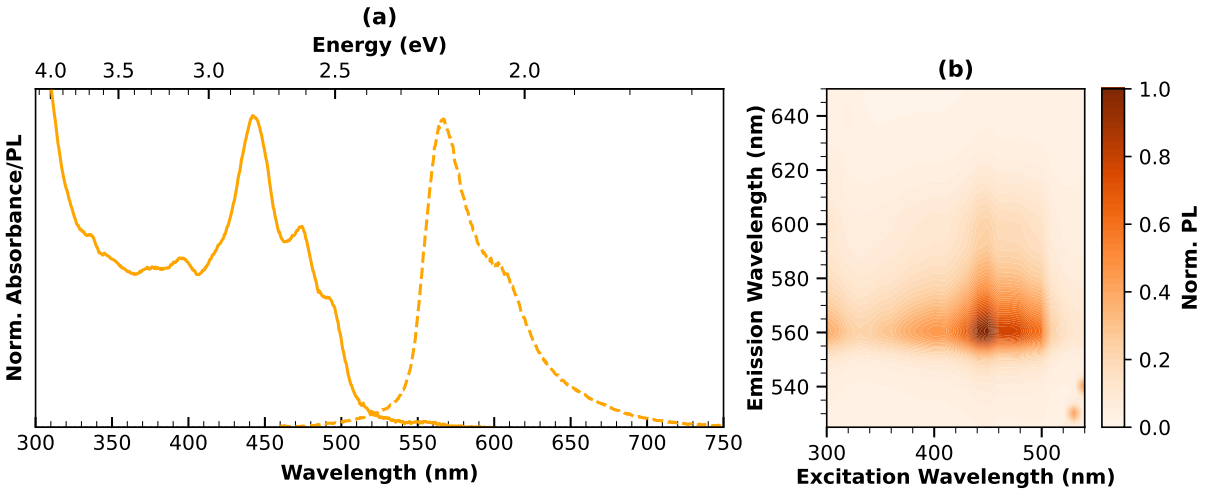

Figure 3.8: (a) Normalized absorption (solid lines) and photoluminescence (dashed lines) of c-NG2 in dichloromethane solutions. (b) Excitation-emission map of c-NG2. [Adapted from [221]].

energy transition is observed at 555 nm and, similar to other NGs, it has an oscillator strength about two orders of magnitude smaller than that of the main transition. The PL spectrum of

c-NG2 (dashed curve) also displays a structured shape with distinct subpeaks at 560 and 600 nm. The energy spacing of approximately 1200 cm^{-1} between these subpeaks is compatible with strong coupling of the electronic transition with $C-C$ stretching modes. The excitation-emission map of Figure 3.8(b) highlights that the emission is independent of the excitation wavelength, confirming that the emission is associated with a single chromophore. The emission QY of c-NG2 has been estimated to be $13 \pm 2\%$, which is almost six times greater than the QY of its smaller counterpart c-NG1. Figure 3.9 displays the kinetic trace of the PL decay of c-NG2, evaluated at

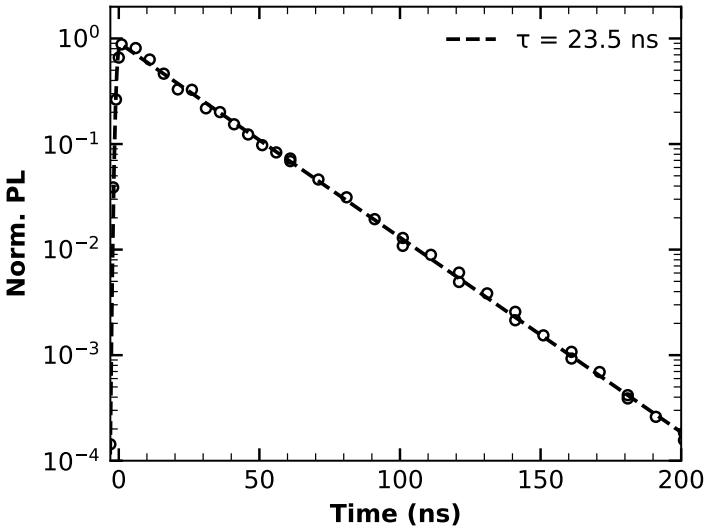

Figure 3.9: Normalized fluorescence decay trace and respective least-squares fitting curve of dichloromethane solution of c-NG2 at $\lambda_{exc} = 440$ nm and $\lambda_{em} = 560$nm. [Adapted from [221]].

an emission wavelength of 560 nm (corresponding to the main peak). The fitted emission lifetime of c-NG2 $\tau = 23.5 \pm 0.3$ ns, is notably longer than that of typical aromatic molecular dyes [167, 235, 243] and the HBC derivative NGs described in the previous section. From the knowledge of PL QY and lifetime, and assuming no sub-nanosecond depopulation of the excited state (as discussed below), the radiative and non-radiative decay rates can be determined: $k_r = 6 \times 10^6$ s^{-1} and $k_{nr} = 4 \times 10^7$ s^{-1}. The relatively small value of k_r aligns with the weakly allowed nature of the emissive electronic transitions. Therefore, in terms of its steady-state features, c-NG2 still exhibits a purely molecular-like behaviour, not too dissimilar from those of typical aromatic molecules and the HBC derivative NGs. However, a closer examination of the relaxation dynamics following photoexcitation reveals the presence of some peculiar photophysical properties that will be discussed hereafter.

Ultraslow spectral evolution of PL

As can be seen from Figure 3.10, the PL band undergoes a slight, but appreciable, gradual change in shape during the first few ns after photoexcitation, primarily manifesting as spectral narrowing. Considering the larger size and, more importantly, the structural complexity introduced by the

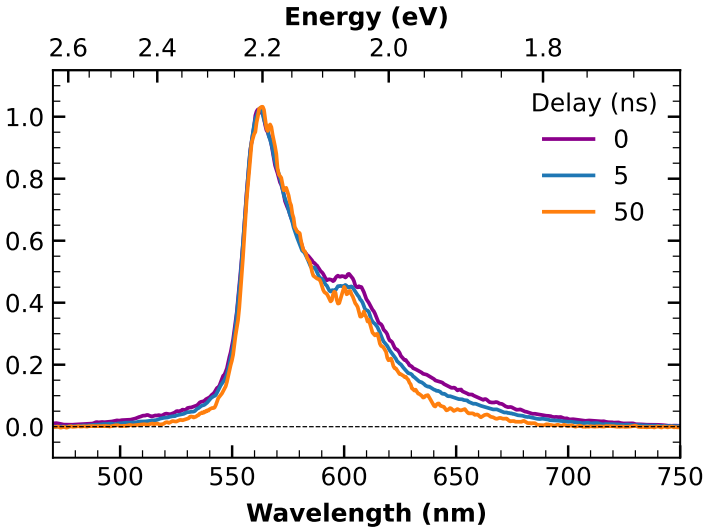

Figure 3.10: Normalized photoluminescence spectra of c-NG2 (λ_{exc} = 440 nm) acquired at different delays after photoexcitation. [Adapted from [221]].

helicene moiety, this unusual behaviour can tentatively attributed to a slow excited-state interconversion between diasteroisomers, occurring on a timescale competitive with the fluorescence lifetime, and already reported for similar NGs [244].

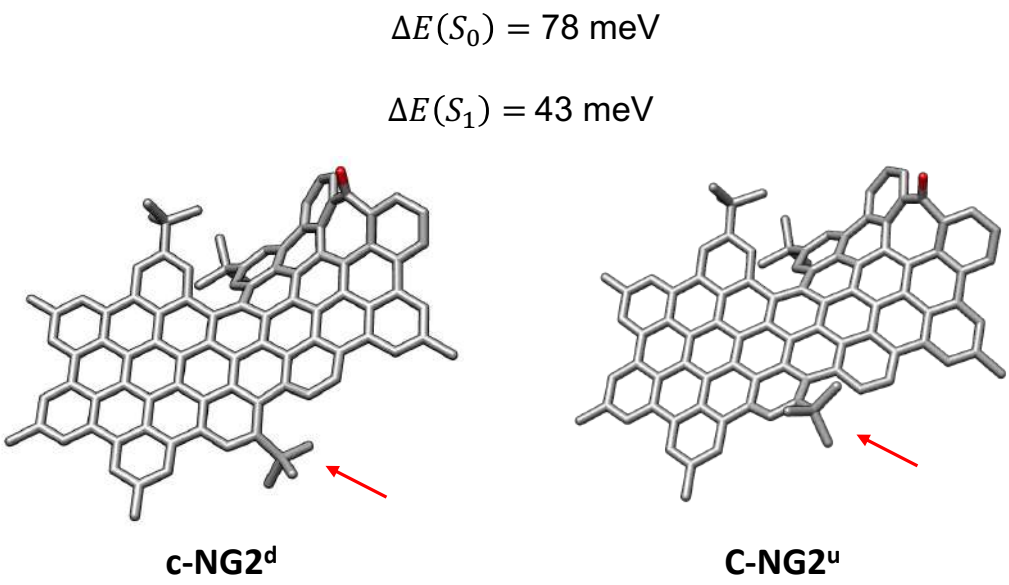

Figure 3.11: Conformer with ^{t}Bu pointing 'down' (c-NG2^d), conformer with ^{t}Bu pointing 'up' (c-NG2^u), and the energy difference between the two conformers in the S_0 and S_1 states. [Adapted from [221]].

Indeed, earlier theoretical calculations [222] have revealed that the most stable diasterioiso-

mer of c-NG2 can exist in two forms: one with the ^{t}Bu group oriented upwards (c-NG2^{u}) and the other with it oriented downwards (c-NG2^{d}) relative to the helicene unit in the molecular skeleton (see Figure 3.11). Among these two forms, c-NG2^{u} is more stable in both the S_0 and S_1 states. Further theoretical calculation performed through the collaboration of research group of Prof. A. Campaña, revealed that, while their energy difference is relatively small in both states ($\Delta E(S_0) = 78$ meV and $\Delta E(S_1) = 43$ meV), it decreases nearly twofold when c-NG2 populates the excited S_1 state. In a broader context, the conformational landscape of c-NG2 is expected to be richer, with various structural motifs having similar energies. These motifs could be relevant to the excited-state evolution of c-NG2, allowing for interconversion between conformers within the long lifetime of c-NG2. Assuming even a slight difference in the fluorescence bandshape of these possible conformers, such a slow interconversion could be at least one of the main causes of the emission bandshape dynamics in Figure 3.9(b), occurring on the nanosecond fluorescence timescale. Moreover, related with this ns spectral evolution, an interesting 'memory effect' with

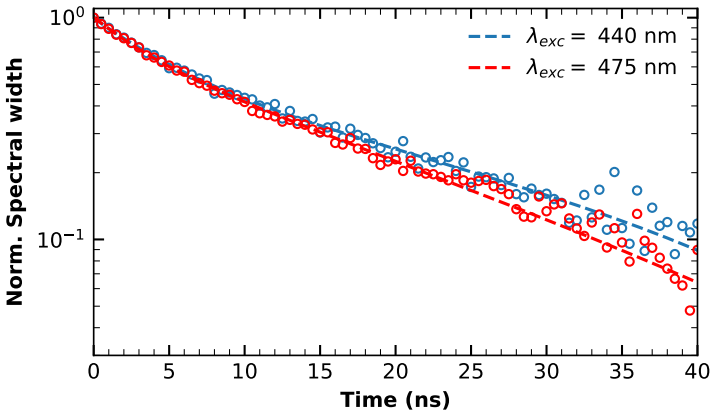

Figure 3.12: Normalized spectral width (σ) narrowing of c-NG2 PL *vs* time excited at 440 nm (blue) and 475 nm (red). The corresponding fitting functions (bi-exponential decay) are reported in dashed lines. The normalization has been obtained by reporting the data as $(\sigma(t) - \sigma(\infty))/(\sigma(0) - \sigma(\infty))$. [Adapted from [221]].

respect to the initial excitation wavelength has also been observed. Figure 3.12 shows the comparison between the spectral widths (σ) of PL band of c-NG2 *vs* time, normalized according to

$$\sigma_{norm}(t) = \frac{\sigma(t) - \sigma(\infty)}{\sigma(0) - \sigma(\infty)} \tag{3.1}$$

It is can be seen that the weighted average timescale of this spectral evolution, as extracted by a bi-exponential fit, is found to be 19 ns when c-NG2 is excited at 440 nm, and 12 ns for excitation at 475 nm. This memory effect is most likely attributable to the distinct nature of the excited states populated at different wavelengths, which in turn influences the pathway through which c-NG2 undergoes the interconversion between the two conformers [245]. Overall, the observation of such an ultraslow evolution of the fluorescence bandshape on nanosecond timescale, which also

retains memory of the initial excitation wavelength, can be seen as a deviation from a simple Kasha-like photophysical response. This deviation probably arises from the huge complexity of the conformational landscape of the c-NG2, which is significantly higher than that of typical small fluorescent molecular systems [167, 235, 243] as well as the distorted HBC derivative NGs presented in the previous section.

Delayed Fluorescence

The spectral evolution of the PL on the ns timescale is not the only non-trivial feature exhibited by c-NG2. Upon closer examination, as depicted in Figure 3.13, in addition to the above discussed "prompt" fluorescence (PF, fitted in red), a second very weak and slower PL decay component (fitted in green) has been found. This latter, which has not been detected in the HBC derivative NGs, is characterized by a lifetime of about 400 ns. Most remarkably, as shown in the inset panel, the spectral shape of the PF component, isolated by gating the emission signal acquisition between 10 ns and 200 ns after photoexcitation, perfectly matches that of the slower component, isolated by gating the emission between 1 µs and 2 µs. This match, without even the slightest redshift, suggests that the slower component may be associated with delayed fluorescence (DF), *i.e.* a fluorescence emission characterized by a longer lifetime, as it occurs after the re-population of the emissive singlet state S_1 from the lowest triplet state T_1 *via* a reverse intersystem crossing $T_1 \rightarrow S_1$ [246, 247]. It is worth noting that measurements in Figure 3.13 have been conducted on

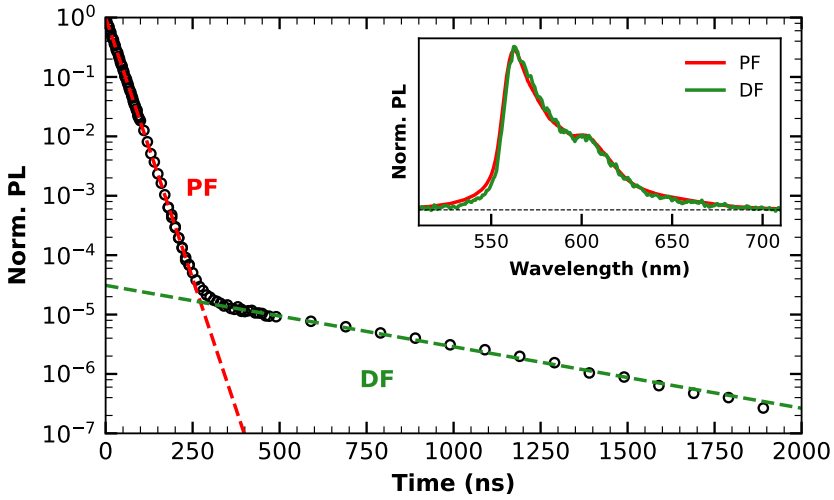

Figure 3.13: Normalized decay of c-NG2 PL (λ_{exc} = 440 nm and λ_{em} = 560 nm), registered over a wider temporal window. Beside the fast, prompt fluorescence (PF), an additional slower, delayed fluorescence (DF) is detected. In the inset the comparison of the spectral shapes of the PF (red) and DF(green). [Adapted from [221]].

an air equilibrated solution, subjected to no degassing procedure before or during measurements. As it is well-known, the triplet excited states are very efficiently quenched by oxygen, [248, 249] resulting in a full suppression of DF in aerated solutions, for which only PF is usually observable.

Consistently, the relative amplitude of the DF to the PF from Figure 3.13 is very small (less than 10^{-4}), accounting for the low probability of occurrence of such a process.

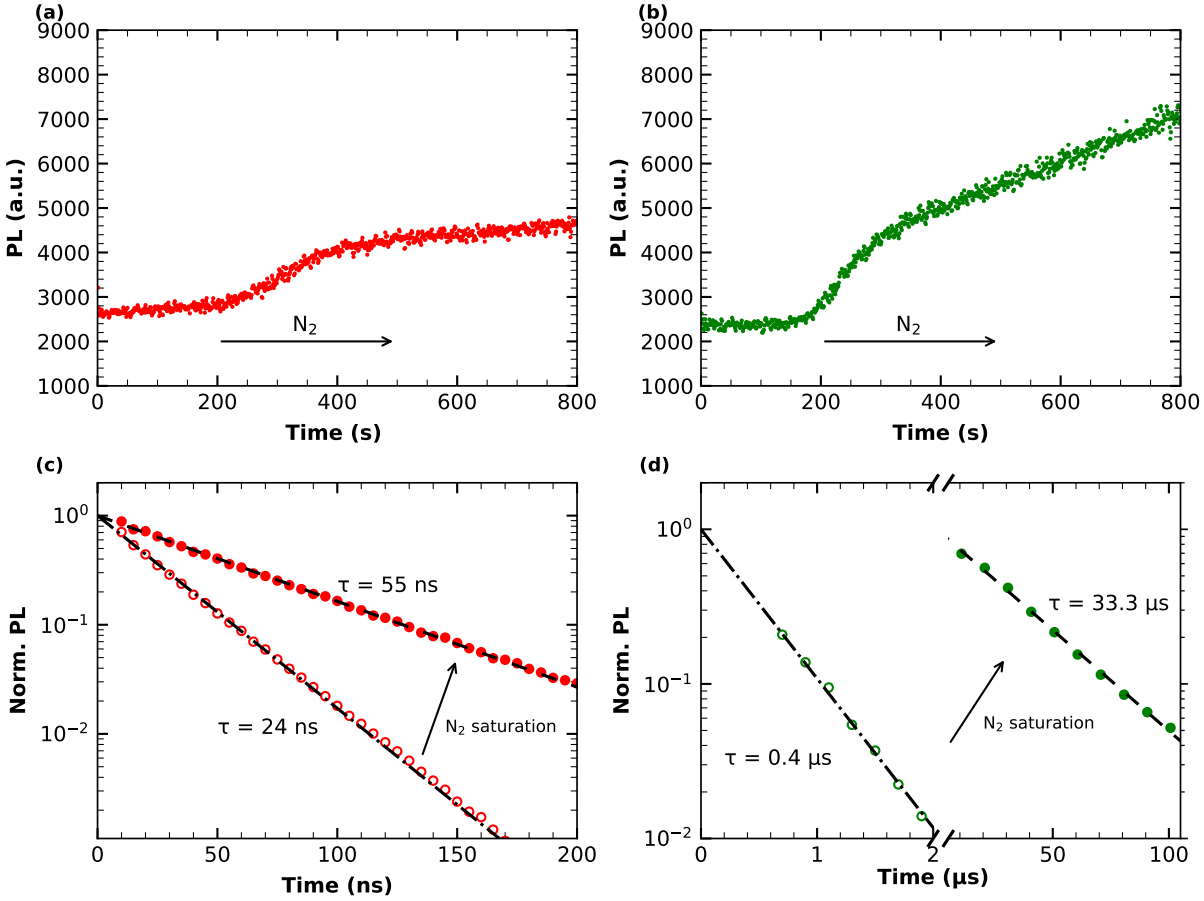

Figure 3.14: (a)-(b) Temporal evolution of (a) prompt fluorescence and (b) delayed fluorescence intensities during the course of nitrogen bubbling of a chlorobenzene solution of c-NG2 (started at about 150 s). (c)-(d): Comparison of excited-state emission decay traces of c-NG2 prompt fluorescence in standard aerated condition (empty circles) and in nitrogen saturated conditions (full circles) of c-NG2 (c) prompt and (d) delayed fluorescence. [Adapted from [221]].

On these grounds, further investigations have been conducted to better understand the origin of delayed fluorescence. Panel (a) and (b) of Figure 3.14 highlight the different responses to nitrogen bubbling, respectively, in the PF and DF intensity of c-NG2. In both cases, an increase in the signal intensity is detected under the same nitrogen flow rate (starting from about 150 s). Nevertheless, the prompt fluorescence component quickly reaches a saturation regime, while the increase of the DF signal is greater, slower, and does not approach a saturation regime within the same time interval. Complementarily, panel (c) and (d) reveal the modification of the PF and DF decay kinetics, respectively, as observed between standard (circles) and nitrogen saturated conditions (dots). After deoxygenation of solution by continuously nitrogen bubbling, the prompt fluorescence lifetime approximately doubles from 24 ns to 55 ns (Figure 3.14(c)). However, under the same nitrogen-saturated conditions, oxygen removal has a more dramatic

effect on the slow emission component: its lifetime increases more than 70 times, from 0.4 µs to 33.3 µs (Figure 3.14). Such a higher sensitivity of the slow emission component to oxygen, compared to the fast one, provides unequivocal evidence of the involvement of a triplet state, even though radiative transition does not originate directly from it.

To discriminate among the various reverse inter-system crossing mechanisms [247] that may be responsible for repopulating S_1 from T_1, the dependence of intensity of PF and DF on photoexcitation intensity under standard aerated conditions has been investigated. Indeed, DF can often originate from a unimolecular thermally-activated process that converts a triplet exciton into a singlet exciton *via* inter-system crossing ($T_1 \rightarrow S_1$), generally favoured by a molecular architecture containing electron-rich and electron-deficient units connected *via* large dihedral angles to reduce singlet-triplet energy difference [250, 251]. However, DF can also result from a bimolecular Triplet-Triplet annihilation (TTA) process, where two triplet excitons combine to form a singlet exciton ($T_1 + T_1 \rightarrow S_1 + S_0$). For energy conservation in this process, it is required that $E(2T_1) > E(S_1)$, as found for some PAHs, occasionally with heterocyclic units [252]. For the sake of completeness, other DF processes that might be mentioned include Singlet Oxygen Feedback Delayed Fluorescence, although it is less common and has received comparatively much fewer mentions in the existing literature [247].

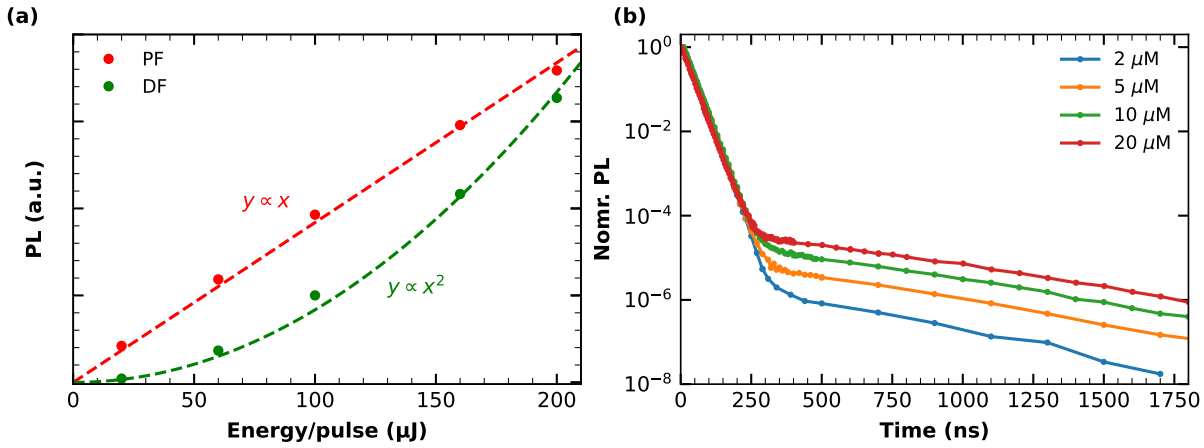

Figure 3.15: (a) Dependence of prompt (in red) and delayed (in green) fluorescence of c-NG2 on excitation intensity. (b) Comparison of time resolved PL curves collected from chlorobenzene solutions of c-NG2 at different concentrations. All the PL data reported in this Figure have been collected at $\lambda_{exc} = 440$ nm and $\lambda_{em} = 560$ nm. [Adapted from [221]].

As shown in Figure 3.15(a), the PF component displays a linear dependence on excitation intensity at 440 nm (in red), indicating linear absorption within the investigated interval and remaining thus far from the saturation regime. In contrast, the DF intensity scales quadratically with the light absorption rate, as expected for bimolecular collisional deactivation processes. This strongly suggests that the slow emission component of c-NG2 can be attributed to a TTA DF mechanism. In a complementary way, the effect of c-NG2 concentration, assessed by the time-resolved PL measurements in Figure 3.15(b), further supports the collision-mediated nature of the DF process. Indeed, increasing the concentration of NG results in an enhancement in the

relative amplitude of DF with respect to the prompt one, as expected for a TTA mechanism. In contrast, a DF due to a thermal mechanism would not depend on the second power of excitation intensity or on the concentration [246, 247, 253].

From an applicative perspective, both the design of new materials capable of delayed fluorescence and the theoretical understanding of its fundamental aspects have recently sparked an intense debate in literature [254, 255]. Indeed, upconversion of triplet states into emissive singlet excited states holds great appeal for optoelectronic applications [254, 256]. TADF has been reported in several nanographenes that have been strategically engineered, often through Boron or Nitrogen doping [250, 255]. Notably, according to literature, c-NG2 represents the first nanographene with an all-carbon core that exhibits a TTA DF. Although the efficiency of TTA DF in the present case remains too low for direct applications, these results open the door to the possibility of harnessing distorted graphene molecules for TTA DF once suitable strategies are developed to enhance the intensity of delayed fluorescence.

Finally, from a more fundamental point of view, one might wondering why delayed fluorescence is missing in c-NG1, despite it representing the smaller NG with the most similar structure to c-NG2. The absence of DF may be associated with less efficient population of the triplet state T_1 of c-NG1, as the intersystem crossing has to compete with the shorter lifetime of S_1 (3.5 ns), which is an order of magnitude smaller than the one of NG2 (23.5 ns).

Ultrafast relaxation dynamics

TA measurements reveal further uncommon features in the optical photocycle of c-NG2. The TA signal shape, shown in Figure 3.16(a), appears quite structured. Clear GSB peaks are observed at approximately 450 and 500 nm, as confirmed by the optimal matching of their shapes and spectral positions with the inverted steady-state absorption. The lack of a perfect spectral matching over the whole steady-state absorption region is ascribed to an overlaying positive ESA, peaking at 470 nm. Unlike the smaller HBC derivative NGs described before, the early-stage relaxation dynamics of c-NG2 exhibit significant differences, primarily characterized by pronounced spectral changes lasting up to a few ps.

The most prominent feature is the rise the ESA peak at 470 nm accompanied by a reduction in the broad ESA contribution at $\lambda > 640$ nm, as depicted in the kinetic traces of Figure 3.16(b) extracted at representative wavelengths. A global change of the shape of the TA signal affects the spectrum in the 500–700 nm region, highlighted by an isosbestic point at approximately 620 nm. These changes persist for several ps after photoexcitation. Thereafter, the entire signal is almost constant for several hundred ps.

Through a global fitting procedure, the TA data can be spectrally decomposed into three *DAS* with lifetimes of $\tau_1 = 180$ fs, $\tau_2 = 8.8$ ps, and $\tau_3 > 1$ ns, shown in Figure 3.17. The third component corresponds to the ns depopulation of the lowest energy singlet excited state. In contrast, interpreting the first two timescales, which govern the initial relaxation dynamics dominated by the 470 nm ESA rise, is less straightforward. Since the 400 nm excitation is expected to initially populate a higher electronic state than the one responsible for emission,

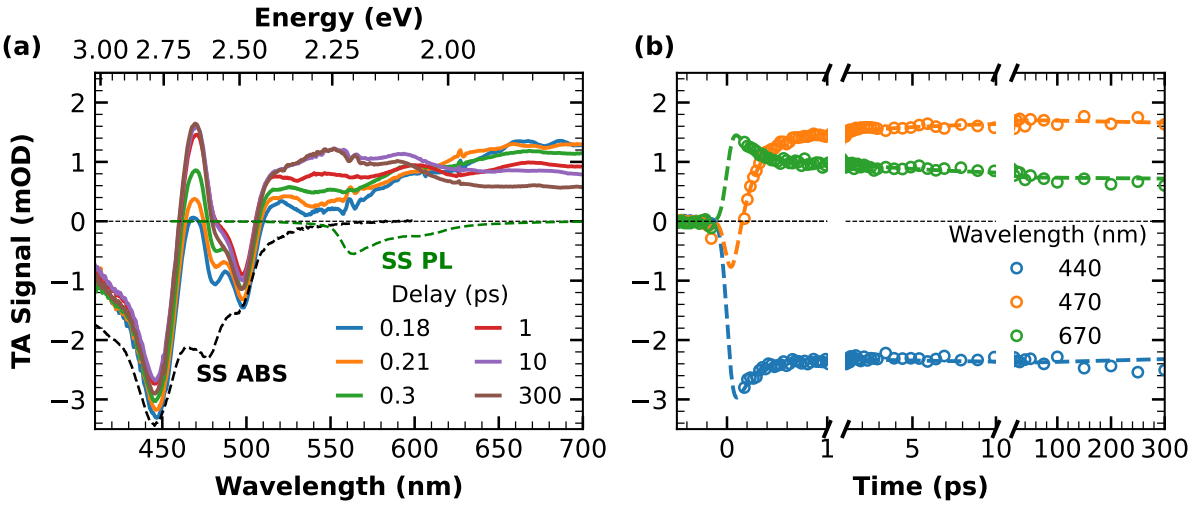

Figure 3.16: (a) TA spectra of chlorobenzene solution of c-NG2 at different time delays from photoexcitation, with the respective steady-state absorption and photoluminescence spectra. (b) TA kinetic traces and relative fitting curves taken at different probe wavelengths. The reported TA data have been collected on a c-NG2 chlorobenzene solution with $\lambda_{exc} = 400$ nm. [Adapted from [221]].

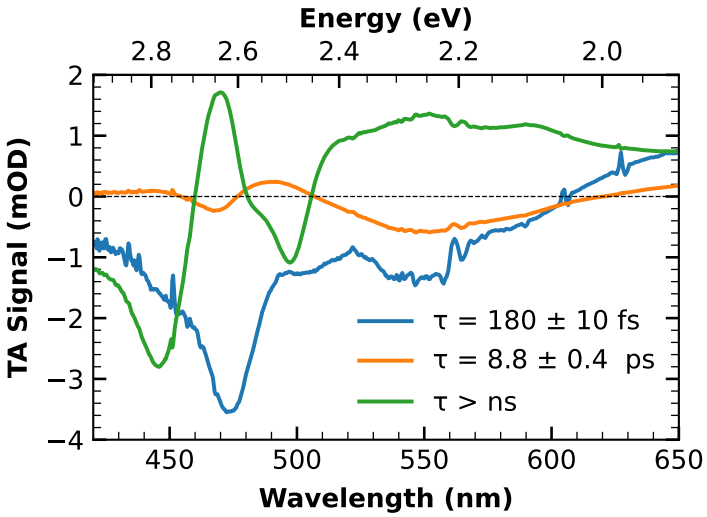

Figure 3.17: Decay Associated Spectra decomposition of TA spectra of c-NG2 ($\lambda_{exc} = 400$ nm) after SVD analysis with corresponding lifetimes. [Adapted from [221]].

one might attribute the early-stage dynamics to internal conversion to the final emissive state. However, such an attribution appears unlikely, as these relaxations persist for several ps, whereas typical time scale for internal conversions in aromatic molecules are on the order of 100 fs and less [242, 257, 258], as also observed in the previous reported NGs.

More to the point, TA measurements performed at a lower excitation energy (510 nm) show

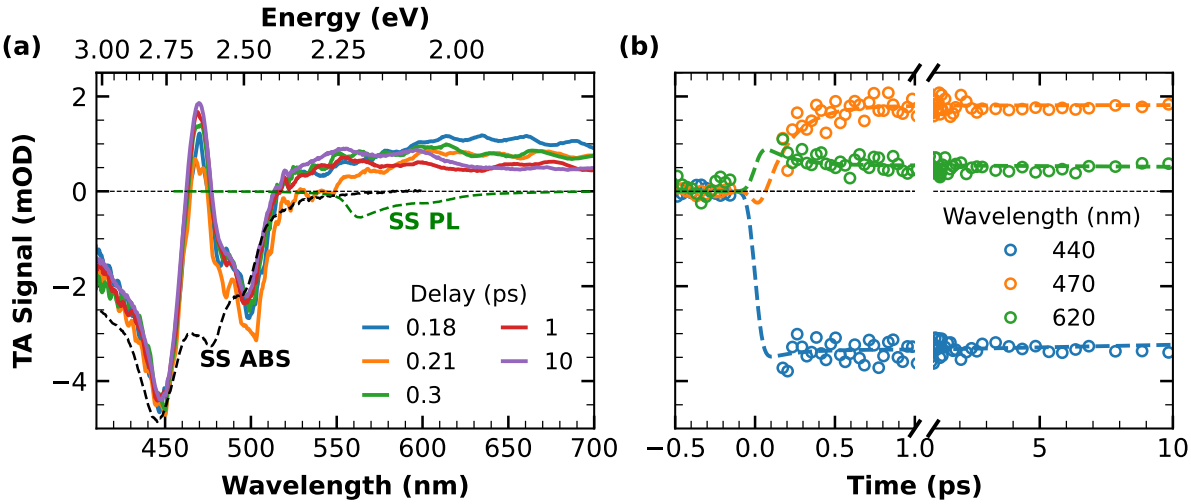

Figure 3.18: (a) TA spectra of chlorobenzene solution of c-NG2 at different time delays from photoexcitation, with the respective steady-state absorption and photoluminescence spectra. (b) TA kinetic traces and relative fitting curves taken at different probe wavelengths. The reported TA data have been collected on a c-NG2 dichloromethane solution with $\lambda_{exc} = 510$ nm. [Adapted from [221]].

the same initial relaxation dynamics (see Figure 3.18). This rules out the possibility of attributing this process to internal conversion.

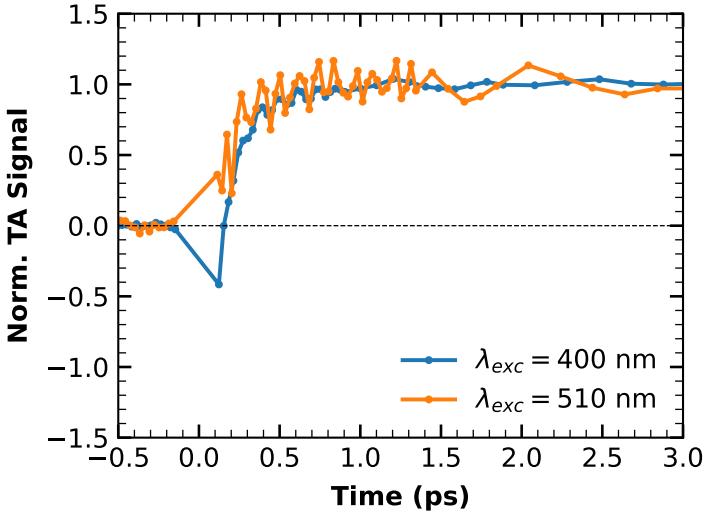

Figure 3.19: Comparison of the normalized TA signal of c-NG2 at the probe wavelength of 470 nm acquired in dichloromethane (blue) and chlorobenzene (orange) solution. [Adapted from [221]].

Furthermore, these dynamics remain unaffected by repeating the measurements in a solvent of different polarity (see Figure 3.19), eliminating solvent-mediated relaxation as a likely cause.

Instead, given the large and distorted structure of c-NG2, these relaxations likely reflect structural rearrangements occurring in the lowest excited state, consistent with previous findings in similar nanosystems [239, 259], and in line with the results from the previously reported nanosecond-resolved fluorescence studies.

Independently of the early-stage dynamics, another very interesting and rather unusual aspect of the TA results emerges by a closer analysis of the spectra in the tens to hundreds of picosecond time range. In fact, the spectra acquired at different pump wavelength exhibit different shapes even after hundreds of picoseconds, as shown in Figure 3.20. Once again, this can be considered as a Kasha-not-obeying "memory effect" of c-NG2, similar to what has been observed in Figure 3.12. Apparently, the relaxation cascades of c-NG2 from the initially excited state are slow enough for the spectroscopic observables to keep memory of the initial excitation energy throughout the whole femtosecond and nanosecond photocycle.

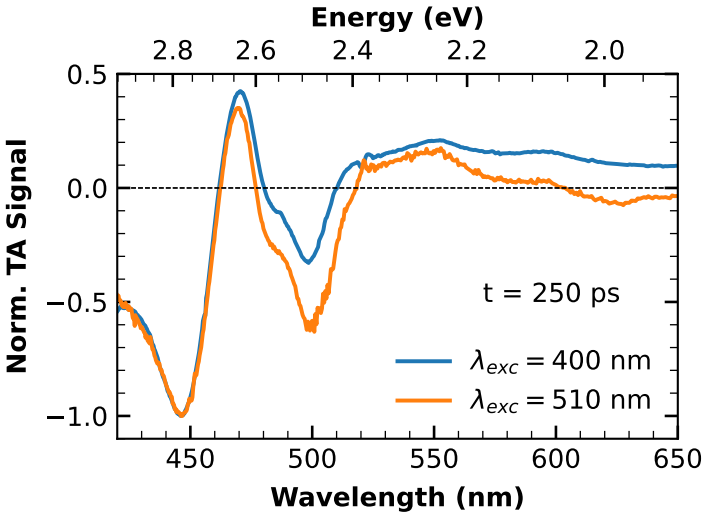

Figure 3.20: Comparison of TA spectra of c-NG2 at a time delay of 250 ps excited at 400 nm (blue) and 510 nm (orange). [Adapted from [221]].

3.3 NG3

The last nanographene presented in this chapter differs from the others because it posses a purely hexagonal network without any heptagon rings in its structure. Additionally, it is the largest one, as it is formed by the fusion of three HBC units, giving it a ribbon shaped structure.

Steady-State properties

As expected, due to its larger π-conjugation, the absorption spectrum of NG3 (Figure 3.21) covers a wider spectral range, extending over almost the entire visible range and, also in this case, its structured shape makes evident the identification of several transitions. NG3 features a very

strong orange photoluminescence (QY= 65 ± 5%), whose spectral shape (orange curve) displays a single and distinct vibronic progression coupled to the emissive electronic transition. Considering

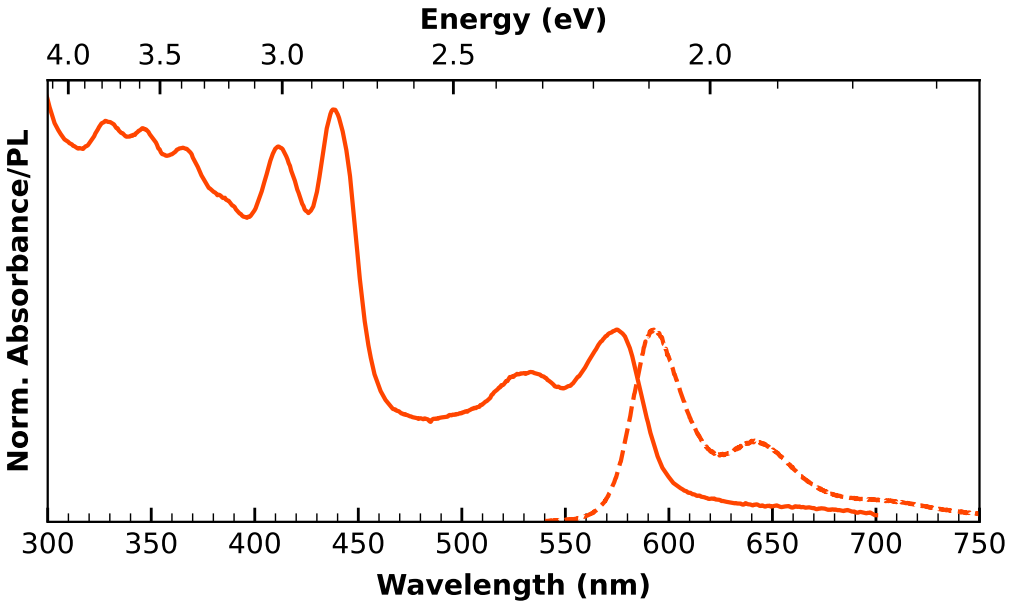

Figure 3.21: Normalized absorption (solid lines) and photoluminescence (dashed lines) of NG3 in chlorobenzene.

the mirror symmetry [96] between the emission and absorption spectra, it is possible to infer that the two lowest energy absorption peaks at 534, 575 nm (∼1330 cm^{-1} spacing) are associated with distinct transitions to different vibrational levels within the first excited electronic state S_1. Similarly, the absorption peaks at about 412 and 438 nm (∼1440 cm^{-1} spacing) are likely associated with different vibrational transitions toward the second excited electronic state S_2. The small absorption-emission Stokes-Shift of ∼530 cm^{-1} is in agreement with the high quantum yield value, suggesting very weak vibrational relaxation in the excited state.

In compliance with Kasha's rule, the same PL shape is observed regardless of excitation wavelength. The PL spectrum can be well-fitted by a Franck-Condon progression [260] (see Figure 3.22) with a zero-phonon line located at 595 nm (2.08 eV), a spacing of ∼1240 cm^{-1} (0.15 eV) compatible with ring breathing modes, and a Huang-Rhys factor $S = 0.6$.

All these aspects contribute to associating a purely molecular behaviour with NG3, which is further corroborated by the mono-exponential decay of the PL band (lifetime $\tau = 3.4 \pm 0.2$ ns) displayed in Figure 3.23(a). Fluorescence decay occurs in the absence of any time-dependent spectral change of the emission bandshape, confirming the existence of a single molecular-like transition, as can be appreciated from Figure 3.23(b), where the normalized emission spectra acquired by gating the PL at different delays from photoexcitation are shown. From the combined knowledge of the emission quantum yield and lifetime it is possible to calculate the radiative and non-radiative decay rates of NG which are $k_r = 1.9 \times 10^8$ s^{-1} and $k_{nr} = 1.0 \times 10^8$ s^{-1}, respectively.

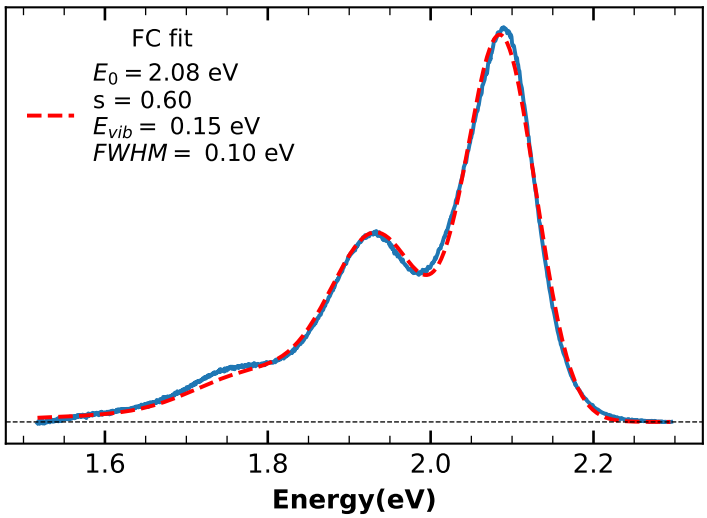

Figure 3.22: Franck-Condon Vibronic Progression fit of PL spectrum of NG3 solution in chlorobenzene.

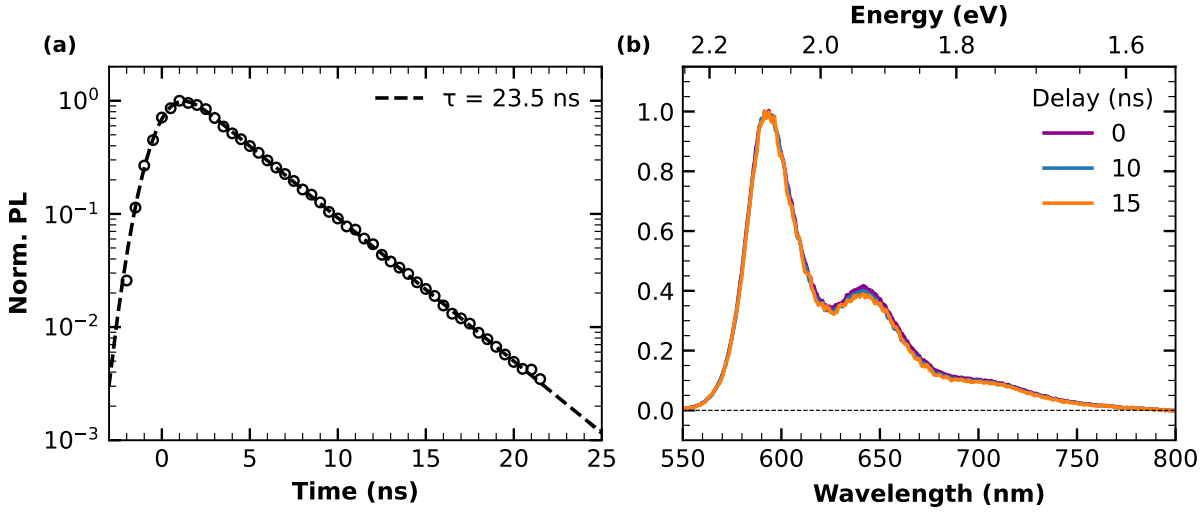

Figure 3.23: (a) Normalized fluorescence decay trace and respective least-squares fitting curve of chlorobenzene solution of NG3 at $\lambda_{exc} = 440$ nm and $\lambda_{em} = 590$nm. (b) Normalized photoluminescence spectra of NG3 ($\lambda_{exc} = 440$ nm) acquired at different delays after photoexcitation.

Transient Absorption Measurements

Figure 3.24 shows the shape of the TA signal of the ribbon-shaped NG3 obtained with a 400 nm pump excitation. According to steady-state characteristics, the spectral shape of the TA signal also results to be quite structured (panel (a)). Therefore, identifying the main peaks characterizing the TA signal can be easily achieved by comparing it to the inverted sign steady state absorption (dashed black curve) and PL (dashed green curve) spectra of Figure 3.21, taking

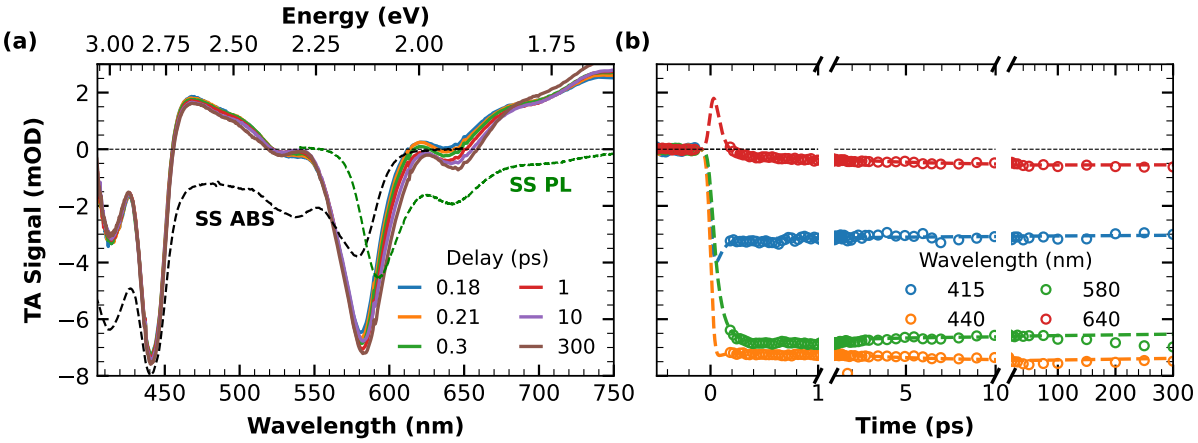

Figure 3.24: (a) TA spectra of chlorobenzene solution of NG3 at different time delays from photoexcitation, with the respective steady-state absorption (dashed black) and photoluminescence (dashed green) spectra. (b) TA kinetic traces and relative fitting curves taken at different probe wavelengths. The reported TA data have been collected on a NG3 chlorobenzene solution with $\lambda_{exc} = 400$ nm.

advantage of their fine-structured shapes. The two negative peaks in the 400-460 nm range are due to a GSB component, while the negative signal between 520 and 650 nm results from the almost overlapping GSB and SE contributions. The lack of a perfect match of the TA spectrum with any linear combination of inverted sign steady-state absorption and PL spectra is due to the superposition of several ESA contributions spanning over the investigated spectral window, as evident from the positivity of the TA signal in the 460-520 nm and $\lambda > 650$ nm spectral ranges.

From a temporal point of view, the main dynamics of the TA signal is related to the SE component, which undergoes a progressive ultrafast increase within the first hundreds of fs after photoexcitation, as highlighted in Figure 3.24(a), where several TA spectra acquired at the earliest delays from photoexcitation are displayed, and also in Figure 3.24(b) showing the TA kinetic traces cut at different probe wavelengths. The entire dynamics can be modelled in terms of three *DAS*, reported in Figure 3.25.

The DAS_1 with a lifetime of $\tau_1 = 70 \pm 10$ fs (blue curve) mainly accounts for the increase in SE contribution mentioned earlier and the concomitant rise of two ESA peaks at about 420 and 540 nm. This is compatible with a fast internal conversion process ($S_2 \rightarrow S_1$) occurring on a timescale of 70 fs, after populating the upper excited state (S_2) by 400 nm excitation. An almost negligible DAS_2 component with a lifetime of $\tau_2 = 5.0 \pm 0.3$ ps (orange curve) seems to be related to a very small redshift of the SE, most likely due to solvation, as inferred from its derivative-like shape with respect to SE. Finally, the DAS_2 with $\tau_3 > 1$ ns (green curve) is associated with the decay of the overall signal occurring on the ns-scale, consistent with the fluorescence lifetime measurements.

TA measurements have also been repeated under pump excitation at 540 nm, with the aim to directly populating the first excited state (see Figure 3.26). As expected, in this case the

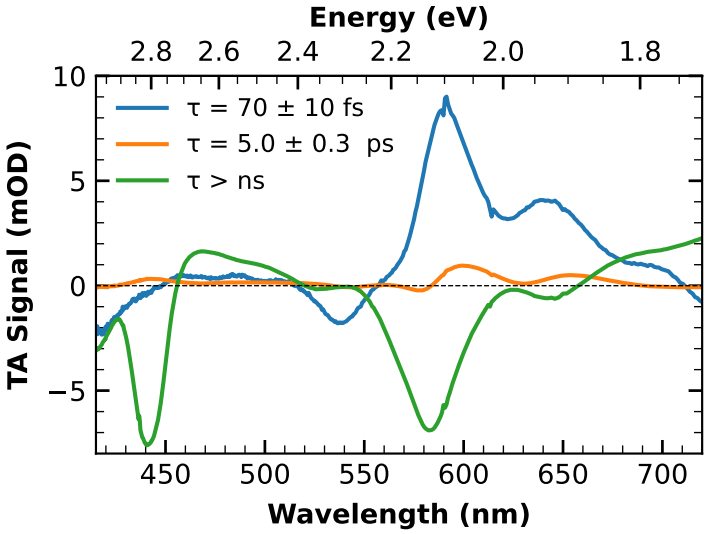

Figure 3.25: Decay Associated Spectra decomposition of TA spectra of NG3 (λ_{exc} = 400 nm) after SVD analysis with corresponding lifetimes.

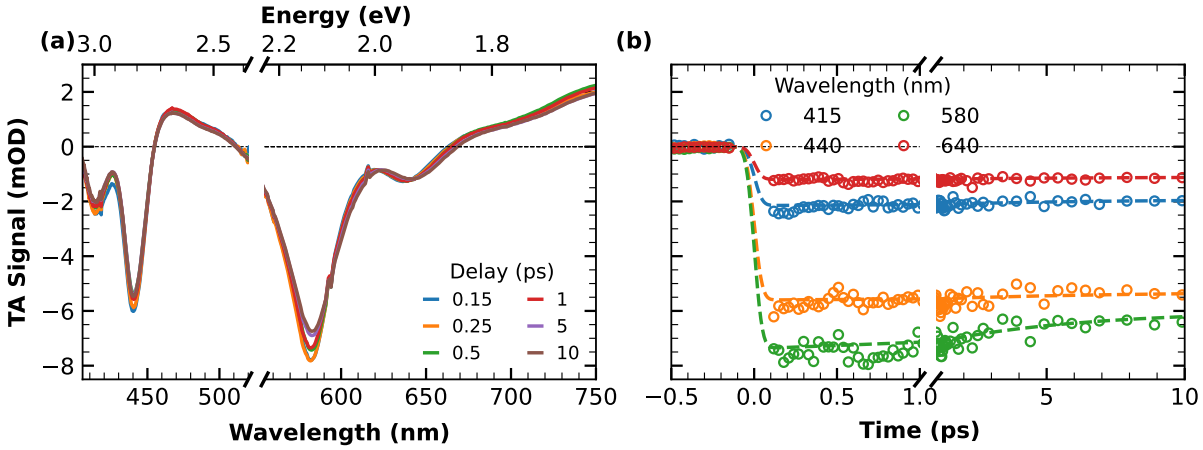

Figure 3.26: (a) TA spectra of chlorobenzene solution of NG3 at different time delays from photoexcitation, with the respective steady-state absorption and photoluminescence spectra. (b) TA kinetic traces and relative fitting curves taken at different probe wavelengths. The reported TA data have been collected on a NG3 chlorobenzene solution with λ_{exc} = 540 nm.

fast <100 fs dynamics is completely absent. Unlike to what observed with the 400 nm pump wavelength, in this case no discernible evolution is appreciated within the same time scale. This outcome further supports the earlier interpretation of an internal-conversion process.

This time, as shown in Figure 3.27, the TA dynamics can be reconstructed by a DAS_1 with $\tau_1 = 4.9 \pm 0.6$ ps, which is compatible on both shape and lifetime with the DAS_2 obtained under 400 nm excitation, and a DAS_2 with $\tau_2 = 900 \pm 200$ ps, accounting for a variation of the polarization of the signal since it was collected in a parallel polarization configuration between

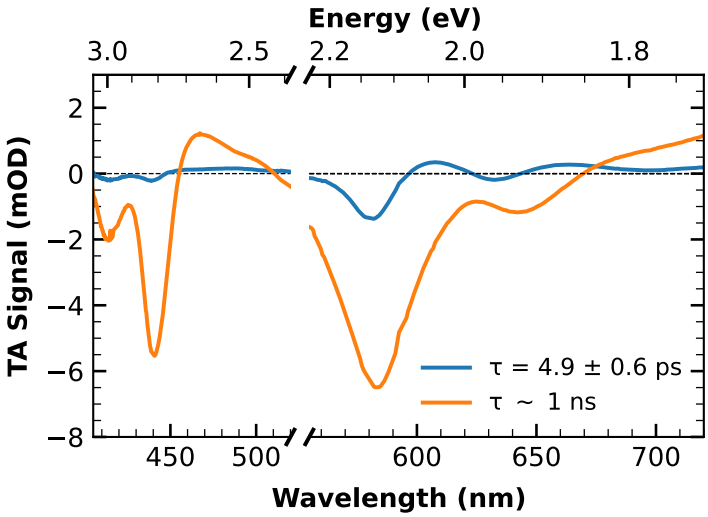

Figure 3.27: Decay Associated Spectra decomposition of TA spectra of NG3 (λ_{exc} = 540 nm) after SVD analysis with corresponding lifetimes.

pump and probe pulses.

3.4 Conclusions

In this chapter, the focus has been on the comprehensive characterization of the photophysical properties of specific atomically precise nanographenes. Through an exhaustive investigation, the intricate relationship between their optical characteristics and their underlying molecular structures has been successfully unveiled. This detailed exploration has demonstrated that even minor alterations in the edge chemistry of these nanographenes, involving the introduction of small chemical groups, can exert a profound influence on their emissive properties. A notable example of this phenomenon is the addition of peripheral bromine atoms, which has a dramatic impact on the nanographenes' photophysics. Specifically, the introduction of bromine atoms enhances an intersystem crossing transition, ultimately leading to a significant reduction in the singlet emission quantum yield.

In general, the findings, when compared to the existing literature, suggest that the incorporation of a heptagon ring into the smaller distorted HBC derivatives does not significantly alter their photophysical behaviour. Despite their slightly distorted structures, these nanographenes exhibit photophysical properties that closely resemble those of typical aromatic molecules, characterized by straightforward and Kasha-obeying responses.

In contrast, the more complex optical behaviour of c-NG2 can be attributed to its richer conformational landscape. c-NG2, with its non-planar extended structure, features a saddle-shaped ketone unit and a helicene moyety further contorts its structure. This unique structural arrangement, combining a large size with a strong distortion from planarity, results in a photophysical

behaviour that deviates from the standard archetypal. Indeed, several atypical features distinguish the optical photocycle of c-NG2, including slow structural relaxation dynamics, nanosecond conformer interconversion, excitation memory effects, and delayed fluorescence. These unusual aspects contribute to making c-NG2's photophysics exceptionally intriguing and distinct from that of typical aromatic molecules.

Lastly, the results highlight that NG3 exhibits a more conventional and regular photophysics. Despite its larger molecular extension, it is essential to note that its structural complexity remains relatively low, as it comprises a purely hexagonal network.

Overall, the results reported through this Chapter suggest that unusual optical properties in NGs may be primarily induced by deep structural distortions rather than size extension, leading them away from the typical molecular behaviour observed in similar contexts. However, conducting more extensive investigations encompassing various atomically-precise NGs is crucial to comprehensively assess the recurrence of such uncommon properties.

Chapter 4

NG-beads

As mentioned, the photophysical characterization of the NGs presented in the preceding chapter serves a double purpose. Indeed, beyond merely studying their stand-alone properties, a key objective of this Thesis is to explore, through the study of specific model systems, how the photophysical properties of atomically precise nanographenes can be modulated when they are integrated into more complex hybrid nanomaterials.

In this perspective, here the interest is on the coupling of NG emission with the modes of a spherical microcavity. The emission properties of a fluorophore can be altered when it is incorporated onto the surface of a spherical microcavity. In such microcavities, visible light propagation undergoes quasi-total internal reflection, and must conform to the boundary conditions imposed by the microsized and spherical surface. This leads to the emergence of distinct photonic resonances in the emission, commonly referred to as Whispering Gallery Modes (WGMs) [261, 262]. To date, a wide variety of luminescent nanomaterials have been employed as gain media to construct WGM-based microcavities [263–272]. However, to the best of our knowledge, the creation of a WGM microcavity based on nanographenes has not been previously documented in the literature. Moreover, beyond the distinctive features of the specific NG-based hybrid system, from a more general perspective, this study also represents the opportunity to investigate the solid-state properties of NGs.

In this chapter, we investigate how the emission properties of NG3 can be modulated by coupling it with the WGMs of polystyrene microparticles. Specifically, after presenting the synthetic method employed for loading NG3 onto the surface of polystyrene beads, a comprehensive analysis of the emission properties exhibited by the resulting NG3-beads will be illustrated, with a specific focus on their WGM-featured spectra, studied at the level of individual particles. Also the design of a proof-of-principle photonic barcode based on the NG3-beads will be presented. The specific choice of selecting NG3 over other NGs is early clarified in this Chapter. Nevertheless, the final part of this Chapter will show the attempts made to produce NG-beads of different colors by employing various NGs.

The findings outlined throughout this chapter will be included in an upcoming paper that is currently being prepared.

4.1 NG loading onto polystyrene beads

The infiltration of NG3 onto polystyrene microspheres was achieved by means of an extremely straightforward self-assembly procedure in solution phase. This approach draws inspiration from previously reported methods employed for doping polystyrene microbeads with quantum dots or fluorescent dyes [228, 229]. However, the efficiency of NG self-assembly onto the surface of polystyrene beads is expected to be particularly high due to the guiding influence of $\pi - \pi$ interactions between the phenyl group of polystyrene and the extensive $\pi-$conjugated structure of NG3 [273].

In fact, as a first attempt, among the various NGs available, NG3 was chosen for specific reasons. From a purely optical perspective, NG3 exhibits the highest emission efficiency (QY= 65 %), a very appealing aspect for designing a luminescent microresonator. Furthermore, NG3 is the ideal candidate also from a morphological standpoint. Indeed, its larger size should maximize the probability of $\pi - \pi$ interactions with the phenyl groups of polsyterene, facilitating spontaneous attachment. Additionally, among the studied NGs, NG3 is the only one lacking a heptagon ring in its structure. This absence of structural distortion should further enhance morphological compatibility with the polystyrene beads whose surface can be considered locally flat over the nanometric extension of NG3.

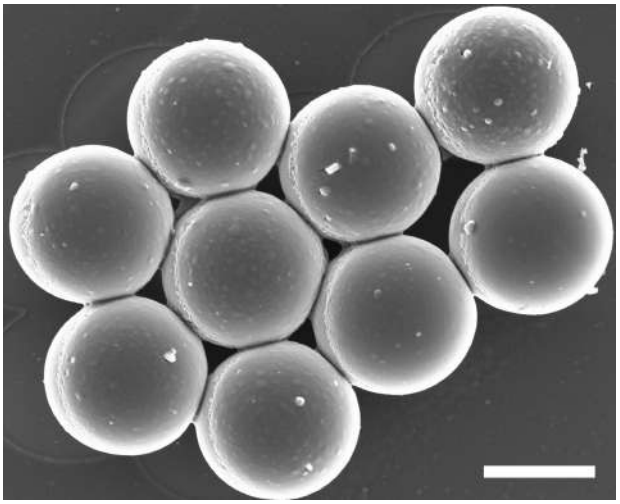

Figure 4.1: SEM image of pristine polystyrene beads. Scale bar is 2 µm.

Self-assembly route

The route employed to incorporate NG3 onto the surface of commercial 3 µm polystyrene microparticles (Polysciences, Inc., polydispersity 5%) is fully outlined in the Materials and Methods Chapter. In summary, the polystyrene microparticles (SEM image reported in Figure 4.1) were first suspended in isopropanol. They were then mixed with a cholorobenzene solution of NG3 and gently stirred at room temperature for 4 hours (as illustrated in the scheme reported in Figure 4.2), to ensure complete adsorption of NG3 onto the bead surfaces. Finally, the NG3-loaded

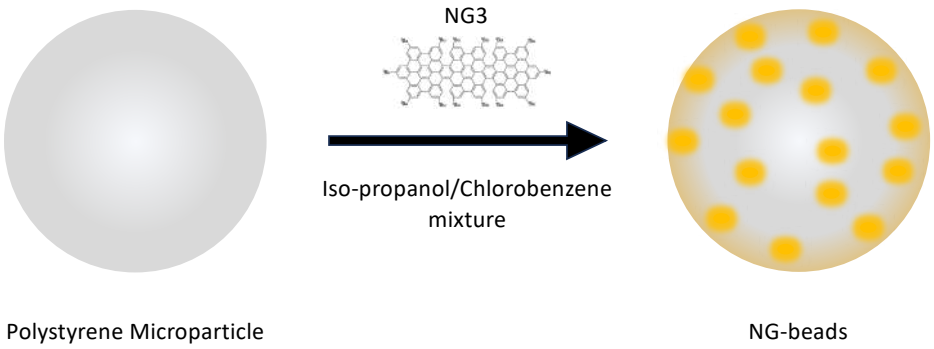

Figure 4.2: Scheme of the protocol used for loading the polsytyrene microparticles with NG3.

microbeads were separated from excess NG3 through centrifugation and subsequently resuspended in isopropanol. The resulting dispersion of NG3-beads was drop-casted onto a microscope slide, left to dry, and then studied using a modular home-built fluorescence microscope.

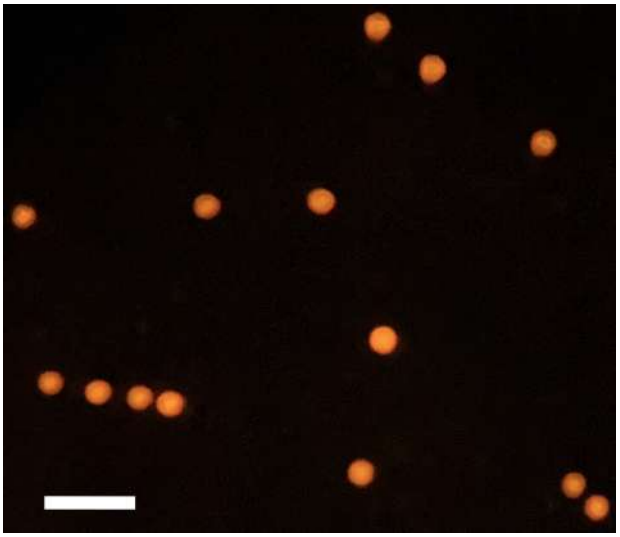

Figure 4.3: Wide-field fluorescence image of NG3-beads under 405 nm excitation. Scale bar is 10 µm.

A wide range of fluorescent molecular dyes or nanomaterials undergo a quenching of their emission in the solid-state, primarily due to self-aggregation [274–279]. However, in contrast, fluorescence imaging shown in Figure 4.3 clearly demonstrates that the adsorption of NG3 onto the surface of polystyrene microparticles does not quench its emission properties but imparts a bright orange luminescence to the beads. To provide a more quantitative analysis, the ensemble PL spectrum obtained by collecting the emission from multiple NG3-beads in a wide-field excitation geometry and reported in Figure 4.4, closely resembles that of a pristine NG3 solution, particularly concerning the main bandshape envelope. Nevertheless, some changes can be appreciated. Firstly, there is a noticeable overall blueshift of the emission band, which can be attributed to alterations in the refrative index of the surrounding medium, which causes a

bathochromic shift. In addition, some non-clear fine structures can be appreciated, and their accurate identification and understanding can be facilitated when studying the PL properties of the NG-beads at a single-particle level.

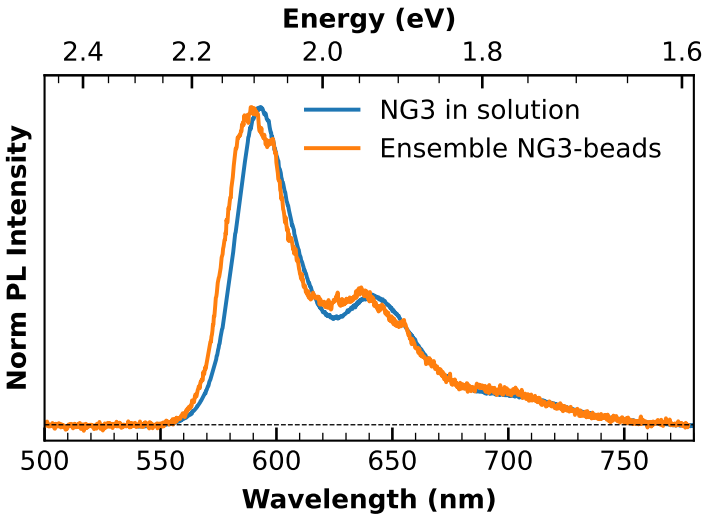

Figure 4.4: Comparison between PL spectrum of NG3 in chlorobenzene solution (blue curve) and ensemble PL spectrum of NG-beads (orange curve).

4.2 WGM in NG3-beads

Several normalized PL spectra of different individual NG3-beads have been vertically-shifted for a better comparison and reported in Figure 4.5. Examining the PL spectra taken at a single-particle level reveals the presence of a series of narrow peaks superimposed upon the conventional PL spectrum of NG3. Notably, this intricate fine structures are nearly imperceptible when observing an ensemble PL spectrum that encompass hundreds of NG3-beads (orange curve of Figure 4.4). The limited visibility of these narrow peaks in the ensemble spectrum (Figure 4.4) can be attributed to the high variability in their spectral position, as can be appreciated from Figure 4.5, resulting in a global averaging which in turn smooths the spectral profile. Moreover, it is worth mentioning that this progression of narrow peaks is barely visible or even entirely absent in the single-particle PL spectrum of many NG3-beads (not shown). This absence, naturally, contributes further to the overall smoothing of the spectral shape of the ensemble PL spectra, determining a reduction of the visibility of fine structures. Regarding the latter point, a quantitative statistical analysis aiming to estimate the relative occurrence of NG3-beads with WGM-featured spectra, has not been conducted. This choice has been made because the focus of this chapter, as will be clarified in the following discussion, has been exclusively on NG3-beads featured by WGM progression in their PL spectra.

To better highlight the distinctive properties of WGM-featured PL spectra, our attention is directed towards a representative single-particle spectrum of a specific NG3-bead, displayed

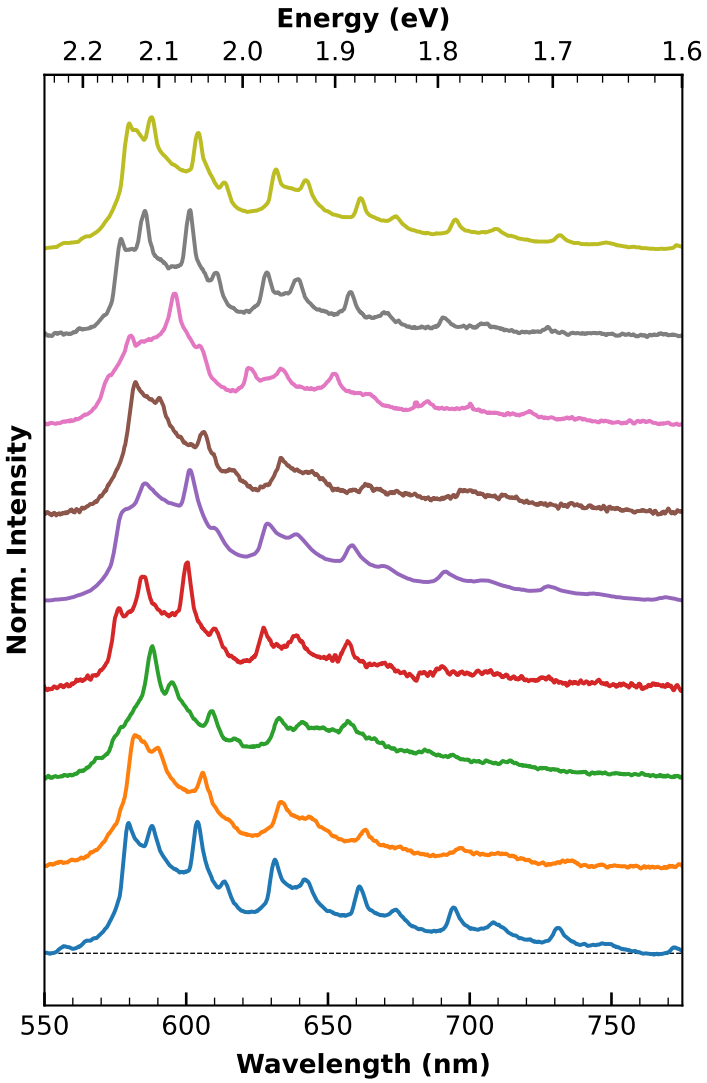

Figure 4.5: PL Spectra of different single NG3-beads taken under 405 nm excitation.

in Figure 4.6(a) and characterized by a notable progression of well-defined sharp peaks (orange curve). A microfluorescence image of the particle under study is displayed in the inset of same Figure. It is evident that the intrinsic emission from NG3 (dashed red curve) is significantly enhanced at specific wavelengths, resulting in an almost regular series of pronounced, narrow peaks overlaying the broader emission envelope corresponding to the usual PL spectrum of NG3. This enhanced emission is expected to be due to microsperical surface of polystyrene bead behaving as a microresonator, causing the emission from NG3 adsorbed on its surface to couple with the WGM resonances of the dielectric microparticle. As a result, this coupling gives rise to a progression of multiple pairs of narrow peaks superimposed onto the broader background given by the regular PL band of NG3.

It is noteworthy that the visibility of WGMs, defined as $V = (I_{peak} - I_{bk})/(I_{peak} + I_{bk})$ according to [280], is surprisingly quite good. In fact, the best visibility of WGMs should be

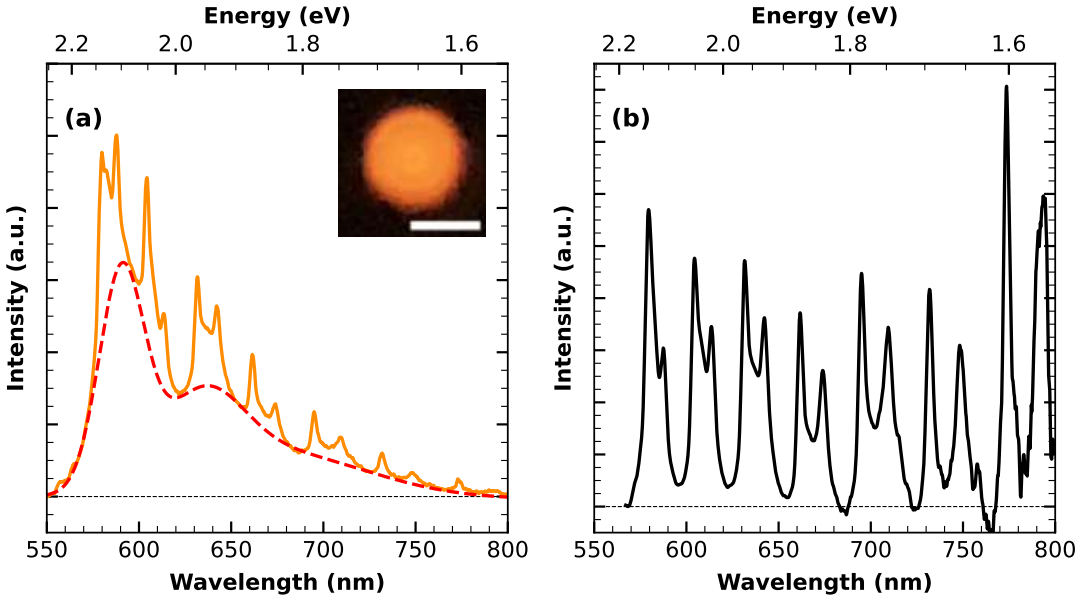

Figure 4.6: (a) PL spectrum of a single NG3-bead (orange curve). For comparison, in dashed red the PL spetrum of chlorobenzene solution of NG3 is shown. The inset shows a fluorescence image of the single NG3-bead. The scale bar is 2 µm. (b) WGM peaks obtained from (a) by subtracting the two spectra and executing the normalization procedure described in the main text.

obtained by positioning the detection away from the excitation spot to minimize the contribution from uncoupled emission [229, 281, 282]. In this context, the good visibility of WGMs observed in Figure 4.6(a) is remarkable, considering that the emission spectrum was acquired by collecting light emitted from the entire single microparticle within a wide-field microscope configuration. This remarkable visibility can likely be attributed to a relatively uniform coverage of the bead's surface by NG3, facilitating a competitive contribution of NG3 emission coupled to WGMs in comparison to the emission of uncoupled NG3.

According to the Mie theory, WGM resonances characterizing an optical spherical microresonator of diameter d lie in correspondence of the transverse electric (TE) and magnetic (TM) eigenmodes dominating the scattering fields, and their spectral positions are theoretically expressed in terms of the radial mode number i and angular mode number q by [261, 283]

$$\lambda_{i,q} = \pi d n_s \left[\nu + \alpha_i \left(\frac{\nu}{2}\right) - \frac{p}{\sqrt{m^2-1}} + \frac{3\alpha_i^2 (4\nu)^{-1/3}}{10} - \frac{p(m^2 - 2p^2/3)}{(m^2-1)^{3/2}} \frac{\alpha_i}{(2\nu^2)^{1/3}} \right]^{-1} \tag{4.1}$$

where $\nu = q + 1/2$, the refractive index contrast $m = n_s/n_e$ is the ratio between the refractive index of the sphere n_s and of the environment n_e, α_i is the i-th zero of the Airy function, and $p = m$ for transverse electric mode polarization or $p = 1/m$ for transverse magnetic mode polarization. Being the NGs located presumably on the surface of the microparticles, their emission is coupled only to WGMs whose field distribution is close to the particle surface. For this reason, in eq. (4.1)

only first radial modes with $i = 1$ are considered. Furthermore, it can be safely assumed $n_e = 1$ with high accuracy, as the measurements were performed in air.

WGMs fitting algorithm

To extract information from the resonance pattern observed in individual microbeads, an adequate fitting algorithm was developed in Python to fit simultaneously the set of multiple WGM peaks like the one displayed in Figure 4.6(a).

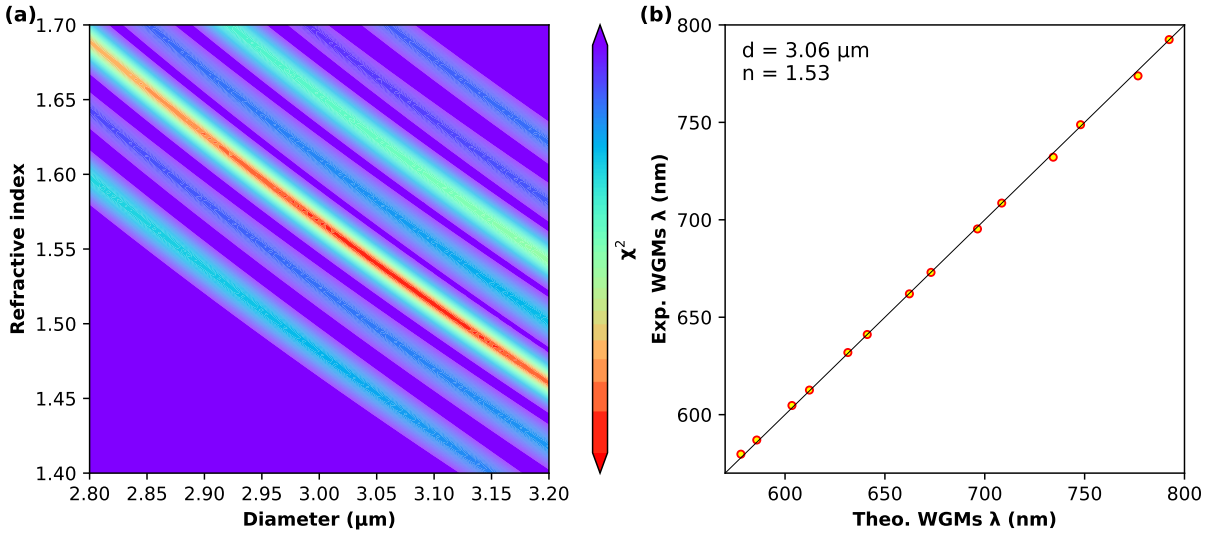

Figure 4.7: (a) $\chi^2(d, n_s)$ colormap of experimental peak positions of WGMs compared to the calculated ones in correspondence of the sampled parameter space given by diameter and refractive index of the microparticle. A logarithmic scale in the colorbar is used to enhance the contrast. (b) Correlation between WGM positions expected theoretically in correspondence of the minimum value of $\chi^2(d^*, n_s^*)$ in (a) and the experimentally observed peak positions.

To do this, firstly the isolation of experimental WGM pattern from the regular PL background is needed. This is achieved by subtracting the regular PL background (dashed red curve of Figure 4.6(a)) from the experimental single particle spectrum of the same Figure. The resulting spectrum is then divided by the same PL background to normalize the magnitude of WGM peaks, obtaining the spectrum reported in Figure 4.6(b). Based on eq. (4.1), a set of WGM positions is generated for each point of the parameter space spanned by d and n_s, representing the diameter and refractive index of the polystyrene bead, respectively. Subsequently, the squared sum of the residuals between the spectral positions of the calculated WGM resonances for each point $\{d, n_s\}$ and the experimental positions of the WGM progression shown in Figure 4.6(b) is evaluated, *i.e.* $\sum_q [\lambda_q^{theo} d, n_s - \lambda_q^{exp}]^2$. This approach allows to obtain a $\chi^2(d, n_s)$ function, depicted as a colormap in Figure 4.7(a). The minimum value (red) of this function corresponds to the couple of best fitting parameters $\{d^*, n_s^*\}$ within the sampled parameter space. By this procedure, a unique pair of d and n_s values can simultaneously fit the entire WGM progression. For example, in the case of the NG3-bead discussed in Figure 4.6, this procedure allowed the estimation of $d = 3.060$

µm and $n_s = 1.530$. Figure 4.7(b) illustrates the optimal correlations between the experimental WGM resonances and those calculated by inserting the best fitting parameters in equation 4.1, confirming the effectiveness of the fitting algorithm.

4.3 Conceptual design of a NG-beads based photonic barcode

Due to the Kasha-obeying behaviour of NG3 fully described in section 3.3, the emission characteristics of each specific NG-bead remain entirely unaffected by the excitation wavelength. This is clearly demonstrated in Figure 4.8, which displays the PL spectra of the same individual NG-bead acquired under both 405 and 532 nm excitations. The positions of the WGM peaks, representing

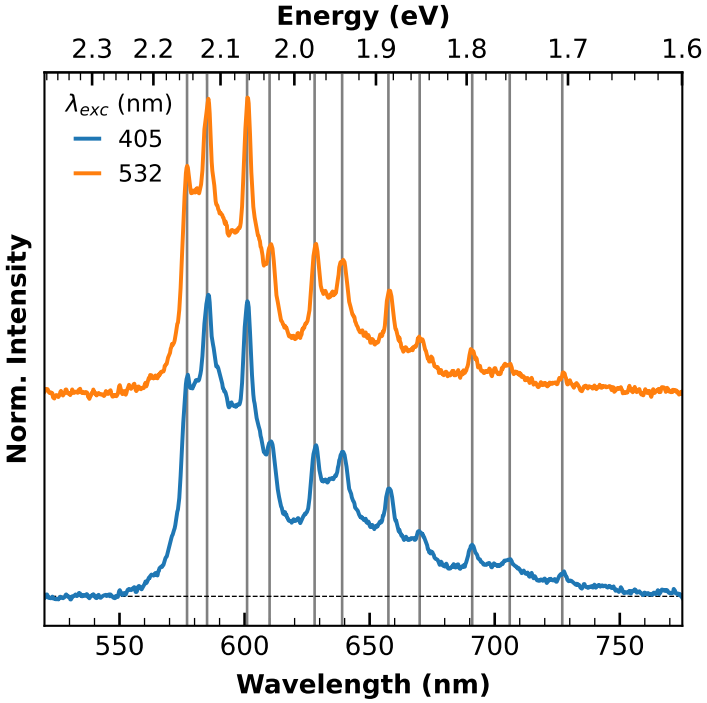

Figure 4.8: Comparison of the emission spectra of the same NG3-bead under 405 nm (blue curve), and 532 nm (orange curve) excitation, taken at single particle level.

the main spectral fine-structures of the PL spectrum, are identical independently of the different excitation wavelength. However, the coupling of NG emission with WGMs offers a simple and effective way to modify the uniform optical characteristics of NG3. While the optical properties at the level of distinct NGs remain perfectly the same, their coupling with even slightly different beads results in distinct NG3 doped beads having non-identical emission spectra, due to the highly variable WGMs associated with the polystyrene microparticles, as will be better discussed in more detail below.

Variability of WGMs progression due to intrinsic polydispersity

The WGM resonances, as said, exhibit a high degree of sensitivity to the size, shape, and refractive index of the optical microresonator. This is quantitatively demonstrated in Figure 4.9, where the position of TE (panel a) and TM (panel b) modes lying in the spectral range of 500-800 nm are simulated based on eq. (4.1). This simulation is performed for a spherical particle with refractive

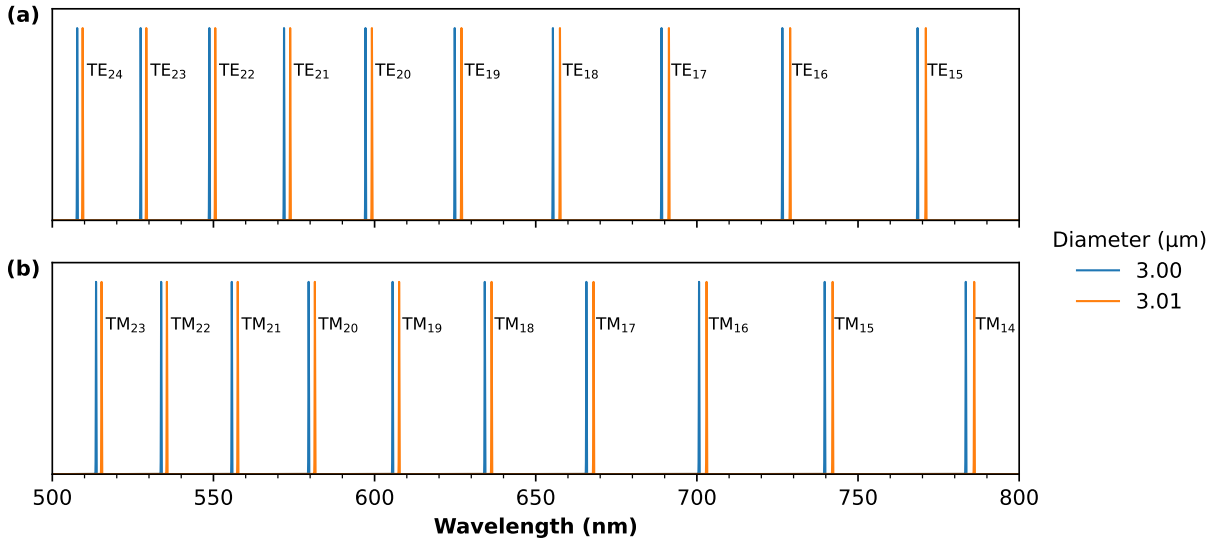

Figure 4.9: (a) TE and (b) TM WGMs calculated for a spherical particle of 3.00 µm (blue) and 3.01 µm (orange) diameter and a refractive index of 1.55.

index n=1.550 and diameter $d = 3.000$ µm (shown in blue) and compared to the same modes obtained for a particle with an identical refractive index but a slightly larger diameter $d = 3.010$ µm (depicted in orange).

For instance, in the case of the TE_{18} mode, such a minute size difference of $\partial d = 10$ nm leads to a spectral shift of $\partial\lambda_{1,18} = 2.2$ nm. In equivalent terms, this demonstrates that the sensitivity of WGM positions to changes in diameter is $\frac{\partial\lambda}{\partial d} \sim 0.22$. These properties make WGM an exceptional tool for the precise estimation of the diameter of individual NG-beads. Notably, the typical FWHM of individual WGM peaks in Figure 4.6 falls within the range of 1 to 3 nm, and their peak positions can be experimentally determined with an accuracy of 0.5 nm or even better. Consequently, the fitting procedure enables the estimation of the diameter of individual particles with an uncertainty as small as $\delta d = 0.5/0.22 \sim 2$ nm. For instance, for the microbead featured in Figure 4.6, this yields a diamater of $d = 3.060 \pm 0.002$ µm. While the absolute accuracy of these measurements may still be influenced by some systematic errors, such as deviations from a perfect spherical shape, it is important to note that at least in terms of relative error, such a $\delta d = 2$ nm uncertainty is 75 times smaller than the nominal polydispersity (5%, equivalent to 150 nm) of the microbeads. It is also at least one order of magnitude better than what can be achieved through both optical imaging and SEM. Thus, the present results are particularly promising for potential applications in metrology or sensing.

Furthermore, the same procedure was applied to approximately ten NG-beads, providing an estimate of their size and refractive index distribution at the ensemble level. The results indicated an average dimaeter of $\langle d \rangle = 3.05 \pm 0.04$ µm and a refractive index of $\langle n_s \rangle = 1.54 \pm 0.02$. Notably, this average refractive index estimation is slightly lower than that expected for polysterene microparticles in the relevant spectral region (1.58 [284]). This discrepancy may be attributed to a minor swelling of the microbeads [229] after the adsorption of the NGs, which could alter the refractive index due to a reduction in density.

WGM-based microlabel array for encoding applications

According to this, even a modest level of variability in the size distribution of the initial polystyrene microparticles leads to significant changes, among different individual NG doped beads, in the pattern of the sharp WGM peaks coupled to the already structured PL envelope. As a consequence, the possibility of observing perfectly identical PL spectra from distinct NG3-beads becomes highly unlikely. This characteristic is well depicted in Figure 4.10, which presents nine randomly chosen NG3-beads. In Figure 4.10(a) their microfluorescence images are reported, while in Figure 4.10(b) their corresponding PL spectra. It is evident that each spectrum offers a unique signature for each specific NG3-bead. While the observed variations from bead to bead are primarily attributed to minute differences in size, additional factors contributing to the uniqueness of each pattern could also include random alterations in the spatial distribution or quantity of NGs adsorbed on a given microbead, or minor deviations from a perfectly sperical shape. In any case, regardless of the specific source of variability, the uniqueness of the finely-structured spectral fingerprint exhibited by each microparticle makes these NG-beads ideal luminescent unclonable labels suitable for the development of photonic encoding, particularly in applications such as anti-counterfeiting measures [285]. More precisely, based on similar reported protocols [286–289], the WGM-featured PL spectrum of each NG3-bead could be for commodity associated to a distinct barcode, containing of a series of bars matching the spectral position of the WGM peaks, with the width of each bar calibrated to correspond proportionally to the relative emission intensity at the corresponding peak. Within this context, Figure 4.10(c) offers a proof-of-concept design for a high-level unclonable photonic microarray constructed from the nine NG-beads. An optical microencoding label of this kind would be exceedingly challenging to replicate, because each of the nine entries in the designed microarray would convey almost unique information associated with a specific NG3-bead. Moreover, unlike similar systems [285, 290, 291], this microtag would benefit significantly from the flexibility given by the possibility to employ a broad range of excitation sources, as the emission pattern can be stimulated by exciting across a broad range of the visible spectrum and it remains unaffected by variations in excitation wavelength.

As previously mentioned, the nominal polydispersity of NG-beads is 75 times larger than the estimated size uncertainty at the level of an individual NG-bead. Even when conservatively attributing bead-to-bead variations, as in Figure 4.10(b), solely to changes in size, which is a very conservative approach, this implies the potential existence of 75 distinct patterns. Consequently, the number of unique microarrays, such as the one in Figure 4.10(c), could reach $75^9 \sim 7.5 \times 10^{16}$.

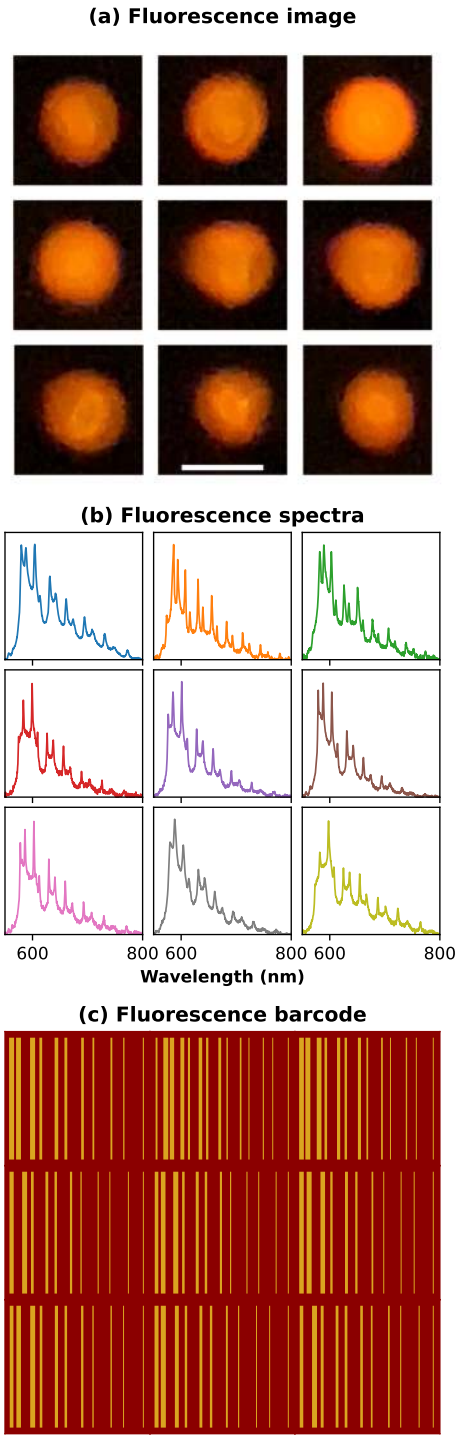

Figure 4.10: (a) Fluorescence microscopy images (scale bar is 3 µm) and (b) fluorescence spectra of nine different NG-beads under a 405 nm excitation, taken at single-particle level. (c) WGM-based microarray barcode.

4.4 Attempts to obtain NG-beads of different colors

As said, as a first attempt, the NG chosen to be incorporated into the polystyrene beads was NG3 due to its superior optical and structural characteristics among the other available options.

Subsequently, following the successful coupling detailed in the preceding sections of this chapter, some additional attempts have been made to produce NG-doped beads of different emission colors, by doping them with other distinct NGs.

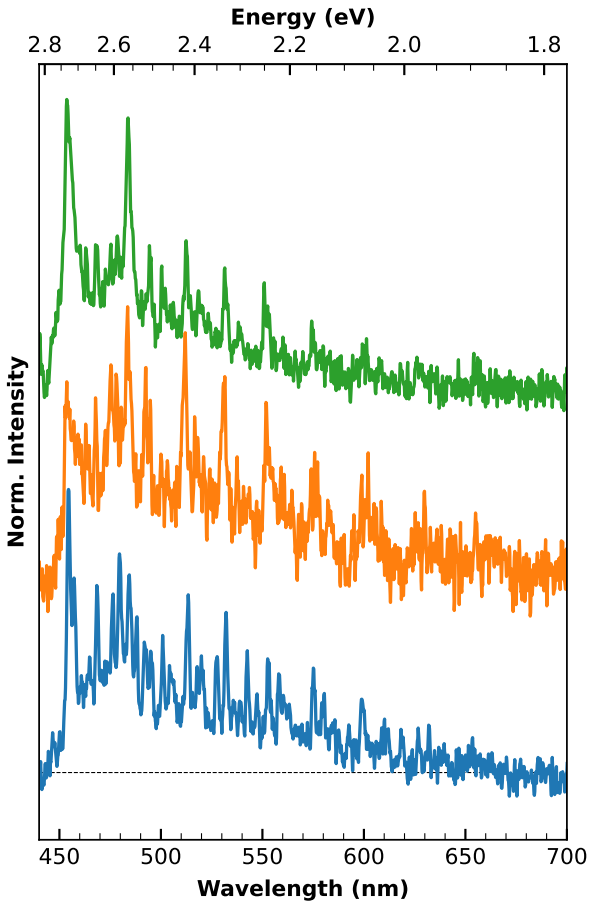

Figure 4.11: Single-particle PL spectra of three distinct c-NG1-beads taken under 405 nm excitation.

With the goal of achieving blue emission, the options considered were c-NG1, m-NG1 and c-Br-NG1, as all of them emit in the 450-500 nm spectral range. Since these NGs share the same structural shape and size, the preference was given to m-NG1 owing to its higher emission quantum yield (QY=5%) respect to others. The same self-assembly approach, which was previously effective with NG3, was successfully repeated with m-NG1, as evidenced by the single-particle spectra of m-NG1-beads presented in Figure 4.11. Compared to NG3-beads, these spectra are characterized by a higher noise, primarily attributed to the use of a 405 nm excitation, which falls within the redder absorption tail of m-NG1 (see Figure 3.2). Consequently, the low absorption at 405 nm results in relatively weak emission. Anyway, despite the noisy, the successful coupling of m-NG1 emission with the WGMs of the polystyrene beads is evident from the presence of some sharp peaks superimposed on the broader emission band of m-NG1 (see Figure 3.2 for comparison). It is worth noting that, as a quality factor $Q \sim \lambda/\Delta\lambda$ comparable to that of NG3-beads is expected, the width of the WGM peaks in Figure 4.11 is narrower than that characterizing the

WGM peaks in the redder part of the spectrum, as observed for the NG3-beads (see Figure 4.5).

Surprisingly, the same self-assembly procedure that worked well for both NG3 and m-NG1 did not yield equally satisfying results when repeated with c-NG2 with the aim to produce yellow-emitting beads, although some of the beads exhibited yellowish luminescence after treatment with c-NG2. Figure 4.12 shows the normalized spectra of four distinct beads after c-NG2 doping. They

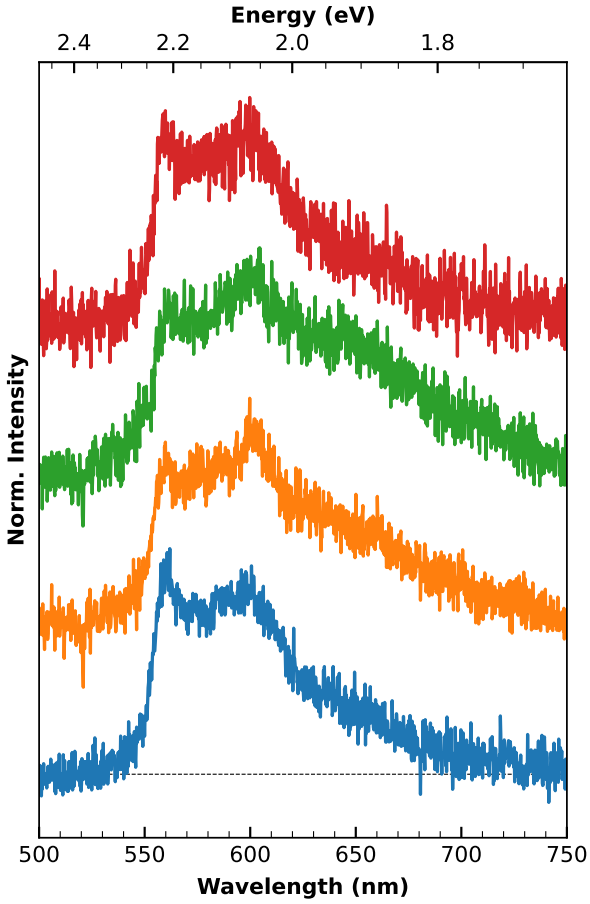

Figure 4.12: Single-particle PL spectra of four distinct m-NG2-beads taken under 405 nm excitation.

are characterized by not only a very low intensity, as can be inferred by the high relative noisy of the spectra, but also by significant change in terms of bandshape and global width if compared to the regular PL spectrum of c-NG2 (see Figure 3.8 for comparison). The altered emission shape is likely attributed to increased electronic interactions between different NGs, leading to aggregation, or between NGs and the surface of the beads. Consequently, some structural distorsion may have occurred, resulting in changes to the vibro-electronic structure that, in turn, manifest as modifications in the emission band. According to this interpretation, a global quenching of the emission could be expected, which would also account for the notably low intensity of the emission. Most importantly, there were non instances of c-NG2 doped beads displaying WGM-featured emission spectra. This observation is in line with the case of m-NG1 and NG3 doped

beads, where some also lacked WG signatures, as mentioned. However, the absence of any c-NG2-beads exhibiting fine WGM structures in their emission spectra raises questions. In particular, it is unclear wheter this can be attributed to a statistically small number of beads examined or if there are more specific factors at play, such as suboptimal morphological compatibility between c-NG2 and the bead surface. This might be related to the more pronounced distortion caused by the presence of a helicene motif in the c-NG2 structure.

From a more practical perspective, the fact that the self-assembly procedure can, in principle, be used to obtain WGM-featured NG-beads of any color is highly appealing. This, is particularly relevant in the realm of encoding applications, such as the conceptual design of photonic micro-tags, as was presented in Figure 4.10. In fact, the encoding capacity could be further enhanced by loading the polystyrene beads with NGs of different emission colors simultaneously. This approach offers several advantages. Firstly, it would broaden the PL spectrum of each individual bead, extending also, as a consequence, the spectral window where the WGM are discernible. Secondly, the non-deterministic randomness of the adsorption of NGs with different emissions to polystyrene beads would introduce a higher level of variability in the emission bandshape of each individual bead. When combined with the intrinsic, albeit slight, size polydispersity of the beads governing the tunability of WGM modes, this heightened variability would further enhance the unclonability probability of each single particle.

4.5 Conclusions

A novel kind of luminescent microresonator based for the first time on atomically-precise NGs has been presented in this Chapter. The loading of NG3 onto the surface of polystyrene microparticles represents a straightforward but effective way to modulate the emission characteristics of the formers, constituting at the same time a new class of functional composite materials. Indeed, when studied at a single-particle level, the emission spectra of the NG doped beads are strongly modulated by pronounced WGM resonances, resulting in a progression of narrow peaks superimposed to the regular PL emission of the NG.

A WGM-based computational approach has been developed to simultaneously estimate both the size and refractive index of single NG-beads, by exploiting only the knowledge of their PL spectrum, without the need for any reference or calibration measurements.

Moreover, it has been fully detailed how the single-particle PL spectrum represents a unique fingerprint of each NG-bead, due to the presence of an intricate finely-structured progression of WGM peaks whose spectral positions are highly dependent on the specific bead. This has permitted to show, albeit as a proof-of-principle demonstration, the potential functional aspect of this type of hybrid material by considering its exploitation to fabricate WGM-based barcodes for optical data recording and information security.

Finally, it has been demonstrated the general applicability of the procedure which can be extended to obtain NG-beads of different emission color simply by changing the NG used as fluorescent medium of the microcavity.

Chapter 5

NG-ring as cage for fullerenes

The preceding chapter has provided an illustrative example of how the optical characteristics of NGs can be modulated through the coupling of their emission with the resonant modes of a spherical microcavity. Specifically, the loading of NGs onto the surface of polystyrene microparticles represents a straightforward and effective way for creating a novel type of NG-based functional hybrid. However, the remarkable inherent chemical versatility of NGs leads to the opportunity to explore the construction of specific binary nanocomposite systems, where both the initial precursors are nanomaterials. In this chapter, another exemplary case is examined through an investigation into the possibility of designing an all-carbon nanohybrid system *via* the coupling of c-NG1 nanographene, suitably functionalized, with C_{60} and C_{70} fullerenes. The investigation of host-guest supramolecular interactions between fullerenes and curved PAHs has gained increasing interest in recent years [219, 220, 292, 293]. As illustrated in the Introduction, sometimes electron-transfer processes have been documented, facilitated also by the strong electron acceptor behaviour of fullerenes [4], rendering the resulting nanohybrid materials appealing for light-driven applications such as photocatalysis, photovoltaics, and artificial photosynthesis [219, 292, 294].

One might expect that the natural structural distortion of c-NG1, arising from the presence of a heptagon ring, could lead to a good shape complementarity with the highly curved surface of fullerenes, thus favouring their binding. However, as will be highlighted, an opportune functionalization of c-NG1 is necessary to favour the spontaneous NG/fullerene assembly. Throughout the Chapter, a fully detailed optical investigation of the complexation between the functionalized NG and C_{60} and C_{70} fullerenes will be illustrated. Most of the results reported in this Chapter have been published in [295].

5.1 Macrocyclization of NG

With these considerations in mind, as first attempt, the possibility of establishing a direct binding between the saddle-shaped c-NG1 and C_{60} fullerene was tested. To assess any complexation of NG with C_{60}, fluorescence-quenching experiments were performed, by evaluating the PL emission

of a toluene solution of c-NG1 at increasing values of concentration of fullerene. Such experiments represent a common standard in the study of supramolecular interactions between fullerenes and fluorescent species [96, 188].

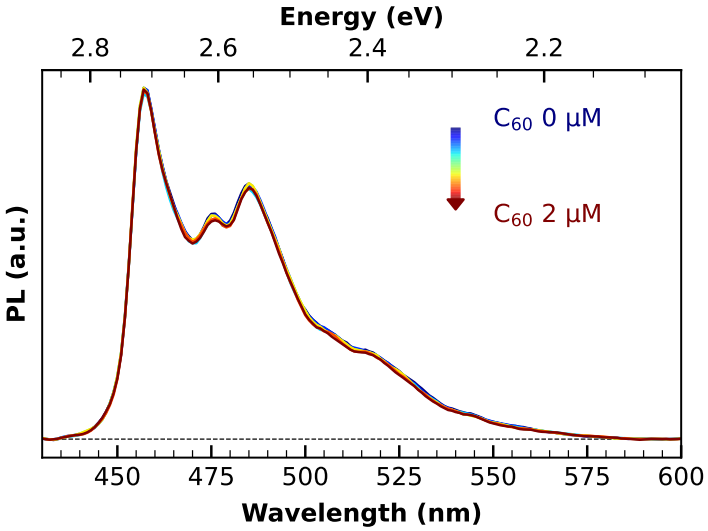

Figure 5.1: PL spectra of c-NG1 toluene solution (1×10^{-6} M) upon addition of increasing amounts of C_{60}.

However, as shown in Figure 5.1, the addition of fullerene does not induce any appreciable effect on the emission of c-NG1. On this basis, it may be interesting to investigate whether appropriate functionalization of the c-NG1 structure, aiming to increase its morphological complementarity with fullerene, could produce more pronounced interactions.

NG functionalization with CPP

With this aim, a cycloparaphenylene derivative was utilized for the functionalization of a c-NG1 analogue, to obtain a ring-shaped cage, which is expected to enhance its fullerene complexation ability. Cycloparaphenylenes (CPPs) are a family of radially π-conjugated nanohoops based on benzene rings [296], which have attracted significant attention over the past decade due to their role of supramolecular hosts [297, 298]. Specifically, their strong affinity for binding with fullerenes is already well-documented [96, 299], rendering them highly regarded structures for hosting fullerenes. Furthermore, the interest on these systems becomes even more pronounced when their structural arrangement is combined with the electronic properties of PAHs [300, 301].

The CPP functionalization of NG, executed by the group of Prof. A. Campaña, followed the scheme illustrated in Figure 5.2. The synthesis starts from a dibromo hept-HBC derivative (1), sharing the same core structure with c-NG1. A macrocyclization reaction is conducted between 1 and the diboronate ester of the para-phenylene precursor 2, yielding compound 3. This compund is then subjected to a final reduction step facilitated by a mixture of $SnCl_2$ and HCl, resulting in

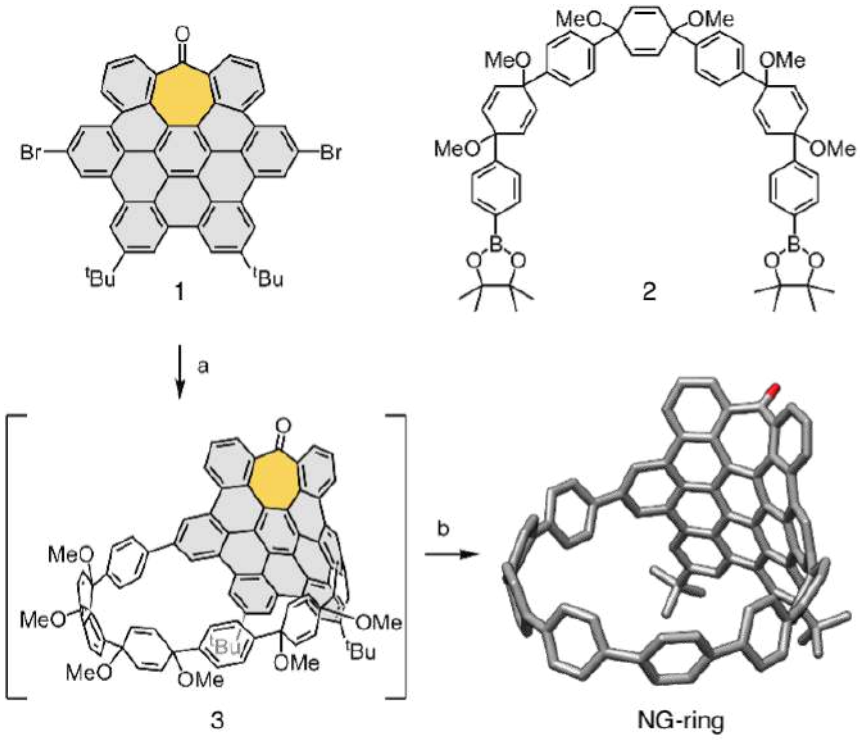

Figure 5.2: Scheme of NG-ring synthesis. [Adapted from [295]].

the final hept-HBC-containing [10]CPP, NG-ring. A comprehensive investigation of the structure of this NG-ring macrocycle can be found in our previously published work [295].

NG-ring

Figure 5.3 provides a summary of the main optical characteristics of the obtained NG-ring macrocycle. Its absorption spectrum (black curve in panel(a)) exhibits two broad bands peaking at approximately 355 and 433 nm. While the spectral position of the primary absorption transition is not markedly different from its not-circular analogue c-NG1, the cyclization process appears to have broadened the bandshape. Furthermore, the relative intensity of the first electronic transition, situated around 430 nm, is notably enhanced. The PL spectrum of NG-ring (blue curve of panel (a)) displays a structured band with two main peaks at 473 and 503 nm (1260 cm^{-1} spacing), related to the vibronic progression of C-C stretching modes. The presence of a second vibronic progression, which was evident in the emision spectrum of c-NG1, is barely discernible here, poorly recognizable from the unresolved peak at ∼490 nm and an additional contribution on the left edge at about 455 nm. Although not dramatic, these variations in the overall electronic strucutre, suggested by the absorption band and the differences in the vibronic coupling inferred from its emission spectrum, can be expected on the basis of the structural alteration of the NG, which now becomes part of a 3D circular arrangement.

The emission quantum yield of the macrocycle was estimated as $3.7 \pm 0.4\%$, surpassing that of c-NG1 (2%). Finally, as shown in Figure 5.3(b), its PL deactivation follows a monoexponential

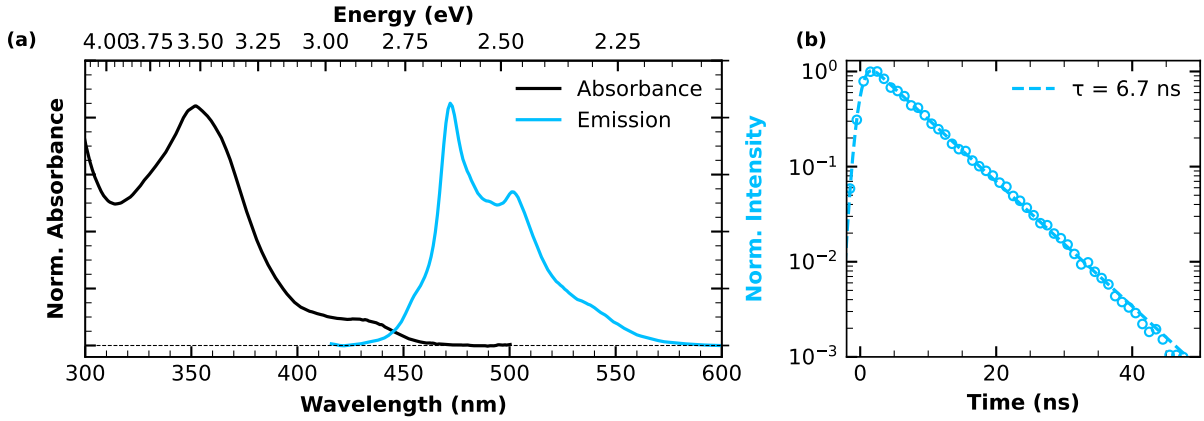

Figure 5.3: (a) Normalized absorption (black curve) and photoluminescence (blue curve) of NG-ring toluene solutions. (b) PL decay and respective least-squares fitting curve of NG-ring toluene solution at $\lambda_{exc} = 400$ nm and $\lambda_{em} = 470$ nm. [Adapted from [295]].

decay, with an estimated lifetime of $\tau = 6.7 \pm 0.2$ ns. Consequently, the radiative and non-radiative decay rates were determined as $k_r = (5.5 \pm 0.7) \times 10^6$ s^{-1} and $k_{nr} = (1.4 \pm 0.2) \times 10^8$ s^{-1}, respectively. Comparing NG-ring to c-NG1, it is evident that macrocyclization does not affect the radiative decay rate but results in a significant reduction in the non-radiative decay rate, which is approximately one order of magnitude lower.

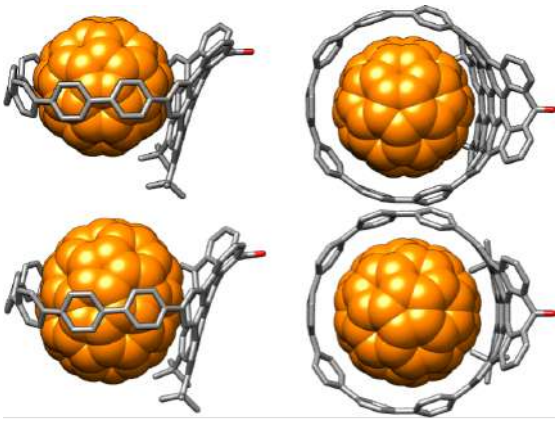

Figure 5.4: DFT (ωB97XD/def2-SVP) optimized structure of the host-guest complex NG-ring@C_{60} (top) and NG-ring@C_{70} (bottom). Left: side view. Right: top view. H atoms have been omitted for clarity. Color coding: C, gray (NG-ring) or orange (C_{60} and C_{70}); O, red. [Adapted from [295]].

The incorporation of c-NG1 with a cycloparaphenylene is expected to enhance its capabilities as supramolecular receptor for fullerenes. As previously mentioned, [10]CPP posses a robust affinity for fullerenes, particularly C_{60}, due to its appropriately sized cavity and shape, which provides an ideal environment for accomodating these curved π systems. Consequently, one could reasonably expect that the NG-ring, which integrates a CPP with the heptagon-containing

HBC unit, would also establish $\pi - \pi$ interactions with fullerenes. A similar behaviour has indeed been reported in the case of a macrocycle created through the fusion of a [10]CPP with a planar HBC [188]. In our case, DFT calculations at the ω B97XD/def2-SVP theory level performed by the research group led by Prof. A. Campaña and reported in [295] substantiate this hypothesis. As reported in Figure 5.4, for NG-ring a suitable size and shape complementarity is predicted for both C_{60} and C_{70} fullerenes. From this point of view, NG-ring is envisioned to function as a nanocage capable of sustaining host-guest interactions, thereby facilitating the spontaneous assembly of a supramolecular complex. This theoretically-expected propensity of NG-ring to bind with fullerenes will be experimentally investigated in the following sections from a photophysical perspective.

5.2 Complexation with C_{60}

Compared to the results shown in Figure 5.1, the scenario is completely different in the case of NG-ring: a simple mixing of a toluene solution of NG-ring with C_{60} is sufficient for the establishment of interactions between the two.

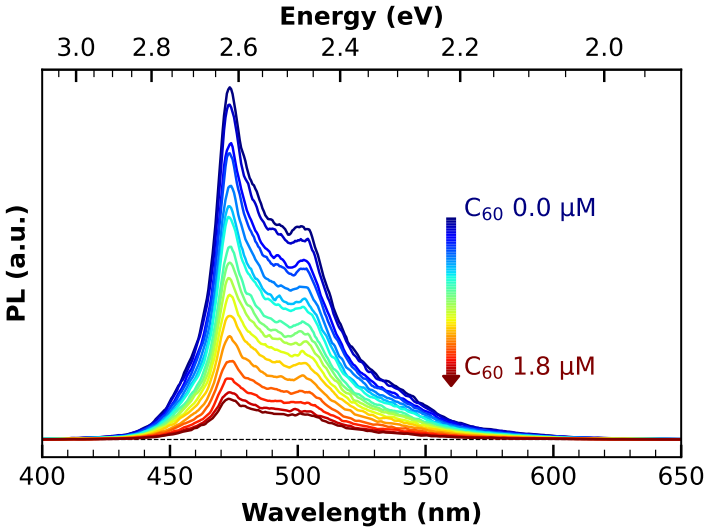

Figure 5.5: PL spectra of NG-ring toluene solution (1×10^{-6} M) upon addition of increasing amounts of C_{60}. [Adapted from [295]].

Indeed, the emission of NG-ring is significantly quenched by C_{60}, as displayed in Figure 5.5, where the PL spectra of a toluene solution of NG-ring are reported for increasing concentrations of C_{60}. As observed, there is no discernable change in the shape of NG-ring emission, but only a progressive reduction of its intensity.

Furthermore, the observed emission quenching is not associated with any alteration in the emission lifetime. As shown in Figure 5.6, the normalized kinetic traces of NG-ring PL decay share the same dynamics, with no changes in the emission lifetime.

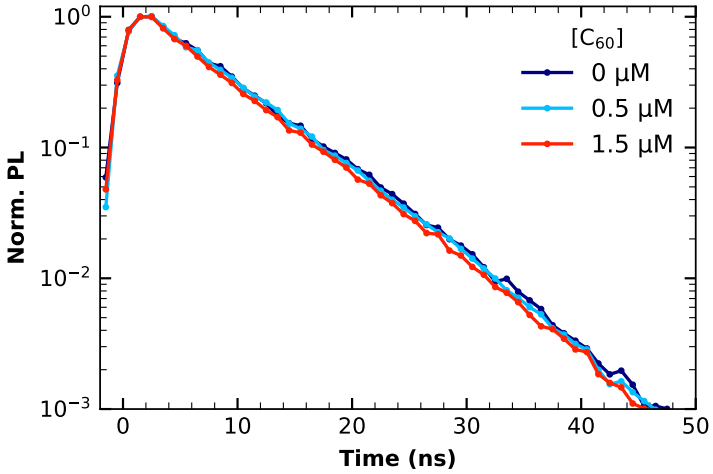

Figure 5.6: Comparison of normalized PL decay of NG-ring toluene solution (1×10^{-6} M) without (darkblue), with 0.5×10^{-6} M (blue) and 1.5×10^{-6} (red) C_{60}, under $\lambda_{exc} = 400$ nm. [Adapted from [295]].

This observation, coupled with the absence of any modifications in the spectral shape of the emission, suggests that the reduction of PL intensity upon the addition of C_{60} may be attributed to a static quenching mechanism, arising from the complexation between NG-ring and C_{60} which switches off the emission of the former, or to a specific quenching mechanism occurring on a timescale faster than the nanosecond.

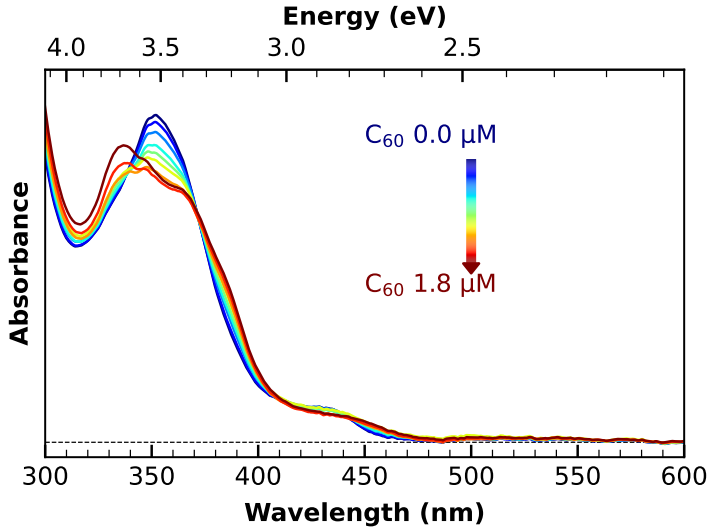

Figure 5.7: Absorption spectra of NG-ring toluene solution (1×10^{-6} M) upon addition of increasing amounts of C_{60}. [Adapted from [295]].

Indeed, strong host-guest interactions are evident even at the ground state level, as demonstrated by the alterations in the spectral shape of the absorption band of NG-ring upon progressive

addition of C_{60}, as highlighted in Figure 5.7. These changes influence the absorption band over a broad spectral range. In particular, the changes affecting the main absorption peak are not so obvious to interpret, as it is worth noting that this spectral region may also contain contribution from the absorption signal of fullerene. In contrast, the noticeable shift and concurrent broadening of the peak around 440 nm can be associated with a complexation behaviour between NG-ring and fullerene.

Stern-Volmer analysis

Figure 5.8 shows the Stern-Volmer plot derived from the fluorescence quenching data of Figure 5.5. In this plot, the fluorescence data are expressed in terms of $I_0/I([C_{60}])$, representing

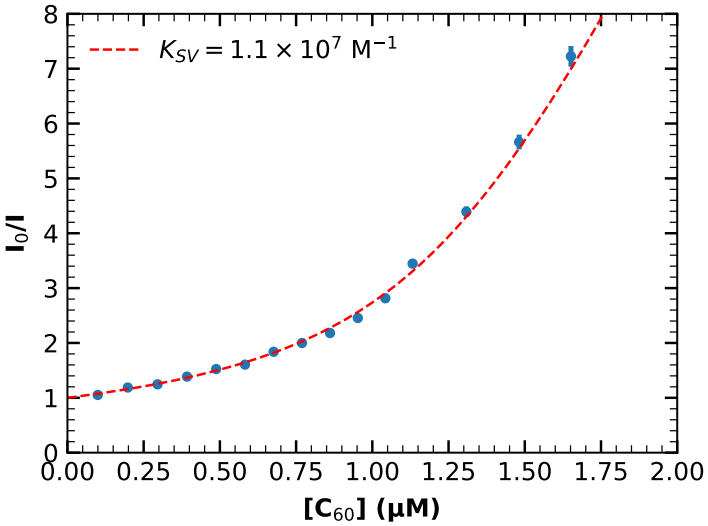

Figure 5.8: Stern-Volmer plot for the quenching of NG-ring PL upon addition of C_{60} and corresponding least-squares fitting curve according to equation 5.5. [Adapted from [295]].

the ratio between the emission intensity I_0 of NG-ring before the C_{60} addition and the emission intensity $I[C_{60}]$ after C_{60} addition at a $[C_{60}]$ concentration. The resulting Stern-Volmer plot, as a function of the C_{60} concentration, exhibit a deviation from linearity. This deviation is manifest as an upward curvature in the data trend. This, at a first glance, appears inconsistent with the intrerpretation of quenching being solely due to the formation of static complexes. Indeed, such a non-linearity is typically associated with collisional-mediated quenching behaviours [96]. Nevertheless, the absence of any change in the PL lifetime ruled out the possibility of dynamical quenching, and supported that the detected quenching should occur by a non-collisional mechanism, associated with the formation of host-guest complexes at the ground state level, in line also with the results provided by the analysis of the absorption spectra (see Figure 5.7)

In fact, the linearity of the Stern-Volmer equation which is commonly used for static quenching titration experiments, arises from the assumption that, given a certain initial concentration of fluorophore $[F]_0$ and quencher $[Q]_0$, the latter remains unmodified at any time. In other words,

changes in the concentration of the quencher are typically neglected because they are usually small. However, in a regime of high quencher depletion due to its effective complexation with the fluorophore, the linear model cannot hold. In more general terms, complex formation is considered as a reversible reaction with an equilibrium constant K, satisfying the equilibrium condition:

$$[FQ] = K[F][Q] \tag{5.1}$$

with

$$\begin{aligned} [F] &= [F]_0 - [FQ] \\ [Q] &= [Q]_0 - [FQ] \end{aligned} \tag{5.2}$$

where $[F]$ and $[Q]$ are respectively the fluorophore and quencher concentration at equilibrium, after a certain concentration of complex $[FQ]$ has formed. The three equations can be combined to obtain

$$[FQ]^2 - \left([F]_0 + [Q]_0 + \frac{1}{K}\right)[FQ] - [F]_0[Q]_0 = 0 \tag{5.3}$$

By solving it for $[FQ]$, only the following solution is physically meaningful:

$$[FQ] = \frac{1}{2}\left([F]_0 + [Q]_0 + \frac{1}{K} - \sqrt{\left([F]_0 + [Q]_0 + \frac{1}{K}\right)^2 - 4[F]_0[Q]_0}\right) \tag{5.4}$$

Thus, assuming that the fluorescence intensity is proportional to the concentration of uncomplexed fluorophore, we can write:

$$\frac{I_0}{I} = \frac{[F]_0}{[F]_0 - [FQ]} = \frac{2}{1 - \frac{1}{[F]_0}\left([Q]_0 + \frac{1}{K} - \sqrt{\left([F]_0 + [Q]_0 + \frac{1}{K}\right)^2 - 4[F]_0[Q]_0}\right)} \tag{5.5}$$

Equation 5.5 represents a generalized version of the Stern-Volmer equation, of which the more common linear Stern-Volmer equation represents a particular case. A similar derivation of the equation has been already reported in literature [302]. The data reported in Figure 5.8 as a function of $[Q]_0$, the concentration of fullerene effectively added to the solution, have been adequately fitted using eq. (5.5), keeping the known parameter $[F]_0$, the starting concentration of NG-ring, fixed. The fitting results closely align with the experimental data, confirming a 1:1 host-guest stoichiometry, and allowed to determine the Stern-Volmer binding constant for the interaction between NG-ring and C_{60} which is: $K_{SV} = (1.1 \pm 0.1) \times 10^7$ M^{-1}. This high value represent a direct evidence of the strong mutual affinity between the two nanosystems. Notably,

the estimated binding constant for the interaction between NG-ring and C_{60} falls within the same order of magnitude as that determined for the association of C_{60} with HBC-[10]CPP (2.33×10^7 M^{-1}) [188] and is almost one order of magnitude higher that the binding constant observed for unmodified [10]CPP (2.79×10^6 M^{-1}) [303].

Furthermore, cyclic and square-wave voltammetry measurements carried by the group of Prof. A. Campaña permitted to estimate the LUMO (lowest unoccupied molecular orbital) of NG-ring at −2.66 eV. Considering that the LUMO of fullerene is located at −3.7 eV, such a favourable alignment of their respective LUMO levels would facilitate an electron transfer process from photoexcited NG-ring to fullerene. Indeed, fullerenes are well-known electron acceptors [304, 305]. Therefore, the previously described emission quenching can be interpreted as a consequence of charge transfer processes occurring within NG-ring@C_{60} complex after photoexcitation.

Ultrafast charge-transfer

With the aim to elucidate the undergoing charge-transfer process and provide direct evidence thereof, ultrafast TA measurements under 400 nm excitation have been performed.

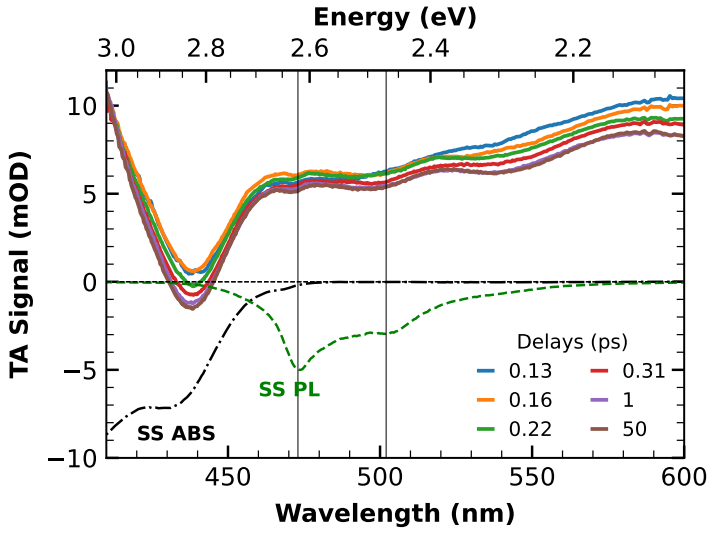

Figure 5.9: Transient absorption spectra acquired at different delays from photoexcitation at 400 nm of NG-ring in toluene (1×10^{-4} M). The signal is compared with the steady state (SS) absorption (ABS) and photoluminescence (PL) spectra to facilitate the identification of the various contributions to the TA signal. [Adapted from [295]].

In Figure 5.9 the TA spectra of bare NG-ring obtained at different time delays from excitation are reported. The TA signal exhibits several spectral features. Firstly, a pronounced negative contribution around 430 nm indicative of GSB. This interpretation is corroborated by the good agreement with the position of the inverted sign steady-state absorption (dash-dotted black curve). An extended ESA contribution spans the entire entire spectral range, culminating in a distinct band around 590 nm. Lastly, a scarcely discernible stimulated emission, is superim-

posed to ESA between 450 and 550 nm, as suggested by the coincidence with the main steady state emission subpeaks (dashed green curve).

Interestingly, the addition of C_{60} to a solution of NG-ring induces significant spectral changes in the TA signal. Figure 5.10 shows the TA spectra of NG-ring in presence of increasing additions of C_{60} fullerene, acquired at a time delay of 130 fs following excitation. The observed changes

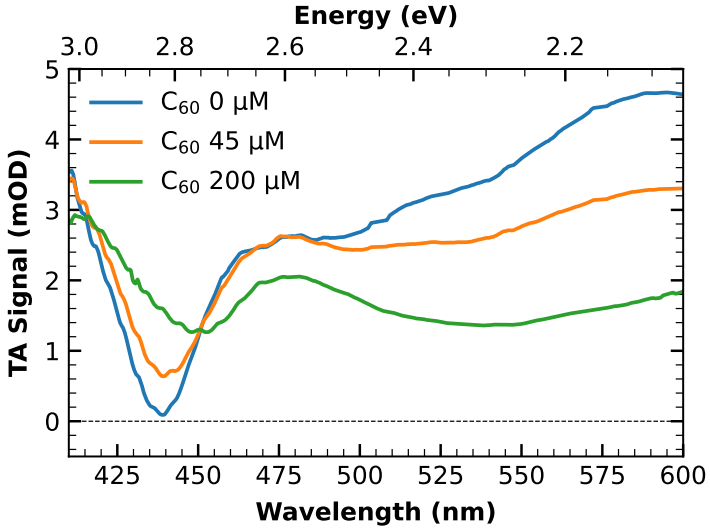

Figure 5.10: Transient absorption spectra at 130 fs delay from photoexcitation at 400 nm of NG-ring in toluene (1×10^{-4} M) in the presence of different concentrations of C_{60}: 0 µM (blue), 45 µM (orange) and 200 µM (green). [Adapted from [295]].

in the TA signal's shape accounts for the change of both ground- and excited electronic states of NG-ring upon binding with C_{60}. More specifically, the GSB peak redshifts from 435 to 450 nm, as a direct consequence of the shift of steady-state absorption spectrum reported in Figure 5.7. Additionally, the subpeaks associated with SE disappear, as expected due to the fluorescence quenching (Figure 5.5).

However, the change in the TA signal of the NG-ring due to the addition of C_{60} goes beyond alterations in spectral shape, as it also affects its temporal evolution. The different relaxation dynamics characterizing the TA signal of NG-ring and NG-ring@C_{60} complex are shown in Figure 5.11. Consistent with the ns-excited state lifetime of NG-ring (see Figure 5.3(b)), its TA signal shows minimal dynamics on the sub-ns timescale, apart from a slight relaxation occurring within the first ps. In contrast, as shown in Figure 5.11, NG-ring@C_{60} complex displays a synchronous decay of the overall TA signal, which is entirely absent in the bare NG-ring (Figure 5.9). Most notably, the data reveal that the spectral variations in the complex are already encountered at the earliest time delays accessible by the setup, as evident when comparing the spectra at 130 fs in the absence and in the presence of C_{60} Figure 5.10. This finding reveals that the electron transfer towards C_{60} is essentially "instantaneous", i.e. it occurs on a timescale faster than time resolution ~100 fs guaranteed by the experiment. Therefore, this charge-transfer transition takes place entirely within the duration of the photoexcitation pulse, leading to a quasi-instantaneous

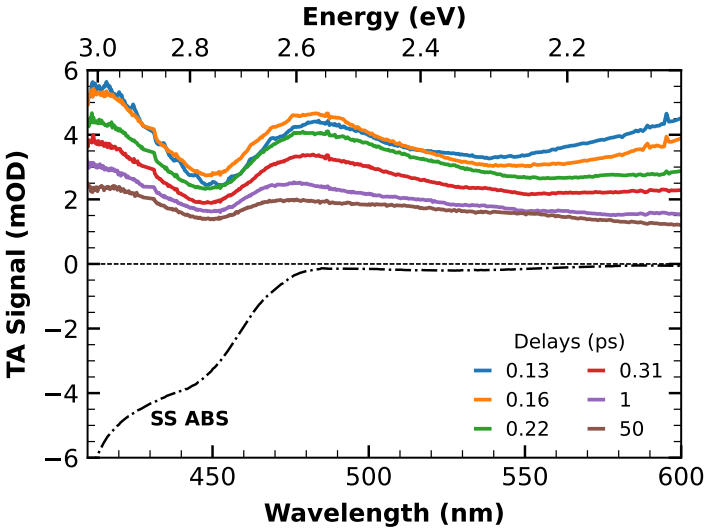

Figure 5.11: Transient absorption spectra acquired at different delays from photoexcitation at 400 nm of NG-ring in toluene (1×10^{-4} M) in presence of C_{60} (2×10^{-4} M). [Adapted from [295]].

separation of electron-hole pairs. Notably, such an ultrafast ($<$ 100 fs) charge separation is two orders of magnitude more efficient than previously reported for the host-guest complex between HBC-[10]CPP and C_{60} [188], where electron transfer from the photoexcited macrocycle to fullerene occurs over several tens of ps.

The different temporal evolution affecting NG-ring when it is complexed with fullerene is also evident from Figure 5.12, showing a comparison between the kinetic traces extracted at a representative probe wavelength of 480 nm from the TA data of NG-ring (blue) and NG-ring@C_{60} (orange), and the corresponding least-square fits with multiexponential decay functions. As previously discussed while analysing the temporal evolution of the spectral shape, noticeable relaxation dynamics significantly affect the TA signal of NG-ring@C_{60} complex within the first ps following photoexcitation, in contrast to bare NG-ring where the TA signal is almost constant. This decay encountered in the case of the complex can be interpreted as the progressive return of the complex back to the ground state, occurring through a back-electron-transfer (BET) from C_{60} to NG-ring. Consequently, the initial ultrafast electron transfer in NG-ring@C_{60} is succeeded by a non-radiative electron hole recombination, whose timescales were determined to be $\tau_1 = 110$ fs and $\tau_2 = 800$ fs through a bi-exponential fit of the data presented in Figure 5.12. The occurrence of such a BET is somehow expected, as the electrostatic interaction will tend to recombine the electrons injected into the fullerene with the hole available in NG-ring.

On the basis of the previously described results, Figure 5.13 illustrates schematically the forward- and back-electron transfer processes occurring within the NG-ring@C_{60} complex, with the corresponding timescales as obtained by the fitting of the TA data.

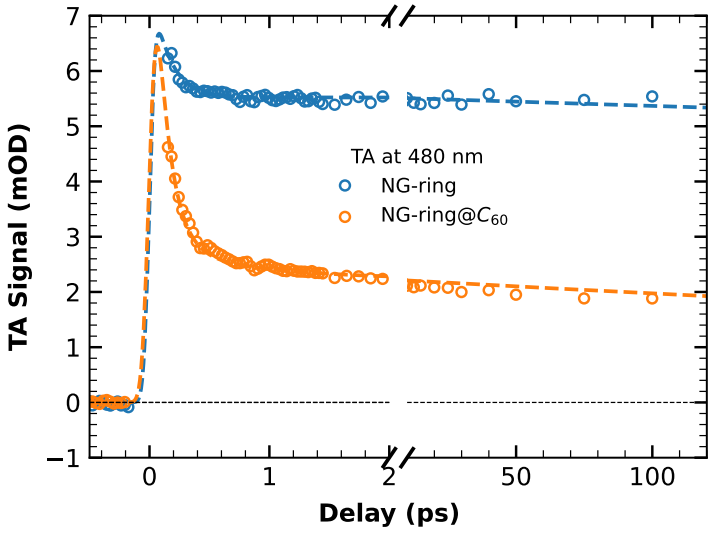

Figure 5.12: Comparison of the TA signal of NG-ring and NG-ring@C_{60} complex at probe wavelength of 480 nm. [Adapted from [295]].

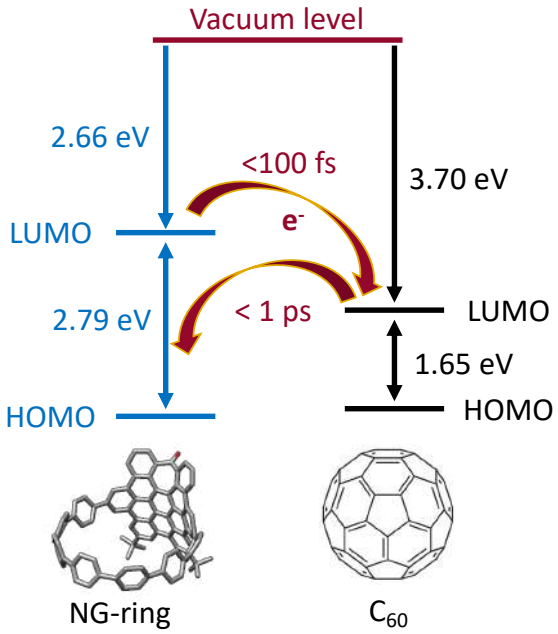

Figure 5.13: Schematized model of forward- and back-electron transfer occurring within NG-ring@C_{60} complex after photoexcitation. The characteristic timescales of the processes as obtained by fitting of the TA data are included.

5.3 Complexation with C70

As mentioned, NG-ring is expected to behave as a cage for both C_{60} and C_{70} fullerenes. On these grounds, the host-guest complexation behaviour of NG-ring with C_{70} has also been investigated.

Figure 5.14 highlights the effect of the progressive addition of C_{70} fullerene to a toluene solution of NG-ring. Specifically, Figure 5.14(a) shows the PL spectra of NG-ring collected at different concentration of C_{70}. As can be noticed, similar to what has been observed in the case of C_{60} (see Figure 5.5), the PL band undergoes a progressive reduction of it emission intensity, without any modification in shape. This quenching behaviour is quantitatively analysed in the inset of the same Figure, which presents a Stern-Volmer plot of the PL data as a function of C_{70} concentration. These data have been fitted according to eq. (5.5), and the resulting binding constant has been estimated to be $K_{SV} = (7.8 \pm 0.8)^6$ M^{-1}, indicating a slightly lower affinity compared to C_{60}. However, the obtained value is still almost three orders of magnitude higher than that characterizing the complexation between C_{70} and unmodified [10]CPP (8.4×10^4 M^{-1}) [303]. The marked increase in the thermodynamic stability of the host-guest complexation C_{70} with NG-ring compared to [10]CPP can be explained by considering the larger π-extended surface of the former. Most remarkably, the inclusion of a NG within CPP is particularly more relevant for the binding affinity with C_{70} than C_{60}, as in the latter case, the embedding of NG within CPP produced an increase of K_{SV} of just an order of magnitude.

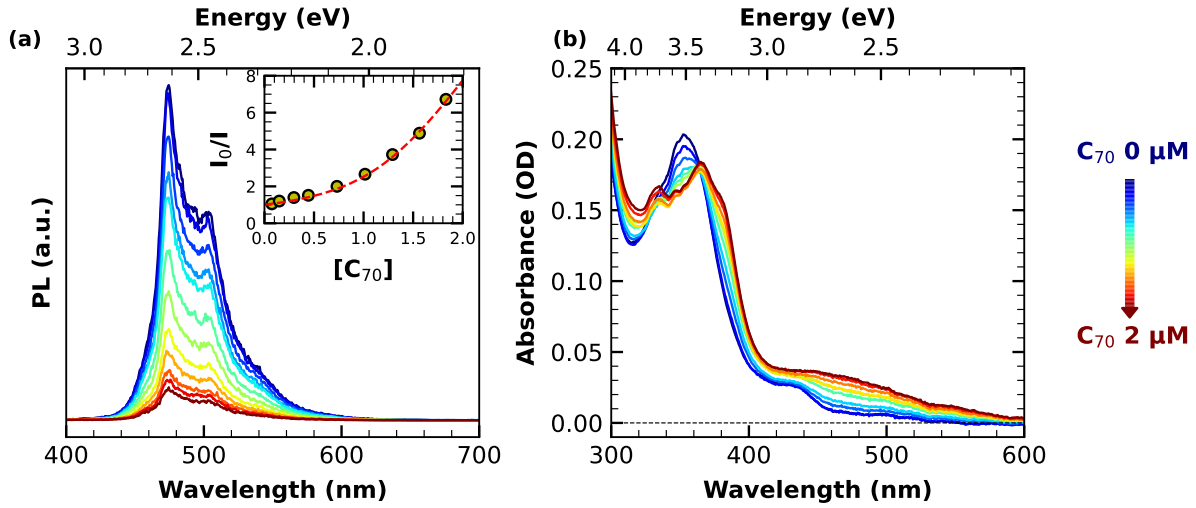

Figure 5.14: (a) PL spectra and (b) absorption spectra of NG-ring toluene solution (1×10^{-6} M) upon addition of increasing amounts of C_{60}. In the inset of panel (a) the Stern-Volmer plot of the corresponding quenching data is reported with the least-squares fitting curve. [Adapted from [295]].

Figure 5.14(b) shows the absorption spectra of NG-ring for increasing concentration of C_{70} added to solution. Also in this case, as was found for C_{60} (see Figure 5.7), the addition of C_{70} produces marked spectral shape modifications that affect the entire band, suggesting once again the establishment of strong ground-state interactions between NG-ring and C_{70}.

The static nature of the PL quenching is further corroborated by the lack of change in the decay dynamics of fluorescence. This is evident from Figure 5.15, which shows the normalized kinetic traces of PL decay for different concentration of C_{70}.

In order to fully reconstruct the relaxation dynamics occurring in the NG-ring@C_{70} complex

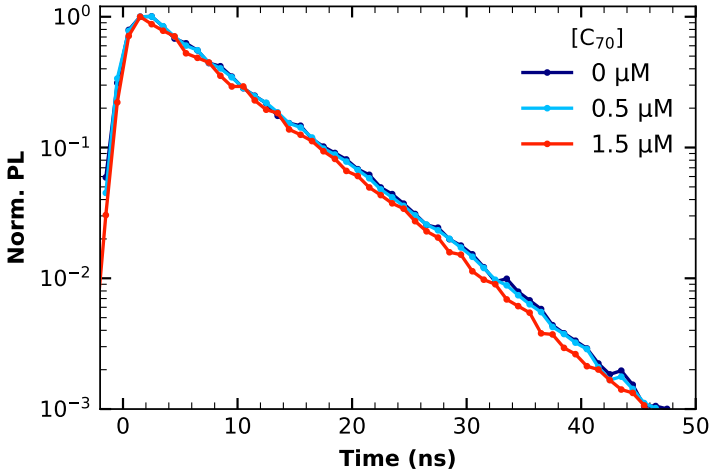

Figure 5.15: Comparison of normalized PL decay of NG-ring toluene solution (1×10^{-6} M) without (darkblue), with 0.5×10^{-6} M (blue) and 1.5×10^{-6} (red) C_{70}, under $\lambda_{exc} = 400$ nm. [Adapted from [295]].

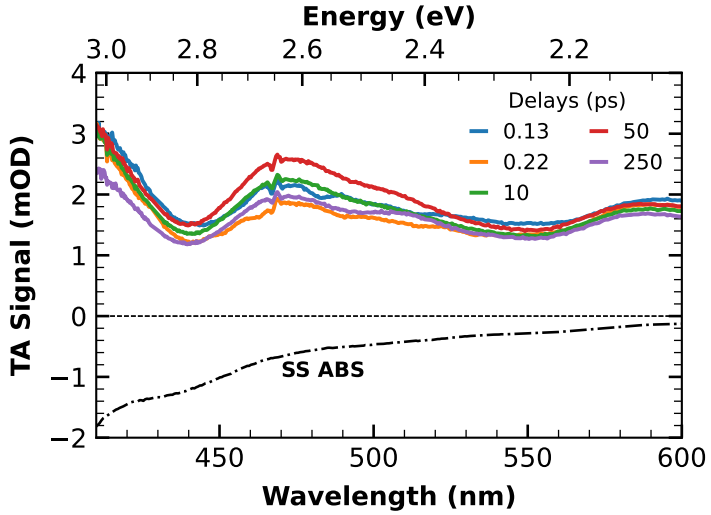

Figure 5.16: Transient absorption spectra acquired at different delays from photoexcitation at 400 nm of NG-ring in toluene (1×10^{-4} M) in presence of C_{60} (2×10^{-4} M). [Adapted from [295]].

after photoexcitation, fs-TA measurements under 400 nm excitation have been performed. The TA data of NG-ring@C_{70} are reported in Figure 5.16, displaying the TA spectra at different time delays from photoexcitation, together with the inverted sign steady-state spectrum of a solution of NG-ring@C_{70} to facilitate comparison. Also in this case, the shape of the TA signal changes compared to that of bare NG-ring (see Figure 5.9) already at the first time delays accessible by the experiment, pointing again to an ultraefficient electron transfer from NG-ring to C_{70} occurring within the time duration of the excitation pulse. The absence of any SE contribution in the TA signal, as well as the results of fluorescence quenching experiments, indicates that the

ground state recovery of the NG-ring@C_{70} complex still occurs through a non-radiative relaxation. However, unlike NG-ring@C_{60}, no obvious decay of the entire TA signal is detected for NG-ring@C_{70} over the ps scale. Thus, the photoinduced charge-separated state of NG-ring@C_{70} is characterized by a remarkably longer-lived character compared to its analogue complex formed by C_{60}. This represents a particularly appealing aspect, since the long-lived charge-separated nature of photoinducible states is crucial from an applicative standpoint, including photocatalytic and photovoltaic applications.

5.4 Conclusions

A specific example of a binary all-carbon nanocomposite involving the binding of a NG-based macrocycle (NG-ring) and C_{60} or C_{70} fullerenes has been presented. An opportune functionalization with a [10]CPP cycloparaphenylene allowed to obtain a new type of ring-shaped macrocycle containing for the first time an heptagon-containing nanographene in its structure. A fully detailed optical investigation permitted to highlight the remarkably high supramolecular receptor ability of NG-ring for binding with fullerenes, mediated by the $\pi - \pi$ interactions established due to the morphological complementarity between the host cavity and the curved guests. The binding constants estimated by fluorescence titrations, are one (with C_{60}) or two (with C_{70}) orders of magnitude higher than those reported for pristine [10]CPP.

The marked association between the two nanocarbon precursors is accompanied by strong change in the relaxation dynamics characterizing the NG-ring after photoexcitation. fs-TA measurements revealed the occurrence of an ultrafast electron transfer from NG-ring to the fullerenes, at least two order of magnitude more efficient than the one observed in a similar system incorporating a purely hexagon HBC unit. This proves the marked electron-donor nature of NG-ring in host-guest complexes involving fullerenes.

Moreover, for NG-ring@C_{70} complex, the absence of any ground state recombination up to the ps timescale suggests for it a long-lived nature for the charge-separated state. This aspect makes it particularly interesting for future studies as it may allow to efficiently harvest the photogenerated charges for prospective light-driven applications.

Results: Part II

Chapter 6

Charge transfer in CD/Ag nanohybrids

As previously mentioned, this Thesis also focuses on the utilization of a second class of luminescent zero-dimensional nanocarbons, commonly referred to as carbon dots (CDs), in the design of new nanohybrid materials. Indeed, CDs, with their water solubility, low cost, ease of synthesis, and numerous surface functional groups, offer high versatility for integration into complex structures through coupling with other species [184, 216, 306, 307]. Moreover, CDs exhibit strong UV-Vis light absorption and electron-transfer behaviours, making them exceptionally attractive for conducting solar-driven catalytic processes, either as photocatalysts themselves [308–310] or in combination with carefully chosen nanomaterials to form composite catalysts [186, 311]. Specifically, the object of the investigation described in the present Chapter, is to harness the unique properties of CDs to construct a specific type of binary nanohybrids, incorporating metallic nanostructures such as silver nanoparticles (AgNPs) or gold nanoparticles (AuNPs). While numerous studies have been reported of metallic nanoparticles coupled with fluorescent molecular dyes or semiconductor quantum dots, the investigation of their coupling with CD is limited to sparse works [192, 194, 312, 313].

A specific class of CDs was utilized in the attempt to design CD@MNPs nanohybdrids by coupling them with commercial gold or home-synthesized silver nanoparticles. Throughout the Chapter, a spectroscopic analysis is conducted to highlight the specific interactions established between the MNPs and the CDs. In particular, AgNPs were found to strongly interact with CDs, and the effect of the former on the emission properties of the latter will also be investigated through ultrafast spectroscopies. Finally, a proof-of-concept test will demonstrate the emerging photocatalytic activity associated with the CD@AgNP nanohybrids. Most of the results reported in this Chapter have been published in [314].

6.1 Employed Carbon Dots

For the described purposes, a particular type of CDs was chosen based on comprehensive investigations conducted by our research group in recent years, encompassing both synthetic preparation

and photophysical properties [17, 48, 53]. These CDs are synthesized through a straightforward bottom-up approach involving a thermally induced decomposition route, as described in the Materials and Methods Chapter. They exhibit a well-defined carbonaceous core with an average size of approximately 4 nm and a highly crystalline nature with a β-C_3N_4 structure, as illustrated in Figure 6.1(a), presenting a HR-TEM image of a single CD adapted from [53]. Infrared absorption measurements indicate that their disordered surface shell primarily hosts $-$COOH (carboxyl), $-CONH_2$ (amide) and $-$OH (hydroxyl) functional groups [53]. The dissociation of carboxylic surface groups imparts a negative net surface charge when CDs are dispersed in water, as indicated by a zeta potential value of $\zeta = -15 \pm 5$ mV under neutral pH conditions.

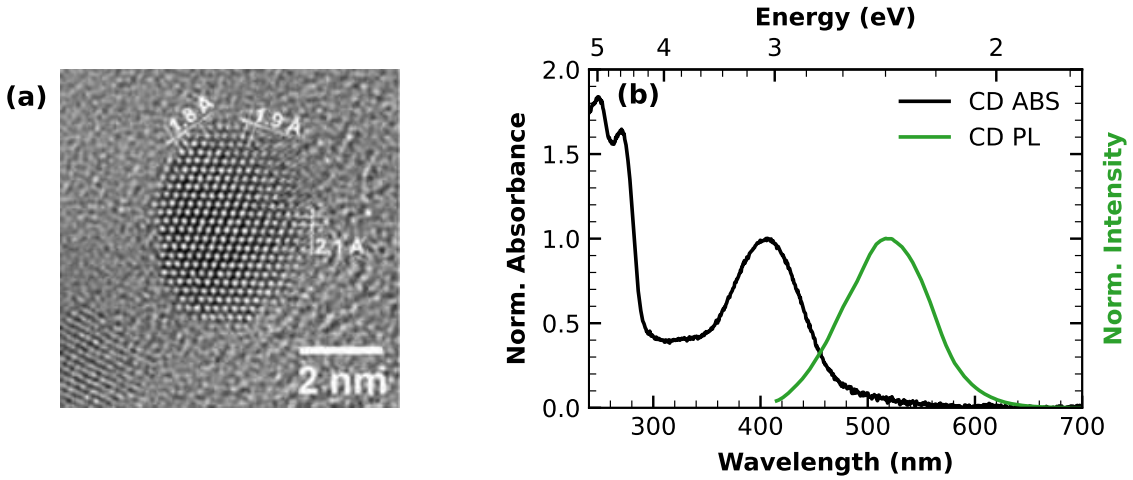

Figure 6.1: (a) HRTEM image of a single CD [adapted from [53]]. (b) Steady-state optical properties of CDs in water: normalized UV-Vis absorption spectrum (black) and the PL spectrum under 410 nm excitation (green).

The peculiar structural characteristics of these CDs, mainly associated with their high nitrogen content, are accompanied by peculiar optical features. Figure 6.1(b) reports the absorption (black curve) and emission (green curve) spectra of CDs. The absorption edge at wavelengths smaller than 300 nm corresponds to band-to-band core transitions, while the prominent absorption band peaking at 410 nm is a characteristic signature of nitrogen-rich bottom-up CDs. This band arises from a sub-gap transition involving the migration of an electron from the inner core of CDs to surface charge traps [315]. The primary optical activity directly associated with these CDs as obtained after synthesis, without any purification procedures, manifests as a visible band which is tunable in a large spectral range, spanning from 510 when excited at 400 nm to 560 with a 550 nm excitation. Their emission quantum yield is 12$\pm$1 % when dispersed in water.

6.2 Metallic Nanoparticles

In the study presented in this Chapter, two types of metallic nanoparticles were utilized in an attempt to construct Carbon/Metallic nanohybrids by exploiting the previously described

CDs. 40 nm AuNPs were commercially purchased from Sigma-Aldrich. In contrast, AgNPs were synthesized in-house using a synthetic route inspired by the well-known Turkevich method [223] fully detailed in the Materials and Methods Chapter. In short, a colloidal solution of AgNPs was obtained through the reduction of an aqueous silver salt solution with sodium citrate, which served the dual role of reducing and capping agent. Figure 6.2 illustrates a typical real-time monitoring of the synthesis. In particular, Figure 6.2(a) shows the extinction spectra collected

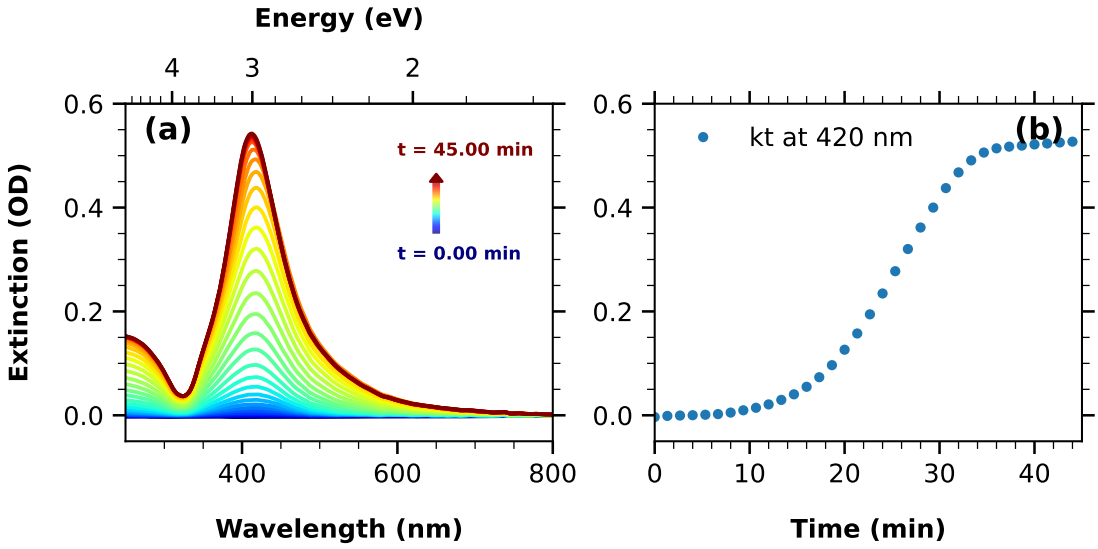

Figure 6.2: Real-time monitoring of AgNPs formation by the collection of (a) the extinction spectra of the solution taken during the synthesis at equidistant time interval from 0 to 45 min after starting the reaction. (b) Reaction kinetic obtained by reporting the signal at 420 nm of data in (a) *vs* reaction time.

at regular time intervals after the reaction was initiated. The rise of the characteristic AgNPs plasmonic band in the 420 nm spectral region provides a clear indication of successful AgNPs formation. Figure 6.2(b) reports a kinetic trace obtained from the left panel in correspondence of the plasmonic peak, highlighting the dynamic behaviour of the synthetic reaction. A saturation regime is approached after approximately 40 minutes, indicating the complete reduction of silver ions.

The particle size of the specific batch of AgNP synthesized for the purpose of this chapter was determined through DLS measurements, yielding diameters of 52 ± 6 nm. As confirmed also from SEM images like the one reported in Figure 6.3, most of the nanoparticles have a quasi-spherical shape, although a highly uniform size distribution is not observed.

In general, the construction and properties of composite nanohybrids could significantly depend on the surface charge of the starting precursors. In our case, the sign and magnitude of the MNPs' surface charge are expected to be critical in determining the ease of coupling to the negatively surface charged CDs. For both the AuNPs and AgNPs, negatively surface charge were revealed by ζ-potential measurements, providing values of $\zeta = -36 \pm 3$ mV and $\zeta = -23 \pm 5$ mV, respectively. In order to have two pairs of identical MNPs differing only in

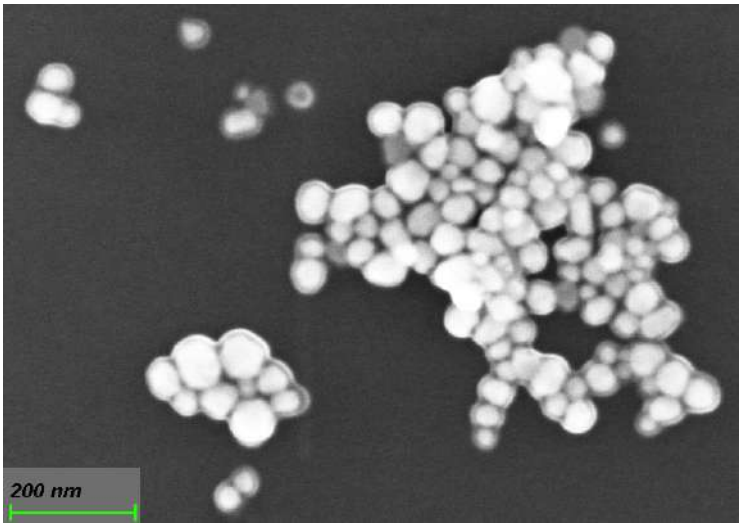

Figure 6.3: SEM image of AgNPs as obtained after synthesis.

the surface charge sign, the starting AuNP− and AgNP− underwent a ligand-exchange procedure with cationic cetyltrimethylammonium bromide (CTAB) molecules, as inspired by previous reports [226, 227] and fully detailed in Materials and Methods Chapter. This procedure resulted

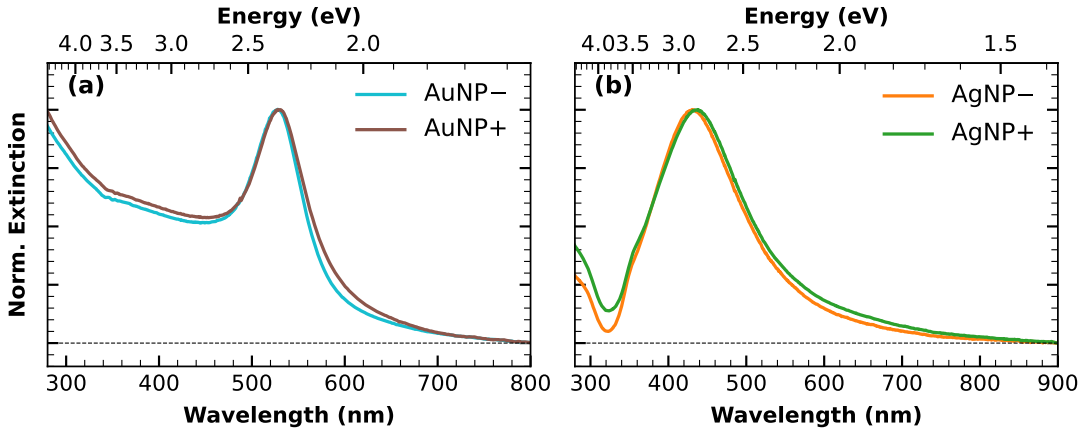

Figure 6.4: (a) Extinction spectra of the starting gold nanoparticles (AuNP−, in blue) and after the ligand-exchange procedure (AuNP+, in grey). (b) Extinction spectra of the starting silver nanoparticles (AgNP−, in orange) and after the ligand-exchange procedure (AuNP+, in green).

in positively surface-charged particles, as confirmed by a change in the sign of their ζ-potential values: $\zeta = +25 \pm 5$ and $\zeta = +33 \pm 6$ mV for AuNP+ and AgNP+, respectively. The different surface capping also led to a small but appreciable shift of the plasmonic bands characterizing the optical extinction spectra of the starting MNPs. This shift is shown in Figure 7.8, where the extinction spectra of the starting AuNP− and AgNP− are compared to their corresponding spectra after the ligand-exchange route, in panels (a) and (b), respectively. The tiny detected shift aligns with the different local environments experienced by the surface of the particles. Additionally, a

slight broadening of the plasmonic bands in the redder part of the spectra was detected and can be attributed to a certain degree of aggregates formation during the ligand exchange-procedure [227, 316]

6.3 Coupling of CDs to MNPs

Spectroscopic measurements were conducted to probe the potential establishment of interactions between CDs and gold or silver nanoparticles. Specifically, the impact of MNPs' addition to an aqueous solution of CDs was investigated by monitoring the effect produced by the former on the emission properties of the latter.

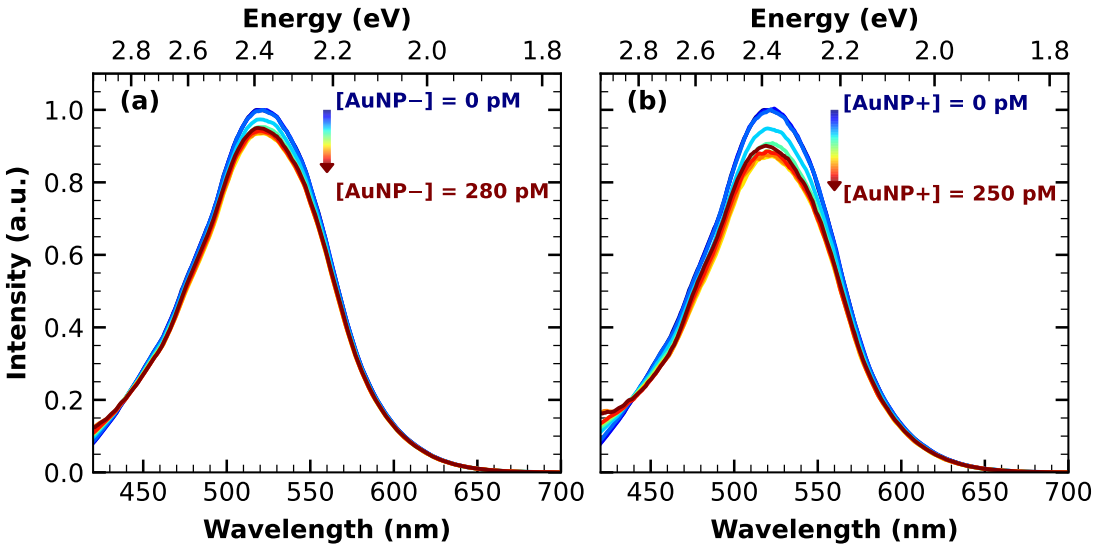

Figure 6.5: PL spectra under 410 nm excitation of an aqueous solution of CDs (∼60 nM) in the presence of an increasing amount of (a) AuNP− and (b) AuNP+, as indicated by arrows.

In Figure 6.5 the PL spectra of CDs solution (acquired under $\lambda_{exc} = 410$ nm) are displayed for increasing molar nanoparticle concentration of AuNP− and AuNP+, shown in panel (a) and (b), respectively. As depicted, only a minor reduction in the emission intensity of the PL band was observed, approaching saturation after the addition of less than one hundred picomolar AuNPs for both the negatively and positively charged surface versions.

In contrast, the addition of silver nanoparticles produced a more pronounced effect, as highlighted in Figure 6.6, where the PL spectra of CDs are presented for incremental additions of small aliquots of AgNPs. Specifically, panels (a) and panel (b) correspond to AgNP− and AgNP+, respectively. As evident, particularly when compared to the previous cases of AuNPs reported in Figure 6.5, the CDs' emission undergoes a significant quenching upon the addition of both types of AgNPs, implying the prompt establishment of some form of interaction between the CDs and silver nanoparticles. Even with exceedingly low concentrations of AgNPs (less than 1 pM), a slight yet appreciable reduction in emission is observed following the initial addition. It is important to note that the emission spectra presented in the Figure 6.6 were corrected [317] for

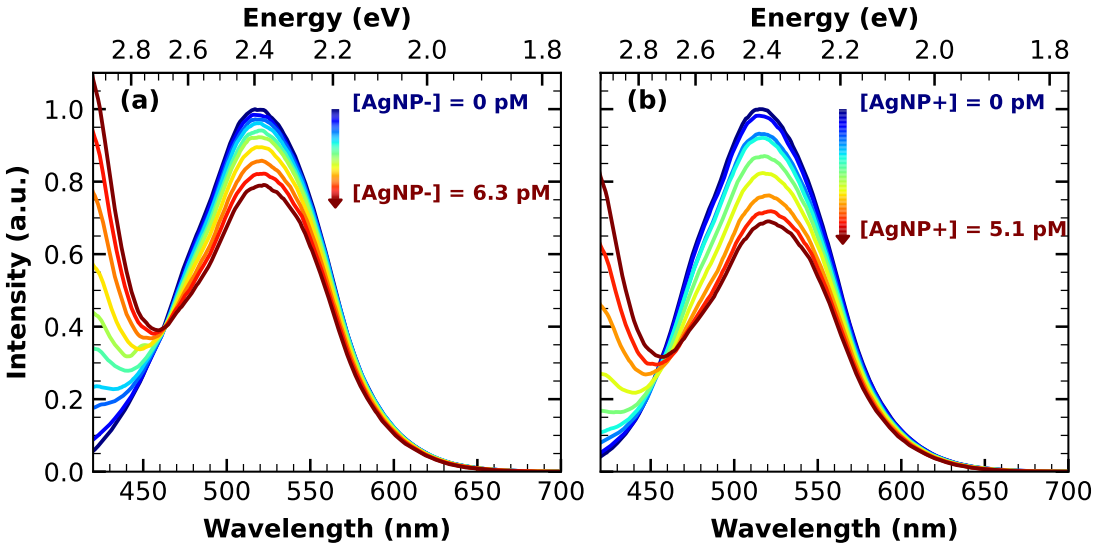

Figure 6.6: PL spectra under 410 nm excitation of a aqueous solution of CDs (∼60 nM) in the presence of an increasing amount of (a) AgNP− and (b) AgNP+, as indicated by arrows. [Adapted from [314]].

the inner-filter-effect caused by the partial absorption of excitation light by the silver nanoparticles. Conversely, the re-absorption of CDs' emission by AgNPs was found to be negligible within the examined concentration range. This can be inferred by the fact that emission quenching is not accompanied by significant alterations in the emission band shape. In fact, the presence of emission-reabsorption effects would otherwise distort the PL bandshape of CDs, due to its partial overlap with the absorption band of AgNPs.

Therefore, having identified that the most significant effects are linked to AgNPs, a more comprehensive optical investigation was carried out and will be presented in the following, to better establish the interactions responsible for the quenching of CD emissions induced by AgNPs.

The specific nature of the observed quenching of CDs' emission by AgNPs can be elucidated through time-resolved fluorescence measurements. Based on the results provided by the latter, a static nature can be ascribed to the quenching in the case of both the types of AgNPs, regardless of their surface charges. Indeed, as illustrated in Figure 6.7, the fluorescence decay of CDs remains unaltered upon the introduction of AgNPs. Aside from a slightly reduced initial intensity, the decay kinetics are identical for both AgNP+ and AgNP− addition. This rules out the possibility of a collisional PL quenching mechanism, which would otherwise result in a proportional reduction in PL lifetimes with increasing quencher concentration. Furthermore, diffusional-type quenching is highly improbable, given the very low concentration of metallic nanoparticles involved. Conversely, a decrease in intensity without changes in lifetimes aligns with the characteristics of static quenching occurring within stable complexes. These findings strongly suggest the spontaneous formation of stable CD@AgNP+ and CD@AgNP− complexes in solution, characterized by specific interaction between the two components, resulting in the suppression of CD emission effectively coupled to the silver nanoparticles.

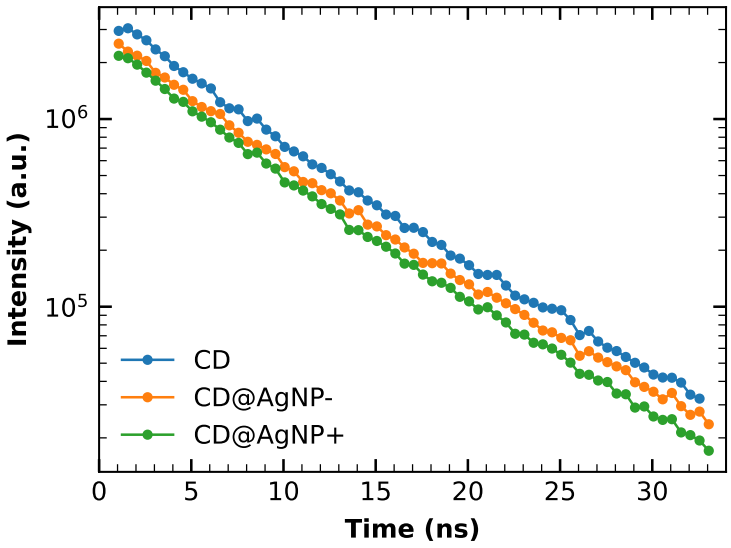

Figure 6.7: Emission decay traces collected from the solutions of pure CDs ∼60 nM (blue), CDs ∼60 nM with the addition of ∼6 pM AgNP− (orange) and CDs ∼60 nM with the addition of ∼5 pM AgNP+ (green). [Adapted from [314]].

The Stern-Volmer plots shown in Figure 6.8, obtained from data of Figure 6.6 by reporting the quantity $I_0/I - 1$ as a function of AgNPs concentration, provide a further quantitative assessment of the quenching behaviour. The clear linear trend observed for AgNP− is not found for AgNP+.

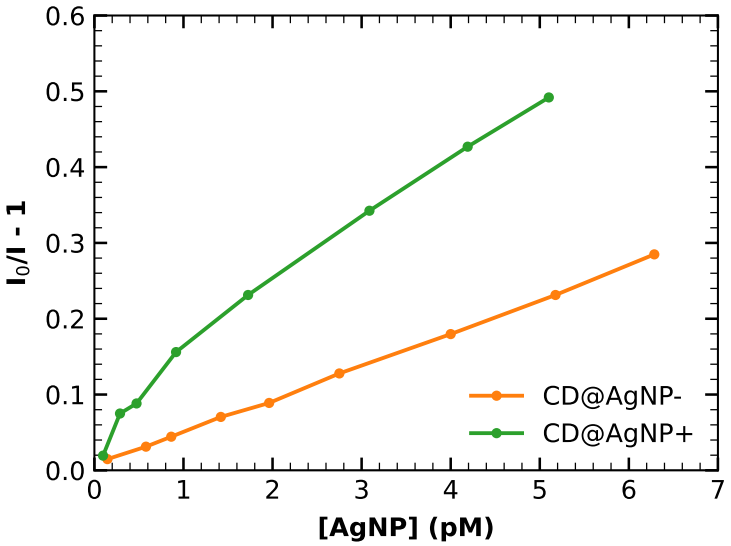

Figure 6.8: Stern–Volmer plots of the CD emission intensity quenched by AgNP− (orange) and AgNP+ (green). [Adapted from [314]].

In the latter case, a notably higher slope is detected, even at low AgNP+ concentrations (<1 pM), which gradually decreases at higher concentrations. Most importantly, the quenching induced by AgNP+ is found to be two to four times greater than that caused by AgNP−, at equivalent

concentration levels.

This finding is consistent with the opposite surface charges of AgNP+ and CDs, which should promote the establishment of mutual interactions. The positively charged quaternary amine present in the CTAB layer covering the AgNPs is expected to strongly interact with the negatively charged COO^- groups on the CD surfaces. Additionally, the non-linear trend observed the Stern-Volmer plot suggests the presence of at least two distinct geometric configurations characterized by varying degree of association. However, the occurrence of a PL quenching also in presence of AgNP−, though to a lesser extent, suggests that the interaction between CDs and AgNP− is not purely electrostatic in nature. In this scenario, one might consider that some hydrogen bonding interactions could take place between citrate ions on AgNP− and either -OH or -COOH groups of CDs.

Additional evidence of the interaction between CDs and AgNPs arises from the alterations observed in the absorption spectra reported in Figure 6.9. Indeed, the extinction spectra of

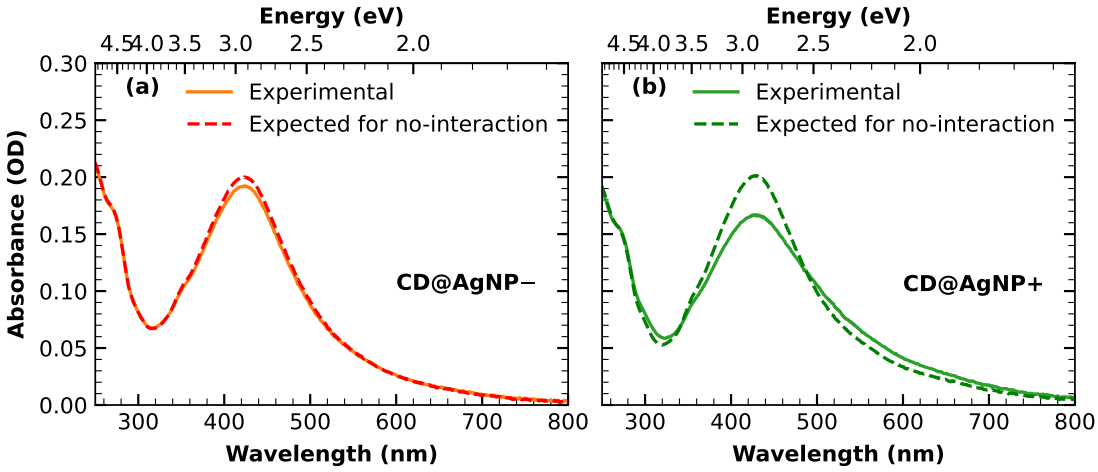

Figure 6.9: The continuous curves represent the experimental optical extinction spectra of mixed solution of CD with (a) AgNP− or (b) AgNP+. The dashed curves represent the corresponding extinction spectra theoretically expected in case of no mutual interactions between the two constituents, as obtained from the weighted sum of the experimental spectra of the two corresponding isolated constituents.

CD@AgNP nanohybrids do not simply correspond to a linear sum of the spectra of the two individual starting constituents. This is evident when comparing the experimentally acquired extinction spectra (continuous curves) of CD@AgNP− and CD@AgNP+ with the theoretically expected extinctions spectra (dashed curves) under the assumption of no interaction. Specifically, the latter spectra are obtained through an appropriate linear combination of the experimental spectra of the two corresponding isolated components, according to their relative dilutions. These differences underscore the existence of strong interactions between CDs and AgNP, even at the ground state level, consistent with the formation of CD@AgNP complexes, as also reported for other fluorophore/metallic nanoparticle systems [318, 319]. Besides, this effect is much more pronounced in the case of AgNP+, in agreement with the PL data presented in Figure 6.6.

In addition to the spectroscopic characterization, CD@AgNP+ solutions were also analysed by HRTEM, through the collaboration of Dr. C. Sourov. Due to the inherently low electron density of CDs, direct imaging of CDs in close proximity or attached to the surfaces of AgNPs is generally a hard task. Nevertheless, direct visualization of CD adhering to the surface of AgNP was observed, as reported in Figure 6.10. This provides additional substantiation that the quenching phenomenon occurs through the formation of stable CD@AgNP nanohybrids, upon the self-assembly of the two components in the solution phase.

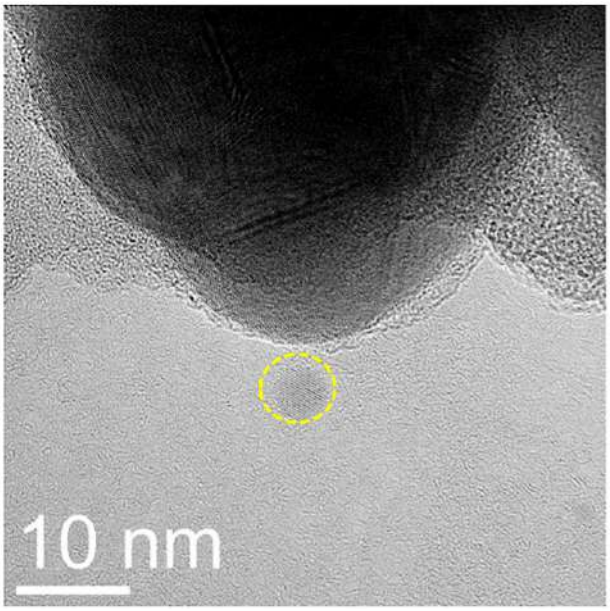

Figure 6.10: HRTEM image of CD@AgNP nanohybrid. Yellow circle highlights a crystalline spot with sizes of ∼4 nm. Low contrast is due to carbon dots in close proximity to the surface of AgNPs. [Adapted from [314]].

6.4 Ultrafast photoinduced electron-transfer in CD@AgNP

Prior computational and experimental investigations of CDs have proposed that their photoexcited state is characterized by an excess of the negative charge on surface groups, making CDs proficient electron donors under photoexcitation [315, 320, 321]. In the case of CD@AgNP+, one could expect that the transfer of a photoexcited electron from CD to the positively charged AgNP+ is energetically favourable. This expectation takes into account the fact that the Fermi level of silver, which is reported to be approximately −4.7 eV for the bulk Ag relative to the vacuum energy level [322], is at a lower energy than the LUMO of CDs (approximately −4 eV *vs* vacuum energy level [9]). Therefore, the observed quenching in CD@AgNP is most likely attributed to an electron transfer from CDs to AgNPs, a phenomenon frequently observed for chromophores in the near proximity of metal surfaces [323]. On these grounds, ultrafast TA measurements were performed to highlight any difference in the relaxation dynamics of bare CD with that of CD@AgNP− and CD@AgNP+, aiming to better unravel the occurrence of charge

transfer within the nanohybrids following photoexcitation,

TA signal of bare CDs

In Figure 6.11, the TA data collected from the a solution of naked CDs are presented as a time-wavelength 2D plot. From it, spectra at various delays following photoexcitation are extracted and displayed in panel b of the same Figure. The TA signal of CDs reveals two main components.

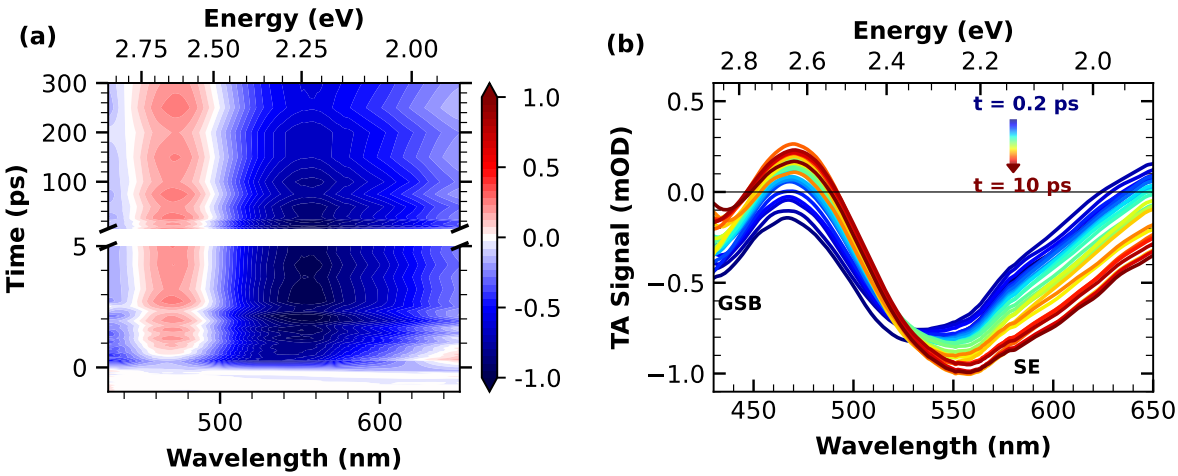

Figure 6.11: (a) Time-wavelength TA plot of the bare CD aqueous solution upon 400 nm excitation and at magic angle detection. (b) Selected TA spectra at different delays from photoexcitation, continuously increasing from 0.2 ps (blue line) to 10 ps (red line), as obtained by horizontal cuts of the 2D plot of the panel (a). [Adapted from [314]].

Firstly, a negative contribution is evident in proximity to the pump wavelength (400 nm). This is primarily associated with the GSB resulting from the ground-state depopulation induced by pump absorption. Secondly, a strong SE is observed to shift from 520 to 550 nm over time. The main spectral evolution involves a dynamical Stokes shift in the the SE signal, i.e. the fluorescence, which occurs within the initial picoseconds and is attributed to solvatochromic relaxation [315]. It is worth noting that a reduction in the negative signal near the pump wavelength is also appreciable. However this reduction can be attributed to the partial disappearance of an overlapping blue SE signal, which, for the sake of our objectives, will not be further explored in this context.

The same experiment was carried out for CD@AgNP− and CD@AgNP+ nanohybrids. Their solutions were prepared by keeping an equivalent CD concentration as in the case of the previously reported measurements, to allow for a better comparison. Under these equivalent conditions, the TA observed in the nanohybrids exhibit an overall resemblance to that of bare CDs. However, the comparisons proposed in Figure 6.12 shows several important differences. Specifically, the negative component associated with the SE appears considerably less intense in the case of CD@AgNP nanohybrids also at the first delay accessible by the experiment (see Figure 6.12(a)).

This reduced SE signal provides additional confirmation of the quenching effect on CDs' emission induced by both types of AgNPs. Most importantly, this finding underscores the rapid nature of the quenching process, which takes place within 300 fs after photoexcitation.

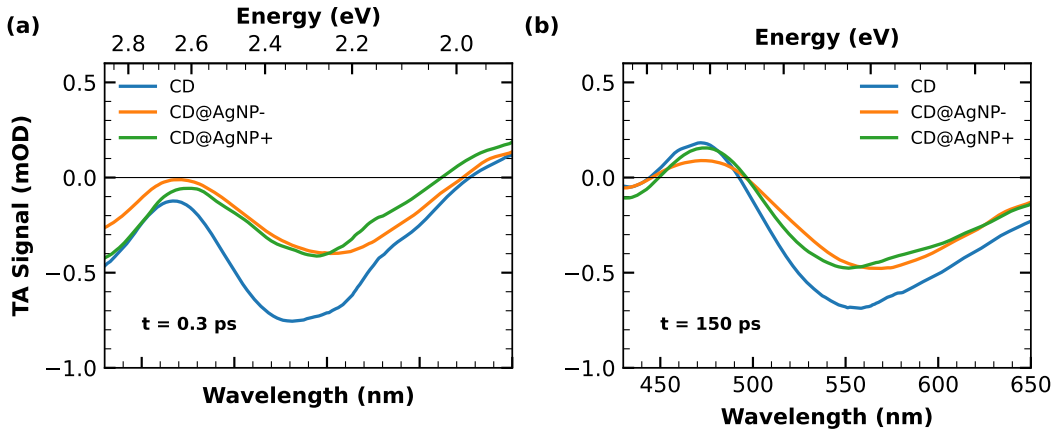

Figure 6.12: Comparison of the TA spectra of the bare CD (blue), CD@AgNP− (orange) and CD@AgNP+ (green) solutions recorded at (a) 0.3 ps and (b) 150 ps after photoexcitation. [Adapted from [314]].

Moreover, a comparison of the GSB signals provides further insights into the mechanism responsible for the quenching. In the case of the solution with positively charged AgNP, a close correspondence between the GSB signal of bare CD (blue curve) and CD@AgNP+ (green curve) is observed, despite the reduction in the SE signal. This suggests that the transfer of the photoexcited electron from CD to positively charged AgNP+ leaves an unpaired hole in CD, thereby preventing their return to the ground state. Interestingly, the GSB signals in the bare CDs and CD@AgNP+ converge and become very similar to each other at longer times (150 ps, see Figure 6.12(b)), suggesting that the charge-separated state eventually recombines through a back electron transfer (BET) from AgNPs to CDs.

Concerning CD@AgNP−, one might expect that an electron transfer is hindered due to the negative surface charge of the accepting metal nanoparticle. Indeed, data collected on CD@AgNP− at early times reveal that in this case, fluorescence quenching (the reduction of the SE) is accompanied by the return of CDs to their ground state, as inferred from the corresponding attenuation of the GSB signal (compare in Figure 6.12(a) blue and orange curves at 420 nm). This difference can be explained by assuming that, instead of electron transfer, CD@AgNP− undergoes an energy transfer from the excited CD to the nearby MNP. In this scenario, the entire electron-hole pair initially formed on CDs is transferred to AgNPs, resulting in the concurrent quenching of both the SE and the GSB signals of CDs. Another plausible explanation would be the occurrence of a very fast BET. In practice, an energy transfer cannot be distinguished from a rapid sequence of electron and back-electron transfer, in a scenario in which both these processes occur within the time resolution of the setup.

To quantify the time scales and the associated spectral evolution, the experimental data of

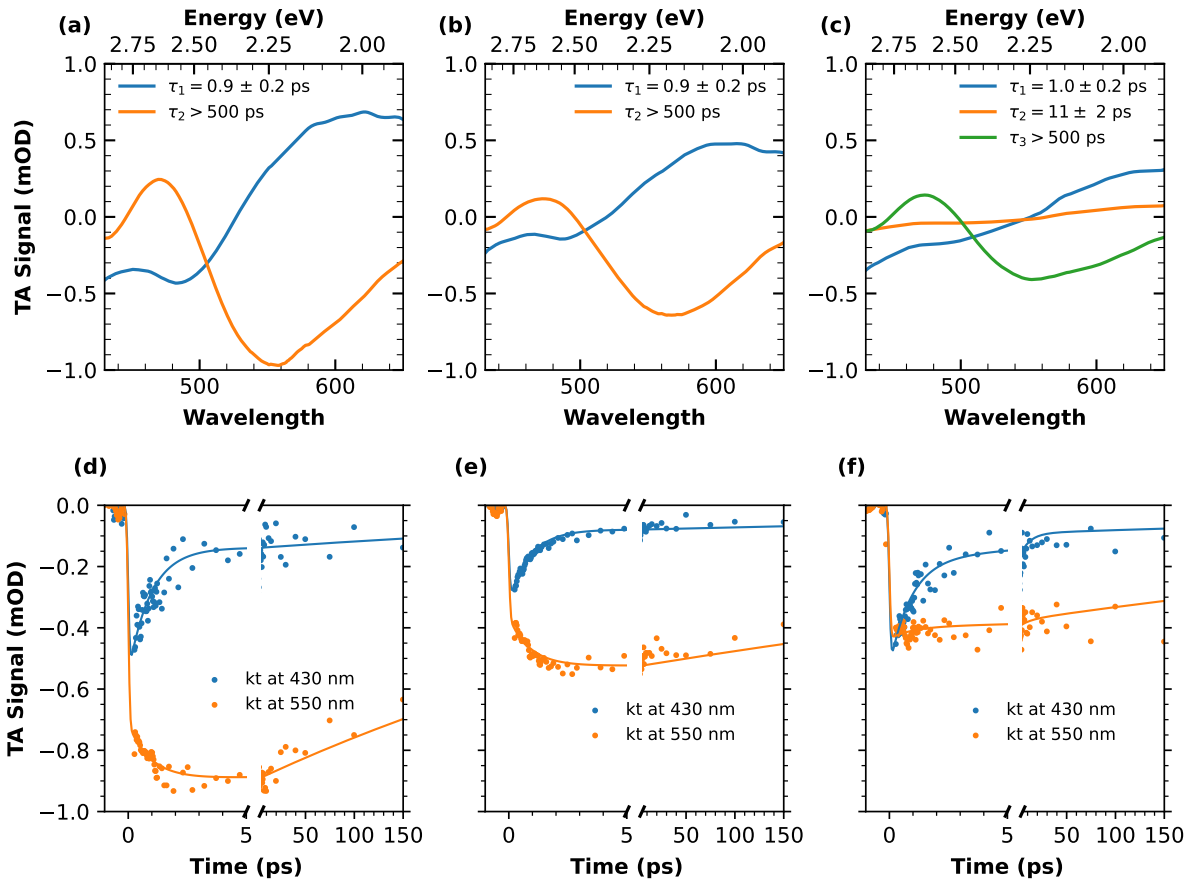

Figure 6.13: Top: DAS spectra from SVD analysis of TA data, with the corresponding lifetimes of (a) bare CD, (b) CD@AgNP− and (c) CD@AgNP+ solutions. Bottom: TA time traces at 430 nm (blue) and 550 nm (orange), with the respective least-squares fitting curves (continuous lines) of (d) CD, (e) CD@AgNP− and (f) CD@AgNP+. [Adapted from [314]].

the three experiments were decomposed via singular value decomposition (SVD) global analysis. The results of this analysis, including DASs and associated lifetimes, are presented in the top panels of Figure 6.13, while fitting curves of selected time traces are shown in the corresponding bottom panels of the same Figure.

Consistent with the explanation provided earlier, the entire spectral evolutions of CD and CD@AgNP− samples are effectively described by similar DAS, differing only by a constant factor, with lifetime of $\tau_1 = 0.9 \pm 0.2$ ps and $\tau_2 > 500$ ps (Figure 6.13(a)-(b)). This latter lifetime accounts for the slow depopulation of the excited state at long times and the concurrent return to the ground state. The time scale τ_1 relates to the red-shift of the spectrum resulting from solvation dynamics, as indicated by the derivative-like line shape with a zero near to the SE peak. In the assumption of a photoinduced energy transfer occurring in less that 300 fs, as responsible of the emission quenching of CDs when coupled to AgNP−, the registered TA signal can be assumed to primarily originate from the fraction of CDs in the solution not bound to AgNP−. Consequently,

the TA dynamics observed in CD@AgNP− and unmodified CDs are nearly identical, as observed. In contrast, as depicted in Figure 6.13(c), an additional dynamic component is evident in the case of CD@AgNP+ solution, characterized by a lifetime of $\tau = 11 \pm 2$ ps. Since this process occurs considerably later than the quasi-instantaneous (< 300 fs) electron-transfer, it can be attributed to a BET from AgNP+ to CDs, ultimately closing the photocycle of the complex. It is somehow surprising how both the atomically-precise NG-ring studied in the previous chapter and the CD presented here exhibit equivalent ultra-high efficiency in electron-donating properties, as the observed timescale of photoinduced electron transfer is comparable for these nanocarbon systems, despite being coupled to significantly different nanomaterials.

6.5 Proof-of-concept photocatalyitc activity

The photoinducible charge-separated state observed, at least for CD@AgNP+, prompted an investigation into their potential photocatalytic applications. To do this, experiments involving the photodegradation under visible-UV light irradiation of methylene blue (MB), a commonly used reference dye for standard photodegradation tests [324, 325], were performed. The MB photodegradation treatments were carried out using either the CD@AgNP− or CD@AgNP+ nanohybrid as photocatalysts, alongside three additional reference experiments involving the bare CD, AgNP− and AgNP+ solutions, respectively. To ensure a fair comparison, the experiments were conducted using five equally concentrated solutions of MB, to which comparable amounts of photocatalysts were added each time. The MB photodegradation was monitored by continuously recording its absorption spectrum over a 90 minutes period under illumination from a Xe lamp. The results are presented in Figure 6.14(a), where the absorption spectra of MB/CD@AgNP+ are overlaid using a color scale accounting for different time delays from the starting of light irradiation.

Figure 6.14(b) compares the photodegradation activities with that found in the other experiments, by reporting the percentage of MB removal overt time, as directly determined from the corresponding evolution of UV-Vis spectra. In the control experiments, minimal photodegradation of MB was observed, although pure AgNP− and AgNP+ solutions exhibited slightly higher and lower photocatalytic efficiency, respectively, compared to bare CDs. This difference may be attributed to variation in MB adsortpion on the photocatalysts due to the cationic nature of the dye. In contrast, both nanohybrids revealed significantly enhanced photodegradation activity. Within 90 minutes of light exposure, CD@AgNP− photocatalyst reduced more than 10% of the MB content, CD@AgNP+ achieved nearly double that efficiency. This result aligns with the earlier observations of stronger electronic interactions in CD@AgNP+, especially considering that the cationic nature of MB likely reduces the photodegradation efficiency of CD@AgNP+, whereas it is favoured in the case of CD@AgNP− nanohybrids due to their larger active surface area for local MB attachment.

Although these experiments were thought just as proof-of-concept tests, they offer further support for the understanding of the underlying processes and confirm the initial interpretations. Notably, both types of CD@AgNP nanohybrids exhibit significant emergent photocatalytic activity, surpassing the capabilities of their individual precursors. The increased photocatalytic activ-

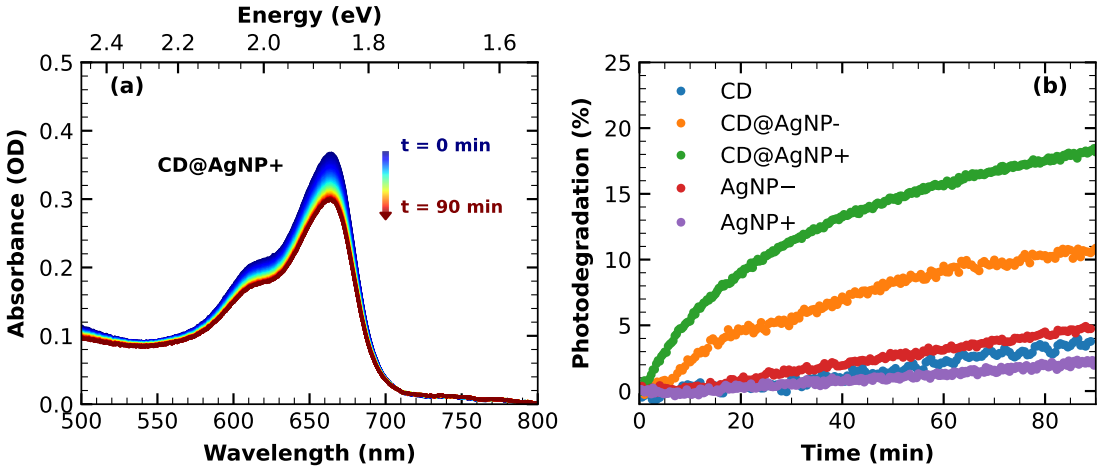

Figure 6.14: (a) UV-vis spectra of methylene blue as a function of the time under continuous illumination in the presence of CD@AgNP+. (b) Percentage of methylene blue photodegradation under continuous illumination in the presence of the bare CDs (blue), CD@AgNP− (orange), CD@AgNP+ (green), pure AgNP− (red) and pure AgNP+ (violet). [Adapted from [314]].

ity of CD@AgNP+ nanohybrid can be attributed to the facilitated electron-transfer mechanism between CD and AgNP+. The photostimulated electron transfer from CD generates quasi-free electrons on the AgNP+ available for subsequent reactions, ultimately responsible for degrading the MB dye. Regarding CD@AgNP− nanohybrids, based on the previous results, the interpretation of the quenching interaction could be equally described either as an energy transfer or as a fast sequence of forward and back-electron transfers. The observation of MB degradation also in presence of CD@AgNP− leans toward the latter interpretation. Moreover, the coexistence of an additional photodegradation mechanism of methylene blue involving hydroxy radicals produced by photoholes [324] cannot be completely ruled out, potentially accounting for the ultrafast ground state recovery of the CDs highlighted by TA data.

6.6 Conclusions

Commercial gold nanoparticles and home-synthesized silver nanoparticles were employed as building blocks of functional nanohybrids obtained by coupling them to a specific type of CDs. Specifically, for each type of metallic nanoparticle, two versions with opposite surface charges were prepared. No significant interactions were established between CDs and gold nanoparticles, regardless of the surface charge of the latter.

Instead, the fully detailed optical investigation presented in this chapter revealed evidence of successful binding between CDs and AgNPs. This binding was primarily demonstrated by the static quenching od CDs' emission due to highly efficient photoinduced electron transfer, occurring within 300 fs.

In proof-of-concept photocatalytic experiments, it was observed that CD@AGNP nanohybrids exhibited emergent photocatalytic activity, which was absent in the starting components. This

emergent photocatalytic activity could be attributed to electronic interactions taking place within the systems.

Furthermore, the results suggest that control over surface charge of silver nanoparticles plays a crucial role in designing functional CD@AgNP nanohybrids. While CDs can indeed be successfully coupled also to negatively charged AgNPs, in comparison to the results achieved with positively charged AgNPs, the negative charge on the metal nanoparticles reduces the fraction of CDs effectively binding to them. Consequently, this reduction impedes electron transfer and hinders the subsequent formation of a long-lived charge-separated pair, which is ultimately responsible for the photocatalytic response.

Besides contributing to the clarification of the specific interactions between CDs and silver nanoparticles at a fundamental level, the reported results are very promising in view of the development of a new class of eco-friendly functional nanohybrids for light-driven catalytic applications.

Chapter 7

Coupling of PEGylated CDs to metallic nanoparticles

In the preceding chapter, the interactions between a specific type of CDs and metallic nanoparticles were assessed. In particular, it was found that AgNPs quench the emission of CDs due to a photoinduced electron transfer from CDs to AgNPs. The occurrence of charge-transfer processes is highly favoured by the close contact between the two nanosystems. Considering this, introducing a physical spacer between these two systems can entirely transform the optical processes involved. Indeed, it is expected that this separation enables more effective exploitation of the localized surface plasmon resonance (LSPR) properties of the metallic nanoparticles. The highly localized fields generated during plasmon resonance excitation allow MNPs to strongly enhance the emission properties of nearby fluorophores *via* electromagnetic field-enhanced excitation or through bi-directional energy exchanges [326–330]. In order for these interactions to occur, it is crucial to prevent charge-transfer processes, which are extremely short-range phenomena, following exponential decay laws with an effective range of a few angstroms [331]. This is usually achieved by maintaining a suitable separation between the emitting fluorophore and MNPs, thereby avoiding direct contact and the consequent competitive quenching processes like those observed in the previous chapter, where direct contact between CDs and AgNPs resulted in the quenching of the CDs' emission. When an opportune separation is present, plasmonic interactions between the fluorophore and MNPs can significantly increase the excitation or radiative decay rate of the fluorophore. Moreover, the extent of enhancement depends on the spectral matching between the optical characteristics of the emitting species and the plasmonic band of the MNPs. In practice, MNPs are widely employed to induce fluorescence enhancement in various types of fluorophores, including organic dyes [327, 332, 333] and quantum dots [326, 334, 335]. However, up to now, works related to plasmonic enhanced fluorescence on CDs are limited to sparse reports [180, 194, 313, 336, 337], and the fundamental mechanism underlying fluorescence enhancement has not been fully elucidated.

With this in mind, a PEGylation through a solvothermal method was executed on the surface of the same CDs from the previous study. Specifically, two polymeric chains of different lengths were used to have the possibility of modulating the thickness of the surface shell covering CDs

and, then, their physical separation from the metallic nanoparticles. The effects of surface PEGylation of CDs are investigated in the first part of the Chapter, with a particular focus on the changes produced in the optical properties of CDs. Thus, after providing some details on the gold and silver nanoparticles, their coupling with PEGylated CDs will be studied from an optical perspective.

7.1 PEGylation of CDs

The green-emitting CDs that were employed in the study of the preceding chapter, have been subjected to a surface passivation in order to create a polymeric shell, acting as a physical spacer between the CDs and any potential external interacting systems. Specifically, the surface functional groups of CDs were reacted with polyethylene glycol (PEG) of two different molecular weights: 400 and 3000 Da. The PEGylation reactions were conducted at 120° C for 24 hours using a hydrothermal route, fully described in the Materials and Methods Chapter.

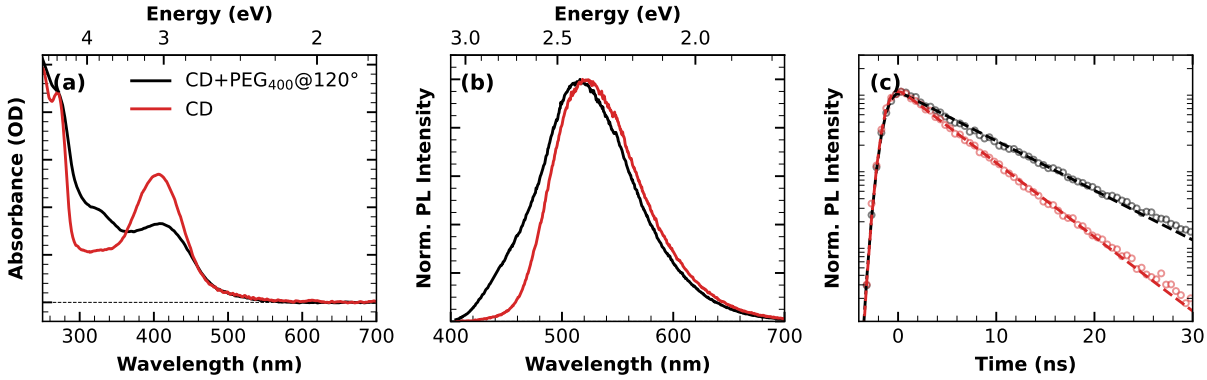

Figure 7.1: Comparison between (a) absorption spectra, (b) PL spectra and (c) PL decay of CDs after (black) and before (red) the PEGylation reaction.

Figure 7.1 summarizes the impact of the PEGylation reaction on the main optical characteristics of CDs, immediately after the high-temperature route. Specifically, Figure 7.1(a) illustrates the comparison between the UV-Vis absorption spectrum of CDs immediately after PEGylation process (black) and that of pristine CDs (red). Notably, the primary observed effect is the decrease of the characteristic band located around 410 nm associated with a sub-gap transition of the nitrogen-rich CDs, along with a broadening of the UV peak at ∼270 nm. This is accompanied by a slight increase in the absorption in the spectral region around 330 nm, which is recognized in literature as the fingerprint of citrazinic acid and related derivatives [315]. Similarly, in Figure 7.1(b), the impact of PEGylation on PL emission is examined, revealing some changes in the PL band. It appears to be more symmetric after the reaction, as evidenced by the increased relative signal in the bluer part of the spectrum. Nevertheless, it seems that the surface passivation does not significantly alter the green electronic transition. Time-resolved PL measurements in Figure 7.1(c) demonstrate that PEGylated CDs exhibit a longer emission lifetime, likely due to PEGylation which determines an improved surface passivation, enabling a better screening effect

from water molecules.

All the data reported in Figure 7.1 were obtained from the solution of CDs immediately following the surface passivation process with PEG400. However, one might expect that this solution contains unreacted CDs, free PEG molecules, and various impurities or aggregates. To address this, size exclusion chromatography (SEC) was employed to purify the sample, aiming to isolate the fraction primarily composed of PEGylated CDs. The SEC procedure involved using 2 mL of the initial sample as eluant and collecting different fractions of the eluate. The absorption spectra of these various fractions are presented in Figure 7.2, with slight vertical shifts applied to facilitate comparison. Based on the spectral characteristics of these absorption spectra, it is possible to group all the fractions into three distinct subsets: fractions 1-2-3 into subset A, fractions 4-5-6 into subset B, and fractions 7-8 into subset C.

In subset A, the spectra of the three fractions display broadened bands at 410 nm and 270 nm compared to those of pristine CDs. This suggests that subset A predominantly contains PEGylated CDs, to which, in the following, it will be referred to as P400-CD. This is also consistent with their early elution due to their expected larger size. Subset B comprises CDs whose absorption spectra closely resemble those of the starting CDs, particularly with a more pronounced peak at approximately 330 nm. The CDs of this subset likely underwent partial or no reaction with PEG. Finally, subset C appears to contain a substantial quantity of big aggregates, as indicated by the extremely broad shape of the absorption spectra extending up to 600 nm.

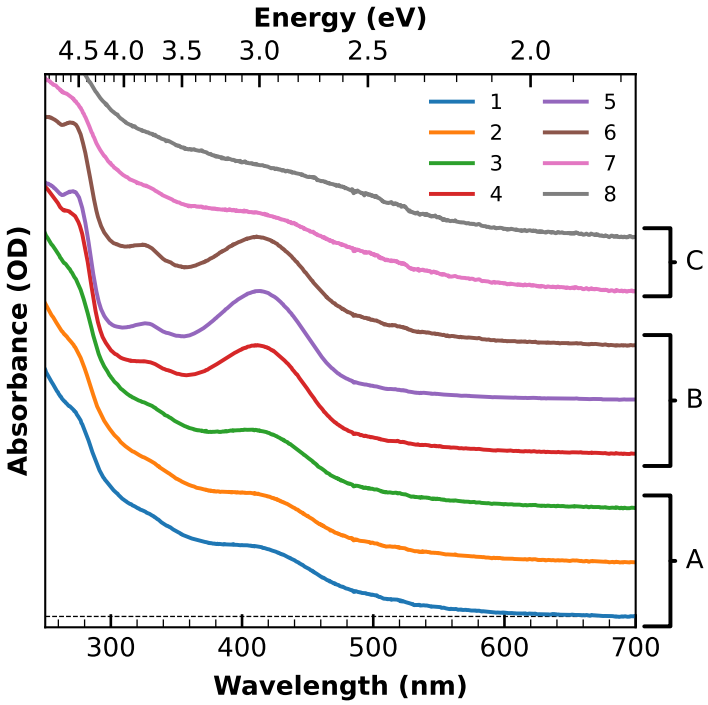

Figure 7.2: Absorption spectra of the different fractions extracted after chromatografic selection from solution of CDs after PEgylation reaction. Based on their spectral characteristics can be grouped into three main subset A, B and C.

Figure 7.3 shows the blank measurements performed as reference to isolate the effects due to effective PEGylation (reported in black) with those arising solely from adding PEG at room temperature without a hydrothermal reaction (reported in green) and subjecting CDs to high-temperature treatment without any PEG addition (reported in magenta). As can be seen from

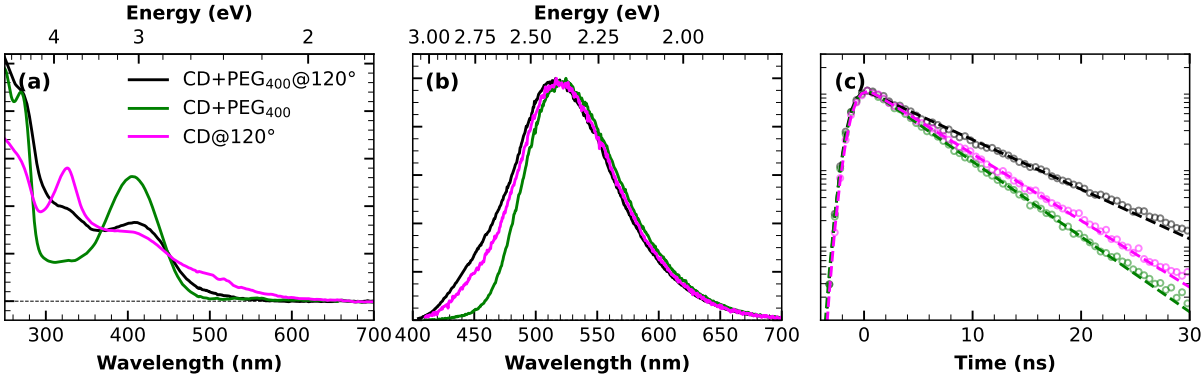

Figure 7.3: Comparison of PEGylation of CDs with blank experiments. (a) Absorption spectra, (b) PL spectra and (c) PL decay of CDs after PEGylation reaction (black) and of the reference samples obtained by simply PEG addition to CDs solution (green) and by thermal treatment of CDs without PEG addition (magenta).

Figure 7.3(a), simple addition of PEG to CDs does not yield significant changes in the UV/Vis spectrum (compare with red curve of Figure 7.1(a)). In contrast, when the CDs undergo the same high-temperature treatment without PEG, substantial alterations in the UV-Vis spectrum shape are observed, significantly different from those registered after PEGylation reaction (black curve). Firstly, there is a much more marked increase in the band at ∼330 nm associated with citrazinic acid. Furthermore, a pronounced broadening in the redder part of the spectrum is noticeable, suggesting for a high-temperature induced aggregation of CDs in solution. From Figure 7.3(b), it can be noticed that the spectral shape of the emission of CDs after PEGylation reaction results in changes similar to those found when high-temperature treatment without PEG addition are performed, whereas the simple addition of PEG does not induce any substantial changes (compare with red curve of Figure 7.1(b)). The reference experiments in Figure 7.3(c) reveal that although the high-temperature treatment alone causes an increase in the emission lifetime, this effect is notably less pronounced compared to the that observed in the case of effective PEGylation. In summary, all these comparisons with blank experiments make it clear that the changes observed in Figure 7.1 can be directly attributed to the effective surface passivation of CDs with PEG400. In fact, the isolated effects of high temperature or simple PEG addition do not produce the same changes.

Furthermore, the effectiveness of surface passivation in P400-CDs was confirmed also from a more morphological point of view, through AFM measurements. In Figure 7.4, an AFM image of pristine CDs (panel (a)) is compared with one of P400-CDs. Evidently, the average size of the P400-CDs is larger than that of the starting CDs, as well as less regular in shape, confirming that a surface coverage of CDs occurred. More quantitatively, image analysis allowed estimation of an average diameter of $d_{AFM} = 4.1$ nm for the starting CDs and $d_{AFM} = 5.2$ nm for P400-CDs,

indicating an average thickness of PEG layer of $(5.2-4.1)/2 \simeq 0.6$ nm. The perfect compatibility of this value with the polymer chain length expected for a 0.4 kDa PEG [338], strongly suggests the presence of a high concentration of PEG molecules arranged on the surface of CDs in a brush configuration [339, 340]. Moreover, it is worth noting that the surface charge of P400-CDs remained negatively charged ($\zeta = -12$ mV), although the absolute value decreased compared to pristine CDs ($\zeta = -15$ mV).

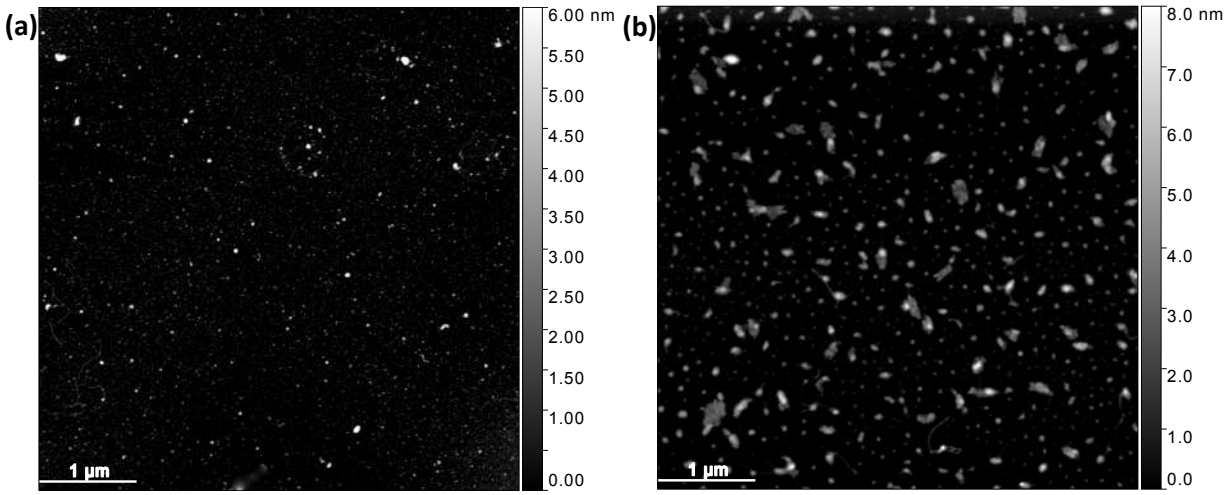

Figure 7.4: AFM images of (a) pristine CDs and (b) CDs after PEGylation belonging to subset A obtained by chromatografic separation.

The same procedure for PEGylating CDs with PEG400 was repeated using a PEG of higher molecular weight and a longer chain, specifically PEG3000. Figure 7.5 compares the absorption

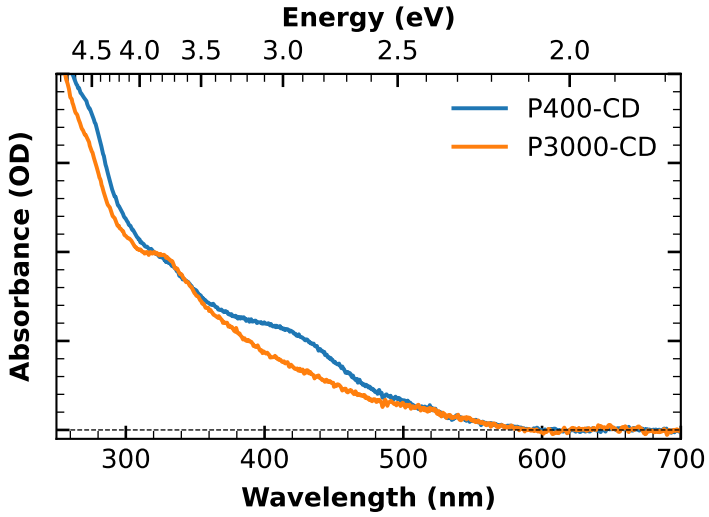

Figure 7.5: Comparison between absorption spectrum of P400-CDs (blue) and P3000-CDs (orange).

spectrum of the P400-CDs with that of P3000-CDs, as obtained after reaction with PEG3000 and subsequent purification through SEC. The successful effectiveness of the reaction with PEG 3000 can be evidenced by the observed modifications in the spectral shape of the absorption spectrum, similar to those encountered in the case of PEGylation with PEG 400. This was done with the aim to obtain CDs characterized by a surface passivation shell of higher thickness. As a consequence, this should allow to assess plasmonic interaction with two families of PEGylated CDs characterized by a surface passivation shell of different thickness. Further morphological characterization is currently ongoing to directly estimate the thickness of the PEG layer also in the case of P3000-CDs. Nevertheless, it is reasonable to assume that, due to the longer length of the polymeric chain, a greater thickness has been achieved. This, once P400-CDs and P3000-CDs are left to interact with plasmonic nanoparticles in solution, should give rise in principle to different interactions, as the physical separation provided by PEG layer between CDs and the external environment is different for the two cases.

7.2 Silver and Gold Nanoparticles

Similar to what was presented in the previous chapter, the objective here is to evaluate any possible interactions that may occur between the CDs and plasmonic nanoparticles in presence of a physical spacer between the two nanosystems. With this aim, gold and silver nanoparticles were synthesized.

AuNPs

AuNPs were synthesized using a seeded growth strategy, inspired by previous works [225], and fully detailed in Materials and Methods Chapter. In summary, the process starts with the creation of a seed solution of citrate-stabilized AuNPs, approximately 10 nm in size, through the classical Turkevich/Frens reaction, which involves the aqueous reduction of tetrachloroauric ($HAuCl_4$) by sodium citrate [223, 341]. These AuNPs serve as seeds and underwent a homogeneous growth process, gradually increasing the size of pre-synthesized Au seed through surface-catalyzed reduction of Au^{3+} by sodium citrate. Repeating this procedure up to five times results in a final generation of AuNPs with a mean size of $d_{AFM} = 13 \pm 1$ nm, as confirmed by AFM measurements (see Figure 7.6). DLS measurements supported this size estimation, providing a value of $d_{DLS} = 13.0 \pm 0.5$ nm. As expected, citrate-stabilization of the surface led to a negative surface charge for the AuNP, with a ζ-potential value of $\zeta = -34 \pm 4$ mV.

AgNPs

AgNPs were home-synthesized using an optimized synthetic route similar to the one used to synthesize the AgNPs employed in the study reported in the preceding chapter, and detailed in Materials and Methods Chapter. This optimized procedure yielded monodisperse AgNPs with a relatively narrow size distribution, and an average diameter of $d_{AFM} = 25 \pm 3$ nm, as measured by AFM (see Figure 7.7). DLS measurements yielded a similar size distribution with $d_{DLS} = 27 \pm 3$

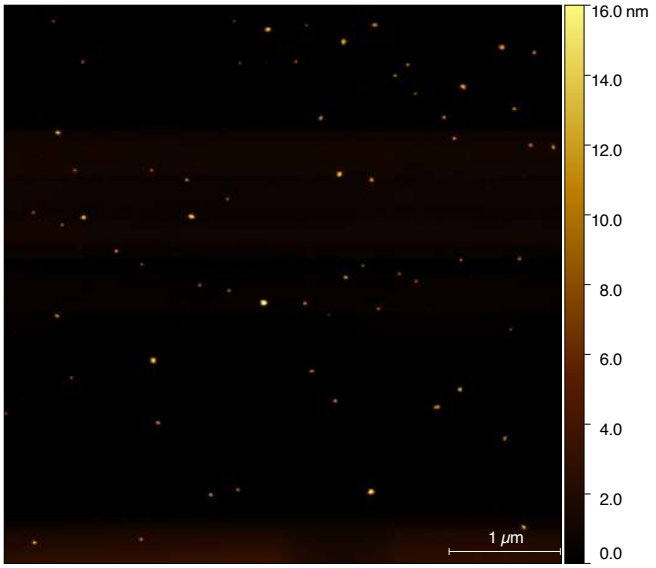

Figure 7.6: AFM image of AuNPs.

nm. As in the case of AuNPs, citrate capping resulted in a negatively charged surface of the AgNP, with a measured value of $\zeta = -23 \pm 3$ mV.

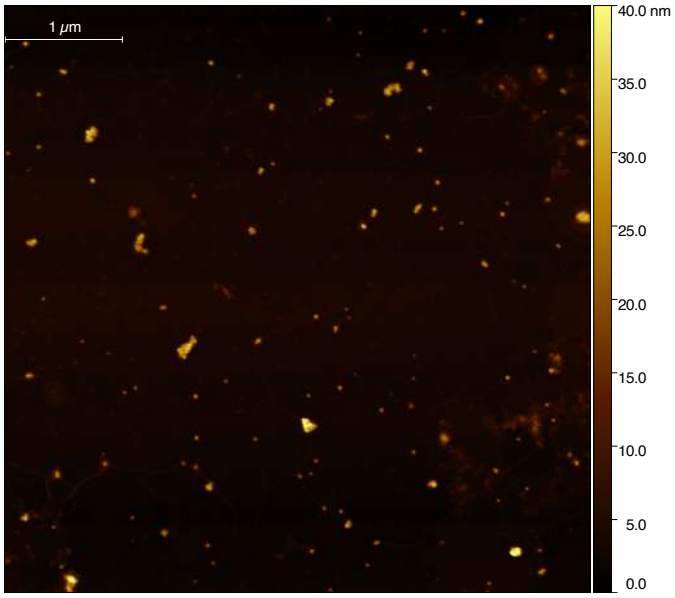

Figure 7.7: AFM image of AgNPs.

Control of surface charge

In order to obtain a second pair of AuNPs and AgNPs with identical morphology but oppositely charged surface, aliquots of the initial negatively charged AuNP− and AgNP− underwent the

same ligand-exchange procedure using CTAB molecules, as employed in the previous study. This procedure successfully yielded AuNP+ and AgNP+ of positively charged surface with ζ-potential values of $\zeta = +28 \pm 5$ mV and $\zeta = +33 \pm 6$ mV, respectively. The comparison of the absorption spectra of MNPs before and after ligand-exchange process further confirms the effectiveness of partial replacement of citrate on the surface of MNPs by CTAB molecules [342, 343]. Specifically, as can be appreciated from Figure 7.8, the plasmonic bands of the initially negatively charged AuNP− and AgNP−, which originally peaked at ∼520 nm and ∼405 nm, respectively, exhibit a redshift to ∼523 nm and ∼413 nm after ligand-exchange procedure. Besides, particularly for AuNPs, a small broadening of the plasmonic bands in the redder part of the spectra was detected, associable to a certain degree of aggregates formation during the ligand exchange-procedure [227, 316].

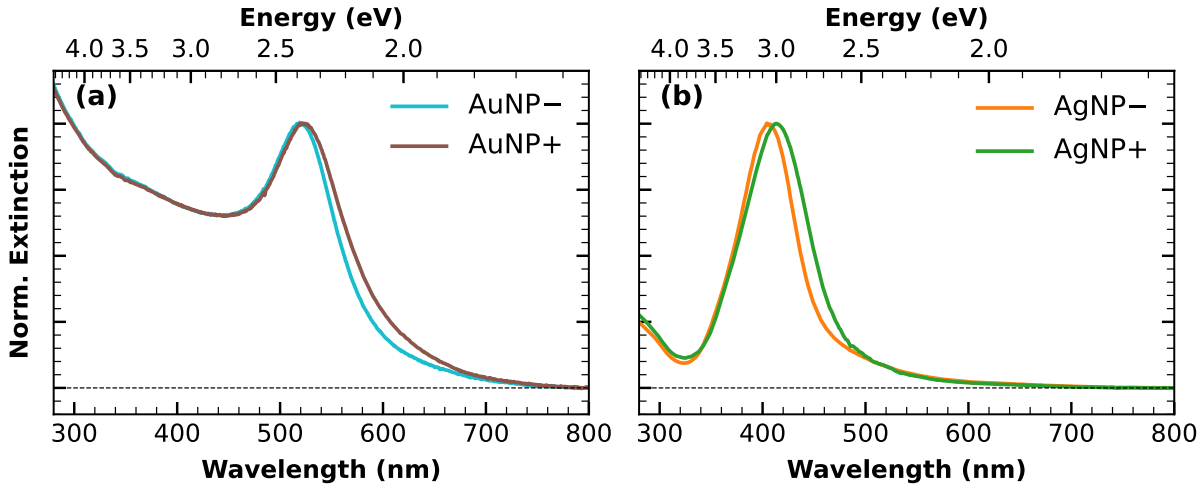

Figure 7.8: Extinction spectra of the starting gold nanoparticles (AuNP−, in blue) and after the ligand-exchange procedure (AuNP+, in brown). (b) Extinction spectra of the starting silver nanoparticle (AgNP−, in orange) and after the ligand-exchange procedure (AuNP+, in green).

7.3 PEG-CDs/MNPs plasmonic interactions

Following the same approach used in the preceding chapter, the potential interactions between P400-CDs and plasmonic nanoparticles were firstly assessed through fluorescence measurements. Figure 7.9(a) shows the PL spectra of an aqueous solution of P400-CDs ($\lambda_{exc} = 410$ nm), for increasing concentration of AuNP+. Notably, the PL intensity undergoes a significant enhancement upon the addition of positively surface charged gold nanoparticles. This enhancement approaches a saturation regime, probably due to a reached chemical equilibrium of the complexed species, after reaching a AuNP+ concentration of $\sim$ 800 pM, determining an overall enhancement of approximately a factor 1.4. Interestingly, Figure 7.9(b) illustrates the same measurements conducted with the addition of AuNP−, instead of AuNP+. As can be appreciated, no significant effect is detected within the same concentration range of gold nanoparticles.

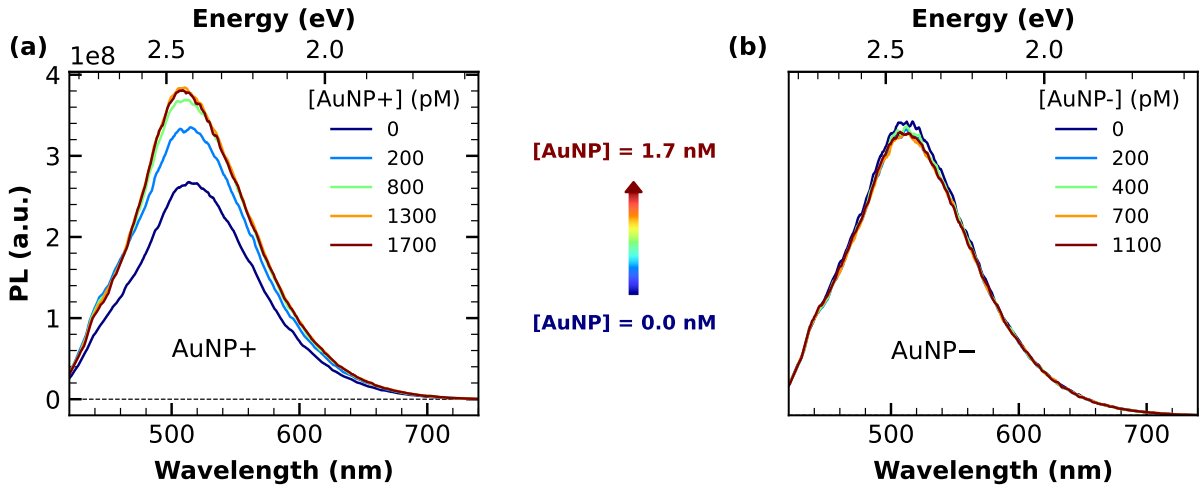

Figure 7.9: PL spectra of P400-CDs aqueous solution under λ_{exc} = 410 nm upon increasing concentration of (a) AuNP+ and (b) AuNP−.

Similar findings were observed in the case of silver nanoparticles. Figure 7.10(a) shows the PL spectra (λ_{exc} = 410 nm) of an aqueous solution of P400-CDs, as AgNP+ was progressively added. In striking contrast to the PL quenching observed with unPEGylated CDs in the presence of silver nanoaprticles (see Figure 6.6), here a strong enhancement in PL intensity is observed for increasing AgNP+ concentration. Specifically, within the investigated range of silver nanoparticles concentration (up to 180 pM), the emission increases by a factor of ∼1.8. Conversely, when negatively surface-charged silver nanoparticles are introduced, no changes in the PL intensity of P400-CD solution are observed, as can be appreciated from Figure 7.10(b).

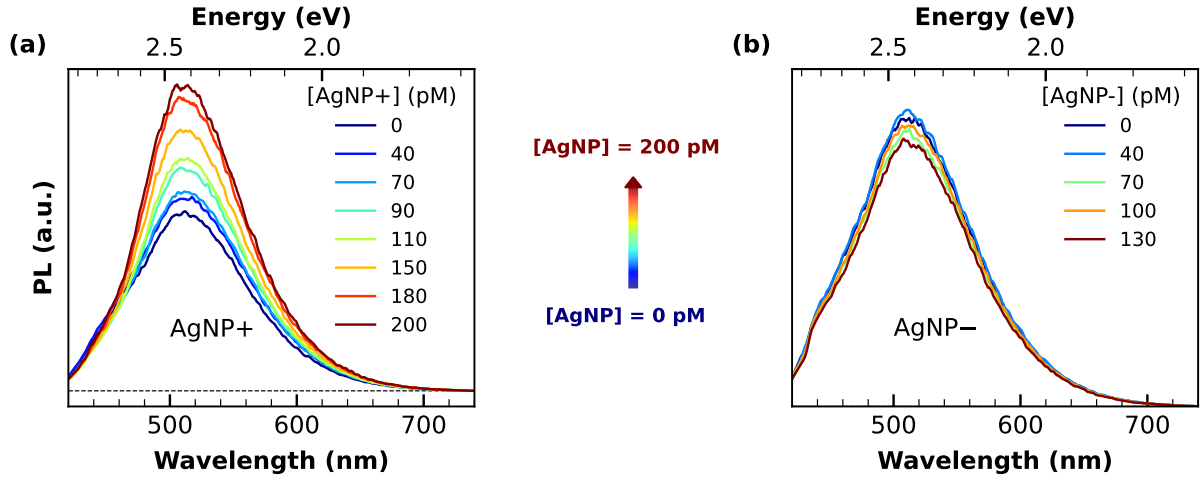

Figure 7.10: PL spectra of P400-CDs aqueous solution under λ_{exc} = 410 nm upon increasing concentration of (a) AgNP+ and (b) AgNP−.

The data from the two preceding figures have been corrected to account for filter effects on

excitation which, particularly for AgNPs, cannot be entirely disregarded. On one hand, the results clearly show the success of the experiment, in that both types of metal nanoparticles are capable of causing a fluorescence enhancement in PEGylated CDs, in sharp contrast with the results of the previous chapter, where only a quenching was observed. On the other hand, the corrected fluorescence spectra clearly demonstrate that in the case of PEGylated CDs, their interactions with MNPs are primarily driven by electrostatic attraction. Indeed, the only interactions observed are between precursors with oppositely charged surfaces. This suggests that P400-CDs do not bind to the surfaces of AuNP− and AgNP−, due to the mutual electrostatic repulsion. In contrast, gold and silver nanoparticles with positively charged surfaces led to significant change in the emission intensity, of P400-CDs, suggesting the occurrence of strong mutual interactions.

Furthermore, it is reasonable to assume that the detected enhancements in the PL of P400-CDs PL, for both AuNP+ and AgNP+, likely result from a competition between quenching and plasmonic enhancement effects. Indeed, despite the chromatografic separation, it is plausible to expect the existence of a certain fraction of CDs that lack complete and uniform surface passivation. This incomplete passivation may potentially result in emission suppression when these CDs directly interact with MNPs in correspondence of locally unPEGylated sites. However, given that PL enhancement stands as the dominant mechanism in this competitive scenario, considering these factors further highlights the impact of PEGylation on the average emission properties of CDs, especially when compared to the quenching behaviour found in absence of PEG layer Figure 6.6.

Enhancement mechanism

Figure 7.11 provides a comparison of the normalized kinetic trace of the PL decay of P400-CDs (in black) with those of P400-CDs in presence of AuNP+ (in red) and AgNP+ (in blue). Notably, the timescale of emission decay remains unchanged in the presence of AgNP+ and exhibits a slight increase in the case of AuNP+ of a factor ~ 1.1 (by evaluating the corresponding timescales as the time required to drop to $1/e$ of initial intensity).

In the case of AgNP+, the presence of a PL enhancement of P400-CDs without any changes in lifetime strongly suggests an effect of near field enhancement (NFE) [344]. This phenomenon can be viewed as a "lightning rod" effect [329], as the electronic transition stimulated at $\lambda_{exc} = 410$ nm in P400-CDs spectrally overlaps with the plasmonic band of the silver nanoparticles (see Figure 7.12(a)), which behave as "nanoantennas". AgNPs optically concentrate the local electric field, resulting in an enhancement in the excitation rate of nearby P400-CDs, for a given incident flux of the excitation beam. Consequently, the enhanced emission arises from P400-CDs experiencing a larger effective absorption cross-section due to the LSPR effect of AgNP−, without any change in the excited state lifetime [345], analogously to what found for other CDs coupled to similar plasmonic nanostructures [313, 346].

In contrast, interpreting the small change observed in the emission decay kinetic of P400-CDs in presence of AuNP+ is less obvious. Although there is a spectral overlap between the emission spectrum of P400-CDs and the plasmonic band of AuNP+ (see Figure 7.12(b)), suggesting the possibility of metal enhanced fluorescence mediated by a Purcell-like effect [344, 347], such a

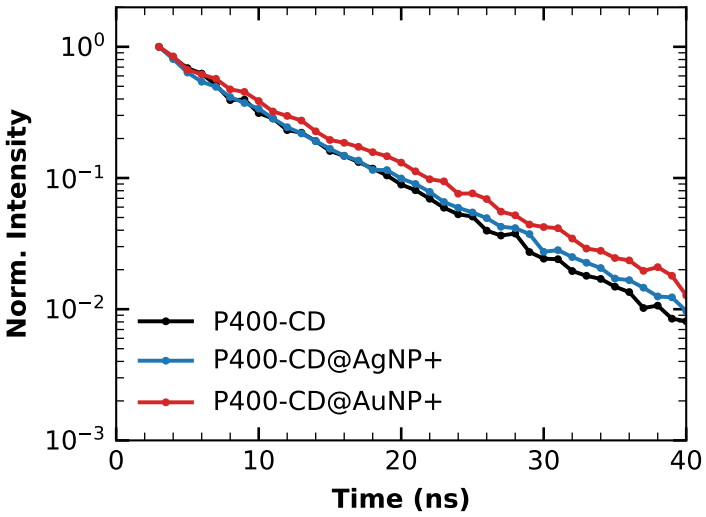

Figure 7.11: PL decay kinetic traces (λ_{exc} = 410 nm, λ_{em} = 520 nm) of aqueous solution of bare P400-CDs (black), P400-CDs with AgNP+ (blue) and P400-CDs with AuNP+ (red).

mechanism typically results in a shortened emission lifetime due to increased radiative decay rate [348, 349]. Therefore, the observation of a slight increase in the emission lifetime contradicts this interpretation. In the attempt to provide an explanation, one could consider the occurrence of an electrostatic screening effect [17] due to specific interactions between cationic CTAB molecules on the surface of AuNP+ and the negatively-charged surface of P400-CDs. This interaction may reduce solvation effects at the surfaces of P400-CDs, leading to a decrease in the non-radiative decay rate, ultimately responsible for the increased emission lifetime. However, regardless of the nature of this specific interaction, it is important to note that the increase in PL lifetime (of a factor $\sim$ 1.1) alone cannot fully account for the PL enhancement (of a factor $\sim$ 1.4) observed in Figure 7.9(a), which is likely due to some plasmonically-mediated effect. In this perspective, the absence of a reduction in the emission lifetime could suggest also for AuNP+ a plasmonic enhancement mechanism of NFE type, similar to what has been observed for AgNP+. However, it is worth mentioning that this mechanism might seem somewhat unlikely because the local field enhancement at λ_{exc} = 410 nm for gold nanoparticles is theoretically expected to be very small. In fact, differently from AgNPs, the plasmon resonance of AuNPs peaks at 520 nm, which is relatively far from λ_{exc}, theoretically leading to a very weak local field enhancement upon excitation at this particular wavelength [344]. On the contrary, a Purcell-like MEF mechanism would be more theoretically plausible, thanks to the favourable spectral matching between the PL of P400-CDs and plasmonic band of gold nanoparticles (see Figure 7.12(b)). Nevertheless, to support this interpretation, one has to speculate the existence of a shortened emission decay component, which is not revealed in Figure 7.11 as it occurs on a sub-ns timescale. Effectively, based on the sparse reported works, MEF in CDs is hardly accompanied by a reduction of emission lifetime on the nanosecond timescale, but whenever a Purcell-like interaction occurs, this latter typically affects only decay components on a sub-ns scale [192, 194]. On these grounds, to unambiguously clarify the nature of the observed plasmonic interactions, further time-resolved

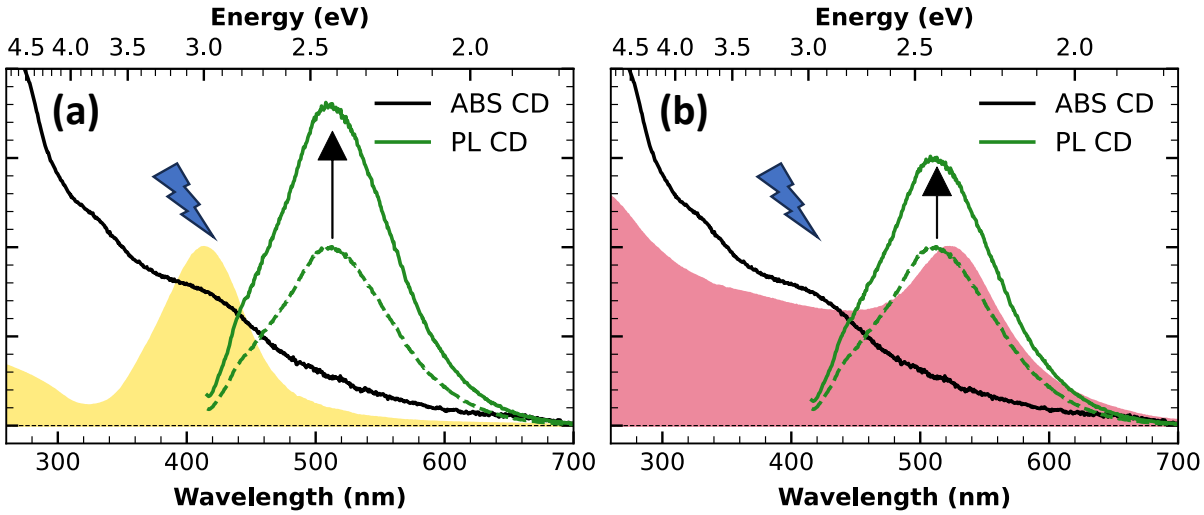

Figure 7.12: (a) Comparison between the absorption (continuous black curve) and the PL spectrum excited at $\lambda_{exc} = 410$ nm (in green) with plasmonic bands of employed (a) silver and (b) gold nanoparticles

PL measurements characterized by a sub-ns temporal resolution will be needed.

As a side note, a recent publication [180] reported that plasmonic interactions between gold nanoparticles and CDs, whose emission matches the plasmonic band of the former, can depend on the specific type of bond established between the two. In particular, the study proposed that in complexes formed by covalent bonds, a more significant PL enhancement can be achieved compared to those formed through dynamic interactions mediated by coulombic attraction. In the latter case, a weaker light-matter interaction has been suggested, and the emission enhancement is less likely to be driven by a Purcell effect [180].

P3000-CDs/MNPs plasmonic interactions

As anticipated, the same PEGylation procedure used to obtain P400-CDs has been repeated with PEG3000 in order to obtain P3000-CDs characterized by a polymeric surface shell of greater thickness. Consequently, the interaction between these P3000-CDs and positively surface charged plasmonic nanoparticles was examined, with the aim of assessing the effect of a longer interaction distance due to the thicker physical spacer provided by the longer PEG chain.

Figure 7.13 shows the impact on the PL spectrum of a P3000-CDs aqueous solution due to the introduction of plasmonic nanoparticles. In particular, from Figure 7.13(a) it is evident that even with the initial addition of AuNP+ (190 pM), a significant enhancement in PL is observed. Similar to what found for P400-CDs and shown in Figure 7.9, no further enhancement is observed with additional gold nanoparticles, suggesting that a saturation regime is rapidly reached. Notably, as can be appreciated from Figure 7.13(b), even with a 70 pM addition of AgNP+ to P3000-CDs , no observable effect on the emission properties of the latter is evident,

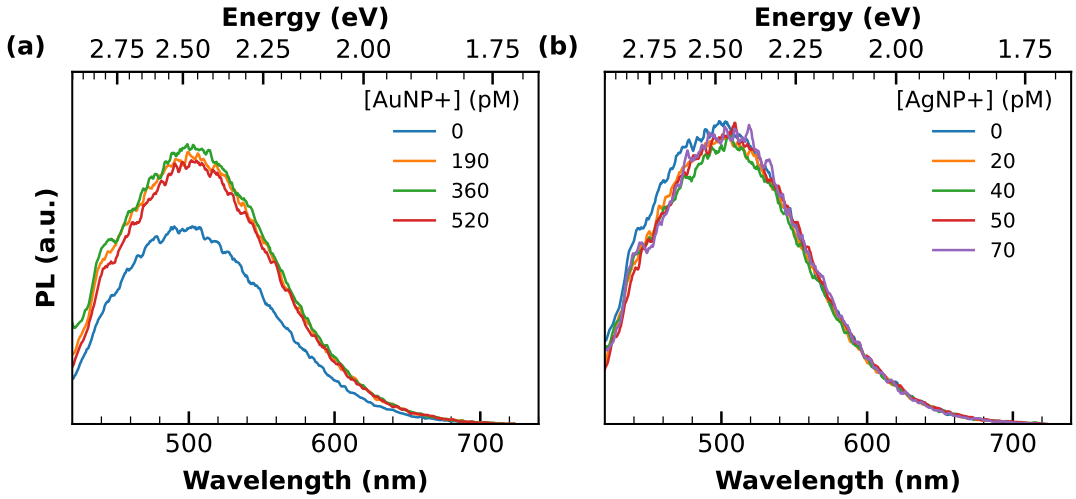

Figure 7.13: PL spectra of P3000-CDs aqueous solution under $\lambda_{exc} = 410$ nm upon increasing concentration of (a) AuNP+ and (b) AgNP+.

whereas within the same concentration range similar addition of AgNP+ to a P400-CDs resulted in an appreciable PL enhancement. Hence, while additional comprehensive studies are necessary to accurately determine the extent of interaction lengths, the data presented imply that AuNP+ can amplify the PL of CDs even at greater interaction distances, while the specific plasmonic interaction provided by AgNP+ appears to be limited to shorter separation distances.

7.4 Conclusions

The results in this chapter demonstrated how the inclusion of a physical spacer can influence the interactions between CDs and plasmonic nanostructures such as gold and silver nanoparticles, particularly by preventing the occurrence of quenching phenomena. Indeed, as discussed in the previous chapter, it was evident that, at least in the case of silver nanoparticles, their close proximity to CDs led to a quenching of the latter's emission properties, highlighting quenching as the predominant outcome in potentially competitive plasmonic interactions.

In contrast, surface passivation of the CDs used in the preceding chapter through a hydrothermal route with PEG, effectively created a dielectric polymeric spacer around the CDs, of varying thickness depending on the length of the specific PEG molecules used.

Even a thin polymeric shell proved sufficient to prevent quenching of CDs by metal nanoparticles, and makes possible, in contrast, an enhancement of the emission in presence of both gold and silver nanoparticles of opposite surface charges. Using PEG of varying lenghts for CD PEGylation allowed to explore the effect of different interactions distances, revealing distinct behaviours for the two types of metallic nanoparticles. Although the specific mechanism behind the enhancement of CD's due to plasmonic interactions with gold nanoparticles deserves further studies, it resulted to persist over longer distances. In contrast, the plasmonic enhancement observed with

silver nanoparticles, associated with Purcell-like interactions, appears to have a shorter-range nature.

Conclusions

The work presented in this Thesis, primarily focused on a fundamental photophysical investigation of luminescent zero dimensional nanocarbons (0DNCs) and their related hybrid systems, has been developed across distinct tracks.

Firstly, the optical photocycles of a palette of various atomically precise nanographenes have been exhaustively reconstructed. This was achieved through a synergistic combination of various steady-state and time-resolved spectroscopic techniques. The use of these methodologies not only facilitated the direct assessment of the fastest relaxation dynamics occurring after photoexcitation, but also allowed to address a significant gap in the existing literature, where such dynamics had been scarcely reported for this category of molecular systems. The investigated NGs were structurally constituted by the integration of one, two or three HBC-type scaffolds in a single aromatic backbone, denoted as NG1, NG2 and NG3, respectively. The smallest NGs of the NG1 family include, in turn, three distinct NGs characterized by the same HBC derivative core but with specific variations in edge chemical groups. Except for the largest NG3, which featured a purely hexagonal planar carbon network, both NG2 and the nanographenes belonging to NG1 family were characterized by structural distortions resulting from the deliberated inclusion of a seven-membered ring. This distortion from planarity was particularly significant for NG2, which also incorporated a helicene moiety, introducing a distinct helical motif to its structure.

In general, the smallest distorted HBC derivatives of NG1 family exhibited fully Kasha-like behaviours, displaying optical features resembling those of standard aromatic molecules despite their distortion. A side-by-side comparative study has permitted to assess the influence of even slight modification in edge functional groups on their optical characteristics, allowing to establish well-defined structure-properties relationships. Different edge functionalization significantly impacted vibronic coupling of the emissive transition, photoinduced relaxation dynamics, radiative and non-radiative rate decay and, clearly, allowed for tuning the emission efficiency in a wide range. An explanatory example of this latter aspect is provided by the dramatical reduction in the emission quantum yield associated with the introduction of peripheral bromine atoms determining a heavy-atom effect which promoted an intersystem crossing transition at the expense of fluorescence emission.

In contrast, the photophysical characterization of the highly distorted NG2 revealed several uncommon spectroscopic features which may stem from the rich conformational landscape of its more intricate structure. In particular, some peculiar properties of NG2 included unusually slow

dynamical structural relaxations in excited state, excitation memory effects on the femtosecond and the nanosecond time scales, and a long-lived delayed fluorescence triggered by a triplet-triplet annihilation mechanism, making NG2 extremely sensitive to oxygen. In this perspective, the higher structural complexity seemingly deviates NG2 from a traditional molecular paradigm, suggesting that large distorted nanocarbons might display novel photophysical behaviours useful in applications such as photoresponsive nanomaterials, photoswitches, or long-lived light emitters.

Despite its larger extension, the structural complexity of NG3 remains relatively low, as it comprises a purely hexagonal network, without any structural distortion or helicity. This simplicity is also reflected in its optical properties, exhibiting conventional behaviour not significantly different from that encountered in smaller aromatic molecules.

More generally, the results confirm the great importance of studying well-defined NGs to unambiguously highlight precise structure-properties correlations and finely tune their characteristics for future applications. Furthermore, the findings provide insight into the possibility of introducing distinctive photophysical characteristics that deviate from typical molecular behaviour.

After a comprehensive analysis of their individual properties, the potential use of molecular NGs in combination with other structures to form hybrid systems has been explored. As first example, NG3 was incorporated as fluorescent medium onto the surface of polystyrene beads acting as microresonators. This incorporation allowed to couple the emission of NG3 with the whispering gallery mode resonances of the microparticles, constituting the first example ever reported of an atomically-precise NG incorporated onto a WGM resonator. At the level of single particles, this coupling resulted in a strong modulation of NG3's emission spectrum by pronounced resonances, producing a progression of sharp peaks superimposed to the broader regular emission. This designed hybrid structure can be in principle exploited for various applications such as metrology, microsensing and micro-lasers. In particular, the randomness given by both the intrinsic polydispersity of polystyrene beads and the specific coupling of NGs, has proven to be an extremely appealing functional property. Indeed, these hardly clonable microsystems, whose emission spectra constitute a unique fingerprint, can be utilized to create a new class of biocompatible photonic microtags for anti-counterfeiting applications.

As a second example, a supramolecular assembly involving an opportunely engineered ring-shaped NG and either C_{60} or C_{70} fullerenes in a 1:1 stoichiometry was reported. This assembly was made feasible by the optimal morphological complementarity between the host ring-shaped NG cavity and the curved fullerene guests. The remarkably high binding constant observed in the complexation of the two carbon systems was found to be accompanied by a strong quenching of the NG-ring's emission. A detailed comparison of the optical properties between the bare NG-ring and their complexed forms with C_{60} and C_{70}, aiming in particular to study the sub-nanosecond dynamics after photoexcitation, revealed photoinduced charge-transfer processes occurring within the NG-ring/fullerene nanohybrids. While the electron transfer process appeared with both C_{60} and C_{70}, the lifetime of the charge-separate state was significantly longer with C_{70}, as no signs of recombination on the picosecond scale were revealed. This prolonged lifetime may pave the way for future applications of such or similar systems in fields exploiting photoinducible charge-separated states such as photocatalysis or photovoltaics.

The two reported NG-based hybrid structures exemplify how NGs can be utilized as versatile building blocks to create structures with different functional properties. They not only differ in size - one being microsized and the other nanosized - but also in how they synergistically utilize and integrate the optical properties of the nanographenic component. Although both cases involve the nanographenic element as a photon absorber, in one case, the emission properties are manipulated by spectral modulation, while in the other, emission is entirely suppressed due to facilitated charge-transfer dynamics leading to the formation of charge-separated states. Despite these differences, both hybrid systems share a remarkable simplicity in their construction, as they were obtained through a self-assembly route in liquid phase, driven by π-π interactions.

This work has also investigated the capability of CDs to interact with metallic nanoparticles. Based on an extensive optical investigation down to the femtosecond scale, the findings confirmed the effective coupling between the two nanosystems. This coupling is primarily evidenced by a quenching of CD's emission, attributed to an exceptionally efficient photoinduced electron transfer, followed by a relatively slower back electron transfer. Proof-of-concept photocatalysis tests revealed that the resulting CD/AgNP nanohybrids can exhibit emergent photocatalytic activity not observed in the initial components, attributed to the electronic interaction within these systems. Additionally, the manipulation of surface charges play a crucial role in designing the functionality of these nanohybrids. The negative charge on the metal nanoparticles reduces the fraction of CD effectively bounded to AgNP, inhibit electron transfer, and hampers the formation of a long-lived charge-separated pair responsible for the photocatalytic response.

Remarkably, it has been shown that an opportune polymeric passivation of the surface of CDs can create a dielectric shell, serving as a physical spacer when they are coupled with other systems, such as plasmonic nanoparticles. In such a case, the absence of direct contact between the interacting systems completely alters the nature of the established interactions. Indeed, through electrostatic binding, both AgNP and AuNP can significantly enhance the emission properties of CDs capped with polymeric molecules through plasmonic interactions. Moreover, these interactions revealed to be specific to the type of plasmonic nanoparticles, as in the case of AuNPs they persisted over a longer distance, while for AgNP they seem to possess a shorter-range nature. Refinement of this method by precisely adjusting the spacing between CDs and plasmonic nanoparticles, along with incorporating other stategies to enhance the intrinsic emission of CDs, could lead to the creation of extremely interesting CD-based plasmonic hybrid nanostructures, holding promise for a wide range of optoelectronic applications.

The examination of so markedly different 0DNC-based hybrid systems presented in this work might initially have appeared to lack a clear common thread due to the profound differences characterizing the various illustrated systems. However, as it should now be clear upon reaching the conclusion of this work, the exploration and analysis of such distinct hybrid systems have further highlighted the significant versatility of 0DNC in integrating into more complex architectures, which can be equipped with novel, specific functional properties that can be effectively designed and finely adjusted to suit particular needs. In this context, besides manipulating the inherent optical properties of specific 0DNCs through their coupling with other systems, as extensively

explored in the fundamental photophysical investigation detailed in this Thesis, the formation of hybrid materials has, in several instances, introduced novel functional properties. These properties were absent in the individual nanomaterials and are exclusively induced by the mutual interactions established within these hybrid systems. This observation confirms that 0DNCs, while showing promise in various applications that are revolutionizing the paradigm of light-emitting nanomaterials, also display potential as building blocks for constructing new classes of smart hybrid materials, thereby further expanding their potential applications.

Bibliography

[1] V. Georgakilas, J. A. Perman, J. Tucek, and R. Zboril, "Broad Family of Carbon Nanoallotropes: Classification, Chemistry, and Applications of Fullerenes, Carbon Dots, Nanotubes, Graphene, Nanodiamonds, and Combined Superstructures". *Chemical Reviews*, 115, pp. 4744–4822, 2015, DOI: 10.1021/cr500304f.

[2] E. Roduner, "Size matters: Why nanomaterials are different". *Chemical Society Reviews*, 35, 7, pp. 583–592, 2006, DOI: 10.1039/b502142c.

[3] H. W. Kroto, J. R. Heath, S. C. O'Brien, R. F. Curl, and R. E. Smalley, "C60: Buckminsterfullerene". *Nature*, 318, pp. 162–163, 1985, DOI: 10.1038/318162a0.

[4] B. M. Illescas and N. Martín, "[60]Fullerene-based electron acceptors". *Comptes Rendus Chimie*, 9, pp. 1038–1050, 2006, DOI: 10.1016/j.crci.2005.11.016.

[5] N. S. Goroff, "Mechanism of Fullerene Formation". *Accounts of Chemical Research*, 29, pp. 77–83, 1996, DOI: 10.1021/ar950162d.

[6] J. Charoenpakdee, O. Suntijitrungruang, and S. Boonchui, "Chirality effects on an electron transport in single-walled carbon nanotube". *Scientific Reports*, 10, 1, p. 18949, 2020, DOI: 10.1038/s41598-020-76047-9.

[7] H. Boehm, R. Setton, and E. Stumpp, "Nomenclature and terminology of graphite intercalation compounds". *Carbon*, 24, pp. 241–245, 1986, DOI: 10.1016/0008-6223(86)90126-0.

[8] K. S. Novoselov, A. K. Geim, S. V. Morozov, D. Jiang, Y. Zhang, S. V. Dubonos, I. V. Grigorieva, and A. A. Firsov, "Electric Field Effect in Atomically Thin Carbon Films". *Science*, 306, pp. 666–669, 2004, DOI: 10.1126/science.1102896.

[9] A. Armano, G. Buscarino, F. Messina, A. Sciortino, M. Cannas, F. M. Gelardi, F. Giannazzo, E. Schilirò, and S. Agnello, "Dynamic modification of Fermi energy in single-layer graphene by photoinduced electron transfer from carbon dots". *Nanomaterials*, 10, 3, 2020, DOI: 10.3390/nano10030528.

[10] M. J. Allen, V. C. Tung, and R. B. Kaner, "Honeycomb Carbon: A Review of Graphene". *Chemical Reviews*, 110, pp. 132–145, 2010, DOI: 10.1021/cr900070d.

[11] X. Xu, R. Ray, Y. Gu, H. J. Ploehn, L. Gearheart, K. Raker, and W. A. Scrivens, "Electrophoretic Analysis and Purification of Fluorescent Single-Walled Carbon Nanotube Fragments". *Journal of the American Chemical Society*, 126, pp. 12736–12737, 2004, DOI: 10.1021/ja040082h.

[12] Y.-P. Sun, B. Zhou, Y. Lin, W. Wang, K. A. S. Fernando, P. Pathak, M. J. Meziani, B. A. Harruff, X. Wang, H. Wang, P. G. Luo, H. Yang, M. E. Kose, B. Chen, L. M. Veca, and S.-Y. Xie, "Quantum-Sized Carbon Dots for Bright and Colorful Photoluminescence". *Journal of the American Chemical Society*, 128, pp. 7756–7757, 2006, DOI: 10.1021/ja062677d.

[13] S. N. Baker and G. A. Baker, "Luminescent carbon nanodots: emergent nanolights". *Angewandte Chemie International Edition*, 49, pp. 6726–6744, 2010, DOI: 10.1002/anie.200906623.

[14] H. Li, Z. Kang, Y. Liu, and S. T. Lee, "Carbon nanodots: Synthesis, properties and applications". *Journal of Materials Chemistry*, 22, 46, pp. 24230–24253, 2012, DOI: 10.1039/c2jm34690g.

[15] S.-T. Yang, L. Cao, P. G. Luo, F. Lu, X. Wang, H. Wang, M. J. Meziani, Y. Liu, G. Qi, and Y.-P. Sun, "Carbon Dots for Optical Imaging in Vivo". *Journal of the American Chemical Society*, 131, pp. 11308–11309, 2009, DOI: 10.1021/ja904843x.

[16] A. Zhu, Q. Qu, X. Shao, B. Kong, and Y. Tian, "Carbon-Dot-Based Dual-Emission Nanohybrid Produces a Ratiometric Fluorescent Sensor for in Vivo Imaging of Cellular Copper Ions". *Angewandte Chemie International Edition*, 51, pp. 7185–7189, 2012, DOI: 10.1002/anie.201109089.

[17] A. Sciortino, A. Madonia, M. Gazzetto, L. Sciortino, E. J. Rohwer, T. Feurer, F. M. Gelardi, M. Cannas, A. Cannizzo, and F. Messina, "The interaction of photoexcited carbon nanodots with metal ions disclosed down to the femtosecond scale". *Nanoscale*, 9, 33, pp. 11902–11911, 2017, DOI: 10.1039/c7nr03754f.

[18] X. Wang, L. Cao, F. Lu, M. J. Meziani, H. Li, G. Qi, B. Zhou, B. A. Harruff, F. Kermarrec, and Y.-P. Sun, "Photoinduced electron transfers with carbon dots". *Chem. Commun.*, 25, pp. 3774–3776, 2009, DOI: 10.1039/B906252A.

[19] K. J. Mintz, B. Guerrero, and R. M. Leblanc, "Photoinduced Electron Transfer in Carbon Dots with Long-Wavelength Photoluminescence". *Journal of Physical Chemistry C*, 122, 51, pp. 29507–29515, 2018, DOI: 10.1021/acs.jpcc.8b06868.

[20] S. Li, I. Skromne, Z. Peng, J. Dallman, A. O. Al-Youbi, A. S. Bashammakh, M. S. El-Shahawi, and R. M. Leblanc, ""Dark" carbon dots specifically "light-up" calcified zebrafish bones". *J. Mater. Chem. B*, 4, 46, pp. 7398–7405, 2016, DOI: 10.1039/C6TB02241C.

[21] A. Sciortino, A. Cannizzo, and F. Messina, "Carbon Nanodots: A Review—From the Current Understanding of the Fundamental Photophysics to the Full Control of the Optical Response". *C*, 4, 4, p. 67, 2018, DOI: 10.3390/c4040067.

[22] Y. Li, Y. Hu, Y. Zhao, G. Shi, L. Deng, Y. Hou, and L. Qu, "An Electrochemical Avenue to Green-Luminescent Graphene Quantum Dots as Potential Electron-Acceptors for Photovoltaics". *Advanced Materials*, 23, pp. 776–780, 2011, DOI: 10.1002/adma.201003819.

[23] D. Pan, J. Zhang, Z. Li, and M. Wu, "Hydrothermal Route for Cutting Graphene Sheets into Blue-Luminescent Graphene Quantum Dots". *Advanced Materials*, 22, pp. 734–738, 2010, DOI: 10.1002/adma.200902825.

[24] W. Chen, C. Hu, Y. Yang, J. Cui, and Y. Liu, "Rapid Synthesis of Carbon Dots by Hydrothermal Treatment of Lignin". *Materials*, 9, 2016, DOI: 10.3390/ma9030184.

[25] Y.-L. Zhang, L. Wang, H.-C. Zhang, Y. Liu, H.-Y. Wang, Z.-H. Kang, and S.-T. Lee, "Graphitic carbon quantum dots as a fluorescent sensing platform for highly efficient detection of Fe3+ ions". *RSC Adv.*, 3, 11, pp. 3733–3738, 2013, DOI: 10.1039/C3RA23410J.

[26] S. Qu, X. Wang, Q. Lu, X. Liu, and L. Wang, "A Biocompatible Fluorescent Ink Based on Water-Soluble Luminescent Carbon Nanodots". *Angewandte Chemie International Edition*, 51, pp. 12215–12218, DOI: 10.

[27] F. Arcudi, L. Dordević, and M. Prato, "Synthesis, Separation, and Characterization of Small and Highly Fluorescent Nitrogen-Doped Carbon NanoDots". *Angewandte Chemie International Edition*, 55, pp. 2107–2112, 2016, DOI: 10.1002/anie.201510158.

[28] J. Zhou, Y. Yang, and C.-y. Zhang, "A low-temperature solid-phase method to synthesize highly fluorescent carbon nitride dots with tunable emission". *Chem. Commun.*, 49, 77, pp. 8605–8607, 2013, DOI: 10.1039/C3CC42266F.

[29] A. Cayuela, M. L. Soriano, and M. Valcárcel, "Photoluminescent carbon dot sensor for carboxylated multiwalled carbon nanotube detection in river water". *Sensors and Actuators, B: Chemical*, PartA, pp. 596–601, 2015, DOI: 10.1016/j.snb.2014.10.102.

[30] A. B. Bourlinos, A. Stassinopoulos, D. Anglos, R. Zboril, M. Karakassides, and E. P. Giannelis, "Surface Functionalized Carbogenic Quantum Dots". *Small*, 4, pp. 455–458, 2008, DOI: 10.1002/smll.200700578.

[31] S. C. Ray, A. Saha, N. R. Jana, and R. Sarkar, "Fluorescent Carbon Nanoparticles: Synthesis, Characterization, and Bioimaging Application". *The Journal of Physical Chemistry C*, 113, pp. 18546–18551, 2009, DOI: 10.1021/jp905912n.

[32] J. Zhou, C. Booker, R. Li, X. Zhou, T.-K. Sham, X. Sun, and Z. Ding, "An Electrochemical Avenue to Blue Luminescent Nanocrystals from Multiwalled Carbon Nanotubes (MWCNTs)". *Journal of the American Chemical Society*, 129, pp. 744–745, 2007, DOI: 10.1021/ja0669070.

[33] B. De and N. Karak, "Recent progress in carbon dot–metal based nanohybrids for photochemical and electrochemical applications". *J. Mater. Chem. A*, 5, 5, pp. 1826–1859, 2017, DOI: 10.1039/C6TA10220D.

[34] X. Wang, L. Cao, S.-T. Yang, F. Lu, M. J. Meziani, L. Tian, K. W. Sun, M. A. Bloodgood, and Y.-P. Sun, "Bandgap-Like Strong Fluorescence in Functionalized Carbon Nanoparticles". *Angewandte Chemie International Edition*, 49, pp. 5310–5314, 2010, DOI: 10.1002/anie.201000982.

[35] P. Anilkumar, X. Wang, L. Cao, S. Sahu, J.-H. Liu, P. Wang, K. Korch, K. N. Tackett II, A. Parenzan, and Y.-P. Sun, "Toward quantitatively fluorescent carbon-based "quantum" dots". *Nanoscale*, 3, 5, pp. 2023–2027, 2011, DOI: 10.1039/C0NR00962H.

[36] D. Reyes, M. Camacho, M. Camacho, M. Mayorga, D. Weathers, G. Salamo, Z. Wang, and A. Neogi, "Laser ablated carbon nanodots for light emission". *Nanoscale research letters*, 11, pp. 1–11, 2016, DOI: 10.1186/s11671-016-1638-8.

[37] D. Reyes, M. Camacho, M. Camacho, M. Mayorga, D. Weathers, G. Salamo, Z. Wang, and A. Neogi, "Laser ablated carbon nanodots for light emission". *Nanoscale research letters*, 11, pp. 1–11, 2016, DOI: 10.1007/s11051-011-0638-y,.

[38] G. H. A. Therese and P. V. Kamath, "Electrochemical synthesis of metal oxides and hydroxides". *Chemistry of materials*, 12, pp. 1195–1204, 2000, DOI: 10.1021/cm990447a.

[39] H. Li, X. He, Z. Kang, H. Huang, Y. Liu, J. Liu, S. Lian, C. Tsang, X. Yang, and S.-T. Lee, "Water-Soluble Fluorescent Carbon Quantum Dots and Photocatalyst Design". *Angewandte Chemie International Edition*, 49, pp. 4430–4434, 2010, DOI: 10.1002/anie.200906154.

[40] H. Zhu, X. Wang, Y. Li, Z. Wang, F. Yang, and X. Yang, "Microwave synthesis of fluorescent carbon nanoparticles with electrochemiluminescence properties". *Chem. Commun.*, 34, pp. 5118–5120, 2009, DOI: 10.1039/B907612C.

[41] M. Amjadi, Z. Abolghasemi-Fakhri, and T. Hallaj, "Carbon dots-silver nanoparticles fluorescence resonance energy transfer system as a novel turn-on fluorescent probe for selective determination of cysteine". *Journal of Photochemistry and Photobiology A: Chemistry*, 309, pp. 8–14, 2015, DOI: 10.1016/j.jphotochem.2015.04.016.

[42] Q. Xu, P. Pu, J. Zhao, C. Dong, C. Gao, Y. Chen, J. Chen, Y. Liu, and H. Zhou, "Preparation of highly photoluminescent sulfur-doped carbon dots for Fe (III) detection". *Journal of Materials Chemistry A*, 3, pp. 542–546, 2015, DOI: 10.1039/C4TA05483K.

[43] D. Wang, X. Wang, Y. Guo, W. Liu, and W. Qin, "Luminescent properties of milk carbon dots and their sulphur and nitrogen doped analogues". *RSC advances*, 4, pp. 51658–51665, 2014, DOI: 10.1039/C4RA11158C.

[44] X. Shan, L. Chai, J. Ma, Z. Qian, J. Chen, and H. Feng, "B-doped carbon quantum dots as a sensitive fluorescence probe for hydrogen peroxide and glucose detection". *Analyst*, 139, pp. 2322–2325, 2014, DOI: 10.1039/C3AN02222F.

[45] A. B. Bourlinos, G. Trivizas, M. A. Karakassides, M. Baikousi, A. Kouloumpis, D. Gournis, A. Bakandritsos, K. Hola, O. Kozak, R. Zboril, et al., "Green and simple route toward boron doped carbon dots with significantly enhanced non-linear optical properties". *Carbon*, 83, pp. 173–179, 2015, DOI: 10.1016/j.carbon.2014.11.032.

[46] S. Sarkar, K. Das, M. Ghosh, and P. K. Das, "Amino acid functionalized blue and phosphorous-doped green fluorescent carbon dots as bioimaging probe". *RSC Advances*, 5, pp. 65913–65921, 2015, DOI: 10.1039/C5RA09905F.

[47] J. Zhou, X. Shan, J. Ma, Y. Gu, Z. Qian, J. Chen, and H. Feng, "Facile synthesis of P-doped carbon quantum dots with highly efficient photoluminescence". *Rsc Advances*, 4, pp. 5465–5468, 2014, DOI: 10.1039/c3ra45294h.

[48] F. Messina, L. Sciortino, R. Popescu, A. M. Venezia, A. Sciortino, G. Buscarino, S. Agnello, R. Schneider, D. Gerthsen, M. Cannas, and F. M. Gelardi, "Fluorescent nitrogen-rich carbon nanodots with an unexpected $\beta - C_3N_4$ nanocrystalline structure". *Journal of Materials Chemistry C*, 4, 13, pp. 2598–2605, 2016, DOI: 10.1039/c5tc04096e.

[49] Y. H. Yuan, Z. X. Liu, R. S. Li, H. Y. Zou, M. Lin, H. Liu, and C. Z. Huang, "Synthesis of nitrogen-doping carbon dots with different photoluminescence properties by controlling the surface states". *Nanoscale*, 8, 12, pp. 6770–6776, 2016, DOI: 10.1039/c6nr00402d.

[50] K. Hola, M. Sudolská, S. Kalytchuk, D. Nachtigallová, A. L. Rogach, M. Otyepka, and R. Zboril, "Graphitic nitrogen triggers red fluorescence in carbon dots". *ACS nano*, 11, pp. 12402–12410, 2017, DOI: 10.1021/acsnano.7b06399.

[51] S. Ghosh, A. M. Chizhik, N. Karedla, M. O. Dekaliuk, I. Gregor, H. Schuhmann, M. Seibt, K. Bodensiek, I. A. T. Schaap, O. Schulz, A. P. Demchenko, J. Enderlein, and A. I. Chizhik, "Photoluminescence of Carbon Nanodots: Dipole Emission Centers and Electron–Phonon Coupling". *Nano Letters*, 14, 10, pp. 5656–5661, 2014, DOI: 10.1021/nl502372x.

[52] Y. Liu, P. Wang, K. S. Fernando, G. E. LeCroy, H. Maimaiti, B. A. Harruff-Miller, W. K. Lewis, C. E. Bunker, Z.-L. Hou, and Y.-P. Sun, "Enhanced fluorescence properties of carbon dots in polymer films". *Journal of Materials Chemistry C*, 4, pp. 6967–6974, 2016, DOI: 10.1039/C6TC01932C.

[53] A. Sciortino, N. Mauro, G. Buscarino, L. Sciortino, R. Popescu, R. Schneider, G. Giammona, D. Gerthsen, M. Cannas, and F. Messina, "$\beta - C_3N_4$ Nanocrystals: Carbon Dots with Extraordinary Morphological, Structural, and Optical Homogeneity". *Chemistry of Materials*, 30, 5, pp. 1695–1700, 2018, DOI: 10.1021/acs.chemmater.7b05178.

[54] H. Zheng, Q. Wang, Y. Long, H. Zhang, X. Huang, and R. Zhu, "Enhancing the luminescence of carbon dots with a reduction pathway". *Chemical communications*, 47, pp. 10650–10652, 2011, DOI: 10.1039/c1cc14741b.

[55] J. Schneider, C. J. Reckmeier, Y. Xiong, M. von Seckendorff, A. S. Susha, P. Kasák, and A. L. Rogach, "Molecular fluorescence in citric acid-based carbon dots". *The Journal of Physical Chemistry C*, 121, pp. 2014–2022, 2017, DOI: 10.1021/acs.jpcc.6b12519.

[56] Z.-H. Wen and X.-B. Yin, "Excitation-independent carbon dots, from photoluminescence mechanism to single-color application". *RSC Adv.*, 6, 33, pp. 27829–27835, 2016, DOI: 10.1039/C5RA27172J.

[57] N. Fuyuno, D. Kozawa, Y. Miyauchi, S. Mouri, R. Kitaura, H. Shinohara, T. Yasuda, N. Komatsu, and K. Matsuda, "Drastic change in photoluminescence properties of graphene quantum dots by chromatographic separation". *Advanced Optical Materials*, 2, pp. 983–989, 2014, DOI: 10.1002/adom.201400200.

[58] J. C. Vinci, I. M. Ferrer, S. J. Seedhouse, A. K. Bourdon, J. M. Reynard, B. A. Foster, F. V. Bright, and L. A. Colón, "Hidden properties of carbon dots revealed after HPLC fractionation". *The Journal of Physical Chemistry Letters*, 4, pp. 239–243, 2013, DOI: 10.1021/jz301911y.

[59] H. Ding, S.-B. Yu, J.-S. Wei, and H.-M. Xiong, "Full-color light-emitting carbon dots with a surface-state-controlled luminescence mechanism". *ACS nano*, 10, pp. 484–491, 2016, DOI: 10.1021/acsnano.5b05406.

[60] L. Guo, J. Ge, W. Liu, G. Niu, Q. Jia, H. Wang, and P. Wang, "Tunable multicolor carbon dots prepared from well-defined polythiophene derivatives and their emission mechanism". *Nanoscale*, 8, pp. 729–734, 2016, DOI: 10.1039/C5NR07153D.

[61] V. Gude, A. Das, T. Chatterjee, and P. K. Mandal, "Molecular origin of photoluminescence of carbon dots: aggregation-induced orange-red emission". *Physical Chemistry Chemical Physics*, 18, pp. 28274–28280, 2016, DOI: 10.1039/C6CP05321A.

[62] X. Miao, X. Yan, D. Qu, D. Li, F. F. Tao, and Z. Sun, "Red emissive sulfur, nitrogen codoped carbon dots and their application in ion detection and theraonostics". *ACS applied materials & interfaces*, 9, pp. 18549–18556, 2017, DOI: 10.1021/acsami.7b04514.

[63] S. Hu, A. Trinchi, P. Atkin, and I. Cole, "Tunable photoluminescence across the entire visible spectrum from carbon dots excited by white light". *Angewandte Chemie International Edition*, 54, pp. 2970–2974, 2015, DOI: 10.1002/anie.201411004.

[64] L. Wang, Y. Wang, T. Xu, H. Liao, C. Yao, Y. Liu, Z. Li, Z. Chen, D. Pan, L. Sun, et al., "Gram-scale synthesis of single-crystalline graphene quantum dots with superior optical properties". *Nature communications*, 5, p. 5357, 2014, DOI: 10.1038/ncomms6357.

[65] N. Mauro, M. A. Utzeri, G. Buscarino, A. Sciortino, F. Messina, G. Cavallaro, and G. Giammona, "Pressure-Dependent Tuning of Photoluminescence and Size Distribution of Carbon Nanodots for Theranostic Anticancer Applications". *Materials*, 13, 2020, DOI: 10.3390/ma13214899.

[66] Y. Zhang, Y. Hu, J. Lin, Y. Fan, Y. Li, Y. Lv, and X. Liu, "Excitation wavelength independence: toward low-threshold amplified spontaneous emission from carbon nanodots". *ACS applied materials & interfaces*, 8, pp. 25454–25460, 2016, DOI: 10.1021/acsami.6b08315.

[67] L. Pan, S. Sun, A. Zhang, K. Jiang, L. Zhang, C. Dong, Q. Huang, A. Wu, and H. Lin, "Truly Fluorescent Excitation-Dependent Carbon Dots and Their Applications in Multicolor Cellular Imaging and Multidimensional Sensing." *Advanced materials (Deerfield Beach, Fla.)*, 27, pp. 7782–7787, 2015, DOI: 10.1002/adma.201503821.

[68] S. Liu, J. Tian, L. Wang, Y. Zhang, X. Qin, Y. Luo, A. M. Asiri, A. O. Al-Youbi, and X. Sun, "Hydrothermal treatment of grass: a low-cost, green route to nitrogen-doped, carbon-rich, photoluminescent polymer nanodots as an effective fluorescent sensing platform for label-free detection of Cu (II) ions". *Advanced materials*, 24, pp. 2037–2041, 2012, DOI: 10.1002/adma.201200164.

[69] D. Bera, L. Qian, T.-K. Tseng, and P. H. Holloway, "Quantum dots and their multimodal applications: a review". *Materials*, 3, pp. 2260–2345, 2010, DOI: 10.3390/ma3042260.

[70] F. P. García de Arquer, D. V. Talapin, V. I. Klimov, Y. Arakawa, M. Bayer, and E. H. Sargent, "Semiconductor quantum dots: Technological progress and future challenges". *Science*, 373, eaaz8541, 2021, DOI: 10.1126/science.aaz8541.

[71] A. P. Alivisatos, A. Harris, N. Levinos, M. Steigerwald, and L. Brus, "Electronic states of semiconductor clusters: Homogeneous and inhomogeneous broadening of the optical spectrum". *The Journal of chemical physics*, 89, pp. 4001–4011, 1988, DOI: 10.1063/1.454833.

[72] A. Sciortino, M. Gazzetto, G. Buscarino, R. Popescu, R. Schneider, G. Giammona, D. Gerthsen, E. J. Rohwer, N. Mauro, T. Feurer, et al., "Disentangling size effects and spectral inhomogeneity in carbon nanodots by ultrafast dynamical hole-burning". *Nanoscale*, 10, pp. 15317–15323, 2018, DOI: 10.1039/C8NR02953A.

[73] T. Gokus, R. Nair, A Bonetti, M Bohmler, A. Lombardo, K. Novoselov, A. Geim, A. Ferrari, and A. Hartschuh, "Making graphene luminescent by oxygen plasma treatment". *ACS nano*, 3, pp. 3963–3968, 2009, DOI: 10.1021/nn9012753.

[74] D. Pan, J. Zhang, Z. Li, C. Wu, X. Yan, and M. Wu, "Observation of pH-, solvent-, spin-, and excitation-dependent blue photoluminescence from carbon nanoparticles". *Chemical Communications*, 46, pp. 3681–3683, 2010, DOI: 10.1039/c000114g.

[75] P. Yu, X. Wen, Y.-R. Toh, and J. Tang, "Temperature-dependent fluorescence in carbon dots". *The Journal of Physical Chemistry C*, 116, pp. 25552–25557, 2012, DOI: 10.1021/jp307308z.

[76] O. Kozak, K. K. R. Datta, M. Greplova, V. Ranc, J. Kaslik, and R. Zboril, "Surfactant-derived amphiphilic carbon dots with tunable photoluminescence". *The Journal of Physical Chemistry C*, 117, pp. 24991–24996, 2013, DOI: 10.1021/jp4040166.

[77] A. Sciortino, E. Marino, B. v. Dam, P. Schall, M. Cannas, and F. Messina, "Solvatochromism unravels the emission mechanism of carbon nanodots". *The journal of physical chemistry letters*, 7, pp. 3419–3423, 2016, DOI: 10.1021/acs.jpclett.6b01590.

[78] H. Wang, C. Sun, X. Chen, Y. Zhang, V. L. Colvin, Q. Rice, J. Seo, S. Feng, S. Wang, and W. Y. William, "Excitation wavelength independent visible color emission of carbon dots". *Nanoscale*, 9, pp. 1909–1915, 2017, DOI: 10.1039/c6nr09200d.

[79] S. Zhu, J. Zhang, X. Liu, B. Li, X. Wang, S. Tang, Q. Meng, Y. Li, C. Shi, R. Hu, et al., "Graphene quantum dots with controllable surface oxidation, tunable fluorescence and up-conversion emission". *Rsc Advances*, 2, pp. 2717–2720, 2012, DOI: 10.1039/c2ra20182h.

[80] L. Sui, W. Jin, S. Li, D. Liu, Y. Jiang, A. Chen, H. Liu, Y. Shi, D. Ding, and M. Jin, "Ultrafast carrier dynamics of carbon nanodots in different pH environments". *Physical Chemistry Chemical Physics*, 18, pp. 3838–3845, 2016, DOI: 10.1039/C5CP07558K.

[81] S. Lu, L. Sui, J. Liu, S. Zhu, A. Chen, M. Jin, and B. Yang, "Near-infrared photoluminescent polymer–carbon nanodots with two-photon fluorescence". *Advanced materials*, 29, p. 1603443, 2017, DOI: 10.1002/adma.201603443.

[82] S. Lu, G. Xiao, L. Sui, T. Feng, X. Yong, S. Zhu, B. Li, Z. Liu, B. Zou, M. Jin, et al., "Piezochromic carbon dots with two-photon fluorescence". *Angewandte Chemie*, 129, pp. 6283–6287, 2017, DOI: 10.1002/anie.201700757.

[83] L. Cao, M. J. Meziani, S. Sahu, and Y.-P. Sun, "Photoluminescence properties of graphene versus other carbon nanomaterials". *Accounts of chemical research*, 46, pp. 171–180, 2013, DOI: 10.1021/ar300128j.

[84] V. Strauss, A. Kahnt, E. M. Zolnhofer, K. Meyer, H. Maid, C. Placht, W. Bauer, T. J. Nacken, W. Peukert, S. H. Etschel, et al., "Assigning electronic states in carbon nanodots". *Advanced Functional Materials*, 26, pp. 7975–7985, 2016, DOI: 10.1002/adfm.201602325.

[85] L. Shi, J. H. Yang, H. B. Zeng, Y. M. Chen, S. C. Yang, C. Wu, H. Zeng, O. Yoshihito, and Q. Zhang, "Carbon dots with high fluorescence quantum yield: the fluorescence originates from organic fluorophores". *Nanoscale*, 8, pp. 14374–14378, 2016, DOI: 10.1039/C6NR00451B.

[86] W Wang, B. Wang, H. Embrechts, C. Damm, A. Cadranel, V. Strauß, M. Distaso, V. Hinterberger, D. M. Guldi, and W. Peukert, "Shedding light on the effective fluorophore structure of high fluorescence quantum yield carbon nanodots". *RSC advances*, 7, pp. 24771–24780, 2017, DOI: 10.1039/C7RA04421F.

[87] M. Righetto, A. Privitera, I. Fortunati, D. Mosconi, M. Zerbetto, M. L. Curri, M. Corricelli, A. Moretto, S. Agnoli, L. Franco, et al., "Spectroscopic insights into carbon dot systems". *The journal of physical chemistry letters*, 8, pp. 2236–2242, 2017, DOI: 10.1021/acs.jpclett.7b00794.

[88] W. Kasprzyk, S. Bednarz, P. Żmudzki, M. Galica, and D. Bogdał, "Novel efficient fluorophores synthesized from citric acid". *RSC advances*, 5, pp. 34795–34799, 2015, DOI: 10.1039/C5RA03226A.

[89] Y. Song, S. Zhu, S. Zhang, Y. Fu, L. Wang, X. Zhao, and B. Yang, "Investigation from chemical structure to photoluminescent mechanism: a type of carbon dots from the pyrolysis of citric acid and an amine". *Journal of Materials Chemistry C*, 3, pp. 5976–5984, 2015, DOI: 10.1039/C5TC00813A.

[90] M. Meloni, L. Stagi, D. Sanna, S. Garroni, L. Calvillo, A. Terracina, M. Cannas, F. Messina, C. M. Carbonaro, P. Innocenzi, and L. Malfatti, "Harnessing Molecular Fluorophores in the Carbon Dots Matrix: The Case of Safranin O". *Nanomaterials*, 12, 14, p. 2351, 2022, DOI: 10.3390/nano12142351.

[91] A. Madonia, G. Minervini, A. Terracina, A. Pramanik, V. Martorana, A. Sciortino, C. M. Carbonaro, C. Olla, T. Sibillano, C. Giannini, E. Fanizza, M. L. Curri, A. Panniello, F. Messina, and M. Striccoli, "Dye-Derived Red-Emitting Carbon Dots for Lasing and Solid-State Lighting". *ACS Nano*, 0, null, 0, DOI: 10.1021/acsnano.3c05566.

[92] N. V. Tepliakov, E. V. Kundelev, P. D. Khavlyuk, Y. Xiong, M. Y. Leonov, W. Zhu, A. V. Baranov, A. V. Fedorov, A. L. Rogach, and I. D. Rukhlenko, "sp2–sp3-Hybridized Atomic Domains Determine Optical Features of Carbon Dots". *ACS Nano*, 13, pp. 10737–10744, 2019, DOI: 10.1021/acsnano.9b05444.

[93] S. Mondal, S. K. Seth, P. Gupta, and P. Purkayastha, "Ultrafast photoinduced electron transfer between carbon nanoparticles and cyclometalated rhodium and iridium complexes". *The Journal of Physical Chemistry C*, 119, pp. 25122–25128, 2015, DOI: 10.1021/acs.jpcc.5b08633.

[94] S. Miao, K. Liang, and B. Kong, "Förster resonance energy transfer (FRET) paired carbon dot-based complex nanoprobes: versatile platforms for sensing and imaging applications". *Materials Chemistry Frontiers*, 4, pp. 128–139, 2020, DOI: 10.1039/C9QM00538B.

[95] P. Yu, X. Wen, Y. R. Toh, Y. C. Lee, K. Y. Huang, S. Huang, S. Shrestha, G. Conibeer, and J. Tang, "Efficient electron transfer in carbon nanodot-graphene oxide nanocomposites". *Journal of Materials Chemistry C*, 2, 16, pp. 2894–2901, 2014, DOI: 10.1039/c3tc32395a.

[96] J. R. Lakowicz. *Principles of fluorescence spectroscopy*. Springer, 2006.

[97] S. Khan, N. C. Verma, Chethana, and C. K. Nandi, "Carbon dots for single-molecule imaging of the nucleolus". *ACS Applied Nano Materials*, 1, pp. 483–487, 2018, DOI: 10.1021/acsanm.7b00175.

[98] B. van Dam, H. Nie, B. Ju, E. Marino, J. M. J. Paulusse, P. Schall, M. Li, and K. Dohnalová, "Excitation-Dependent Photoluminescence from Single-Carbon Dots". *Small*, 13, p. 1702098, 2017, DOI: https://doi.org/10.1002/smll.201702098.

[99] Z. Liu, S. Fu, X. Liu, A. Narita, P. Samorì, M. Bonn, and H. I. Wang, "Small Size, Big Impact: Recent Progress in Bottom-Up Synthesized Nanographenes for Optoelectronic and Energy Applications". *Advanced Science*, 9, p. 2106055, 2022, DOI: 10.1002/advs.202106055.

[100] L. Chen, Y. Hernandez, X. Feng, and K. Müllen, "From nanographene and graphene nanoribbons to graphene sheets: Chemical synthesis". *Angewandte Chemie - International Edition*, 51, 31, pp. 7640–7654, 2012, DOI: 10.1002/anie.201201084.

[101] X. Feng, W. Pisula, and K. Müllen, "Large polycyclic aromatic hydrocarbons: Synthesis and discotic organization". *Pure and Applied Chemistry*, 81, 12, pp. 2203–2224, 2009, DOI: 10.1351/PAC-CON-09-07-07.

[102] I. C.-Y. Hou, V. Diez-Cabanes, A. Galanti, M. Valasek, M. Mayor, J. Cornil, A. Narita, P. Samori, and K. Mullen, "Photomodulation of two-dimensional self-assembly of azobenzene–hexa-peri-hexabenzocoronene-azobenzene triads". *Chemistry of Materials*, 31, pp. 6979–6985, 2019, DOI: 10.1021/acs.chemmater.9b01535.

[103] J. Wu, W. Pisula, and K. Müllen, "Graphenes as potential material for electronics". *Chemical reviews*, 107, pp. 718–747, 2007, DOI: 10.1021/cr068010r.

[104] Z. Wang, Željko Tomović, M. Kastler, R. Pretsch, F. Negri, V. Enkelmann, and K. Müllen, "Graphitic Molecules with Partial "Zig/Zag" Periphery". *Journal of the American Chemical Society*, 126, 25, pp. 7794–7795, 2004, DOI: 10.1021/ja048580d.

[105] W. Hendel, Z. Khan, and W. Schmidt, "Hexa-peri-benzocoronene, a candidate for the origin of the diffuse interstellar visible absorption bands ?" *Tetrahedron*, 42, 4, pp. 1127–1134, 1986, DOI: 10.1016/S0040-4020(01)87517-7.

[106] J. M. Hughes, Y. Hernandez, D. Aherne, L. Doessel, K. Müllen, B. Moreton, T. W. White, C. Partridge, G. Costantini, A. Shmeliov, M. Shannon, V. Nicolosi, and J. N. Coleman, "High Quality Dispersions of Hexabenzocoronene in Organic Solvents". *Journal of the American Chemical Society*, 134, 29, pp. 12168–12179, 2012, DOI: 10.1021/ja303683v.

[107] P. Haines, D. Reger, J. Träg, V. Strauss, D. Lungerich, D. Zahn, N. Jux, and D. M. Guldi, "On the photophysics of nanographenes-investigation of functionalized hexa-: Peri -hexabenzocoronenes as model systems". *Nanoscale*, 13, 2, pp. 801–809, 2021, DOI: 10.1039/d0nr06802k.

[108] M. C. Drummer, V. Singh, N. Gupta, J. L. Gesiorski, R. B. Weerasooriya, and K. D. Glusac, "Photophysics of nanographenes: from polycyclic aromatic hydrocarbons to graphene nanoribbons". *Photosynthesis Research*, 151, pp. 163–184, 2021, DOI: 10.1007/s11120-021-00838-y.

[109] A. Narita, X. Y. Wang, X. Feng, and K. Müllen, "New advances in nanographene chemistry". *Chemical Society Reviews*, 44, 18, pp. 6616–6643, 2015, DOI: 10.1039/c5cs00183h.

[110] M. Y. Han, B. Özyilmaz, Y. Zhang, and P. Kim, "Energy band-gap engineering of graphene nanoribbons". *Physical review letters*, 98, p. 206805, 2007, DOI: 10.1103/PhysRevLett.98.206805.

[111] D. V. Kosynkin, A. L. Higginbotham, A. Sinitskii, J. R. Lomeda, A. Dimiev, B. K. Price, and J. M. Tour, "Longitudinal unzipping of carbon nanotubes to form graphene nanoribbons". *Nature*, 458, 7240, pp. 872–876, 2009, DOI: 10.1038/nature07872.

[112] A. L. Higginbotham, D. V. Kosynkin, A. Sinitskii, Z. Sun, and J. M. Tour, "Lower-defect graphene oxide nanoribbons from multiwalled carbon nanotubes". *ACS nano*, 4, pp. 2059–2069, 2010, DOI: 10.1021/nn100118m.

[113] L. Jiao, L. Zhang, X. Wang, G. Diankov, and H. Dai, "Narrow graphene nanoribbons from carbon nanotubes". *Nature*, 458, pp. 877–880, 2009, DOI: 10.1038/nature07919.

[114] P. Ruffieux, S. Wang, B. Yang, C. Sánchez-Sánchez, J. Liu, T. Dienel, L. Talirz, P. Shinde, C. A. Pignedoli, D. Passerone, et al., "On-surface synthesis of graphene nanoribbons with zigzag edge topology". *Nature*, 531, pp. 489–492, 2016, DOI: 10.1038/nature17151.

[115] A. Cayuela, M. L. Soriano, C. Carrillo-Carrión, and M. Valcárcel, "Semiconductor and carbon-based fluorescent nanodots: The need for consistency". *Chemical Communications*, 52, 7, pp. 1311–1326, 2016, DOI: 10.1039/c5cc07754k.

[116] L. Li, G. Wu, G. Yang, J. Peng, J. Zhao, and J. J. Zhu. *Focusing on luminescent graphene quantum dots: Current status and future perspectives*. 2013. DOI: 10.1039/c3nr33849e.

[117] W. Chen, G. Lv, W. Hu, D. Li, S. Chen, and Z. Dai, "Synthesis and applications of graphene quantum dots: a review". *Nanotechnology Reviews*, 7, pp. 157–185, 2018, DOI: 10.1515/ntrev-2017-0199.

[118] S.-H. Choi, "Unique properties of graphene quantum dots and their applications in photonic/electronic devices". *Journal of Physics D: Applied Physics*, 50, p. 103002, 2017, DOI: 10.1088/1361-6463/aa5244.

[119] R. Liu, D. Wu, X. Feng, and K. Mullen, "Bottom-up fabrication of photoluminescent graphene quantum dots with uniform morphology". *Journal of the American Chemical Society*, 133, pp. 15221–15223, 2011, DOI: 10.1021/ja204953k.

[120] C. Hu, Y. Liu, Y. Yang, J. Cui, Z. Huang, Y. Wang, L. Yang, H. Wang, Y. Xiao, and J. Rong, "One-step preparation of nitrogen-doped graphene quantum dots from oxidized debris of graphene oxide". *Journal of Materials Chemistry B*, 1, pp. 39–42, 2013, DOI: 10.1039/C2TB00189F.

[121] X. Zhou, Y. Zhang, C. Wang, X. Wu, Y. Yang, B. Zheng, H. Wu, S. Guo, and J. Zhang, "Photo-Fenton reaction of graphene oxide: a new strategy to prepare graphene quantum dots for DNA cleavage". *ACS nano*, 6, pp. 6592–6599, 2012, DOI: 10.1021/nn301629v.

[122] H. Tetsuka, R. Asahi, A. Nagoya, K. Okamoto, I. Tajima, R. Ohta, and A. Okamoto, "Optically tunable amino-functionalized graphene quantum dots". *Advanced Materials*, 24, pp. 5333–5338, 2012, DOI: 10.1002/adma.201201930.

[123] Y. Dong, C. Chen, X. Zheng, L. Gao, Z. Cui, H. Yang, C. Guo, Y. Chi, and C. M. Li, "One-step and high yield simultaneous preparation of single-and multi-layer graphene quantum dots from CX-72 carbon black". *Journal of Materials Chemistry*, 22, pp. 8764–8766, 2012, DOI: 10.1039/C2JM30658A.

[124] J. Bai, X. Duan, and Y. Huang, "Rational fabrication of graphene nanoribbons using a nanowire etch mask". *Nano letters*, 9, pp. 2083–2087, 2009, DOI: 10.1021/nl900531n.

[125] Y. Dai, H. Long, X. Wang, Y. Wang, Q. Gu, W. Jiang, Y. Wang, C. Li, T. H. Zeng, Y. Sun, et al., "Versatile graphene quantum dots with tunable nitrogen doping". *Particle & Particle Systems Characterization*, 31, pp. 597–604, 2014, DOI: 10.1002/ppsc.201300268.

[126] X. Li, X. Wang, L. Zhang, S. Lee, and H. Dai, "Chemically derived, ultrasmooth graphene nanoribbon semiconductors". *science*, 319, pp. 1229–1232, 2008, DOI: 10.1126/science.1150878.

[127] L. Xie, L. Jiao, and H. Dai, "Selective etching of graphene edges by hydrogen plasma". *Journal of the American Chemical Society*, 132, pp. 14751–14753, 2010, DOI: 10.1021/ja107071g.

[128] L. Lu, Y. Zhu, C. Shi, and Y. T. Pei, "Large-scale synthesis of defect-selective graphene quantum dots by ultrasonic-assisted liquid-phase exfoliation". *Carbon*, 109, pp. 373–383, 2016, DOI: 10.1016/j.carbon.2016.08.023.

[129] J. Shen, Y. Zhu, C. Chen, X. Yang, and C. Li, "Facile preparation and upconversion luminescence of graphene quantum dots". *Chemical communications*, 47, pp. 2580–2582, 2011, DOI: 10.1039/C0CC04812G.

[130] C. Zhou, W. Jiang, and B. K. Via, "Facile synthesis of soluble graphene quantum dots and its improved property in detecting heavy metal ions". *Colloids and Surfaces B: Biointerfaces*, 118, pp. 72–76, 2014, DOI: 10.1016/j.colsurfb.2014.03.038.

[131] F. Yuan, Z. Wang, X. Li, Y. Li, Z. Tan, L. Fan, and S. Yang, "Bright multicolor bandgap fluorescent carbon quantum dots for electroluminescent light-emitting diodes". *Advanced materials*, 29, p. 1604436, 2017, DOI: 10.1002/adma.201604436.

[132] J. Lu, P. S. E. Yeo, C. K. Gan, P. Wu, and K. P. Loh, "Transforming C60 molecules into graphene quantum dots". *Nature Nanotechnology*, 6, 4, pp. 247–252, 2011, DOI: 10.1038/nnano.2011.30.

[133] A. Stabel, P. Herwig, K. Müllen, and J. P. Rabe, "Diodelike Current–Voltage Curves for a Single Molecule–Tunneling Spectroscopy with Submolecular Resolution of an Alkylated,peri-Condensed Hexabenzocoronene". *Angewandte Chemie International Edition in English*, 34, 15, pp. 1609–1611, 1995, DOI: 10.1002/anie.199516091.

[134] C. D. Simpson, J. D. Brand, A. J. Berresheim, L. Przybilla, H. J. Räder, and K. Müllen, "Synthesis of a Giant 222 Carbon Graphite Sheet". *Chemistry – A European Journal*, 8, pp. 1424–1429, 2002, DOI: 10.1002/1521-3765(20020315)8:6<1424::AID-CHEM1424>3.0.CO;2-Z.

[135] X. Yan, X. Cui, and L. shi Li, "Synthesis of Large, Stable Colloidal Graphene Quantum Dots with Tunable Size". *Journal of the American Chemical Society*, 132, 17, pp. 5944–5945, 2010, DOI: 10.1021/ja1009376.

[136] X. Yan, B. Li, X. Cui, Q. Wei, K. Tajima, and L.-s. Li, "Independent tuning of the band gap and redox potential of graphene quantum dots". *The journal of physical chemistry letters*, 2, pp. 1119–1124, 2011, DOI: 10.1021/jz200450r.

[137] X.-Y. Wang, A. Narita, W. Zhang, X. Feng, and K. Müllen, "Synthesis of Stable Nanographenes with OBO-Doped Zigzag Edges Based on Tandem Demethylation-Electrophilic Borylation". *Journal of the American Chemical Society*, 138, 29, pp. 9021–9024, 2016, DOI: 10.1021/jacs.6b04092.

[138] T. Dumslaff, Y. Gu, G. M. Paternò, Z. Qiu, A. Maghsoumi, M. Tommasini, X. Feng, F. Scotognella, A. Narita, and K. Müllen, "Hexa-peri-benzocoronene with two extra K-regions in an ortho-configuration". *Chemical Science*, 11, pp. 12816–12821, 2020, DOI: 10.1039/d0sc04649c.

[139] I. R. Márquez, N. Fuentes, C. M. Cruz, V. Puente-Muñoz, L. Sotorrios, M. L. Marcos, D. Choquesillo-Lazarte, B. Biel, L. Crovetto, E. Gómez-Bengoa, M. T. González, R. Martin, J. M. Cuerva, and A. G. Campaña, "Versatile synthesis and enlargement of functionalized distorted heptagon-containing nanographenes". *Chemical Science*, 8, 2, pp. 1068–1074, 2017, DOI: 10.1039/C6SC02895K.

[140] Q. Chen, D. Wang, M. Baumgarten, D. Schollmeyer, K. Müllen, and A. Narita, "Regioselective Bromination and Functionalization of Dibenzo[¡i¿hi¡/i¿ , ¡i¿st¡/i¿]ovalene as Highly Luminescent Nanographene with Zigzag Edges". *Chemistry – An Asian Journal*, 14, 10, pp. 1703–1707, 2019, DOI: 10.1002/asia.201801822.

[141] S. Zhao, J. Lavie, L. Rondin, L. Orcin-Chaix, C. Diederichs, P. Roussignol, Y. Chassagneux, C. Voisin, K. Müllen, A. Narita, et al., "Single photon emission from graphene quantum dots at room temperature". *Nature Communications*, 9, p. 3470, 2018, DOI: 10.1038/s41467-018-05888-w.

[142] Y.-M. Liu, H. Hou, Y.-Z. Zhou, X.-J. Zhao, C. Tang, Y.-Z. Tan, and K. Müllen, "Nanographenes as electron-deficient cores of donor-acceptor systems". *Nature communications*, 9, p. 1901, 2018, DOI: 10.1038/s41467-018-04321-6.

[143] I. R. Márquez, S. Castro-Fernández, A. Millán, and A. G. Campaña, "Synthesis of distorted nanographenes containing seven- and eight-membered carbocycles". *Chemical Communications*, 54, 50, pp. 6705–6718, 2018, DOI: 10.1039/C8CC02325E.

[144] S. H. Pun and Q. Miao, "Toward negatively curved carbons". *Accounts of Chemical Research*, 51, pp. 1630–1642, 2018, DOI: 10.1021/acs.accounts.8b00140.

[145] M. A. Majewski and M. Stepien, "Bowls, hoops, and saddles: synthetic approaches to curved aromatic molecules". *Angewandte Chemie International Edition*, 58, pp. 86–116, 2019, DOI: 10.1002/anie.201807004.

[146] Y. Fei, Y. Fu, X. Bai, L. Du, Z. Li, H. Komber, K. H. Low, S. Zhou, D. L. Phillips, X. Feng, and J. Liu, "Defective Nanographenes Containing Seven-Five-Seven (7-5-7)-Membered Rings". *Journal of the American Chemical Society*, 143, 5, pp. 2353–2360, 2021, DOI: 10.1021/jacs.0c12116.

[147] Y. Nakakuki, T. Hirose, H. Sotome, H. Miyasaka, and K. Matsuda, "Hexa-peri-hexabenzo-[7]helicene: Homogeneously π-Extended Helicene as a Primary Substructure of Helically Twisted Chiral Graphenes". *Journal of the American Chemical Society*, 140, 12, pp. 4317–4326, 2018, DOI: 10.1021/jacs.7b13412.

[148] J. Urieta-Mora, M. Krug, W. Alex, J. Perles, I. Fernández, A. Molina-Ontoria, D. M. Guldi, and N. Martín, "Homo and Hetero Molecular 3D Nanographenes Employing a Cyclooctatetraene Scaffold". *Journal of the American Chemical Society*, 142, 9, pp. 4162–4172, 2020, DOI: 10.1021/jacs.9b10203.

[149] Y. Shen and C.-F. Chen, "Helicenes: synthesis and applications". *Chemical reviews*, 112, pp. 1463–1535, 2012, DOI: 10.1021/cr200087r.

[150] T. Fujikawa, Y. Segawa, and K. Itami, "Synthesis, structures, and properties of π-extended double helicene: a combination of planar and nonplanar π-systems". *Journal of the American Chemical Society*, 137, pp. 7763–7768, 2015, DOI: 10.1021/jacs.5b03118.

[151] D. Reger, P. Haines, K. Y. Amsharov, J. A. Schmidt, T. Ullrich, S. Bönisch, F. Hampel, A. Görling, J. Nelson, K. E. Jelfs, D. M. Guldi, and N. Jux, "A Family of Superhelicenes: Easily Tunable, Chiral Nanographenes by Merging Helicity with Planar π Systems". *Angewandte Chemie International Edition*, 60, pp. 18073–18081, 2021, DOI: 10.1002/anie.202103253.

[152] S. Míguez-Lago, I. F. A. Mariz, M. A. Medel, J. M. Cuerva, E. Maçôas, C. M. Cruz, and A. G. Campaña, "Highly contorted superhelicene hits near-infrared circularly polarized luminescence". *Chemical Science*, 13, 35, pp. 10267–10272, 2022, DOI: 10.1039/D2SC03452B.

[153] H.-J. Yen, H. Tsai, M. Zhou, E. F. Holby, S. Choudhury, A. Chen, L. Adamska, S. Tretiak, T. Sanchez, S. Iyer, et al., "Structurally Defined 3D Nanographene Assemblies via Bottom-Up Chemical Synthesis for Highly Efficient Lithium Storage". *Advanced Materials*, 28, pp. 10250–10256, 2016, DOI: 10.1002/adma.201603613.

[154] R. Kumar, H. Aggarwal, and A. Srivastava. *Of Twists and Curves: Electronics, Photophysics, and Upcoming Applications of Non-Planar Conjugated Organic Molecules*. Aug. 2020. DOI: 10.1002/chem.201905071.

[155] S. Castro-Fernández, C. M. Cruz, I. F. A. Mariz, I. R. Márquez, V. G. Jiménez, L. Palomino-Ruiz, J. M. Cuerva, E. Maçôas, and A. G. Campaña, "Two-Photon Absorption Enhancement by the Inclusion of a Tropone Ring in Distorted Nanographene Ribbons". *Angewandte Chemie International Edition*, 59, 18, pp. 7139–7145, 2020, DOI: 10.1002/anie.202000105.

[156] Y. Dai, Y. Liu, K. Ding, and J. Yang, "A short review of nanographenes: structures, properties and applications". *Molecular Physics*, 116, 7-8, pp. 987–1002, 2018, DOI: 10.1080/00268976.2018.1433881.

[157] G. Eda, Y.-Y. Lin, C. Mattevi, H. Yamaguchi, H.-A. Chen, I.-S. Chen, C.-W. Chen, and M. Chhowalla, "Blue photoluminescence from chemically derived graphene oxide". *Advanced materials*, 22, pp. 505–509, 2010, DOI: 10.1002/adma.200901996.

[158] L. Kittiratanawasin and S. Hannongbua, "The effect of edges and shapes on band gap energy in graphene quantum dots". *Integrated Ferroelectrics*, 175, pp. 211–219, 2016, DOI: 10.1080/10584587.2016.1204893.

[159] L. Yang, C.-H. Park, Y.-W. Son, M. L. Cohen, and S. G. Louie, "Quasiparticle energies and band gaps in graphene nanoribbons". *Physical review letters*, 99, p. 186801, 2007, DOI: 10.1103/PhysRevLett.99.186801.

[160] X. Yan, X. Cui, and L.-s. Li, "Synthesis of large, stable colloidal graphene quantum dots with tunable size". *Journal of the American Chemical Society*, 132, pp. 5944–5945, 2010, DOI: 10.1021/ja1009376.

[161] X. Yan, X. Cui, B. Li, and L.-s. Li, "Large, solution-processable graphene quantum dots as light absorbers for photovoltaics". *Nano letters*, 10, pp. 1869–1873, 2010, DOI: 10.1021/nl101060h.

[162] D. Medina-Lopez, T. Liu, S. Osella, H. Levy-Falk, N. Rolland, C. Elias, G. Huber, P. Ticku, L. Rondin, B. Jousselme, D. Beljonne, J.-S. Lauret, and C. Stephane, "Interplay of structure and photophysics of individualized rod-shaped graphene quantum dots with up to 132 sp^2 carbon atoms". *Nature Communications*, 14, p. 4728, 2023, DOI: 10.1038/s41467-023-40376-w.

[163] S. Zhao, L. Rondin, G. Delport, C. Voisin, U. Beser, Y. Hu, X. Feng, K. Müllen, A. Narita, S. Campidelli, and J. Lauret, "Fluorescence from graphene nanoribbons of well-defined structure". *Carbon*, 119, pp. 235–240, 2017, DOI: 10.1016/j.carbon.2017.04.043.

[164] G. M. Paternò, Goudappagouda, Q. Chen, G. Lanzani, F. Scotognella, and A. Narita, "Large polycyclic aromatic hydrocarbons as graphene quantum dots: from synthesis to spectroscopy and photonics". *Advanced Optical Materials*, 9, p. 2100508, 2021, DOI: 10.1002/adom.202100508.

[165] V. Bonal, R. Muñoz-Mármol, F. G. Gámez, M. Morales-Vidal, J. M. Villalvilla, P. G. Boj, J. A. Quintana, Y. Gu, J. Wu, J. Casado, and M. A. Díaz-García, "Solution-processed nanographene distributed feedback lasers". *Nature Communications*, 10, 1, p. 3327, 2019, DOI: 10.1038/s41467-019-11336-0.

[166] Q. Xu, Q. Zhou, Z. Hua, Q. Xue, C. Zhang, X. Wang, D. Pan, and M. Xiao, "Single-particle spectroscopic measurements of fluorescent graphene quantum dots". *ACS Nano*, 7, 12, pp. 10654–10661, 2013, DOI: 10.1021/nn4053342.

[167] R. Rieger and K. Müllen, "Forever young: polycyclic aromatic hydrocarbons as model cases for structural and optical studies". *Journal of Physical Organic Chemistry*, 23, pp. 315–325, 2010, DOI: 10.1002/poc.1644.

[168] J. Lavie, V. B. Vu, D. Medina-Lopez, Y. Dappe, T. Liu, L. Rondin, J.-S. Lauret, S. Latil, and S. Campidelli, "Bottom-Up Synthesis, Dispersion and Properties of Rectangular-Shaped Graphene Quantum Dots". *Helvetica Chimica Acta*, 106, e202300034, 2023, DOI: 10.1002/hlca.202300034.

[169] M. D. Watson, A. Fechtenkötter, and K. Müllen, "Big Is Beautiful-"Aromaticity" Revisited from the Viewpoint of Macromolecular and Supramolecular Benzene Chemistry". *Chemical Reviews*, 101, pp. 1267–1300, 2001, DOI: 10.1021/cr990322p.

[170] K. Kato, K. Takaba, S. Maki-Yonekura, N. Mitoma, Y. Nakanishi, T. Nishihara, T. Hatakeyama, T. Kawada, Y. Hijikata, J. Pirillo, L. T. Scott, K. Yonekura, Y. Segawa, and K. Itami, "Double-Helix Supramolecular Nanofibers Assembled from Negatively Curved Nanographenes". *Journal of the American Chemical Society*, 143, pp. 5465–5469, 2021, DOI: 10.1021/jacs.1c00863.

[171] Ž. Tomović, M. D. Watson, and K. Müllen, "Superphenalene-based columnar liquid crystals". *Angewandte Chemie International Edition*, 43, pp. 755–758, 2004, DOI: 10.1002/anie.200352855.

[172] R. Muñoz-Mármol, F. Gordillo, V. Bonal, J. M. Villalvilla, P. G. Boj, J. A. Quintana, A. M. Ross, G. M. Paternò, F. Scotognella, G. Lanzani, A. Derradji, J. C. Sancho-García, Y. Gu, J. Wu, J. Casado, and M. A. Díaz-García, "Near-Infrared Lasing in Four-Zigzag Edged Nanographenes by 1D versus 2D Electronic π-Conjugation". *Advanced Functional Materials*, 31, p. 2105073, 2021, DOI: 10.1002/adfm.202105073.

[173] Y. Huang, F. Xu, L. Ganzer, F. V. Camargo, T. Nagahara, J. Teyssandier, H. Van Gorp, K. Basse, L. A. Straasø, V. Nagyte, et al., "Intrinsic properties of single graphene nanoribbons in solution: synthetic and spectroscopic studies". *Journal of the American Chemical Society*, 140, pp. 10416–10420, 2018, DOI: 10.1021/jacs.8b06028.

[174] J. P. Mora-Fuentes, A. Riaño, D. Cortizo-Lacalle, A. Saeki, M. Melle-Franco, and A. Mateo-Alonso, "Giant Star-Shaped Nitrogen-Doped Nanographenes". *Angewandte Chemie International Edition*, 58, pp. 552–556, 2019, DOI: 10.1002/anie.201811015.

[175] H. Tetsuka, A. Nagoya, T. Fukusumi, and T. Matsui, "Molecularly Designed, Nitrogen-Functionalized Graphene Quantum Dots for Optoelectronic Devices". *Advanced Materials*, 28, 23, pp. 4632–4638, 2016, DOI: 10.1002/adma.201600058.

[176] G. M. Beneventi, M. Krug, D. Reger, N. Jux, and D. M. Guldi, "Towards understanding the competition of electron and energy transfer in "molecular" nanographenes on the example of hexa-peri-hexabenzocoronene". *Journal of Photochemistry and Photobiology C: Photochemistry Reviews*, 56, p. 100602, 2023, DOI: 10.1016/j.jphotochemrev.2023.100602.

[177] N. Mauro, M. A. Utzeri, A. Sciortino, F. Messina, M. Cannas, R. Popescu, D. Gerthsen, G. Buscarino, G. Cavallaro, and G. Giammona, "Decagram-Scale Synthesis of Multicolor Carbon Nanodots: Self-Tracking Nanoheaters with Inherent and Selective Anticancer Properties". *ACS Applied Materials & Interfaces*, 14, pp. 2551–2563, 2022, DOI: 10.1021/acsami.1c19599.

[178] C. Van Pham, A. F. Madsuha, T. V. Nguyen, and M. Krueger, "Graphene-quantum dot hybrid materials on the road to optoelectronic applications". *Synthetic Metals*, 219, pp. 33–43, 2016, DOI: 10.1016/j.synthmet.2016.04.029.

[179] O. Salihoglu, N. Kakenov, O. Balci, S. Balci, and C. Kocabas, "Graphene-quantum dot hybrid optoelectronics at visible wavelengths". *ACS Photonics*, 5, pp. 2384–2390, 2018, DOI: 10.1021/acsphotonics.8b00163.

[180] I. A. Arefina, D. A. Kurshanov, A. A. Vedernikova, D. V. Danilov, A. V. Koroleva, E. V. Zhizhin, A. A. Sergeev, A. V. Fedorov, E. V. Ushakova, and A. L. Rogach, "Carbon Dot Emission Enhancement in Covalent Complexes with Plasmonic Metal Nanoparticles". *Nanomaterials*, 13, p. 223, 2023, DOI: 10.3390/nano13020223.

[181] L. Wang, H. Zhang, X. Zhou, Y. Liu, and B. Lei, "Preparation, characterization and oxygen sensing properties of luminescent carbon dots assembled mesoporous silica microspheres". *Journal of colloid and interface science*, 478, pp. 256–262, 2016, DOI: 10.1016/j.jcis.2016.06.026.

[182] A. P. Litvin, X. Zhang, E. V. Ushakova, and A. L. Rogach, "Carbon Nanoparticles as Versatile Auxiliary Components of Perovskite-Based Optoelectronic Devices". *Advanced Functional Materials*, 31, p. 2010768, 2021, DOI: 10.1002/adfm.202010768.

[183] W. Liu, C. Li, Y. Ren, X. Sun, W. Pan, Y. Li, J. Wang, and W. Wang, "Carbon dots: surface engineering and applications". *Journal of Materials Chemistry B*, 4, pp. 5772–5788, 2016, DOI: 10.1039/c6tb00976j.

[184] A. Madonia, M. Martin-Sabi, A. Sciortino, S. Agnello, S. Agnello, M. Cannas, S. Ammar, F. Messina, F. Messina, and D. Schaming, "Highly Efficient Electron Transfer in a Carbon Dot-Polyoxometalate Nanohybrid". *Journal of Physical Chemistry Letters*, 11, 11, pp. 4379–4384, 2020, DOI: 10.1021/acs.jpclett.0c01078.

[185] S. Sahu, Y. Liu, P. Wang, C. E. Bunker, K. S. Fernando, W. K. Lewis, E. A. Guliants, F. Yang, J. Wang, and Y.-P. Sun, "Visible-light photoconversion of carbon dioxide into organic acids in an aqueous solution of carbon dots". *Langmuir*, 30, pp. 8631–8636, 2014, DOI: 10.1021/la5010209.

[186] L. Cao, S. Sahu, P. Anilkumar, C. E. Bunker, J. Xu, K. S. Fernando, P. Wang, E. A. Guliants, K. N. Tackett, and Y.-P. Sun, "Carbon nanoparticles as visible-light photocatalysts for efficient CO2 conversion and beyond". *Journal of the American Chemical Society*, 133, pp. 4754–4757, 2011, DOI: 10.1021/ja200804h.

[187] J. Jin, S. Zhu, Y. Song, H. Zhao, Z. Zhang, Y. Guo, J. Li, W. Song, B. Yang, and B. Zhao, "Precisely controllable core–shell Ag@ carbon dots nanoparticles: application to in situ super-sensitive monitoring of catalytic reactions". *ACS Applied Materials & Interfaces*, 8, pp. 27956–27965, 2016, DOI: 10.1021/acsami.6b07807.

[188] Q. Huang, G. Zhuang, H. Jia, M. Qian, S. Cui, S. Yang, and P. Du, "Photoconductive Curved-Nanographene/Fullerene Supramolecular Heterojunctions". *Angewandte Chemie International Edition*, 58, pp. 6244–6249, 2019, DOI: 10.1002/anie.201900084.

[189] C. Li, Y. Zhu, X. Zhang, X. Yang, and C. Li, "Metal-enhanced fluorescence of carbon dots adsorbed Ag@ SiO 2 core-shell nanoparticles". *RSC advances*, 2, pp. 1765–1768, 2012, DOI: 10.1039/C2RA01032A.

[190] J. Zong, X. Yang, A. Trinchi, S. Hardin, I. Cole, Y. Zhu, C. Li, T. Muster, and G. Wei, "Photoluminescence enhancement of carbon dots by gold nanoparticles conjugated via PAMAM dendrimers". *Nanoscale*, 5, pp. 11200–11206, 2013, DOI: 10.1039/C3NR02527F.

[191] M. Li, S. K. Cushing, Q. Wang, X. Shi, L. A. Hornak, Z. Hong, and N. Wu, "Size-dependent energy transfer between CdSe/ZnS quantum dots and gold nanoparticles". *Journal of Physical Chemistry Letters*, 2, 17, pp. 2125–2129, 2011, DOI: 10.1021/jz201002g.

[192] K. Yuan, R. Qin, J. Yu, X. Li, L. Li, X. Yang, X. Yu, Z. Lu, X. Zhang, and H. Liu, "Effects of localized surface plasmon resonance of Ag nanoparticles on luminescence of carbon dots with blue, green and yellow emission". *Applied Surface Science*, 502, 2020, DOI: 10.1016/j.apsusc.2019.144277.

[193] R. Prajapati, A. Bhattacharya, and T. K. Mukherjee, "Resonant excitation energy transfer from carbon dots to different sized silver nanoparticles". *Physical Chemistry Chemical Physics*, 18, 41, pp. 28911–28918, 2016, DOI: 10.1039/c6cp05451j.

[194] A. N. Emam, A. A. Mostafa, M. B. Mohamed, A. S. Gadallah, and M. El-Kemary, "Enhancement of the Collective Optical Properties of Plasmonic Hybrid Carbon Dots via Localized Surface Plasmon". *Journal of Luminescence*, 200, pp. 287–297, 2018, DOI: 10.1016/j.jlumin.2018.03.045.

[195] D. Zhao, C. Chen, L. Lu, F. Yang, and X. Yang, "A dual-mode colorimetric and fluorometric "light on" sensor for thiocyanate based on fluorescent carbon dots and unmodified gold nanoparticles". *Analyst*, 140, 24, pp. 8157–8164, 2015, DOI: 10.1039/c5an01926e.

[196] C. Zou, M. F. Foda, X. Tan, K. Shao, L. Wu, Z. Lu, H. S. Bahlol, and H. Han, "Carbon-dot and quantum-dot-coated dual-emission core–satellite silica nanoparticles for ratiometric intracellular Cu2+ imaging". *Analytical chemistry*, 88, pp. 7395–7403, 2016, DOI: 10.1021/acs.analchem.6b01941.

[197] R. Prasad, S. Aiyer, D. S. Chauhan, R. Srivastava, and K. Selvaraj, "Bioresponsive carbon nano-gated multifunctional mesoporous silica for cancer theranostics". *Nanoscale*, 8, pp. 4537–4546, 2016, DOI: 10.1039/C5NR06756A.

[198] M. Wang, Y. Han, Z. Guo, Z. Huang, and W. Yang, "N-Doped Carbon Dots Embedded in Silica Nanoparticles with Multicolor Luminescence for Light-Emitting Devices". *ACS Applied Nano Materials*, 4, pp. 13625–13632, 2021, DOI: 10.1021/acsanm.1c03057.

[199] X. Liu, N. Zhang, T. Bing, and D. Shangguan, "Carbon dots based dual-emission silica nanoparticles as a ratiometric nanosensor for Cu2+". *Analytical chemistry*, 86, pp. 2289–2296, 2014, DOI: 10.1021/ac404236y.

[200] L. He, H. Zhang, H. Fan, X. Jiang, W. Zhao, and G. Q. Xiang, "Carbon-dot-based dual-emission silica nanoparticles as a ratiometric fluorescent probe for vanadium (V) detection in mineral water samples". *Spectrochimica Acta Part A: Molecular and Biomolecular Spectroscopy*, 189, pp. 51–56, 2018, DOI: 10.1016/j.saa.2017.08.010.

[201] Y. Qiao, C. Liu, and X. Zheng, "Enhancing the quantum yield and Cu2+ sensing sensitivity of carbon dots based on the nano-space confinement effect of silica matrix". *Sensors and Actuators B: Chemical*, 259, pp. 211–218, 2018, DOI: 10.1016/j.snb.2017.12.061.

[202] N. Tejwan, A. K. Saini, A. Sharma, T. A. Singh, N. Kumar, and J. Das, "Metal-doped and hybrid carbon dots: A comprehensive review on their synthesis and biomedical applications". *Journal of Controlled Release*, 330, pp. 132–150, 2021, DOI: 10.1016/j.jconrel.2020.12.023.

[203] V. Strauss, J. T. Margraf, T. Clark, and D. M. Guldi, "A carbon-carbon hybrid-immobilizing carbon nanodots onto carbon nanotubes". *Chemical Science*, 6, pp. 6878–6885, 2015, DOI: 10.1039/C5SC02728D.

[204] T. Skaltsas, A. Stergiou, D. D. Chronopoulos, S. Zhao, H. Shinohara, and N. Tagmatarchis, "All-Carbon Nanosized Hybrid Materials: Fluorescent Carbon Dots Conjugated to Multiwalled Carbon Nanotubes". *Journal of Physical Chemistry C*, 120, 16, pp. 8550–8558, 2016, DOI: 10.1021/acs.jpcc.6b02267.

[205] A. Sciortino, F. Ferrante, N. Mauro, G. Buscarino, L. Sciortino, G. Giammona, M. Cannas, D. Duca, and F. Messina, "Disclosing the emissive surface traps in green-emitting carbon nanodots". *Carbon*, 173, pp. 454–461, 2021, DOI: 10.1016/j.carbon.2020.11.030.

[206] X. Guo, B. Han, Y. Gao, D. Liu, J. Chen, P. Chen, L. Xu, and C. Cui, "Enhanced emission from CH3NH3PbBr3 perovskite films by graphene quantum dot modification". *Materials Research Express*, 7, p. 016415, 2020, DOI: 10.1088/2053-1591/ab61a6.

[207] Z. Li, C. Liu, G. Ren, W. Han, L. Shen, and W. Guo, "Cations Functionalized Carbon Nano-Dots Enabling Interfacial Passivation and Crystallization Control for Inverted Perovskite Solar Cells". *Solar RRL*, 4, p. 1900369, 2020, DOI: 10.1002/solr.201900369.

[208] Y. Ma, H. Zhang, Y. Zhang, R. Hu, M. Jiang, R. Zhang, H. Lv, J. Tian, L. Chu, J. Zhang, et al., "Enhancing the performance of inverted perovskite solar cells via grain boundary passivation with carbon quantum dots". *ACS applied materials & interfaces*, 11, pp. 3044–3052, 2018, DOI: 10.1021/acsami.8b18867.

[209] Q. Guo, F. Yuan, B. Zhang, S. Zhou, J. Zhang, Y. Bai, L. Fan, T. Hayat, A. Alsaedi, and Z. Tan, "Passivation of the grain boundaries of CH 3 NH 3 PbI 3 using carbon quantum dots for highly efficient perovskite solar cells with excellent environmental stability". *Nanoscale*, 11, pp. 115–124, 2019, DOI: 10.1039/C8NR08295B.

[210] D. Benetti, E. Jokar, C.-H. Yu, A. Fathi, H. Zhao, A. Vomiero, E. W.-G. Diau, and F. Rosei, "Hole-extraction and photostability enhancement in highly efficient inverted perovskite solar cells through carbon dot-based hybrid material". *Nano Energy*, 62, pp. 781–790, 2019, DOI: 10.1016/j.nanoen.2019.05.084.

[211] J. Wang, M. Li, W. Shen, W. Su, and R. He, "Ultrastable carbon quantum dots-doped MAPbBr3 perovskite with silica encapsulation". *ACS applied materials & interfaces*, 11, pp. 34348–34354, 2019, DOI: 10.1021/acsami.9b12058.

[212] X. Gan, S. Yang, J. Zhang, G. Wang, P. He, H. Sun, H. Yuan, L. Yu, G. Ding, and Y. Zhu, "Graphite-N doped graphene quantum dots as semiconductor additive in perovskite solar cells". *ACS applied materials & interfaces*, 11, pp. 37796–37803, 2019, DOI: 10.1021/acsami.9b13375.

[213] X. Zhang, Q. Zeng, Y. Xiong, T. Ji, C. Wang, X. Shen, M. Lu, H. Wang, S. Wen, Y. Zhang, et al., "Energy level modification with carbon dot interlayers enables efficient perovskite solar cells and quantum dot based light-emitting diodes". *Advanced Functional Materials*, 30, p. 1910530, 2020, DOI: 10.1002/adfm.201910530.

[214] T. Umeyama, T. Hanaoka, H. Yamada, Y. Namura, S. Mizuno, T. Ohara, J. Baek, J. Park, Y. Takano, K. Stranius, et al., "Exclusive occurrence of photoinduced energy transfer and switching of its direction by rectangular π-extension of nanographenes". *Chemical Science*, 10, pp. 6642–6650, 2019, DOI: 10.1039/C9SC01538H.

[215] V. V. Gobre and A. Tkatchenko, "Scaling laws for van der Waals interactions in nanostructured materials". *Nature communications*, 4, p. 2341, 2013, DOI: 10.1038/ncomms3341.

[216] Y. Liu, S. Roy, S. Sarkar, J. Xu, Y. Zhao, and J. Zhang. *A review of carbon dots and their composite materials for electrochemical energy technologies*. Oct. 2021. DOI: 10.1002/cey2.134.

[217] X. Yu, S. Fu, M. Mandal, X. Yao, Z. Liu, W. Zheng, P. Samorì, A. Narita, K. Müllen, D. Andrienko, et al., "Tuning interfacial charge transfer in atomically precise nanographene–graphene heterostructures by engineering van der Waals interactions". *The Journal of Chemical Physics*, 156, 2022, DOI: 10.1063/5.0081074.

[218] O. J. Achadu, M. Managa, and T. Nyokong, "Fluorescence behaviour of supramolecular hybrids containing graphene quantum dots and pyrene-derivatized phthalocyanines and porphyrins". *Journal of Photochemistry and Photobiology A: Chemistry*, 333, pp. 174–185, 2017, DOI: 10.1016/j.jphotochem.2016.10.029.

[219] S. Zank, J. M. Fernández-García, A. J. Stasyuk, A. A. Voityuk, M. Krug, M. Solà, D. M. Guldi, and N. Martín, "Initiating Electron Transfer in Doubly Curved Nanographene Upon Supramolecular Complexation of C60". *Angewandte Chemie International Edition*, 61, e202112834, 2022, DOI: 10.1002/anie.202112834.

[220] A. H. G. David, S. Míguez-Lago, C. M. Cruz, J. M. Cuerva, V. Blanco, and A. G. Campaña, "Heptagon-Containing Saddle-Shaped Nanographenes: Self-Association and Complexation Studies with Polycyclic Aromatic Hydrocarbons and Fullerenes". *Organic Materials*, 03, 01, pp. 051–059, 2021, DOI: 10.1055/s-0041-1722848.

[221] M. Reale, A. Sciortino, C. Cruz, M. Cannas, E. Maçoas, A. Campaña, and F. Messina, "The photophysics of distorted nanographenes: Ultra-slow relaxation dynamics, memory effects, and delayed fluorescence". *Carbon*, 206, pp. 45–52, 2023, DOI: 10.1016/j.carbon.2023.02.001.

[222] C. M. Cruz, I. R. Márquez, I. F. Mariz, V. Blanco, C. Sánchez-Sánchez, J. M. Sobrado, J. A. Martín-Gago, J. M. Cuerva, E. Maçôas, and A. G. Campaña, "Enantiopure distorted ribbon-shaped nanographene combining two-photon absorption-based upconversion and circularly polarized luminescence". *Chemical Science*, 9, 16, pp. 3917–3924, 2018, DOI: 10.1039/c8sc00427g.

[223] J. Turkevich, P. C. Stevenson, and J. Hillier, "A study of the nucleation and growth processes in the synthesis of colloidal gold". *Discuss. Faraday Soc.*, 11, 0, pp. 55–75, 1951, DOI: 10.1039/DF9511100055.

[224] D. Paramelle, A. Sadovoy, S. Gorelik, P. Free, J. Hobley, and D. G. Fernig, "A rapid method to estimate the concentration of citrate capped silver nanoparticles from UV-visible light spectra". *Analyst*, 139, 19, pp. 4855–4861, 2014, DOI: 10.1039/c4an00978a.

[225] N. G. Bastús, J. Comenge, and V. Puntes, "Kinetically controlled seeded growth synthesis of citrate-stabilized gold nanoparticles of up to 200 nm: Size focusing versus ostwald ripening". *Langmuir*, 27, 17, pp. 11098–11105, 2011, DOI: 10.1021/la201938u.

[226] J. Lim, N. E. Lee, E. Lee, and S. Yoon, "Surface modification of citrate-capped gold nanoparticles using ctab micelles". *Bulletin of the Korean Chemical Society*, 35, 8, pp. 2567–2569, 2014, DOI: 10.5012/bkcs.2014.35.8.2567.

[227] R. Li, Z. Wang, X. Gu, C. Chen, Y. Zhang, and D. Hu, "Study on the Assembly Structure Variation of Cetyltrimethylammonium Bromide on the Surface of Gold Nanoparticles". *ACS Omega*, 5, 10, pp. 4943–4952, 2020, DOI: 10.1021/acsomega.9b03823.

[228] M. Han, X. Gao, J. Z. Su, and S. Nie, "Quantum-dot-tagged microbeads for multiplexed optical coding of biomolecules". *Nature Biotechnology*, 19, 7, pp. 631–635, 2001, DOI: 10.1038/90228.

[229] S. Jana, X. Xu, A. Klymchenko, A. Reisch, and T. Pons, "Microcavity-Enhanced Fluorescence Energy Transfer from Quantum Dot Excited Whispering Gallery Modes to Acceptor Dye Nanoparticles". *ACS Nano*, 15, 1, pp. 1445–1453, 2021, DOI: 10.1021/acsnano.0c08772.

[230] C. Ruckebusch, M. Sliwa, P. Pernot, A. de Juan, and R. Tauler, "Comprehensive data analysis of femtosecond transient absorption spectra: A review". *Journal of Photochemistry and Photobiology C: Photochemistry Reviews*, 13, pp. 1–27, 2012, DOI: 10.1016/j.jphotochemrev.2011.10.002.

[231] I. H. van Stokkum, D. S. Larsen, and R. van Grondelle, "Global and target analysis of time-resolved spectra". *Biochimica et Biophysica Acta (BBA) - Bioenergetics*, 1657, pp. 82–104, 2004, DOI: 10.1016/j.bbabio.2004.04.011.

[232] M. Reale, A. Sciortino, M. Cannas, E. Maçoas, A. H. G. David, C. M. Cruz, A. G. Campaña, and F. Messina, "Atomically Precise Distorted Nanographenes: The Effect of Different Edge Functionalization on the Photophysical Properties down to the Femtosecond Scale". *Materials*, 16, 2023, DOI: 10.3390/ma16020835.

[233] A. Keerthi, I. C.-Y. Hou, T. Marszalek, W. Pisula, M. Baumgarten, and A. Narita, "Hexa-peri-hexabenzocoronene with Different Acceptor Units for Tuning Optoelectronic Properties". *Chemistry – An Asian Journal*, 11, pp. 2710–2714, 2016, DOI: 10.1002/asia.201600638.

[234] M. Kastler, W. Pisula, D. Wasserfallen, T. Pakula, and K. Müllen, "Influence of Alkyl Substituents on the Solution- and Surface-Organization of Hexa- p eri -hexabenzocoronenes". *Journal of the American Chemical Society*, 127, 12, pp. 4286–4296, 2005, DOI: 10.1021/ja0430696.

[235] D. C. Harris and M. D. Bertolucci. *Symmetry and Spectroscopy: an introduction to vibrational and electronic spectroscopy*. Oxford University Press, 1978.

[236] Y. Qin, X. Xie, Z. Pang, G. Liu, X. Dong, S. Shen, Y. Zhang, C. Lee, Y. Yi, P. Wang, and Y. Wang, "Deuterium Renders Fast Risc and Low Non-Radiation Decays of TADF Emitters". *Advanced Optical Materials*, 2023, DOI: 10.1002/adom.202300981.

[237] D. R. Lee, K. H. Lee, W. Shao, C. L. Kim, J. Kim, and J. Y. Lee, "Heavy Atom Effect of Selenium for Metal-Free Phosphorescent Light-Emitting Diodes". *Chemistry of Materials*, 32, 6, pp. 2583–2592, 2020, DOI: 10.1021/acs.chemmater.0c00078.

[238] G. Biagiotti, I. Perini, B. Richichi, and S. Cicchi, "Novel Synthetic Approach to Heteroatom Doped Polycyclic Aromatic Hydrocarbons: Optimizing the Bottom-Up Approach to Atomically Precise Doped Nanographenes". *Molecules*, 26, 20, p. 6306, 2021, DOI: 10.3390/molecules26206306.

[239] J. Clark, T. Nelson, S. Tretiak, G. Cirmi, and G. Lanzani, "Femtosecond torsional relaxation". *Nature Physics*, 8, 3, pp. 225–231, 2012, DOI: 10.1038/nphys2210.

[240] X. Tan, T. L. Gustafson, C. Lefumeux, G. Burdzinski, G. Buntinx, and O. Poizat, "Solvation Dynamics Probed by Femtosecond Transient Absorption Spectroscopy: Vibrational Cooling and Conformational Relaxation in S1 trans-4,4'-Diphenylstibene". *The Journal of Physical Chemistry A*, 106, 14, pp. 3593–3598, 2002, DOI: 10.1021/jp013176b.

[241] A. Ajdarzadeh, C. Consani, O. Bräm, A. Tortschanoff, A. Cannizzo, and M. Chergui, "Ultraviolet transient absorption, transient grating and photon echo studies of aqueous tryptophan". *Chemical Physics*, 422, pp. 47–52, 2013, DOI: 10.1016/j.chemphys.2013.01.036.

[242] M. Nazari, C. D. Bösch, A. Rondi, A. Francés-Monerris, M. Marazzi, E. Lognon, M. Gazzetto, S. M. Langenegger, R. Häner, T. Feurer, A. Monari, and A. Cannizzo, "Ultrafast dynamics in polycyclic aromatic hydrocarbons: the key case of conical intersections at higher excited states and their role in the photophysics of phenanthrene monomer". *Physical Chemistry Chemical Physics*, 21, 31, pp. 16981–16988, 2019, DOI: 10.1039/C9CP03147B.

[243] R. Dabestani and I. N. Ivanov, "A Compilation of Physical, Spectroscopic and Photophysical Properties of Polycyclic Aromatic Hydrocarbons". *Photochemistry and Photobiology*, 70, 1, pp. 10–34, 1999, DOI: 10.1111/j.1751-1097.1999.tb01945.x.

[244] C. M. Cruz, S. Castro-Fernández, E. Maçôas, J. M. Cuerva, and A. G. Campaña, "Undecabenzo[7]superhelicene: A Helical Nanographene Ribbon as a Circularly Polarized Luminescence Emitter". *Angewandte Chemie International Edition*, 57, 45, pp. 14782–14786, 2018, DOI: 10.1002/anie.201808178.

[245] S. J. Bradley, M. Chi, J. M. White, C. R. Hall, L. Goerigk, T. A. Smith, and K. P. Ghiggino, "The role of conformational heterogeneity in the excited state dynamics of linked diketopyrrolopyrrole dimers". *Physical Chemistry Chemical Physics*, 23, 15, pp. 9357–9364, 2021, DOI: 10.1039/D1CP00541C.

[246] F. B. Dias, T. J. Penfold, and A. P. Monkman, "Photophysics of thermally activated delayed fluorescence molecules". *Methods and Applications in Fluorescence*, 5, 1, 2017, DOI: 10.1088/2050-6120/aa537e.

[247] G. Croizat, A. Gregor, E. Gerelli, J. Joniova, M. Scholz, and G. Wagnières, "A general framework for non-exponential delayed fluorescence and phosphorescence decay analysis, illustrated on Protoporphyrin IX". *Journal of Photochemistry and Photobiology B: Biology*, 209, 2020, DOI: 10.1016/j.jphotobiol.2020.111887.

[248] O. L. J. Gijzeman, F. Kaufman, and G. Porter, "Oxygen quenching of aromatic triplet states in solution. Part 1". *Journal of the Chemical Society, Faraday Transactions 2*, 69, p. 708, 1973, DOI: 10.1039/f29736900708.

[249] F. Wilkinson and A. A. Abdel-Shafi, "Mechanism of Quenching of Triplet States by Oxygen: Biphenyl Derivatives in Acetonitrile". *The Journal of Physical Chemistry A*, 101, 30, pp. 5509–5516, 1997, DOI: 10.1021/jp970706o.

[250] S. M. Suresh, E. Duda, D. Hall, Z. Yao, S. Bagnich, A. M. Slawin, H. Bässler, D. Beljonne, M. Buck, Y. Olivier, A. Köhler, and E. Zysman-Colman, "A Deep Blue B,N-Doped Heptacene Emitter That Shows Both Thermally Activated Delayed Fluorescence and Delayed Fluorescence by Triplet-Triplet Annihilation". *Journal of the American Chemical Society*, 142, 14, pp. 6588–6599, 2020, DOI: 10.1021/jacs.9b13704.

[251] M. Micheva, S. Baluschev, and K. Landfester, "Thermally activated delayed fluorescence in an optically accessed soft matter environment". *Journal of Materials Chemistry C*, 10, 12, pp. 4533–4545, 2022, DOI: 10.1039/D1TC04915A.

[252] K. J. Fallon, E. M. Churchill, S. N. Sanders, J. Shee, J. L. Weber, R. Meir, S. Jockusch, D. R. Reichman, M. Y. Sfeir, D. N. Congreve, and L. M. Campos, "Molecular Engineering of Chromophores to Enable Triplet–Triplet Annihilation Upconversion". *Journal of the American Chemical Society*, 142, 47, pp. 19917–19925, 2020, DOI: 10.1021/jacs.0c06386.

[253] Y.-Z. Shi, H. Wu, K. Wang, J. Yu, X.-M. Ou, and X.-H. Zhang, "Recent progress in thermally activated delayed fluorescence emitters for nondoped organic light-emitting diodes". *Chemical Science*, 13, 13, pp. 3625–3651, 2022, DOI: 10.1039/D1SC07180G.

[254] D. Y. Kondakov, "Triplet-triplet annihilation in highly efficient fluorescent organic Light-Emitting Diodes: Current state and future outlook". *Philosophical Transactions of the Royal Society A: Mathematical, Physical and Engineering Sciences*, 373, 2044, 2015, DOI: 10.1098/rsta.2014.0321.

[255] X. Wu, J. W. Huang, B. K. Su, S. Wang, L. Yuan, W. Q. Zheng, H. Zhang, Y. X. Zheng, W. Zhu, and P. T. Chou, "Fabrication of Circularly Polarized MR-TADF Emitters with Asymmetrical Peripheral-Lock Enhancing Helical B/N-Doped Nanographenes". *Advanced Materials*, 34, 1, 2022, DOI: 10.1002/adma.202105080.

[256] Y. Tao, K. Yuan, T. Chen, P. Xu, H. Li, R. Chen, C. Zheng, L. Zhang, and W. Huang, "Thermally activated delayed fluorescence materials towards the breakthrough of organoelectronics". *Advanced Materials*, 26, 47, pp. 7931–7958, 2014, DOI: 10.1002/adma.201402532.

[257] O. Bräm, A. A. Oskouei, A. Tortschanoff, F. van Mourik, M. Madrid, J. Echave, A. Cannizzo, and M. Chergui, "Relaxation Dynamics of Tryptophan in Water: A UV Fluorescence Up-Conversion and Molecular Dynamics Study". *The Journal of Physical Chemistry A*, 114, 34, pp. 9034–9042, 2010, DOI: 10.1021/jp101778u.

[258] O. Braem, T. J. Penfold, A. Cannizzo, and M. Chergui, "A femtosecond fluorescence study of vibrational relaxation and cooling dynamics of UV dyes". *Physical Chemistry Chemical Physics*, 14, 10, pp. 3513–3519, 2012, DOI: 10.1039/c2cp23167k.

[259] G. M. Paternò, Q. Chen, R. Munõz-Mármol, M. Guizzardi, V. Bonal, R. Kabe, A. J. Barker, P. G. Boj, S. Chatterjee, Y. Ie, J. M. Villalvilla, J. A. Quintana, F. Scotognella, K. Müllen, M. A. Diáz-Garciá, A. Narita, and G. Lanzani, "Excited states engineering enables efficient near-infrared lasing in nanographenes". *Materials Horizons*, 9, 1, pp. 393–402, 2022, DOI: 10.1039/d1mh00846c.

[260] M. A. Saidani, A. Benfredj, S. Romdhane, F. Kouki, and H. Bouchriha, "Role of intermolecular coupling and electron-nuclear coupling in the photophysics of oligothiophenes". *Physical Review B*, 86, 16, p. 165315, 2012, DOI: 10.1103/PhysRevB.86.165315.

[261] C. C. Lam, P. T. Leung, and K. Young, "Explicit asymptotic formulas for the positions, widths, and strengths of resonances in Mie scattering". *Journal of the Optical Society of America B*, 9, 9, p. 1585, 1992, DOI: 10.1364/JOSAB.9.001585.

[262] L. Cai, J. Pan, Y. Zhao, J. Wang, and S. Xiao, "Whispering Gallery Mode Optical Microresonators: Structures and Sensing Applications". *physica status solidi (a)*, 217, 6, 2020, DOI: 10.1002/pssa.201900825.

[263] R. S. Moirangthem and A. Erbe, "Interfacial refractive index sensing using visible-excited intrinsic zinc oxide photoluminescence coupled to whispering gallery modes". *Applied Physics Letters*, 103, 5, 2013, DOI: 10.1063/1.4817273.

[264] A. Paunoiu, R. S. Moirangthem, and A. Erbe, "Whispering gallery modes in intrinsic TiO 2 microspheres coupling to the defect-related photoluminescence after visible excitation". *physica status solidi (RRL) – Rapid Research Letters*, 9, 4, pp. 241–244, 2015, DOI: 10.1002/pssr.201510012.

[265] M. B. Price, K. Lewellen, J. Hardy, S. M. Lockwood, C. Zemke-Smith, I. Wagner, M. Gao, J. Grand, K. Chen, J. M. Hodgkiss, E. L. Ru, and N. J. L. K. Davis, "Whispering-Gallery Mode Lasing in Perovskite Nanocrystals Chemically Bound to Silicon Dioxide Microspheres". *The Journal of Physical Chemistry Letters*, 11, 17, pp. 7009–7014, 2020, DOI: 10.1021/acs.jpclett.0c02003.

[266] X. Liu, S. T. Ha, Q. Zhang, M. de la Mata, C. Magen, J. Arbiol, T. C. Sum, and Q. Xiong, "Whispering Gallery Mode Lasing from Hexagonal Shaped Layered Lead Iodide Crystals". *ACS Nano*, 9, 1, pp. 687–695, 2015, DOI: 10.1021/nn5061207.

[267] A. E. Zhukov, N. V. Kryzhanovskaya, E. I. Moiseev, and M. V. Maximov, "Quantum-dot microlasers based on whispering gallery mode resonators". *Light: Science and Applications*, 10, 1, p. 80, 2021, DOI: 10.1038/s41377-021-00525-6.

[268] Y. Zhi, J. Valenta, and A. Meldrum, "Structure of whispering gallery mode spectrum of microspheres coated with fluorescent silicon quantum dots". *Journal of the Optical Society of America B*, 30, 11, p. 3079, 2013, DOI: 10.1364/JOSAB.30.003079.

[269] G. Wei, X. Wang, and L. Liao, "Recent Advances in Organic Whispering-Gallery Mode Lasers". *Laser And Photonics Reviews*, 14, 11, 2020, DOI: 10.1002/lpor.202000257.

[270] W. Zhang, J. Yao, and Y. S. Zhao, "Organic Micro/Nanoscale Lasers". *Accounts of Chemical Research*, 49, 9, pp. 1691–1700, 2016, DOI: 10.1021/acs.accounts.6b00209.

[271] C. Zhang, C.-L. Zou, Y. Zhao, C.-H. Dong, C. Wei, H. Wang, Y. Liu, G.-C. Guo, J. Yao, and Y. S. Zhao, "Organic printed photonics: From microring lasers to integrated circuits". *Science Advances*, 1, 8, 2015, DOI: 10.1126/sciadv.1500257.

[272] Y. Kawabe, C. Spiegelberg, A. Schülzgen, M. F. Nabor, B. Kippelen, E. A. Mash, P. M. Allemand, M. Kuwata-Gonokami, K. Takeda, and N. Peyghambarian, "Whispering-gallery-mode microring laser using a conjugated polymer". *Applied Physics Letters*, 72, 2, pp. 141–143, 1998, DOI: 10.1063/1.120668.

[273] C. Wei, S.-Y. Liu, C.-L. Zou, Y. Liu, J. Yao, and Y. S. Zhao, "Controlled Self-Assembly of Organic Composite Microdisks for Efficient Output Coupling of Whispering-Gallery-Mode Lasers". *Journal of the American Chemical Society*, 137, 1, pp. 62–65, 2015, DOI: 10.1021/ja5112817.

[274] N. G. Zhegalova, S. He, H. Zhou, D. M. Kim, and M. Y. Berezin, "Minimization of self-quenching fluorescence on dyes conjugated to biomolecules with multiple labeling sites via asymmetrically charged NIR fluorophores". *Contrast Media And Molecular Imaging*, 9, 5, pp. 355–362, 2014, DOI: 10.1002/cmmi.1585.

[275] S. R. Mujumdar, R. B. Mujumdar, C. M. Grant, and A. S. Waggoner, "Cyanine-Labeling Reagents: Sulfobenzindocyanine Succinimidyl Esters". *Bioconjugate Chemistry*, 7, 3, pp. 356–362, 1996, DOI: 10.1021/bc960021b.

[276] J. Wang, Y. Yang, and X. Liu, "Solid-state fluorescent carbon dots: quenching resistance strategies, high quantum efficiency control, multicolor tuning, and applications". *Materials Advances*, 1, 9, pp. 3122–3142, 2020, DOI: 10.1039/D0MA00632G.

[277] X. Ma, R. Sun, J. Cheng, J. Liu, F. Gou, H. Xiang, and X. Zhou, "Fluorescence Aggregation-Caused Quenching versus Aggregation-Induced Emission: A Visual Teaching Technology for Undergraduate Chemistry Students". *Journal of Chemical Education*, 93, 2, pp. 345–350, 2016, DOI: 10.1021/acs.jchemed.5b00483.

[278] D. Zhou, D. Li, P. Jing, Y. Zhai, D. Shen, S. Qu, and A. L. Rogach, "Conquering Aggregation-Induced Solid-State Luminescence Quenching of Carbon Dots through a Carbon Dots-Triggered Silica Gelation Process". *Chemistry of Materials*, 29, 4, pp. 1779–1787, 2017, DOI: 10.1021/acs.chemmater.6b05375.

[279] A. Vujačić, V. Vasić, M. Dramićanin, S. P. Sovilj, N. Bibić, S. Milonjić, and V. Vodnik, "Fluorescence Quenching of 5,5'-Disulfopropyl-3,3'-dichlorothiacyanine Dye Adsorbed on Gold Nanoparticles". *The Journal of Physical Chemistry C*, 117, 13, pp. 6567–6577, 2013, DOI: 10.1021/jp311015w.

[280] D. Morrish, X. Gan, and M. Gu, "Observation of orthogonally polarized transverse electric and transverse magnetic oscillation modes in a microcavity excited by localized two-photon absorption". *Applied Physics Letters*, 81, 27, pp. 5132–5134, 2002, DOI: 10.1063/1.1531222.

[281] S. Pang, R. E. Beckham, and K. E. Meissner, "Quantum dot-embedded microspheres for remote refractive index sensing". *Applied Physics Letters*, 92, 22, 2008, DOI: 10.1063/1.2937209.

[282] H. T. Beier, G. L. Coté, and K. E. Meissner, "Whispering Gallery Mode Biosensors Consisting of Quantum Dot-Embedded Microspheres". *Annals of Biomedical Engineering*, 37, 10, pp. 1974–1983, 2009, DOI: 10.1007/s10439-009-9713-2.

[283] A. Matsko and V. Ilchenko, "Optical resonators with whispering-gallery modes-part I: basics". *IEEE Journal of Selected Topics in Quantum Electronics*, 12, 1, pp. 3–14, 2006, DOI: 10.1109/JSTQE.2005.862952.

[284] J. Lutti, W. Langbein, and P. Borri, "A monolithic optical sensor based on whispering-gallery modes in polystyrene microspheres". *Applied Physics Letters*, 93, 15, 2008, DOI: 10.1063/1.2998652.

[285] X. Yu, H. Zhang, and J. Yu, "Luminescence anti-counterfeiting: From elementary to advanced". *Aggregate*, 2, 1, pp. 20–34, 2021, DOI: 10.1002/agt2.15.

[286] F. Ramiro-Manzano, R. Fenollosa, E. Xifré-Pérez, M. Garín, and F. Meseguer, "Porous Silicon Microcavities Based Photonic Barcodes". *Advanced Materials*, 23, 27, pp. 3022–3025, 2011, DOI: 10.1002/adma.201100986.

[287] A. Santos, V. S. Balderrama, M. Alba, P. Formentín, J. Ferré-Borrull, J. Pallarès, and L. F. Marsal, "Nanoporous Anodic Alumina Barcodes: Toward Smart Optical Biosensors". *Advanced Materials*, 24, 8, pp. 1050–1054, 2012, DOI: 10.1002/adma.201104490.

[288] Z. Gao, C. Wei, Y. Yan, W. Zhang, H. Dong, J. Zhao, J. Yi, C. Zhang, Y. J. Li, and Y. S. Zhao, "Covert Photonic Barcodes Based on Light Controlled Acidichromism in Organic Dye Doped Whispering-Gallery-Mode Microdisks". *Advanced Materials*, 29, 30, 2017, DOI: 10.1002/adma.201701558.

[289] B. Xu, S. Yang, X. Feng, T. Zhang, Z. Gao, and Y. S. Zhao, "Dual-stimuli responsive photonic barcodes based on perovskite quantum dots encapsulated in whispering-gallery-mode microspheres". *Journal of Materiomics*, 9, 3, pp. 423–430, 2023, DOI: 10.1016/j.jmat.2022.12.009.

[290] R. Gao, X. Fang, and D. Yan, "Recent developments in stimuli-responsive luminescent films". *Journal of Materials Chemistry C*, 7, 12, pp. 3399–3412, 2019, DOI: 10.1039/C9TC00348G.

[291] W. Hong, Z. Yuan, and X. Chen, "Structural Color Materials for Optical Anticounterfeiting". *Small*, 16, 16, 2020, DOI: 10.1002/smll.201907626.

[292] S. J. Kang, J. B. Kim, C. Chiu, S. Ahn, T. Schiros, S. S. Lee, K. G. Yager, M. F. Toney, Y. Loo, and C. Nuckolls, "A Supramolecular Complex in Small-Molecule Solar Cells based on Contorted Aromatic Molecules". *Angewandte Chemie International Edition*, 51, 34, pp. 8594–8597, 2012, DOI: 10.1002/anie.201203330.

[293] X. Gu, H. Li, B. Shan, Z. Liu, and Q. Miao, "Synthesis, Structure, and Properties of Tetrabenzo[7]circulene". *Organic Letters*, 19, 9, pp. 2246–2249, 2017, DOI: 10.1021/acs.orglett.7b00714.

[294] N. J. Tremblay, A. A. Gorodetsky, M. P. Cox, T. Schiros, B. Kim, R. Steiner, Z. Bullard, A. Sattler, W. So, Y. Itoh, M. F. Toney, H. Ogasawara, A. P. Ramirez, I. Kymissis, M. L. Steigerwald, and C. Nuckolls, "Photovoltaic Universal Joints: Ball-and-Socket Interfaces in Molecular Photovoltaic Cells". *ChemPhysChem*, 11, 4, pp. 799–803, 2010, DOI: 10.1002/cphc.200900941.

[295] J. P. Mora-Fuentes, M. D. Codesal, M. Reale, C. M. Cruz, V. G. Jiménez, A. Sciortino, M. Cannas, F. Messina, V. Blanco, and A. G. Campaña, "Heptagon-Containing Nanographene Embedded into [10]Cycloparaphenylene". *Angewandte Chemie International Edition*, 62, 21, 2023, DOI: 10.1002/anie.202301356.

[296] S. E. Lewis, "Cycloparaphenylenes and related nanohoops". *Chemical Society Reviews*, 44, 8, pp. 2221–2304, 2015, DOI: 10.1039/C4CS00366G.

[297] D. Lu, Q. Huang, S. Wang, J. Wang, P. Huang, and P. Du, "The Supramolecular Chemistry of Cycloparaphenylenes and Their Analogs". *Frontiers in Chemistry*, 7, 2019, DOI: 10.3389/fchem.2019.00668.

[298] Y. Xu and M. von Delius, "The Supramolecular Chemistry of Strained Carbon Nanohoops". *Angewandte Chemie International Edition*, 59, 2, pp. 559–573, 2020, DOI: 10.1002/anie.201906069.

[299] Y. Xu, R. Kaur, B. Wang, M. B. Minameyer, S. Gsänger, B. Meyer, T. Drewello, D. M. Guldi, and M. von Delius, "Concave–Convex $\pi-\pi$ Template Approach Enables the Synthesis of [10]Cycloparaphenylene–Fullerene [2]Rotaxanes". *Journal of the American Chemical Society*, 140, pp. 13413–13420, 2018, DOI: 10.1021/jacs.8b08244.

[300] M. Hermann, D. Wassy, and B. Esser, "Conjugated Nanohoops Incorporating Donor, Acceptor, Hetero- or Polycyclic Aromatics". *Angewandte Chemie International Edition*, 60, pp. 15743–15766, 2021, DOI: https://doi.org/10.1002/anie.202007024.

[301] N. Grabicki, K. T. D. Nguyen, S. Weidner, and O. Dumele, "Confined Spaces in [n]Cyclo-2,7-pyrenylenes". *Angewandte Chemie International Edition*, 60, pp. 14909–14914, 2021, DOI: https://doi.org/10.1002/anie.202102809.

[302] K. Campbell, A. Zappas, U. Bunz, Y. S. Thio, and D. G. Bucknall, "Fluorescence quenching of a poly(para-phenylene ethynylenes) by C 60 fullerenes". *Journal of Photochemistry and Photobiology A: Chemistry*, 249, pp. 41–46, 2012, DOI: 10.1016/j.jphotochem.2012.08.015.

[303] T. Iwamoto, Y. Watanabe, H. Takaya, T. Haino, N. Yasuda, and S. Yamago, "Size- and Orientation-Selective Encapsulation of C 70 by Cycloparaphenylenes". *Chemistry – A European Journal*, 19, 42, pp. 14061–14068, 2013, DOI: 10.1002/chem.201302694.

[304] H.-S. Lin, I. Jeon, R. Xiang, S. Seo, J.-W. Lee, C. Li, A. Pal, S. Manzhos, M. S. Goorsky, Y. Yang, S. Maruyama, and Y. Matsuo, "Achieving High Efficiency in Solution-Processed Perovskite Solar Cells Using C 60 /C 70 Mixed Fullerenes". *ACS Applied Materials And Interfaces*, 10, 46, pp. 39590–39598, 2018, DOI: 10.1021/acsami.8b11049.

[305] A. V. Baskar, M. R. Benzigar, S. N. Talapaneni, G. Singh, A. S. Karakoti, J. Yi, A. H. Al-Muhtaseb, K. Ariga, P. M. Ajayan, and A. Vinu, "Self-Assembled Fullerene Nanostructures: Synthesis and Applications". *Advanced Functional Materials*, 32, 6, 2022, DOI: 10.1002/adfm.202106924.

[306] M. Zulfajri, S. Sudewi, S. Ismulyati, A. Rasool, M. Adlim, and G. G. Huang. *Carbon dot/polymer composites with various precursors and their sensing applications: A review.* Sept. 2021. DOI: 10.3390/coatings11091100.

[307] A. Cadranel, J. T. Margraf, V. Strauss, T. Clark, and D. M. Guldi, "Carbon Nanodots for Charge-Transfer Processes". *Accounts of Chemical Research*, 52, 4, pp. 955–963, 2019, DOI: 10.1021/acs.accounts.8b00673.

[308] Z. Ma, H. Ming, H. Huang, Y. Liu, and Z. Kang, "One-step ultrasonic synthesis of fluorescent N-doped carbon dots from glucose and their visible-light sensitive photocatalytic ability". *New Journal of Chemistry*, 36, 4, p. 861, 2012, DOI: 10.1039/c2nj20942j.

[309] S. Bhattacharyya, F. Ehrat, P. Urban, R. Teves, R. Wyrwich, M. Döblinger, J. Feldmann, A. S. Urban, and J. K. Stolarczyk, "Effect of nitrogen atom positioning on the trade-off between emissive and photocatalytic properties of carbon dots". *Nature Communications*, 8, 1, p. 1401, 2017, DOI: 10.1038/s41467-017-01463-x.

[310] S. Chandra, S. Pradhan, S. Mitra, P. Patra, A. Bhattacharya, P. Pramanik, and A. Goswami, "High throughput electron transfer from carbon dots to chloroplast: a rationale of enhanced photosynthesis". *Nanoscale*, 6, 7, pp. 3647–3655, 2014, DOI: 10.1039/C3NR06079A.

[311] S. Xie, H. Su, W. Wei, M. Li, Y. Tong, and Z. Mao, "Remarkable photoelectrochemical performance of carbon dots sensitized TiO 2 under visible light irradiation". *J. Mater. Chem. A*, 2, 39, pp. 16365–16368, 2014, DOI: 10.1039/C4TA03203A.

[312] T. Nozaki, T. Kakuda, Y. B. Pottathara, and H. Kawasaki, "A nanocomposite of N-doped carbon dots with gold nanoparticles for visible light active photosensitisers". *Photochemical and Photobiological Sciences*, 18, 5, pp. 1235–1241, 2019, DOI: 10.1039/c9pp00035f.

[313] A. Sciortino, A. Panniello, G. Minervini, N. Mauro, G. Giammona, G. Buscarino, M. Cannas, M. Striccoli, and F. Messina, "Enhancing carbon dots fluorescence via plasmonic resonance energy transfer". *Materials Research Bulletin*, 149, 2022, DOI: 10.1016/j.materresbull.2022.111746.

[314] M. Reale, S. Chandra, G. Buscarino, A. Emanuele, M. Cannas, O. Ikkala, A. Sciortino, and F. Messina, "Photoinduced charge separation in functional carbon–silver nanohybrids". *Phys. Chem. Chem. Phys.*, 24, 21, pp. 12974–12983, 2022, DOI: 10.1039/D2CP00668E.

[315] M. Gazzetto, A. Sciortino, M. Nazari, E. Rohwer, G. Giammona, N. Mauro, T. Feurer, F. Messina, and A. Cannizzo, "Photocycle of Excitons in Nitrogen-Rich Carbon Nanodots: Implications for Photocatalysis and Photovoltaics". *ACS Applied Nano Materials*, 3, 7, pp. 6925–6934, 2020, DOI: 10.1021/acsanm.0c01259.

[316] S. Skoglund, T. A. Lowe, J. Hedberg, E. Blomberg, I. O. Wallinder, S. Wold, and M. Lundin, "Effect of laundry surfactants on surface charge and colloidal stability of silver nanoparticles". *Langmuir*, 29, 28, pp. 8882–8891, 2013, DOI: 10.1021/la4012873.

[317] A. Credi and L. Prodi, "From observed to corrected luminescence intensity of solution systems: an easy-to-apply correction method for standard spectrofluorimeters". *Spectrochimica Acta Part A: Molecular and Biomolecular Spectroscopy*, 54, 1, pp. 159–170, 1998, DOI: 10.1016/S1386-1425(97)00224-2.

[318] G. Battistini, P. G. Cozzi, J. P. Jalkanen, M. Montalti, L. Prodi, N. Zaccheroni, and F. Zerbetto, "The erratic emission of pyrene on gold nanoparticles". *ACS Nano*, 2, 1, pp. 77–84, 2008, DOI: 10.1021/nn700241w.

[319] S. Franzen, J. C. W. Folmer, W. R. Glomm, and R. O'Neal, "Optical Properties of Dye Molecules Adsorbed on Single Gold and Silver Nanoparticles". *The Journal of Physical Chemistry A*, 106, 28, pp. 6533–6540, 2002, DOI: 10.1021/jp025536g.

[320] F. Arcudi, V. Strauss, L. Dordević, A. Cadranel, D. M. Guldi, and M. Prato, "Porphyrin Antennas on Carbon Nanodots: Excited State Energy and Electron Transduction". *Angewandte Chemie International Edition*, 56, 40, pp. 12097–12101, 2017, DOI: 10.1002/anie.201704544.

[321] F. Zu, F. Yan, Z. Bai, J. Xu, Y. Wang, Y. Huang, and X. Zhou, "The quenching of the fluorescence of carbon dots: A review on mechanisms and applications". *Microchimica Acta*, 184, 7, pp. 1899–1914, 2017, DOI: 10.1007/s00604-017-2318-9.

[322] X. Zhang, Y. L. Chen, R. S. Liu, and D. P. Tsai, "Plasmonic photocatalysis". *Reports on Progress in Physics*, 76, 4, 2013, DOI: 10.1088/0034-4885/76/4/046401.

[323] P. V. Kamat, "Photophysical, photochemical and photocatalytic aspects of metal nanoparticles". *Journal of Physical Chemistry B*, 106, 32, pp. 7729–7744, 2002, DOI: 10.1021/jp0209289.

[324] A Houas, "Photocatalytic degradation pathway of methylene blue in water". *Applied Catalysis B: Environmental*, 31, 2, pp. 145–157, 2001, DOI: 10.1016/S0926-3373(00)00276-9.

[325] I. Khan, K. Saeed, I. Zekker, B. Zhang, A. H. Hendi, A. Ahmad, S. Ahmad, N. Zada, H. Ahmad, L. A. Shah, T. Shah, and I. Khan, "Review on Methylene Blue: Its Properties, Uses, Toxicity and Photodegradation". *Water*, 14, 2, p. 242, 2022, DOI: 10.3390/w14020242.

[326] K. Ray, R. Badugu, and J. R. Lakowicz, "Metal-Enhanced Fluorescence from CdTe Nanocrystals: A Single-Molecule Fluorescence Study". *Journal of the American Chemical Society*, 128, 28, pp. 8998–8999, 2006, DOI: 10.1021/ja061762i.

[327] M. Pelton, J. Aizpurua, and G. Bryant, "Metal-nanoparticle plasmonics". *Laser and Photonics Reviews*, 2, 3, pp. 136–159, 2008, DOI: 10.1002/lpor.200810003.

[328] V. Giannini, A. I. Fernández-Domínguez, S. C. Heck, and S. A. Maier, "Plasmonic Nanoantennas: Fundamentals and Their Use in Controlling the Radiative Properties of Nanoemitters". *Chemical Reviews*, 111, 6, pp. 3888–3912, 2011, DOI: 10.1021/cr1002672.

[329] M. E. Kabbash, A. R. Rashed, K. V. Sreekanth, A. D. Luca, M. Infusino, and G. Strangi, "Plasmon-Exciton Resonant Energy Transfer: Across Scales Hybrid Systems". *Journal of Nanomaterials*, 2016, 2016, DOI: 10.1155/2016/4819040.

[330] K. Li, N. J. Hogan, M. J. Kale, N. J. Halas, P. Nordlander, and P. Christopher, "Balancing Near-Field Enhancement, Absorption, and Scattering for Effective Antenna–Reactor Plasmonic Photocatalysis". *Nano Letters*, 17, 6, pp. 3710–3717, 2017, DOI: 10.1021/acs.nanolett.7b00992.

[331] H. Tavernier and M. Fayer, "Distance dependence of electron transfer in DNA: The role of the reorganization energy and free energy". *Journal of Physical Chemistry B*, 104, 11541 – 11550, 2000, DOI: 10.1021/jp001362w.

[332] F. Tam, G. P. Goodrich, B. R. Johnson, and N. J. Halas, "Plasmonic enhancement of molecular fluorescence". *Nano Letters*, 7, 2, pp. 496–501, 2007, DOI: 10.1021/nl062901x.

[333] L. Zhao, T. Ming, H. Chen, Y. Liang, and J. Wang, "Plasmon-induced modulation of the emission spectra of the fluorescent molecules near gold nanorods". *Nanoscale*, 3, 9, pp. 3849–3859, 2011, DOI: 10.1039/c1nr10544b.

[334] T. B. Hoang, G. M. Akselrod, C. Argyropoulos, J. Huang, D. R. Smith, and M. H. Mikkelsen, "Ultrafast spontaneous emission source using plasmonic nanoantennas". *Nature Communications*, 6, 1, p. 7788, 2015, DOI: 10.1038/ncomms8788.

[335] O. Bitton, S. N. Gupta, and G. Haran. *Quantum dot plasmonics: From weak to strong coupling*. 2019. DOI: 10.1515/nanoph-2018-0218.

[336] L. Efremushkin, S. K. Bhunia, R. Jelinek, and A. Salomon, "Carbon Dots-Plasmonics Coupling Enables Energy Transfer and Provides Unique Chemical Signatures". *Journal of Physical Chemistry Letters*, 8, 24, pp. 6080–6085, 2017, DOI: 10.1021/acs.jpclett.7b02778.

[337] J. M. Katzen, C. Tserkezis, Q. Cai, L. H. Li, J. M. Kim, G. Lee, G.-R. Yi, W. R. Hendren, E. J. G. Santos, R. M. Bowman, and F. Huang, "Strong Coupling of Carbon Quantum Dots in Plasmonic Nanocavities". *ACS Applied Materials And Interfaces*, 12, 17, pp. 19866–19873, 2020, DOI: 10.1021/acsami.0c03312.

[338] L. Almásy, O. P. Artykulnyi, V. I. Petrenko, O. I. Ivankov, L. A. Bulavin, M. Yan, and V. M. Haramus, "Structure and Intermolecular Interactions in Aqueous Solutions of Polyethylene Glycol". *Molecules*, 27, 2022, DOI: 10.3390/molecules27082573.

[339] C. Cruje and D. Chithrani, "Polyethylene Glycol Functionalized Nanoparticles for Improved Cancer Treatment". *Reviews in Nanoscience and Nanotechnology*, 3, 2014, DOI: 10.1166/rnn.2014.1042.

[340] M. Li, S. Jiang, J. Simon, D. Paßlick, M.-L. Frey, M. Wagner, V. Mailänder, D. Crespy, and K. Landfester, "Brush Conformation of Polyethylene Glycol Determines the Stealth Effect of Nanocarriers in the Low Protein Adsorption Regime". *Nano Letters*, 21, pp. 1591–1598, 2021, DOI: 10.1021/acs.nanolett.0c03756.

[341] G. FRENS, "Controlled Nucleation for the Regulation of the Particle Size in Monodisperse Gold Suspensions". *Nature Physical Science*, 241, 105, pp. 20–22, 1973, DOI: 10.1038/physci241020a0.

[342] A. M. Smith, K. A. Johnston, S. E. Crawford, L. E. Marbella, and J. E. Millstone, "Ligand density quantification on colloidal inorganic nanoparticles". *The Analyst*, 142, 1, pp. 11–29, 2017, DOI: 10.1039/C6AN02206E.

[343] J. B. ten Hove, L. M. I. Schijven, J. Wang, and A. H. Velders, "Size-controlled and water-soluble gold nanoparticles using UV-induced ligand exchange and phase transfer". *Chemical Communications*, 54, 95, pp. 13355–13358, 2018, DOI: 10.1039/C8CC05899G.

[344] G. Bisker and D. Yelin, "Noble-metal nanoparticles and short pulses for nanomanipulations: theoretical analysis". *Journal of the Optical Society of America B*, 29, 6, p. 1383, 2012, DOI: 10.1364/JOSAB.29.001383.

[345] D. M. Schaadt, B. Feng, and E. T. Yu, "Enhanced semiconductor optical absorption via surface plasmon excitation in metal nanoparticles". *Applied Physics Letters*, 86, 6, 2005, DOI: 10.1063/1.1855423.

[346] Y. Liu, C. Y. Liu, Z. Y. Zhang, W. D. Yang, and S. D. Nie, "Plasmon-enhanced photoluminescence of carbon dots-silica hybrid mesoporous spheres". *Journal of Materials Chemistry C*, 3, 12, pp. 2881–2885, 2015, DOI: 10.1039/c4tc02599g.

[347] M. Achermann, "Exciton-plasmon interactions in metal-semiconductor nanostructures". *Journal of Physical Chemistry Letters*, 1, 19, pp. 2837–2843, 2010, DOI: 10.1021/jz101102e.

[348] T. Soller, M. Ringler, M. Wunderlich, T. A. Klar, J. Feldmann, H.-P. Josel, Y. Markert, A. Nichtl, and K. Kürzinger, "Radiative and Nonradiative Rates of Phosphors Attached to Gold Nanoparticles". *Nano Letters*, 7, 7, pp. 1941–1946, 2007, DOI: 10.1021/nl070623b.

[349] H. Choi, S.-J. Ko, Y. Choi, P. Joo, T. Kim, B. R. Lee, J.-W. Jung, H. J. Choi, M. Cha, J.-R. Jeong, I.-W. Hwang, M. H. Song, B.-S. Kim, and J. Y. Kim, "Versatile surface plasmon resonance of carbon-dot-supported silver nanoparticles in polymer optoelectronic devices". *Nature Photonics*, 7, 9, pp. 732–738, 2013, DOI: 10.1038/nphoton.2013.181.

Scientific publications

- M. Reale, S. Chandra, G. Buscarino, A. Emanuele, M. Cannas, O. Ikkala, A. Sciortino, F. Messina, "Photoinduced charge separation in functional carbon–silver nanohybrids", *Physical Chemistry Chemical Physics*, 2022, 24, 12974-12983 **(10.1039/D2CP00668E)**.

- M. Reale, A. Sciortino, C.M. Cruz, M. Cannas, E. Maçoas, A.G. Campaña, F. Messina, "The photophysics of distorted nanographenes: Ultra-slow relaxation dynamics, memory effects, and delayed fluorescence", *Carbon*, 2023, 206, 45-52 **(10.1016/j.carbon.2023.02.001)**.

- M. Reale, A. Sciortino, M. Cannas, E. Maçoas, A. H. G. David, C. M. Cruz, A. G. Campaña, F. Messina, **Atomically Precise Distorted Nanographenes: The Effect of Different Edge Functionalization on the Photophysical Properties down to the Femtosecond Scale**, *Materials*, 2023, 16, 835 **(10.3390/ma16020835)**.

- J. P. Mora-Fuentes, M. D. Codesal, M. Reale, C. M. Cruz, V. Jiménez, A. Sciortino, M. Cannas, F. Messina, V. Blanco, A.G. Campaña, **Heptagon-Containing Nanographene Embedded into [10]Cycloparaphenylene**, *Angewandte Chemie International Edition*, 2023, 62, e202301356 **(10.1002/anie.202301356)**.

- A. Pramanik, A. Sciortino, M. Reale,P. Pasbakhsh, G. Cavallaro, M. Cannas, G. Lazzara, F. Messina, **Naturally Occurring Halloysite Nanotubes as Light Scatterers for Stable Random Lasing Applications**, *ACS Applied Nano Materials*, 2023, 6, 15896-15905 **(10.1021/acsanm.3c02840)**.

- F. C. Herrera, V. Sireus, P. Rassu, L. Stagi, M. Reale, A. Sciortino, F. Messina, G. J. A. A. Soler-Illia, L. Malfatti, P. Innocenzi **Chemical Design of Efficient Photoelectrodes by Heterogeneous Nucleation of Carbon Dots in Mesoporous Ordered Titania Films**, *Chemistry of Materials*, 2023, 35, 8009-8019 **(10.1021/acs.chemmater.3c01164)**.

Oral Communications to International Conferences

- **M. Reale**, A. Sciortino, G. Buscarino, A. Emanuele, N. Mauro, M. Cannas, F. Messina, "Self-assembled Carbon dot-Plasmonic nanohybrids with remarkable charge separation and photocatalytic properties", **eMRS 2021 Fall**.
- **M. Reale**, S. Chandra, G. Buscarino, A. Emanuele, M. Cannas, A. Sciortino, F. Messina, "Photoinduced charge separation in self-assembled Carbon dot-Plasmonic functional nanohybrids", **eMRS 2022 Spring**.
- **M. Reale**, A. Sciortino, M. Cannas, E. Maçôas, A. G. Campaña, F. Messina, "Structural-Photophysical Relationships in Atomically-Precise Distorted Nanographenes", **Carbon 2022 (London)**.
- **M. Reale**, S. Chandra, G. Buscarino, A. Emanuele, M. Cannas, O. Ikkala, A. Sciortino, F. Messina, "Modulation of Optical Properties in Self-Assembled Carbon dot-Plasmonic functional Nanohybrids", **eMRS Spring 2023 (Strasbourg)**.
- **M. Reale**, A. Sciortino, M. Cannas, E. Maçôas, C. M. Cruz, A. G. Campaña, F. Messina, "Tailoring the photophysics of atomically-precise distorted nanographenes by structural engineering", **eMRS Spring 2023 (Strasbourg)**.

Poster Contributions

- **M. Reale**, A. Sciortino, G. Buscarino, A. Emanuele, N. Mauro, M. Cannas, F. Messina, "Charge Separation and Photocatalysis in Carbon dot-Plasmonic nanohybrids", **7th Nano Today Conference**

Acknowledgements

Since the early days of my PhD, I realized that it would be the final stage of my overall "course of study". Although I don't entirely agree with the idea that my life as a "student" is over, even from a merely etymological point of view, the official conclusion of my cursus studiorum requires me to thank all those people who, more or less directly, have contributed to my formation.

My first thanks go to my supervisor, Fabrizio. Firstly, for your constant support, which has started exactly four years ago at the beginning of my master's thesis work and has persisted ever since. The continuous sharing of your scientific experience has allowed me to learn so much in such an optimistic and, I dare say, enjoyable way that a PhD becomes such a pleasant experience that I would do again a thousand times. With you, even the desperate detection of the signal arising from a single photon, or the boring procedure of paper submission, become funny. I have always admired your pervasive, enthusiastic, and contagious passion, from which I hope to continue to be "infected". I consider myself privileged to have had the opportunity to work with you, as well as with Alice.

Honestly, although just recently I discovered that you were my official co-supervisor, I have always considered you as such for the help you have given me over these three years, filled with countless advices and suggestions that I think I have always followed... except for one: 'no measurements on Friday afternoon'. I confess that I have disregarded this several times. I hope to become capable like you in finding the overlap between micrometric laser beams by eye.

I wish to express special gratitude to my namesake, Marco, who initiated me into the job of Experimental Physicist. It's always a great pleasure to engage in conversation about science with you... but also about football. I would like to extend my thanks to the other seniores of the Labsam group: Prof. Gelardi, Simone A., and Giampiero. Thank you for your contribution to my scientific education and the various suggestions received over these years in several occasions, more or less formal. Thanks to all of you for how you welcomed me into your group, always characterized by a pleasant and cheerful atmosphere, of which I am proud to be a part. I wish to thank also Emanuele M., you enriched my last year of PhD with a lot of suggestions and ideas. Thank you!

I also want to express particular gratitude to Prof. A. G. Campaña's group, which provided many of the samples studied during my work, and to Prof. E. Reguera. It has been a pleasure, and will continue to be, to collaborate scientifically with you.

I would like to thank all my colleagues who acceded as roommates in the 'young people' room, which I had to leave a few days ago with a bit of "homesickness". Thanks to Angelo, Federico, Angela, Francesca, Roberta (why are you in our room?), Ludovico, Tanzeel, Pietro, Ashim, Antonino, Emanuele S., and the new entries Simone B. and Salvo.

With some more, with some less, we spent many pleasant days, filled with laughters, lunches, snacks, ice-creams, sweets... but also discussions, scientific or not, and above all shared joys when our lab sessions were ok and, perhaps more often, mutual support when the measurements had no sense or the instruments decided to take a break.

Looking back to the University years, thanks go to various colleagues, especially Dario, Giovanni and Vito with whom, along with Emanuele S., we formed the Lab-bot group. Thanks to you too, those years flew by!

Although not directly related to my University formation I take this opportunity to thank all the friends, "fanta-coaches", the classmates of the legendary III B, and the companions of adventures, who honor me with their friendship, many of whom are spread around the World. Your support has certainly been crucial for me in these years (or rather, decades... yes, we are getting old...). Thank you guys!

Thinking in particular to my "umbertini" years, I wish this to be an occasion to thank all the teachers who contributed to my education and formation. Without intending to undermine the others, I owe special thanks to Prof. Pampi. You were decisive in growing my passion for Science, as well in the choice of my academic study. "You've wasted on studying law", you used to tell me. And now I am here, concluding a PhD in Physics and Chemistry.

I could go on in this non-Nashovian chain of acknowledgements because I feel that I owe a lot to many. But I certainly can't mention everyone. Therefore, for last, but not least, I must mention and thank my whole family for the immeasurable support and vicinity. Certainly, I never learned any physics from you, quite the opposite... but you taught me most of everything else, especially the value of dedication to work seasoned with selflessness and spirit of sacrifice. Without these, I would hardly have made it. You have been, and will be, the most important boundary conditions (even if you can't fully appreciate the gratitude behind such an expression) that have allowed me to be what I am today (perhaps this sounds more like a fault than a merit). Overall, I think you are quite proud of me, also you missing grandparents that I still feel at my side. Also for this, I want to thank you. I will be forever grateful to you.

Marco